Ramiro Pérez Campos
Antonio Contreras Cuevas
Rodrigo A. Esparza Muñoz *Editors*

Characterization of Metals and Alloys

Springer

Characterization of Metals and Alloys

Ramiro Pérez Campos • Antonio Contreras Cuevas
Rodrigo A. Esparza Muñoz
Editors

Characterization of Metals and Alloys

Springer

Editors
Ramiro Pérez Campos
Centro de Física Aplicada y
Tecnología Avanzada (CFATA)
Querétaro, México

Rodrigo A. Esparza Muñoz
Centro de Física Aplicada y
Tecnología Avanzada (CFATA)
Querétaro, México

Antonio Contreras Cuevas
Instituto Mexicano del Petróleo
Distrito Federal
México

ISBN 978-3-319-31693-2 ISBN 978-3-319-31694-9 (eBook)
DOI 10.1007/978-3-319-31694-9

Library of Congress Control Number: 2016952548

Printed on acid-free paper

This Springer imprint is published by Springer Nature
The registered company is Springer International Publishing AG Switzerland

Preface

"Characterization of Metals and Alloys" includes a compilation of the best research works presented in Symposium 5B "Structural and chemical characterization of metals, alloys and compounds," from the XXIV International Materials Research Congress (IMRC-2015). The XXIV International Materials Research Congress was held on August 16–20, 2015, in Cancún, Mexico. IMRC was organized by the Sociedad Mexicana de Materiales (SMM). About 1850 registered participants from more than 50 countries participated in the 36 different symposia, workshops, plenary lectures, and tutorial courses. The 36 symposia that comprise the technical program of IMRC-2015 are grouped in several clusters, namely, Nanoscience and Nanotechnology, Bio-inspired Materials, Materials for Energy, Fundamentals of Materials Science, Materials Characterization, Materials for Specific Applications, Magnetic and Electronic Materials, and General.

The articles contained in this book include characterization of materials prepared by different fabrication and production methods; the book covers state-of-the-art and experimental techniques commonly used in modern materials characterization of metals and alloys. In addition, the book introduces advanced techniques, including: scanning probe microscopy, aberration-corrected scanning transmission electron microscopy, Raman spectroscopy, Fourier transform infrared spectroscopy, and field emission scanning electron microscopy (FESEM). This book covers several aspects of the structural and chemical characterization of the materials such as metals, alloys, steels, welding, nanomaterials, and coatings. The materials are amorphous, crystalline, powders, coatings, fibers, and thin films, and were prepared with different techniques. Structural characterization techniques include: scanning electron microscopy (SEM), X-ray diffraction (XRD), transmission electron microscopy (TEM), aberration-corrected scanning transmission electron microscopy (STEM), Raman spectroscopy, optical microscopy (OM), Fourier transform infrared spectroscopy (FTIR), differential thermal analysis (DTA), electrochemical impedance spectroscopy (EIS), differential scanning calorimetry (DSC), finite element method (FEM), thermoluminescence (TL), and laser emission.

The structure of the book is classified in nine parts: (1) Characterization of Steels Used in the Oil Industry, (2) Characterization of Copper Alloys, (3) Characterization of Steels by Applying Heat Treatment, (4) Characterization of Thin Layers and Coatings, (5) Characterization of Materials Obtained by Mechanical Milling, (6) Characterization of Materials for Medical Applications, (7) Characterization of Materials for Industrial Applications, (8) Characterization of Welding and Joining of Materials, and (9) Characterization of Intermetallic Materials.

Santiago de Querétaro, México Dr. Ramiro Pérez Campos
Distrito Federal, México Dr. Antonio Contreras Cuevas
Santiago de Querétaro, México Dr. Rodrigo A. Esparza Muñoz

Acknowledgments

We would like to thank Springer editorial for publishing this book, as well as the committee assigned for the edition of the book and the reviewers of the articles for their valuable comments, which have certainly helped to improve the quality of the manuscripts. We also wish to thank the Sociedad Mexicana de Materiales (SMM), Centro de Física Aplicada y Tecnología Avanzada (CFATA) from Universidad Nacional Autónoma de México (UNAM), and Instituto Mexicano del Petróleo (IMP) for their support in organizing the Symposium 5B “Structural and chemical characterization of metals, alloys and compounds,” belonging to XXIV International Materials Research Congress (IMRC-2015) from which the articles are included in this book. Additionally, we would like to thank all the authors of the articles who have worked to improve the quality of the articles considering reviewers’ comments, which are the result of their valuable research work and make possible the edition of this book.

Finally, we would like to thank those who have worked to make this congress an exciting and fruitful meeting.

List of Abbreviations

A	Austenite
AE	Auxiliary electrode
AF	Acicular ferrite
AISI	American Iron and Steel Institute
API	American Petroleum Institute
ASME	American Society of Mechanical Engineers
ASTM	American Standard Testing Machine
AT	Aging time
B	Bainite
BM	Base metal
CBD	Chemical bath deposition
CCT	Continuous cooling transformation
CSA	Canadian Standards Association
DNV	Det Norske Veritas
DPI	Digital processing image
DSAW	Double submerged arc welding
DSC	Differential scanning calorimetry
Ea	Activation energy
EDM	Electrical discharge machining
EDS	Energy-dispersive spectroscopy
EDX	Energy-dispersive X-ray
EIS	Electrochemical impedance spectroscopy
ERW	Electric resistance welding
F	Ferrite
FEA	Finite element analysis
FTIR	Fourier transform infrared spectroscopy
GMAW	Gas metal arc welding
HA	Hydroxyapatite

HAZ	Heat-affected zone
HE	Hydrogen embrittlement
HEM	High-energy milling
HIC	Hydrogen-induced cracking
HRTEM	High-resolution transmission electron microscopy
HSLA	High-strength low alloys
HT	Heat treatment
HV	Hardness Vickers
IEAW	Indirect electric arc welding
IMRC	International Materials Research Congress
IRS	Infrared spectroscopy
ISO	International Standards Organization
LPCVD	Low-pressure chemical vapor deposition
M	Martensite
MPF	Mapping of polycrystalline flow
MPY	Mils-inch per year
NACE	National Association of Corrosion Engineers
NDT	Nondestructive testing
OES	Optical emission spectroscopy
OM	Optical microscopy
P	Perlite
PC	Polarization curves
PWHT	Post-weld heat treatment
RE	Reference electrode
RS	Raman spectroscopy
SAE	Society of Automotive Engineers
SAW	Submerged arc welding
SCC	Stress corrosion cracking
SCE	Saturated calomel electrode
SEM	Scanning electron microscopy
SMM	Sociedad Mexicana de Materiales
SS	Stainless steel
SSRT	Slow strain rate test
STEM	Scanning transmission electron microscopy
TEM	Transmission electron microscopy
TGA	Thermal gravimetric analysis
TL	Thermoluminescence
TMCP	Thermomechanical controlled processing
UTS	Ultimate tensile strength
UV-Vis	Ultraviolet–visible spectroscopy
YS	Yield strength

Biography of Editors

Dr. Ramiro Pérez Campos received his bachelor's and master's degrees in physics at the National Polytechnic Institute in México. He obtained his Ph.D. in physics at the University of Alberta, Canada, in 1983. He also carried out postdoctoral work at the KFA in Jülich, Germany. He was awarded an Alexander Von Humboldt postdoctoral scholarship. He is the author of more than 170 scientific papers, all of them related to the applications of the transmission electron microscope in materials science. Dr. Ramiro Pérez Campos has cultivated lines of research related with theoretical simulations of images obtained by transmission electron microscopy (TEM). Theoretical simulations have been based on electron diffraction using the theory of Bethe and the multilayer model. Currently, he is the director of Centro de Física Aplicada y Tecnología Avanzada (CFATA) from Universidad Nacional Autónoma de México (UNAM).

Dr. Antonio Contreras Cuevas received his bachelor's degree in mechanical engineering in 1994. He received a master's degree in metallurgy and materials science at Universidad Michoacana in 1997. He obtained his Ph.D. in 2002 in metallurgy and materials science from Universidad Nacional Autónoma de México (UNAM). Since 2003, he has been a pipeline materials researcher for the Mexican Petroleum Institute. He is a member of NACE and the Mexican Materials Society, and he belongs to the National Research System. His main research areas include stress corrosion cracking (SCC), root cause analysis (RCA), materials characterization, synthesis and characterization of composite materials, and pipeline integrity. He is the author of more than 60 scientific papers related to materials characterization by different techniques.

Dr. Rodrigo A. Esparza Muñoz obtained his Ph.D. in metallurgy and materials science at the Universidad Michoacana de San Nicolás de Hidalgo (UMSNH), México, in 2007. He carried out two postdoctoral stays, one of them in the Universidad Nacional Autónoma de México (UNAM) and the other one in the University of Texas at San Antonio (UTSA). He is the author of more than 50 scientific papers, most of them related to the characterization of nanomaterials using high-resolution transmission electron microscopy and aberration-corrected scanning transmission electron microscopy. He is a researcher at Centro de Física Aplicada y Tecnología Avanzada (CFATA) from Universidad Nacional Autónoma de México (UNAM).

Contents

Part I Characterization of Steels Used in the Oil Industry

Part II Characterization of Copper Alloys

Part III Characterization of Steels Applying Heat Treatment

Part IV Characterization of Thin Layers and Coatings

Part V Characterization of Materials Obtained by Mechanical Milling

Part VI Characterization of Materials for Medical Applications

Part VII Characterization of Materials for Industrial Applications

Part VIII Characterization of Welding and Joining of Materials

Part IX Characterization of Intermetallic Materials

Part I

Characterization of Steels Used in the Oil Industry

This part includes three chapters related to characterization of steels of common use in the oil and petrochemical industry. The first chapter includes a mechanical and microstructural characterization of API X70 steel after a non-conventional heat treatment is applied. After applying the heat treatment to X70 steel, it yielded tensile properties similar to those exhibited by an X100 steel. These benefits are obtained by taking advantage of the temperature at which the NbC begin to solubilize promoting partial austenitic grain growth followed by rapid cooling so that a predominant acicular ferrite microstructure is obtained. The second chapter is about corrosion inhibition of API X52 pipeline steel in chloride solutions adding non-ionic surfactant evaluated by electrochemical impedance spectroscopy (EIS) and potentiodynamic polarization curves. Standard free energy calculation suggested that surfactant is adsorbed physically into the X52 steel surface and consequently a decrease in corrosion rate is observed.

The third chapter shows a study on the microstructure and mechanical properties in joining ASTM A36 structural steel welded in marine environment at several depths (10, 20, 30, and 40 m). The results show that there is an inverse relationship between the increase in depth at which the welding is performed and the mechanical properties.

API steels (X52 and X70) evaluated are steels of high strength and have a good corrosion resistance with the suitable cathodic protection system and coating. Both of them are used in the transportation of hydrocarbides. On the other hand, ASTM A36 steel is used very commonly in structural marine applications.

The main techniques used in the characterization of these materials are:

- Scanning electron microscopy (SEM).
- X-ray diffraction (XRD).
- Electrochemical impedance spectroscopy (EIS).
- Polarization curves.
- Optical microscopy (OM).
- Mechanical tests.

Chapter 1
Mechanical and Metallurgical Properties of Grade X70 Steel Linepipe Produced by Non-conventional Heat Treatment

C. Natividad, R. García, V.H. López, L.A. Falcón, and M. Salazar

Abstract A nonconventional heat treatment in API X70 steel samples was carried out by heating the steel up to 1050 °C and holding for 30 min at this temperature. Subsequently, the samples were cooled in water and air. There has been recently a growing demand for higher-grade linepipes that can help to reduce the total cost of long linepipes. The application of high-strength linepipes such as API X70 and X80 grades has been increasing in recent years. The use of high-strength linepipe steels improves the efficiency of transportation by enabling large volumes under high internal pressure. Increasing yield strength and therefore thinner wall thickness enable the industry to reduce the costs of all components through the limitation of string weight. In this work, an API X70 has been developed through nonconventional heat treatment to create the suitable microstructure (acicular ferrite) which provides good toughness and sour service properties due to the bainite obtained in the microstructure. To assess the effect of the heat treatment, mechanical properties were evaluated. These results were related with the microstructures and precipitate distribution in the steel.

Keywords API X70 • Nonconventional heat treatment • Acicular ferrite • Bainite • Sour service

---

C. Natividad (✉) • R. García • V.H. López.
Instituto de Investigación en Metalurgia y Materiales (IIMM) de la Universidad
Michoacana de San Nicolás de Hidalgo, Morelia, Michoacán, México
e-mail: consnatividad@yahoo.com.mx

L.A. Falcón
Facultad de Metalurgia de la Universidad Autónoma de Coahuila, Monclova, Coahuila, Mexico

M. Salazar
Instituto Mexicano del Petróleo, Eje Central Lázaro Cárdenas Norte 152, San Bartolo
Atepehuacan, C.P. 07730 México, México

R. Pérez Campos et al. (eds.), *Characterization of Metals and Alloys*, DOI 10.1007/978-3-319-31694-9_1

1.1 Introduction

Offshore and gas exploration and production is moving in to water depths greater than 3000 m, which are challenging the well-established designs and pipes used. Pipes for these applications are exposed to high collapse pressure, to high axial loads, and partly to fatigue in the girth welds. In the early 1960s, medium carbon steel was the material used in linepipe industry. The technological development in welding processes, use of microalloying element in steel, and thermomechanical control process (TMCP) have enabled the industry in producing high-strength steels, therefore moving to low-carbon steels with high strength as well as weldability. This has further helped in reducing the specific steel consumption in oil and gas transportation. The current focus on less wall thickness at strength level leads to the use of X80 and X100 grades of steel [1–4].

Mechanical and corrosion properties of API X70 are improved by the addition of alloying and control of parameters on TMCP, such as soaking temperature, rolling temperature, finishing temperature, cooling rate, and cooling interrupt temperature [5–15]. Sulfide stress cracking (SSC) is a kind of hydrogen-related problem of linepipe steels for transportation of crude oil and natural gas containing hydrogen sulfide. The demand for high-strength steel for linepipe with sour gas resistance has increased. Manufacturing this kind of steel pipe requires a strict steel-making practice and a controlled thermomechanical schedule with an additional accelerated cooling procedure. It is well known that the API X70 steel is susceptible to corrosion in solutions containing NaCl and H_2S [16–19]. Hydrogen uptake decreases the tensile properties such as yield strength, ultimate strength, and elongation [20] and causes cracking known as hydrogen-induced cracking (HIC). With the aim of improving SSC resistance of API X70 steel, various techniques during steel-making processes are required such as addition of proper alloying elements, microstructure control, high cleanness, and Ca treatment [1, 9–11, 21–24].

Among various types of microstructure, acicular ferrite has been known as the optimum microstructure which has excellent combination of high strength and good toughness, mainly due to its relatively high density of dislocations and fine-grained nature [25–28]. However, judicious selection of microalloying elements and optimization of process parameters is essential to obtain the required microstructure [29]. The coarse ferrite grains and the relatively low dislocation density enhanced hydrogen buildup in the stress-concentrated zone ahead of the crack tip, facilitating decohesion and cracking of particles in this zone [30, 31]. Therefore, most of the API X70 to X100 grades linepipe steels utilize the acicular ferrite structure to obtain the balanced properties required for linepipe applications. However, acicular ferrite in linepipe steels nucleated mainly at nucleation sites of dislocation substructures within deformed austenite grain, unlike the bainite, which nucleated at grain boundary of austenite. Increased acicular ferrite content in the microstructure improved HIC resistance and SSC resistance, while bainite and martensite/austenite constituents are harmful for the resistance in sour environments [14, 32]. The steels with a fine-grained, bainite-ferrite structure possess a much better combination of strength and SCC resistance than those with a ferrite + pearlite structure. An increase in the pearlite content in the microstructure has a detrimental effect on the SCC resistance of linepipe steels with a ferrite + pearlite structure [33].

Because is has greater requirements for welding high-strength steels, such as X80 and X100, it proposed to obtain a steel of equal or higher strength than X80 from an API X70 steel by applying a nonconventional heat treatment in order to achieve the acicular ferrite-dominated microstructure.

1.2 Experimental

The material used in the present study was API 5L X70 pipe with an outside diameter of 740 mm and a wall thickness of 11.35 mm. The chemical composition of this steel is shown in Table 1.1. Specimens of 70 mm × 150 mm were heat-treated at 1050 °C for 30 min and cooled in water or air. Heat-treated and as-received plates were machined in dog bone shape according to ASTM A370 [34] for tensile testing. Impact test with Charpy V-notch specimens (CVN 10 mm × 10 mm × 55 mm) was carried out at 0 °C according to ASTM E23 [35].

Microhardness measurements were conducted in the as-received steel and in the heat-treated samples. The as-received steel was etched for 15 s in 2.5 % nital. Microstructural analysis was carried out by optical (OM) and scanning electron microscopy (SEM).

1.3 Results and Discussion

Figure 1.1 shows the microstructure of the API X70 steel in the different conditions: as-received, nonconventional heat-treated water-cooled, and heat-treated air-cooled. In the as-received material, Fig. 1.1a shows a microstructure characterized by polygonal ferrite grains (F) and perlite bands (P), typical of this type of steel. Figure 1.1b shows a microstructure composed of fine acicular ferrite (AF) and bainite (B) which was the result of the nonconventional heat treatment when the sample was cooled rapidly with water.

This type of microstructure is preferred to reduce the susceptibility to SCC, as reported by references [32, 33]. Figure 1.1c reveals that when the steel was cooled

Table 1.1 Chemical composition of X70 steel (wt.%)

Steel	C	Mn	Si	P	S	Al	Nb	Cu	Cr	Ni	V	Ti
X70	0.08	1.604	0.31	0.019	0.005	0.023	0.03	0.013	0.138	0.012	0.046	0.01

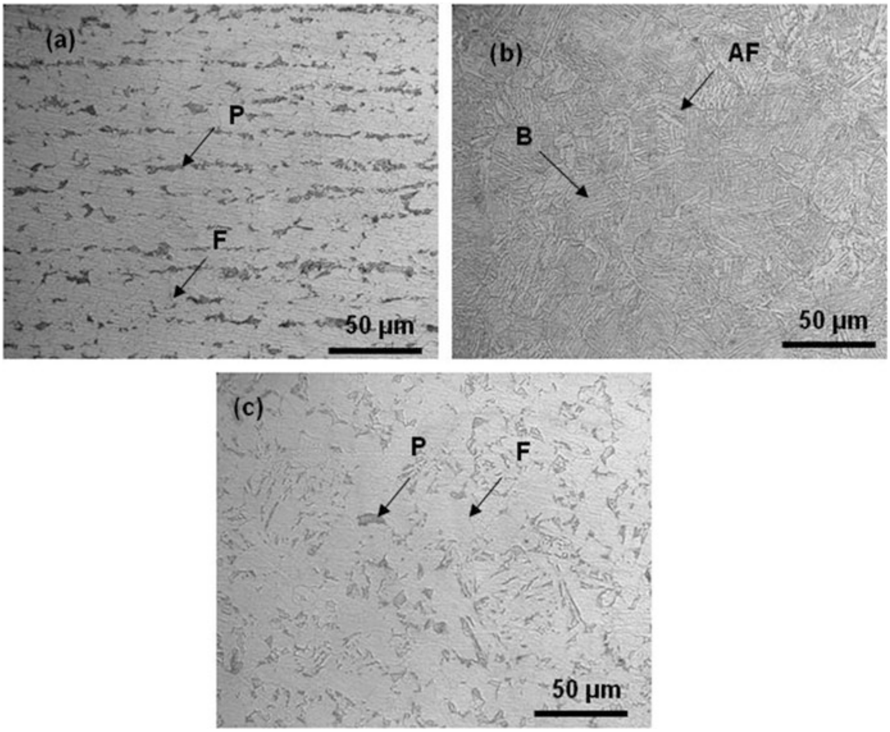

Fig. 1.1 Optical images of the microstructure of API X70 steel: (**a**) as-received, (**b**) heat-treated water-cooled, and (**c**) heat-treated air-cooled. F, ferrite (*gray phase*); P, perlite (*dark phase*); AF, acicular ferrite; and B, Bainite

more slowly, the microstructure is similar to the one obtained by a normalizing heat treatment: polygonal ferrite and perlite areas with longer grain size than the as-received material.

Figure 1.2 shows the stress-strain curves obtained from API X70 with and without heat treatment. Tensile properties and impact results are summarized in Table 1.2 along with impact results.

The results obtained by tensile tests show that heat treatment with water-cooling leads to higher tensile strength as is reported by [1–4]. Although ductility decreased, it has been reported that the microstructure of acicular ferrite and bainite obtained with the nonconventional heat treatment is resistant to SCC [33] but not for sour environments [14, 32]. According to the literature, for the impact test, the minimum impact energy requirements for a design factor of 0.625 is 48 J [36]; in the present work, it was 60 J of energy absorbed. In the fracture surfaces analyzed by SEM, it is evident that both specimens exhibited a kind of ductile fracture, since they showed micro-plastic deformation, nucleation, and coalescence of microvoids around nonmetallic inclusions (Fig. 1.3a). These inclusions were

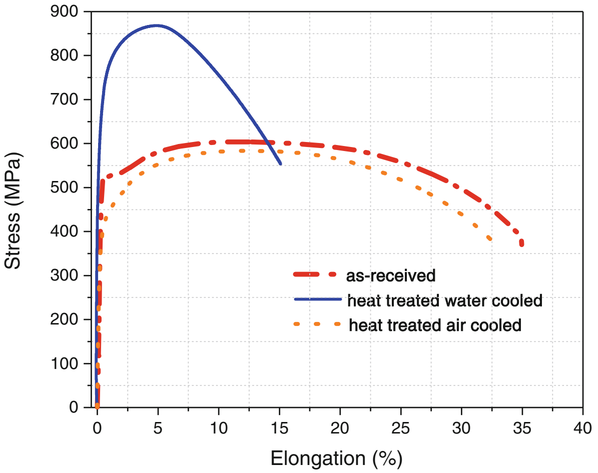

Fig. 1.2 Stress-elongation curves for API X70 steel

Table 1.2 Summary of mechanical properties obtained for API X70 steel with and without heat treatment

Steel (X70)	UTS (MPa)	YS (MPa)	$\sigma_{RUPTURE}$ (MPa)	EL (%)	EA (J)
As-received	604	522	350	35	176
Heat-treated water-cooled	868	644	550	15.2	60
Heat-treated air-cooled	584	512	375	34.7	130

UTS ultimate tensile strength, *YS* yield strength, $\sigma_{RUPTURE}$ fracture stress or rupture strength, *EL* elongation, *EA* energy absorbed

identified by energy-dispersive X-ray spectroscopy (EDX), attached to the SEM, as well as iron-manganese sulfides. Figure 1.3d shows the EDX spectra corresponding to these inclusions. The inclusions are mainly composed by Fe, Mn, S, Mg, and Ca. These elements can form (Fe,Mn)S, MnS, and globular inclusions or Fe-Mn-S as reported in literature [37].

The limits of hardness recommended for avoiding SSC are in the range of 20–30 HRC (240–250 Hv), but the 22 HRC and its equivalent in the other hardness scale is the more common reported by the standard [36]. Although the limits of hardness are not always an effective guide for the selection of material, these limits are the more common requirements for the line-pipes in sour service. The results of the hardness measurements obtained are presented in Fig. 1.4. Hardness obtained from heat-treated water-cooled samples increased in a range of 280–310 Hv. For the room temperature-cooled specimen, the hardness decreased from 180 to 200 Hv, and for the as-received specimen, its hardness was 200–220 Hv.

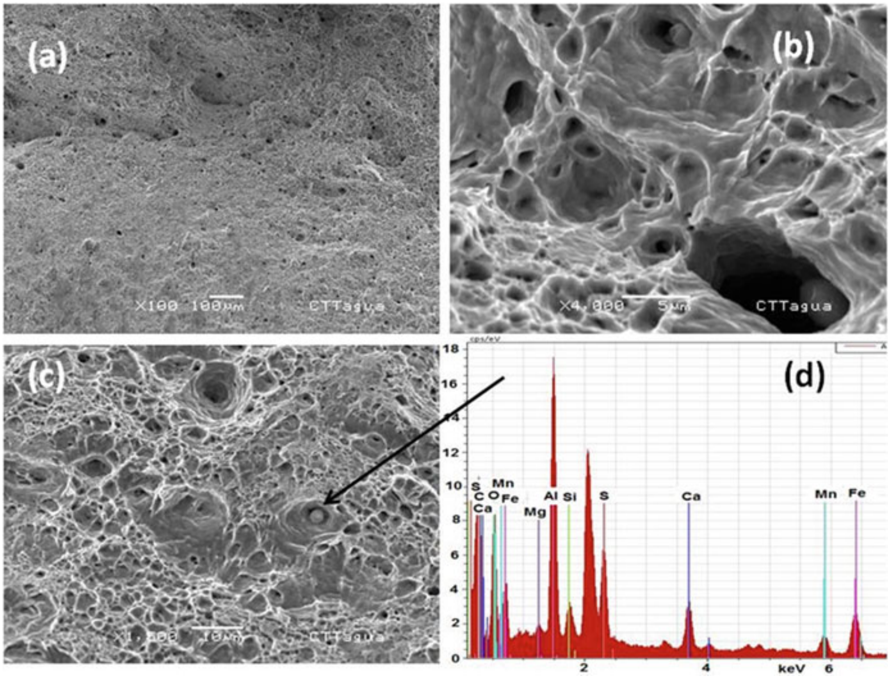

Fig. 1.3 SEM micrographs obtained from fractured samples water-cooled by tensile test, (**a**) shows the typical fracture ductile, (**b** and **c**) shows a globular inclusion, and (**d**) X-ray compositional spectrum of inclusions is showed in (c)

Fig. 1.4 Hardness measurements in as-received and heat-treated API X70 steel

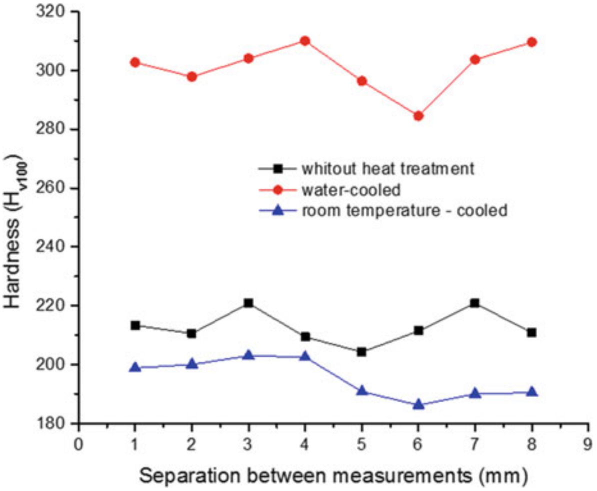

1.4 Conclusions

Heat treatment applied to an API 5L X70 pipe steel to 1050 °C for 30 min following water-cooling yields acicular ferrite and bainite microstructure with mechanical strength 250 MPa higher than as-received steel. Although hardness increased with heat-treating, the average value is below the permissible limit for service. The results obtained with the nonconventional heat treatment yield similar properties as API 5L X120 steel. However, the high hardness of this steel prevents its use with sour hydrocarbons. The findings of this study imply that is possible to reduce the wall thickness of linepipes to transport sweet crude oil.

Acknowledgements The authors would like to thank CONACYT for sponsoring the postdoctorate stay of C. Natividad and financial support of this investigation.

References

1. Lakshminarasimham B, Wadnerkar R, Borkar M (2012), Steel plate processing for linepipes in oil and gas transport. In: Materials science and technology conference, vol 2, pp 917–928
2. Wiebe J, Bruns C, Toma D (2013), Weldability of heavy wall seamless line pipe steel X80. In: ISOPE conference
3. Omweng GM, Frankel GS, Bruce WA, Ramirez JE, Koch G (2003), Performance of welded high-strength low alloy steels in sour environments. Corrosion 59:640–653
4. Kim ChM, Lee JB, Yoo JY (2005), A study on the metallurgical and mechanical characteristics of the weld joint of X80 steel. In: ISOPE conference paper
5. Ha HM, Ai JH, Scully JR (2014), Effects of prior cold work on hydrogen trapping and diffusion in API X-70 line pipe steel during electrochemical charging. Corrosion 70:166–184
6. Reepmeyer O, Liessem A, Schroeder J, Maerten B, Combaud F, Fluess P, Buirette C (2013), UOE pipes for ultra-deep water. In: Proceedings of the annual offshore technology conference, application, vol 1, pp 354–366
7. Ung KS, Young KK, Young YB (2004), The Effect of chromium and molybdenum on the susceptibility to sulfide stress cracking of API X70 grade linepipe steels. In: NACE conference paper
8. Toma D, Rohden V, Kubla G (2011), Development of API X70-X80 grades heavy-wall seamless pipes with low temperature toughness. In: OTC conference paper
9. Toma D, Guido K, Volker R (2013), API X70Q-X80Q heavy-wall seamless pipes for sour-service application. In: ISOPE conference paper
10. Mendoza R, Alanis M, Perez R, Alvarez O, Gonzalez C, Islas J (2002), On the processing of Fe-C-Mn-Nb steels to produce plates for linepipes with sour gas resistance. Mater Sci Eng A 337:115–120
11. Mendoza R, Huante J, Alanis M, Gonzalez-Rivera C, Juarez-Islas JA (1999), Slab cracking after continuous casting of API 5L X-70 grade steel for linepipe sour gas application. Ironmaking Steelmaking 26:205–209
12. Masato S, Mutsuo H, Haruo K (1986), Mill trial for application of accelerated cooling combined with controlled rolling to X70 linepipe steel plates. Trans Iron Steel Inst Jpn 26:790–797
13. Saxena A, Kumar S, Prakash K, Datta R, Jha BK, Siciliano F, Misra RDK, Chaudhuri SK (2011), Development of API X-70 grade plates and strips in SAIL. Mater Manuf Processes 26:161–164

14. Beidokhti B, Dolati A, Koukabi AH (2009), Effects of alloying elements and microstructure on the susceptibility of the welded HSLA steel to hydrogen-induced cracking and sulfide stress cracking. Mater Sci Eng A 507:167–173
15. Shirband Z, Shishesaz MR, Ashrafi A (2012), Investigating the effect of heat treatment on hydrogen permeation behavior of API X-70 steel. Phase Transit 85:503–511
16. Arzola S, Mendoza-Flores J, Duran-Romero R, Genesca J (2006), Electrochemical behavior of API X70 steel in hydrogen sulfide-containing solutions. In: NACE journal paper
17. Fang BY, Han EH, Wang JQ, Ke W (2007), Stress corrosion cracking of X-70 linepipe steel in near neutral pH solution subjected to constant load and cyclic load testing. Corros Eng Sci Technol 42:123–129
18. Arzola S, Genescá J (2005), The effect of H2S concentration on the corrosion behavior of API 5L X-70 steel. J Solid State Electrochem 9:197–200
19. Contreras A, Salazar M, Albiter A, Galván R, Vega O (2011), Assessment of Stress Corrosion Cracking on linepipe Steels Weldments used in the Petroleum Industry by Slow Strain Rate Tests. In: Sudnik W (ed), Arc Welding, Intech, Croatia
20. Bellahcene T, Capelle J, Aberkane M, Azari Z (2012), Effect of hydrogen on mechanical properties of linepipe API 5L X70 steel. Appl Mech Mater 146:213–225
21. Kim WK, Kim KY, Yun TW, Yang BY (2008), The effect of metallurgical factors on SSC of high strength linepipe steel, 08496. In: NACE conference paper
22. Mendoza R, Huante J, Camacho V, Alvarez-Fregoso O, Juarez-Islas JA (1999), Development of an API 5L X-70 grade steel for sour gas resistance linepipe application. J Mater Eng Perform 8:549–555
23. Yang BY, Kang KB, Kim CM (2005). Development of high strength hot rolled steel strip for sour service. In: NACE Conference Paper, 05110
24. Zhao MC, Tang B, Shan YY, Yang K (2003), Role of microstructure on sulfide stress cracking of oil and gas linepipe steels. Metall Mater Trans A 34A:1089–1096
25. Kim YM, Lee H, Kim NJ, Yoo JY (2005), Microstructural characteristics of acicular ferrite in linepipe steels, I-05-372. In: ISOPE, conference paper
26. Yang X, Salem M, Palmiere EJ (2010), The effect of processing conditions and cooling rate on the microstructure and properties of API X-70 and API X-100 steels, Mater Manuf Process 25:48–53
27. Salem M, Al-Muaili SM, Palmiere EJ (2009), The effect of processing conditions and cooling rate on API X-70 and X-100 grade steels. In: Materials science and technology conference and exhibition 3:1644–1651
28. Hwang B, Kim YM, Lee S, Kim NJ, Ahn SS (2005), Correlation of microstructure and fracture properties of API X70 linepipe steels. Metall Mater Trans A 36:725–739
29. Reip CP, Shanmugam S, Misra RDK (2006) High strength microalloyed CMn(V–Nb–Ti) and CMn(V–Nb) linepipe steels processed through CSP thin-slab technology: Microstructure, precipitation and mechanical properties. Mater Sci Eng A, 424:307–317
30. Haq AJ, Muzaka K, Dunne DP, Calka A, Pereloma EV (2013) Effect of microstructure and composition on hydrogen permeation in X70 linepipe steels. Int J Hydrogen Energy 38:2544–2556
31. Hejazi D, Haq AJ, Yazdipour N, Dunne DP, Calka A, Barbaro F, Pereloma EV (2012) Effect of manganese content and microstructure on the susceptibility of X70 linepipe steel to hydrogen cracking. Mater Sci Eng A 551:40–49
32. Ro KS (2000), Improvement on the sulfide stress corrosion cracking properties of hot rolled line-pipe steels. Corrosion 2000 NACE, 00382
33. Lu BT, Luo JL (2006), Relationship between yield strength and near-neutral pH stress corrosion cracking resistance of linepipe steels - an effect of microstructure. NACE J 62:129–140
34. ASTM A 370 (2014), Standard test methods and definitions for mechanical testing of steel products

35. ASTM E 23 (2013), Standard test methods for notched bar impact testing of metallic materials
36. American Petroleum Institute (2013), Specification for line pipe. API specification 5L, 45th edn. American Petroleum Institute, Washington, DC
37. Ray A, Paul S, Jha S (1995), Effect of inclusions and microstructural characteristics on the mechanical properties and fracture behavior of HSLA steel. J Mater Eng Perform 4:679–688, Springer

Chapter 2
Corrosion Inhibition of X52 Pipeline Steel in Chloride Solutions Using Nonionic Surfactant

L.M. Quej, A. Contreras, and J. Aburto

Abstract Two concentrations of NPE-4 nonionic surfactant and corrosion inhibitor (CI) commercially available were added to NaCl (2.45 % and 3 %) and ocean water solutions (OWS) in order to study the corrosion process of API X52 pipeline steel. Corrosion inhibition of X52 pipeline steel in chloride solutions was evaluated by using electrochemical impedance spectroscopy (EIS) and potentiodynamic polarization curves. EIS analyses showed that 3 % NaCl was the more corrosive solution for X52 steel. Adding CI to 3 %NaCl solution improves the corrosion resistance of X52 steel; however, adding CI to OWS, the corrosion control of X52 steel was more evident preventing the pitting, salts embedding, and corrosion under deposits. X52 steel exposure to solutions adding surfactant as corrosion inhibitor after having been evaluated through polarization curves displayed low corrosion rates (0.88 mm/year). Standard free energy calculation suggested that surfactant is adsorbed physically into the X52 steel surface. Meanwhile, it was observed that CI was more difficult to adsorb on X52 steel surface, and consequently corrosion was higher than adding surfactant to chloride solutions.

Keywords X52 steel • Surfactant • Corrosion inhibitor • Polarization curves • Electrochemical impedance spectroscopy (EIS)

2.1 Introduction

In oil industry, the internal cleaning of pipelines is carried out using acid environment like inhibited HCl [1–4]. This type of solution is widely recommended as the cheapest way to dissolve deposit of carbonate compounds inside the pipelines and includes a surfactant that acts as an additive capable of inhibiting the corrosive effect of HCl. Migahed et al. studied the inhibition process of internal corrosion of pipelines using nonionic surfactants in the presence of 1 M HCl solution [1].

L.M. Quej (✉) • A. Contreras • J. Aburto
Instituto Mexicano del Petróleo, Eje Central Lázaro Cárdenas Norte 152,
Col. San Bartolo Atepehuacan, C. P. 07730 México, Mexico
e-mail: lquej@imp.mx

R. Pérez Campos et al. (eds.), *Characterization of Metals and Alloys*, DOI 10.1007/978-3-319-31694-9_2

Migahed's works suggested that surfactants act as good corrosion inhibitors using low concentrations and the adsorption of surfactant molecules on steel increases with increasing the tensioactive molecular size than for high concentrations and low molecular size. Another work evaluated the corrosion inhibition of mild steel using nonionic surfactants in the presence of 0.05 M NaCl solution with rotating cylinder electrode at 1000 rpm [5]. This work reported that the surfactant is adsorbed on metal surfaces acting as a corrosion inhibitor. However, the inhibitory action depends significantly from the critical micellar concentration (CMC) [6, 7]. Another study characterized the protective effect of cationic surfactants on carbon steel surfaces in the presence of 1 M HCl [8].

The results of this study revealed that the real and imaginary impedance response was higher with increasing the dosage of surfactant. However, the electrical double layer capacitance values have negative effects when the surfactant concentration is increased, due to the adsorption of surfactant molecules on metal surface. It is important to mention that others' works considered the use of anionic, cationic, and nonionic compounds that inhibit the steel corrosion process in acid solutions [9–12]. Moreover, the oil recovery in México is every time more difficult due to heavy and extra-heavy petroleum production. In addition, the deposited sediment, solids, and salts dissolved can provoke the increase of the viscosity in the petroleum.

The production of heavy and extra-heavy oil presents important challenges that require significant technological developments in the oil industry. Also, the high viscosity of the petroleum can provoke corrosion by erosion. It is well known that surfactants are used for reducing the viscosity in the heavy and extra-heavy petroleum [13, 14]. Thus, the surfactant dosage into heavy petroleum is able to improve its fluidity and easy transportation. In this way, the chemical properties of nonionic NPE-4 surfactant have been applied in heavy and extra-heavy petroleum production [13]. According to previously described, the electrochemical study of surfactants and its inhibitory properties in contact with salts, like chloride solutions or carbonate compounds that are found inside the pipeline during the heavy and extra-heavy petroleum production and can be related to the embedding or corrosion under deposits generated on the internal pipeline surface, is of great interest.

In the present work, inhibition of X52 pipeline steel corrosion in the presence of ocean water and two concentrations of NaCl solutions as well as two dosages of nonionic NPE-4 surfactant and corrosion inhibitor (CI) commercially available was studied. To carry out this study, the electrochemical impedance spectroscopy (EIS) and potentiodynamic polarization curves were proposed because of its usefulness and there was consideration to study the corrosion process in short time. First, the EIS characterization of the pipeline steel was performed in an aqueous solution mainly composed of ocean water solution (OWS) and two concentrations of NaCl as a blank. EIS analysis was carried out using equivalent circuits, where it is possible to discuss the modifications of the EIS diagrams with the presence of different steps occurring simultaneously. Based on polarization curves, the adsorption and inhibition properties were evaluated. The electrochemical behavior was related to the modification of the steps involved in the corrosion process of the pipeline steel in the chloride solutions, obtaining good inhibitory properties for the surfactant.

2.2 Experimental

2.2.1 Steel Used (Electrode)

A rod from X52 pipeline steel with 0.5 cm^2 of exposure area like working electrode (WE) was used. Rod graphite as an auxiliary electrode (AE) and a saturated calomel electrode (SCE) as a reference electrode were used. In all metallic coupons (WE), the exposed surfaces were prepared by mechanical grinding with up to 600-grit water-cooled SiC papers so as to obtain a reproducible surface and subsequently cleaned in an ultrasonic bath for 1 min in acetone. Nominal chemical composition of X52 pipeline steel is shown in Table 2.1.

2.2.2 Test Solutions

The NaCl corrosive solutions tests were prepared as follow: 2.45 g and 3.0 g of NaCl were weighed and dissolved in 1000 mL of deionized water. OWS was prepared according to ASTM D1141 standard [15]. For the electrochemical evaluation, a constant volume of 100 mL of each blank was used. The former dissolution of nonionic surfactant and CI commercially available was prepared in isopropyl alcohol to reach 30,000 mg/L (solution A). In this way, solution A was used to prepare 30 and 60 mg/L of each molecule. The electronic structure, mesoscopic simulations, and analytical characterization of NPE-4 molecule were reported in previous work [13].

2.2.3 Electrochemical Evaluations

All electrochemical characterizations were carried out in an electrochemical cell with three-electrode arrangement. Electrochemical testing was performed in a potentiostat-galvanostat AUTOLAB model PGSTAT30 at open-circuit potential (OCP). The EIS tests were obtained using 10 mV of perturbation and 10 kHz to 10 mHz of frequency after 1 h of exposure of working electrode at 30°C and 600 rpm in the corrosive solutions. Potentiodynamic polarization curves were measured by potential scanning from ±300 mV vs. OCP at a sweep rate of 1 mV/s.

Table 2.1 Chemical composition of the API X52 pipeline steel (wt %)

C	Mn	Si	P	S	Cu	Cr	Ni	Nb	V	Ti	Al	Fe
0.08	1.05	0.26	0.019	0.003	0.019	0.02	0.02	0.041	0.054	0.002	0.038	Bal.

2.3 Results and Discussion

2.3.1 Electrode

The electrodes used in the electrochemical evaluations were machined from API X52 pipeline steel. This steel has the microstructure typical of low-carbon steels, which consisted of perlite (dark grains) and ferrite. The average grain size in this steel was around 10–20 μm as is shown in Fig. 2.1. Low-carbon steels tend to have a ferrite-perlite structure containing little perlite in the grain boundaries mainly.

2.3.2 Electrochemical Impedance Spectroscopy (EIS)

Nyquist plots for X52 steel exposed to the three solutions are shown in Fig. 2.2. Significant changes toward low real and imaginary impedance values are observed in the profile obtained in 3 % NaCl. Meanwhile, OWS showed an increase in impedance values. In addition, the presence of inductive loop at low frequencies is obtained in all electrolytes.

Recently, it was reported that the inductive behavior can be related to the adsorption of the neutralizing amines on 1018 steel surface [16]. In the present study, this behavior is associated with the pitting corrosion and metallic dissolution of X52 pipeline steel by chloride environments. As a first approach for fitting the impedance diagrams shown in Fig. 2.2, a Randles equivalent circuit was used omitting the

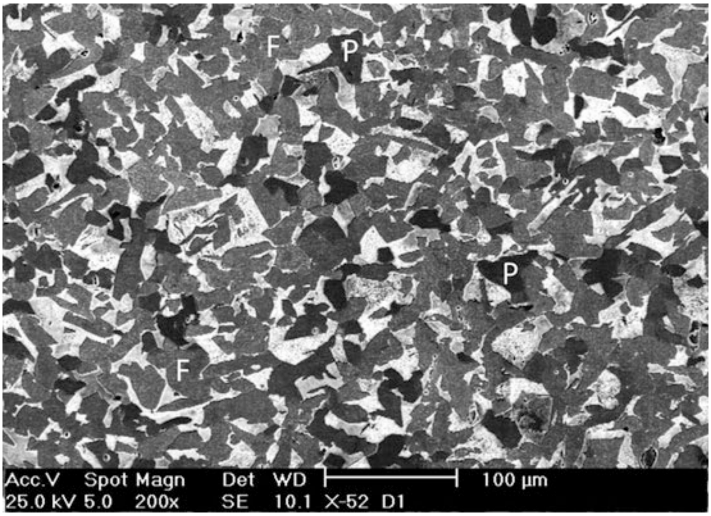

Fig. 2.1 Typical microstructure of API X52 steel

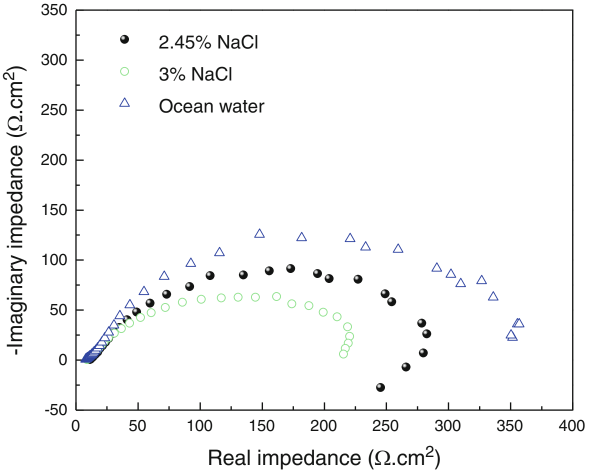

Fig. 2.2 Nyquist diagrams of X52 steel exposed to three chloride solutions obtained after 1 h, at 30 °C and 600 rpm

inductive response and using Boukamp program [17]. This equivalent circuit is related to the corrosion mechanism occurring at the different interfaces involving solution resistance (R_s), corrosion product properties (R_{cp} and C_{cp}), charge transfer resistance associated with X52 steel oxidation (R_{ct}), and capacitance contribution of the electrical double layer (C_{edl}) on X52 steel/chloride solution interface as is shown in Table 2.2. The capacitance values were evaluated from constant phase element (CPE: Q_i, specifically Y_{0i}), using the equation reported in previous work [18].

The ionic conductivity of the chloride solutions in the absence of surfactant and CI is similar ($R_s \approx 10\,\Omega\,\text{cm}^2$). It had been established that an increase in the pseudocapacitance values can be related with the decrease of resistance properties and the formation of iron oxides with a porous and non-protective nature on the metal surface [19]. In this manner, the pseudocapacitance values (C) obtained for 3 % NaCl can be related to the formation of more active iron oxides on X52 steel surface than X52 exposed to 2.45 % NaCl and OWS. This behavior is in agreement with the qualitative analysis of Nyquist diagrams showed in Fig. 2.2. Besides, it can be corroborated that the porous nature of the corrosion products formed on the X52 steel in chloride solutions given n values ($n < 1$). The E_{corr} values for each system were as follows: −0.610 V vs. SCE for 3 % NaCl, −569 V vs. SCE for 2.45 % NaCl, and −0.567 V vs. SCE for OWS corroborating that 3 % NaCl solution was more active to the corrosion process.

The presence of surfactant eliminated the inductive loop associated to pitting corrosion and metallic dissolution of X52 steel exposed to chloride environments. Thus, a beneficial effect of 60 mg/L nonionic NPE-4 surfactant in 2.45 % NaCl (Fig. 2.3a) and 30 mg/L nonionic NPE-4 surfactant in 3 % NaCl (Fig. 2.3b) was

Table 2.2 EIS values obtained after the best fitting of the experimental data

Solution	R_s (Ω cm^2)	R_{cp} (Ω cm^2)	Y_{cp} (S/cm^{2}s^n) × 10^{-3}	n_{cp}	C_{cp} (μF/cm^2)	R_{ct} (Ω cm^2)	Y_{ct} (S/cm^{2}s^n) × 10^{-4}	n_{ct}	C_{edl} (μF/cm^2)
2.45 % NaCl	10	20	1.530	0.6	214	276	1.432	0.8	119
3 % NaCl	9	52	2.364	0.6	691	194	5.573	0.9	349
OWS	10	85	0.0308	0.8	10.8	385	3.393	0.7	198

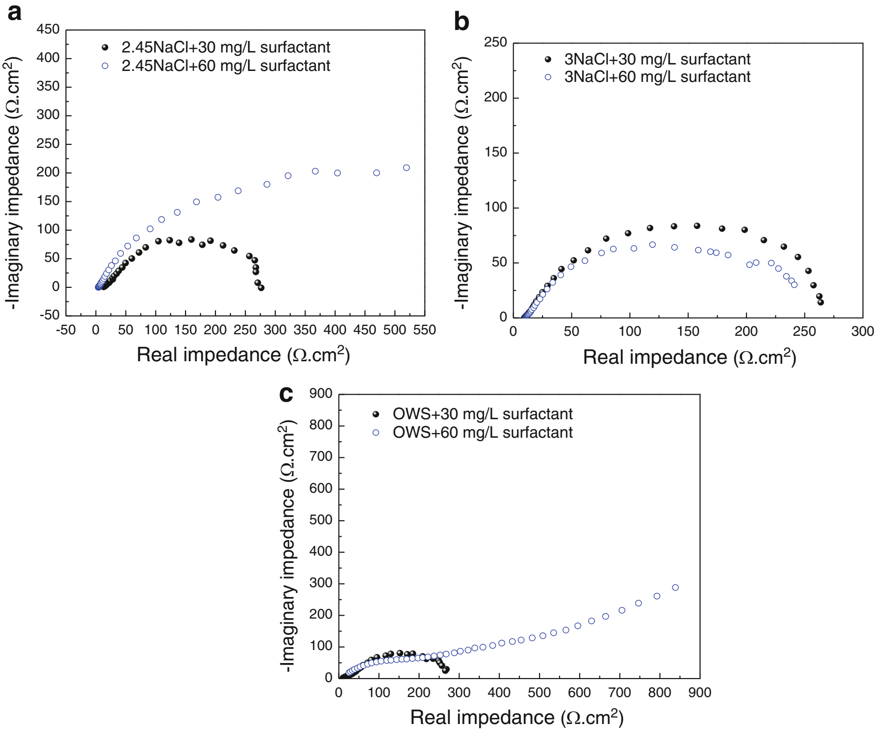

Fig. 2.3 Nyquist diagrams for X52 steel exposed to the three chloride solutions adding 30 and 60 mg/L nonionic NPE-4 surfactant at 30 °C and 600 rpm. (**a**) 2.45 % NaCl, (**b**) 3 % NaCl, and (**c**) OWS

obtained. Additionally, a significant effect of inhibition-diffusion process was reached when 60 mg/L surfactant was added in OWS (Fig. 2.3c).

Figure 2.4 shows the Nyquist diagram comparisons of corrosion inhibition process of X52 steel exposed to the most and less corrosive electrolyte (3 % NaCl and OWS, respectively). It is observed that X52 steel was protected when corrosion inhibitor (CI) was added to 3 % NaCl solution.

However, when X52 steel was exposed to OWS and adding surfactant, it displayed a much higher real and imaginary impedance values than X52 steel exposed to OWS adding CI.

Tables 2.3 and 2.4 show a summary of results obtained from the Nyquist diagram comparisons of the corrosion inhibition process of X52 steel exposed to the most and less corrosive electrolyte (3 % NaCl and OWS, respectively) adding 30 and 60 mg/L nonionic NPE-4 surfactant and CI. The results indicate that E_{corr} is most negative when 30 mg/L of CI is added on both solution (3 % NaCl and OWS).

The lowest ionic conductivity (R_{s}) is obtained when 60 mg/L is added to 3 % NaCl solution. However, R_{s} is very similar when both molecules are added in OWS.

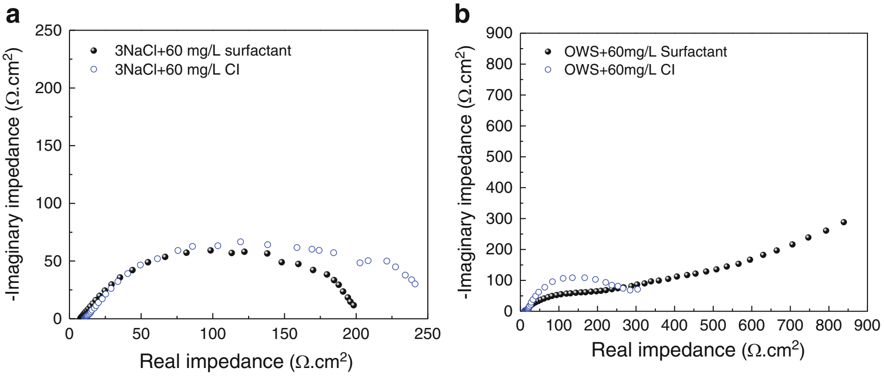

Fig. 2.4 Nyquist diagrams of X52 steel exposed to chloride solutions adding 60 mg/L surfactant and 60 mg/L CI at 30 °C and 600 rpm: (**a**) 3 % NaCl solution and (**b**) OWS

The decrease of resistance (R_{cp}) and increase of pseudocapacitance values (C_{cp}) related to the corrosion products formed on the X52 pipeline steel surface may be produced by the pitting or dissolution of iron oxides when surfactant is added to 3 % NaCl solution. The formation of such products can increase the corrosion process activity due to surface heterogeneity enlargement, provoking an increment in the layer thickness as compared to those acquired adding CI. However, the increase of charge transfer resistance (R_{ct}) and decrease of (C_{edl}) related to the electrical double layer pseudocapacitance formed on X52 pipeline steel surface may be originated by the poor dissolution or little formation of iron oxides with a homogeneous nature and protective properties when CI is added to 3 % NaCl solution.

On the other hand, when X52 steel surface is in contact with the OWS, a good corrosion control is observed when surfactant is added in both concentrations. Thus, a significant effect of corrosion inhibition process was observed adding 30 and 60 mg/L of surfactant, which may be related to competition between the electroactive species and the surfactant adsorption at the active sites of the X52 steel surface.

Also, the above means that the surfactant is more strongly adsorbed on X52 steel surface, suggesting that the surfactant provides better corrosion inhibition properties in the presence of chloride, sulfate, and carbonate compounds mainly. In this way, the surfactant is able to control the salts embedding and corrosion under deposits. Also it is important to mention that the same molecule cannot be used in different corrosive environments as corrosion inhibitor.

Table 2.3 EIS values obtained after the best fitting of the experimental data obtained for X52 steel exposed to 3 % NaCl solution adding surfactant and CI

Molecule	Dosage (mg/L)	E_{corr} (V vs. SCE)	R_{s} (Ω cm^2)	R_{cp} (Ω cm^2)	C_{cp} (μF/cm^2)	R_{ct} (Ω cm^2)	C_{edl} (μF/cm^2)
Surfactant	30	−0.513	9.8	22	533	212	417
Surfactant	60	−0.595	3.4	5.5	842	226	842
CI	30	−0.636	10	33	485	251	100
CI	60	−0.560	12	36	10.8	243	197

Table 2.4 EIS values obtained after the best fitting of the experimental data obtained for X52 steel exposed to OWS adding surfactant and CI

Molecule	Dosage (mg/L)	E_{corr} (V vs. SCE)	R_s (Ω cm^2)	R_{cp} (Ω cm^2)	C_{cp} (μF/cm^2)	R_{ct} (Ω cm^2)	C_{edl} (μF/cm^2)
Surfactant	30	−0.562	9.2	4.5	14.8	252	116
Surfactant	60	−0.596	8.9	218	151	985	98
CI	30	−0.611	8.8	15	2820	397	511
CI	60	−0.559	10	12	281	216	308

2.3.3 Volume Fraction of Microstructural Regions

Potentiodynamic polarization curves were obtained in order to study the effect of nonionic NPE-4 surfactant and CI on the corrosion inhibition properties of X52 pipeline steel exposed to OWS that can generate salts embedding or corrosion under deposits. Figure 2.5 shows the polarization curves for X52 steel exposed to OWS, OWS adding 60 mg/L surfactant, and OWS adding 60 mg/L CI. OWS plus 60 mg/L of NPE-4 surfactant displaced the corrosion current density (i_{corr}) toward lower values. For the blank (OWS), a loop at −0.665 V vs. SCE of the cathodic branch is obtained; this loop can be related to salts embedding. Thus, it is possible that salts embedding dissolve when surfactant is added into the OWS. Corrosion rate (CR) was determined from i_{corr} using Eq. 2.1 [20].

$$\mathrm{CR}\left(\frac{\mathrm{mm}}{\mathrm{year}}\right) = \frac{i_{\mathrm{corr}} A_{\mathrm{w}}}{zF\rho} = 11595.7206 * i_{\mathrm{corr}} \tag{2.1}$$

The following values were used: atomic weight $A_{\mathrm{w}} = 55.85\,\mathrm{g/mol}$, $z = 2$ electrons, $F = 96,500\,\mathrm{C/mol}$, and density $\rho = 7.87\,\mathrm{gcm}^{-3}$.

The summary results obtained from polarization curves (E_{corr}, i_{corr}, Tafel slopes of the anodic (β_{a}) and cathodic (β_{c}) branches and CR) are shown in Table 2.5. In this table, it is observed that the corrosive solution is affected by the addition of surfactant, which in turns changes the E_{corr} toward more negative potential value. Furthermore, the presence of surfactant considerably changed β_{a} and β_{c} branches. When surfactant is added to OWS, CR indicates that the surfactant acted as corrosion inhibitor and modified the actives sites and cathodic reaction on steel surface, which may happen by chemical or physical adsorption effect.

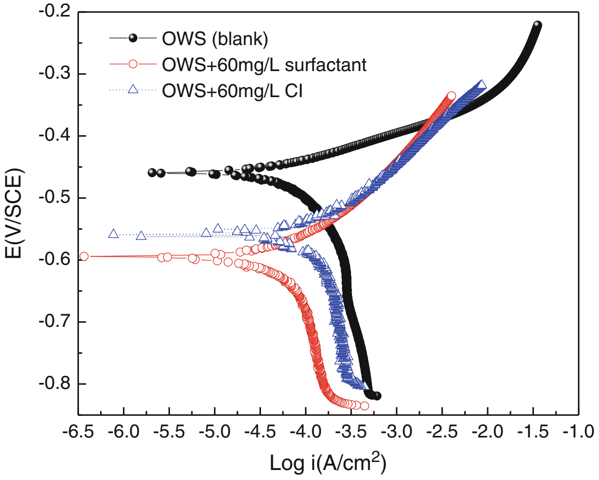

Fig. 2.5 Potentiodynamic polarization curves obtained for X52 steel exposed to OWS

Table 2.5 Electrochemical parameters obtained from polarization curves of X52 steel

Solution	E_{corr} (mV/SCE)	i_{corr} (A/cm^2)	β_a (V/dec)	β_c (V/dec)	CR (mm/year)
OWS (blank)	−0.461	1.561×10^{-4}	0.099	−0.259	1.81
OWS + 60 mg/L surfactant	−0.596	7.591×10^{-5}	0.134	−0.641	0.88
OWS + 60 mg/L CI	−0.559	9.923×10^{-5}	0.141	−0.723	1.15

Table 2.6 Adsorption constant and Gibbs free energy

Solution	Concentration (Mol/L)	θ	ln (55.5*k_{ads})	$\Delta G°$ (kJ/mol)
OWS + 60 mg/L surfactant	0.1550	0.5343	6.0182	−14.91
OWS + 60 mg/L CI	0.1729	0.0423	2.6523	−6.57

2.3.4 Adsorption Process

The degree of surface coverage of the active sites (θ) and the adsorption equilibrium constant (k_{ads}) of the metallic surface was calculated by Eqs. 2.2–2.4 that is associated with adsorption isotherms of Langmuir, Frumkin, Freundlich, and Temkin [21, 22]. K_{ads} is directly related to the standard free energy of adsorption reaction (ΔG°_{ads}) by equation 2.5. The surfactant and CI concentration, θ, and the Gibbs free energy calculated are given in Table 2.6.

$$\theta = \left[\frac{i_{corr.blank} - i_{corr.surfactant}}{i_{corr.blank}}\right] = \left[\frac{CR_{blank} - CR_{surfactant}}{CR_{blank}}\right] \tag{2.2}$$

$$\frac{C_{surfactant}}{\theta} = \frac{1}{k_{ads}} + C_{surfactant} \tag{2.3}$$

$$k_{ads} = \frac{1}{C_{surfactant\left(\frac{1}{\theta}-1\right)}} \tag{2.4}$$

$$\Delta G^{\circ}_{ads} = -RT \ln\left(55.5 k_{ads}\right) \tag{2.5}$$

The adsorption constant (k_{ads}) and Gibbs free energy ($-\Delta G^{\circ}_{ads}$) for X52 steel exposed to OWS adding surfactant displayed higher values than adding CI, which means that the surfactant is more easily adsorbed on X52 steel surface and as a result it provides a higher corrosion inhibition. It is well known that a negative value of ΔG°_{ads} indicates that adsorption occurred spontaneously with the formation of a film strongly adsorbed on the metal surface [21, 22]. Furthermore, ΔG°_{ads} around −20 kJ/mol or lower is associated with electrostatic interactions between the charged molecules and the charged metal, which indicates that a process of physical adsorption may occur [11, 23]. In this manner, X52 steel exposed to OWS adding 60 mg/L (0.1550 M) surfactant exhibited a physical adsorption process. However, X52 steel exposed to OWS adding 60 mg/L CI is more difficult to adsorb on X52 steel surface, and consequently the iron oxide products can increase the corrosion process activity.

2.3.5 Surface Analysis After Electrochemical Test

Figures 2.6 and 2.7 show images of the X52 steel surface after carrying out the electrochemical tests (after 1 h, at 30 °C and 600 rpm). Figure 2.6 shows some images of the surface finish of X52 steel exposed to 3 % NaCl solution obtained after electrochemical test. It can be observed the electrochemical responses for corrosion damage and inhibition using a surfactant. Visual analyses carried out after electrochemical test suggests that X52 steel in contact with 3 %NaCl solution exhibits different types of corrosion damage when adding surfactant and CI. Adding 30 mg/L of surfactant generates little rust corrosion products on steel surface (Fig. 2.6b), while adding 30 mg/L of CI, a greater oxidation and rust was observed (Fig. 2.6c).

Figure 2.7 shows some images of the surface finish of X52 steel exposed to OWS obtained after electrochemical test. It can be observed that OWS generates different types of corrosion on the X52 steel compared to 3 %NaCl solution. In this case,

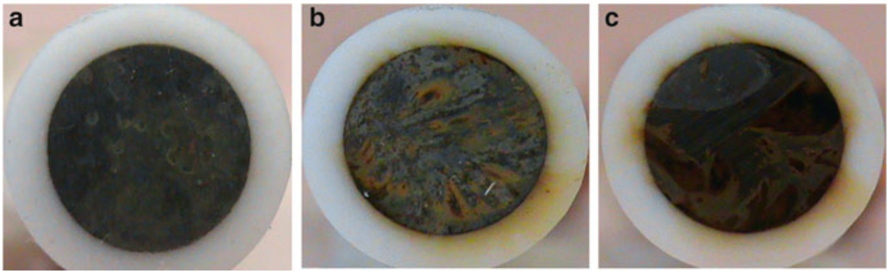

Fig. 2.6 Surface finish of X52 steel exposed to 3 % NaCl solution, obtained after electrochemical test; (**a**) blank, (**b**) adding 30 mg/L surfactant, and (**c**) adding 30 mg/L CI

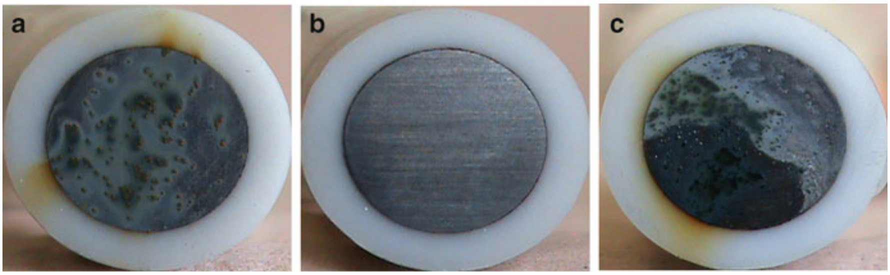

Fig. 2.7 Surface finished of X52 steel exposed to OWS, obtained after electrochemical test; (**a**) blank, (**b**) adding 60 mg/L surfactant, and (**c**) adding 60 mg/L CI

the corrosion type observed was pitting. X52 steel exposed to OWS with 60 mg/L of surfactant practically maintains free of corrosion products the X52 steel surface (Fig. 2.7b). However, some traces of rust can be observed, but were easily removed and were not found as evidence of pitting. In X52 steel exposed to OWS with 60 mg/L of CI, severe corrosion damage was observed.

2.4 Conclusions

The corrosion inhibition on X52 pipeline steel exposed to chloride solutions adding two concentrations of surfactant and corrosion inhibitor was studied. EIS analyses showed that 3 % NaCl was the more corrosive solution for X52 steel. Adding CI to OWS improves the corrosion resistance of X52 steel in a better way than adding CI to 3 %NaCl solution. The best corrosion inhibition was observed when the X52 steel was exposed to OWS adding 60 mg/L, obtaining a CR of 0.088 mm/year. Nonionic NPE-4 surfactant acts as a corrosion inhibitor in OWS preventing the pitting, salts embedding, or corrosion. The adsorption constant (k_{ads}) and Gibbs free energy (ΔG°_{ads}) for X52 steel exposed to OWS adding surfactant (60 mg/L) displayed higher values than adding CI, which means that surfactant is more easily adsorbed on X52 steel surface and as a result provides a higher corrosion inhibition.

References

1. Migahed MA, Abd-El-Raouf M, Al-Sabagh AM, Abd-El-Bary HM (2005), Effectiveness of some non-ionic surfactants as corrosion inhibitors for carbon steel pipelines in oil fields. Electrochem Acta 50:4683–4689
2. Negm NA, Al Sabagh AM, Migahed MA, Abdel Bary HM, El Din HM (2010), Effectiveness of some diquaternary ammonium surfactants as corrosion inhibitors for carbon steel in 0.5M HCl solution. Corros Sci 52:2122–2132
3. Free ML (2002), Understanding the effect of surfactant aggregation on corrosion inhibition of mild steel in acidic medium, Corros Sci 44:2865–2870
4. Amin MA, Khaled KF (2010), Monitoring corrosion and corrosion control of iron in HCl by non-ionic surfactants of the TRITON-X-series-Part 1. Tafel polarization, ICP-AES and EFM studies. Corros Sci 52:1762–1770
5. Wang W, Free ML (2004), Prediction and measurement of corrosion inhibition of mild steel using nonionic surfactants in chloride media. Corros Sci 46:2601–2611
6. Free ML (2002), Development and application of useful equations to predict corrosion inhibition by different surfactants in various aqueous environment. Corrosion 58:1025–1030
7. Free ML (2004), A new corrosion inhibition model for surfactants that more closely accounts for actual adsorption than traditional models that assume physical coverage is proportional to inhibition. Corros Sci 46:3101–3113
8. Hegazy MA (2009), A novel Schiff base-based cationic gemini surfactants: synthesis and effect on corrosion inhibition of carbon steel in hydrochloric acid solution. Corros Sci 51:2610–2618
9. Elachouri M, Hajji MS, Kertit S, Essassi EM, Salem M, Coudert R (1995), Some surfactants in the series of 2-(Alkyldimethylammonio) alkanol bromides as inhibitors of the corrosion of iron in acid chloride solution, Corros Sci 37:381–389

10. Hegazy MA, Abdallah M, Ahmed H (2010), Novel cationic gemini surfactants as corrosion inhibitors for carbon steel pipelines. Corros Sci 52:2897–2904
11. Borse MS, Devi S (2006), Importance of head group polarity in controlling aggregation properties of cationic gemini surfactants. Adv. Colloid Interface Sci 123–126:387–399
12. Fuchs-Godec R (2007), Inhibitory effect of non-ionic surfactants of the TRITON-X series on the corrosion of carbon steel in sulphuric acid. Electrochim Acta 52:4974–4981
13. Valencia D, Aburto J, García-Cruz I (2013), Electronic structure and mesoscopic simulations of nonylphenol ethoxylate surfactants. A combined DFT and DPD study. Molecules 18:9441–9450
14. Martínez-Palou R, Cerón-Camacho R, Chávez B, Vallejo AA, Villanueva-Negrete D, Castellanos J, Karamath J, Reyes J, Aburto J (2013), Demulsification of heavy crude oil-in-water emulsions: A comparative study between microwave and thermal heating. Fuel 113:407–414
15. ASTM D-1141 (2013), Standard practice for the preparation of substitute ocean water
16. Quej-Aké L, Cabrera-Sierra R, Arce-Estrada E, Marín-Cruz J (2008), EIS evaluation of the effect of neutralizing and inhibitor compounds on corrosion process of 1018 carbon steel in acid solutions typical of atmospheric distillations plants. Int J Electrochem Sci 3:56–66
17. Bouckamp BA (1993), Users manual equivalent circuit, Faculty of Chemical Technology, 4.51, University of Twente, Netherlands
18. Pech-Canul MA, Chi-Canul LP (1999), Investigation of the inhibitive effect of N-phosphono-methyl-glycine on the corrosion of carbon steel in neutral solutions by electrochemical techniques. Corrosion 55:948–956
19. Bonnel A, Dabosi F, Deslouis C, Duprat M, Keddam M, Tribollet B (1983), Corrosion study of a carbon steel in neutral chloride solutions by impedance techniques. J Electrochem Soc 130:753–761
20. Perez N (2004), Electrochemistry and corrosion science, 1st edn. Massachusetts
21. Rosen MJ (1989), Surfactants and interfacial phenomena, 2nd edn. New York
22. Shaw DJ (2000), Introduction to colloid and surface chemistry, 4th edn. Great Britain Butterworth, Heinemann
23. Mu GA, Li XH (2005), Inhibition of cold rolled steel corrosion by Tween-20 in sulfuric acid: weight loss, electrochemical and AFM approaches. J Colloid Interface Sci 289:184–192

Chapter 3
Effect on the Microstructure and Mechanical Properties of the Structural Steel Welded in Marine Environment

M. Flores, J.J. Ruiz, F. Macías, and J. Acevedo

Abstract Recently, oil deposits were found in ever deeper waters. In this context, it is important to study the water depth effect on parameters in repair and maintenance operations of pipelines for extraction and/or transportation of crude oil, of which there is limited information in literature. This paper shows a study of the effect of the water depth on the microstructure and mechanical properties in joining structural steel welded in a marine environment in steels with a maximum CE (carbon equivalent) of 0.37 %. Wet welding coupons of steel ASTM A36 were joined by the manual metal arc welding (MMAW) process at depths of 10, 20, 30, and 40 m, using AWS Broco SoftTouch as filler metal (3.17 mm diameter) inside a simulation hyperbaric chamber. Image analysis was applied to welded coupons, with the aim to obtain the phase quantification and porosity as well as mechanical properties. The results show that there is an inverse relationship between the increase in depth at which the welding is performed and the mechanical properties, while the filler metal properties were kept constant. Microstructural changes vary as a function of the depth at which repair-maintenance is performed, with an increase in growing phase shift which is highly undesirable because of their brittleness and hardness.

Keywords MMAW • Wet • Welding • Mechanical properties • Depth

3.1 Introduction

The success in looking for light oil in deep water and the growth of the offshore energy industry and the need to build submerged such as offshore platforms and pipelines themselves of this economic activity driving, make wet welding becomes one of the most efficient options for the construction, repair, and maintenance of offshore structure site options, due to the low cost and the time of application [1]. Currently, the marine environment solder is applied in two main ways: the first is the

---

M. Flores (✉) • J.J. Ruiz • F. Macías • J. Acevedo.
COMIMSA-Saltillo, Calle Ciencia y Tecnología # 790, C.P: 25290 Saltillo, Coah., Mexico
e-mail: mflores@comimsa.com

R. Pérez Campos et al. (eds.), *Characterization of Metals and Alloys*, DOI 10.1007/978-3-319-31694-9_3

underwater welding in a wet environment, which is done directly in the submerged part, and the second is the underwater welding in a dry environment, which allows the diver/welder be within a habitat that provides a dry environment under a body of water [2].

It has been shown to influence the depth variation along multipass wet underwater welding and the mechanical properties of steels, using stress tests observing the decrease in the tensile strength with increasing depth. This relationship is promoted with increasing of depth and porosity [3].

Johnson et al. [4] show that the wet marine welding of steels produces three basic microstructures: ferrite, bainite, and martensite. This author also discusses the environmental effects of water, such as salinity and pressure change, on the chemistry and microstructure of the welded metal, but just mentions that the effect of water temperature in the cooling rate is small. On the other hand, Hernandez [5] demonstrated that due to rapid cooling and solidification of the weld metal, ferrite and allotriomorphic ferrite are formed. Also, Hernández and Ballesteros [5, 6] comment that the depth is not an important factor affecting the microstructure for the 10–40 m of depth. Currently, wet welding has become one of the most efficient options for the construction, repair, and in-site maintenance of offshore structures due to the low cost and the application time.

So, one of the main problems of wet welding is the decomposition of water (hydrogen and oxygen) that interacts strongly with the weld pool; this causes the formation of pores, cracks, and nonmetallic inclusions that affect the mechanical properties of the cord. Also, cooling is subjected to the welding that affects the mechanical properties of the cord provoking the appearance of a microstructure susceptible to cracking hydrogen and also contributing to the rapid gas retention during solidification of the weld metal [7, 8].

The work performed previously does not clarify the effect of depth in the microstructure and mechanical properties. For this reason, in this work presents result in the pressure range 10–40 m deep in structural steels used in offshore, in order to contribute to the development of welded joints working at different depths.

3.2 Experimental

An experiment was conducted at different depths of 10, 20, 30, and 40 m using ASTM A36 steel like base material, which is used for building structures in the coast, structures in offshore platforms, piers piles, pipes driving, piles of bridges, ships, etc. [9]. The chemical composition of ASTM A36 steel plate is shown in Table 3.1 [10]. This steel presents a tensile strength of 58,000–80,000 PSI and yield stress of 36,000 PSI [10]. The steel has a carbon equivalent of 0.3 suggesting that have good weldability under water and are not susceptible to hydrogen cracking, so the ASTM A36 structural steel with $CE = 0.3093$ meets this requirement [11].

Table 3.1 Chemical composition according to the results of chemical analysis to ASTM A36 steel plate, % e.p.) (% parts per million)

ASTM A36	Fe	C	Mn	Si	Cr	Ni	P
	98.77	0.16	0.83	0.11	0.02	0.04	0.013
	S	Mo	Cu	V	Nb	Ti	W
	0.004	0.01	0.022	0.004	0.007	0.004	0.002

Fig. 3.1 Design of the joint bevel in "V" with support for the realization of the test welds in steel ASTM A36

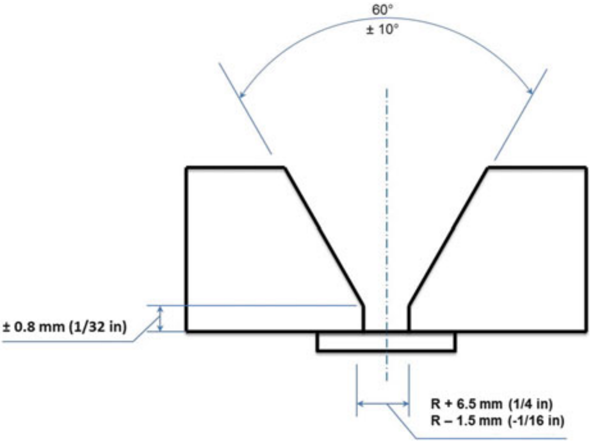

Table 3.2 Chemical composition of coated electrode Broco Underwater Soft-Touch E7014 [10]

Designation (% e.p.)								
AWS E7014	C	Si	Mn	P	S	Cu	Al	Cr
	0.072	0.244	1.185	0.012	0.002	0.016	0.024	0.024
	Mo	Ni	V	Ti	Nb	Co	Fe	
	0.005	0.023	0.015	0.008	0.017	0.009	Bal.	

E70XX electrodes like filler metal were used during the MMAW process, the experiment was conducted in a hyperbaric chamber pressurized with capacity of 31 atm (atmosphere) absolute pressure equal to 300 m depth. The welding system has a multi-process machine 300 A with direct current and constant voltage up to 29 V, with an efficiency of 100 %. Samples were prepared for metallography and tensile tests [10].

The joints were prepared with bevel "V" with support for the application of wet welding cords as shown in Fig. 3.1.

Table 3.2 shows the chemical composition of the coated electrode Broco Underwater SoftTouch E7014 used as filler for performing wet stamps. This electrode has a tensile strength of 70,000 PSI [10].

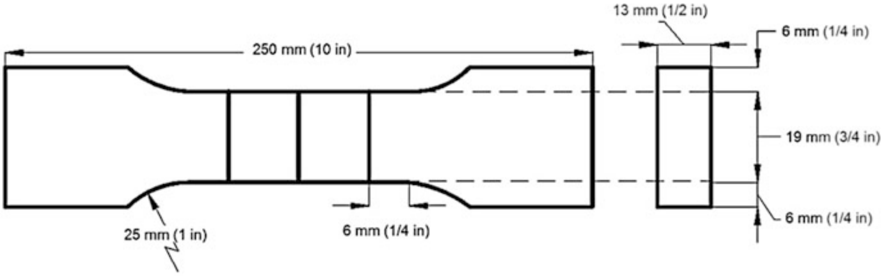

Fig. 3.2 Schematic representation of tensile specimen dimensions [11]

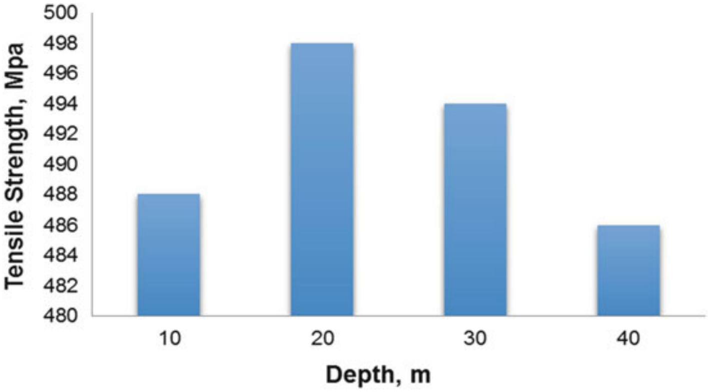

Fig. 3.3 Results of tensile tests in function of welding deep

For metallographic microstructure analysis, HNO_3 5 % (Nital) was used for 10 s for a subsequent observation of the microstructure obtained through an Olympus PMG-3, and Klemm's y was used for 30 s. Phase quantification was performed using the software AxioVision Rel. 4.8. Tensile tests were performed with a Tinius Olsen Super L290 machine with a load of 600 kN; samples were machined according to AWS D3.6 [11]. In Fig. 3.2, dimensions of the specimen are shown.

3.3 Results and Discussion

Figure 3.3 shows the results of tensile tests on samples developed at different depths are exhibited. It is observed that at 10 m, the tensile strength is 488 MPa, while at 20 m it increases to 498 MPa; this value decreases slightly at depths of 30 m with 494 MPa and 40 m with 486 MPa. The results confirm that with increasing depth, the tensile strength tends to decrease, with a notable increase in tension at 20 m.

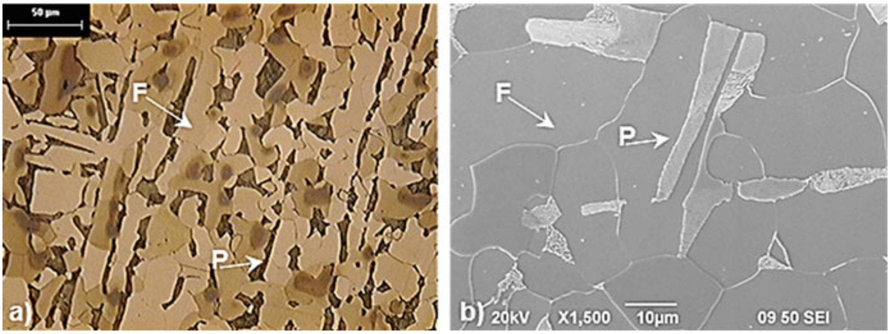

Fig. 3.4 A36 steel micrographs obtained in (**a**) optical microscope at 50× attacked with Klemm's and in (**b**) SEM at 1500× attacked with Nital 5 %, where F=ferrite and (P)=perlite

Figure 3.4 shows micrographs taken in the base metal, A36, in (a) optical microscope at 50× and (b) SEM (scanning electron microscope) to 1500×, where a ferrite-pearlite matrix is observed with an average hardness of 157 HV.

Figure 3.5 shows micrographs taken at 50× of each of the depths studied, in the HAZ (heat-affected zone), and weld metal (MA) is shown. It is seen in the HAZ at depths of 10 m which is constituted by Widmanstätten ferrite (FW), martensite block (M), ferrite in the grain boundary (FLG), and ferrite blocks, while the filler metal matrix mostly found acicular ferrite, ferrite blocks, and FLG. The same microstructures are presented in the other in different depth percentages; also observed in the specimen of 40 m is the presence of microcracks in the HAZ, where the phases were Widmanstätten ferrite and martensite blocks.

The results of the quantification phases are shown in Figs. 3.6 and 3.7. In Fig. 3.6, the variation of the percentage of phase with respect to the depth is shown. The phases present in the filler metal weld bead have a higher percentage of ferrite in block and acicular ferrite, without the presence of martensite and bainite. The ferrite in block is one of the phases having a greater variation as a function of the depth of welding at 10 m depth is 75 % and increases to 95 % at 30 m. While at 20 m depth, the microstructure has 73 % of ferrite block (acicular ferrite) and only 3 % Widmanstätten ferrite. At 20 m depth the content of acicular ferrite is bigger and lower content of FLG Widmanstätten ferrite was observed.

Figure 3.7 shows the microstructure present in the HAZ, which shows that there is a Widmanstätten ferrite increase with increasing depth. At 10 m, FW content is 40–65 % increasing to 40 m, and the content of acicular ferrite remains in the specimen of 20 m and 40 m with an average of 9 %.

Both block martensite and bainite are present in the samples welded at 10, 30, and 40 m finding a maximum of 1.8 % to note that these phases were found mainly in areas between steps. The content of the ferrite block is held constant at depths of 10, 20, and 30 m at 50 % and decreases to 40–26 % m, while the FLG at 20 m has the highest content up to 6 %, and this is decreasing to less than 1 % at 40 m.

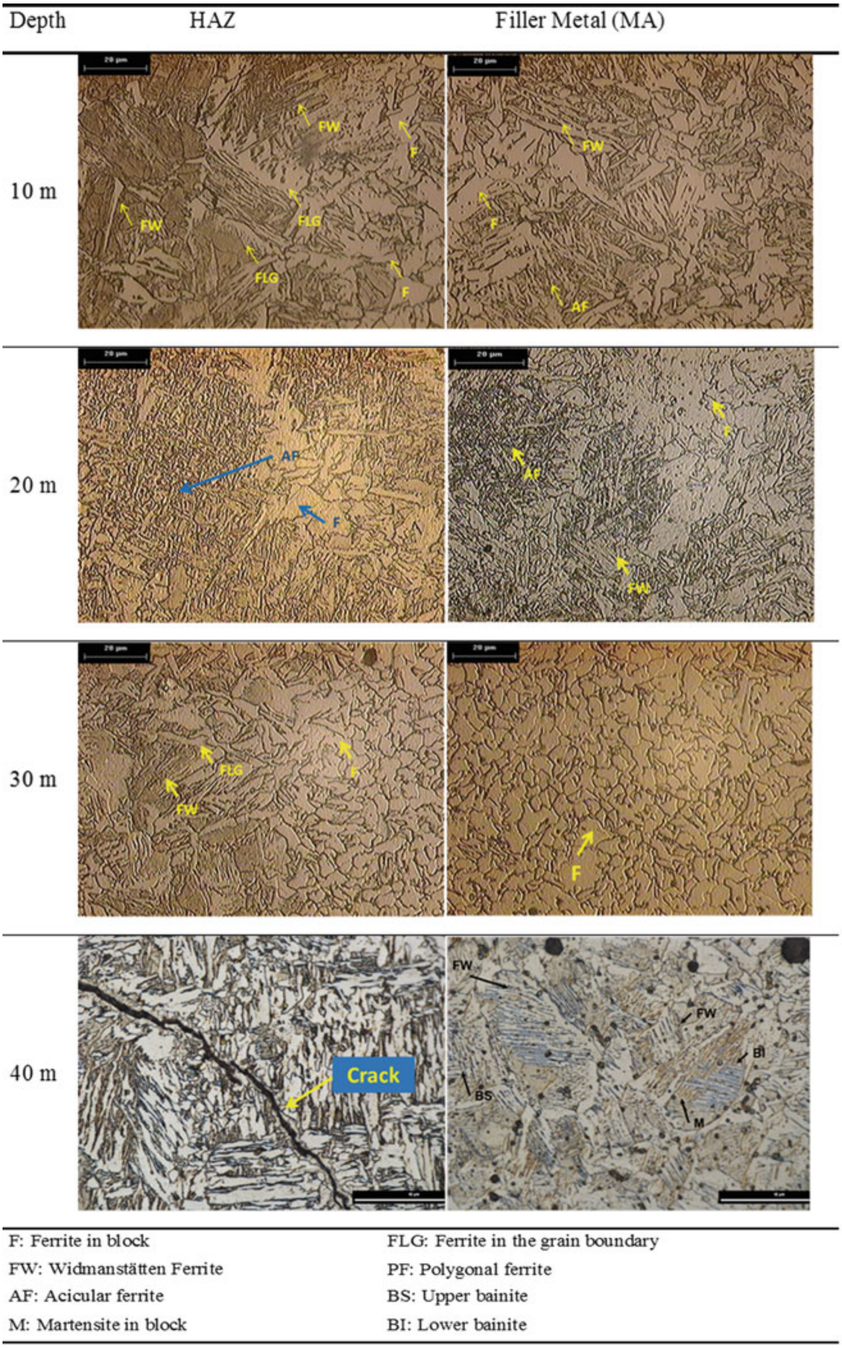

Fig. 3.5 Representative microstructures of weld seams at depths of 10, 20, 30, and 40 m

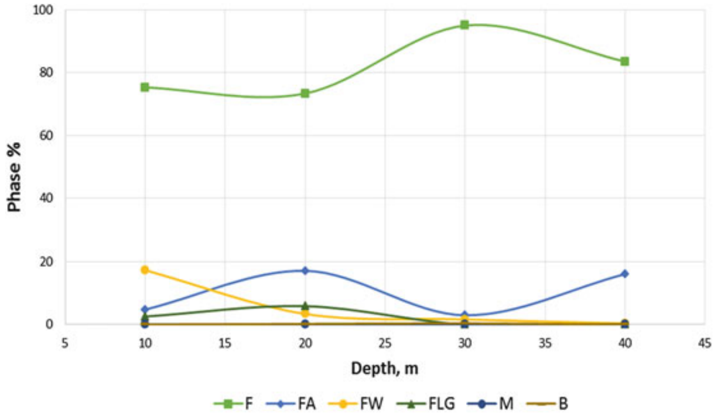

Fig. 3.6 Microstructure-depth ratio presented in the wet filler metal welding

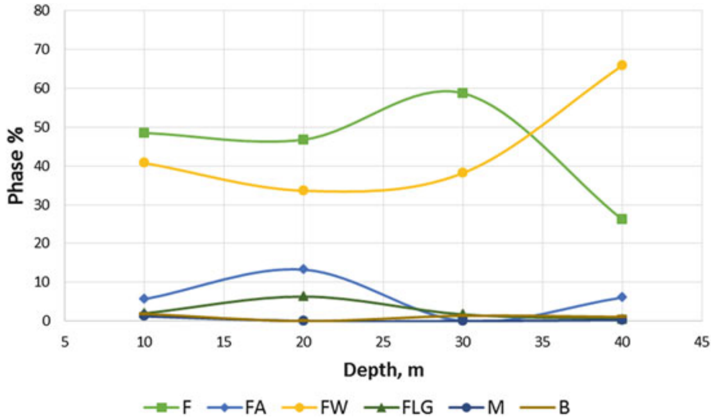

Fig. 3.7 Microstructure-depth ratio presented in the HAZ in wet welding

Table 3.3 presents a summary of the results of stress tests and microstructure, naming specimens as M1 to the depth of 10 m (33 ft), the same with the M2 to 20 m (66 ft), etc. It is shown that depth promotes a decreasing tensile strength, which is consistent with results reported by Rowe et al. [3]. This behavior regards that, as the depth increases, the porosity percentage is increasing as reported elsewhere [4]. This behavior is very noticeable in the specimens welded at 30 m and 40 m depth.

This phenomenon may be associated with the dissociation of water into H and O and the formation of CO(g) and CO_2(g) that become trapped in the weld bead due to the cooling rate of the weld; In addition, the pore size increases as the depth increases [5, 12]. The reduction in mechanical properties with increasing depth is the microstructure-depth ratio obtained from the results of quantification of phases: as the depth decreases, ferrite block content and FA and the contents of FLG, FW, martensite, and bainite (the latter are found in percentages smaller than

Table 3.3 Results of tension test and microstructure of the test coupons welded with the process MMAW to 10, 20, 30, and 40 m

Test	Classification, AWS	Depth, m (ft)	Microstructure HAZ	Tensile (MPa)
M1	E7014	10 (33)	F+FW	488
M2	E7014	20 (66)	F+FW	498
M3	E7014	30 (98)	F+FW	494
M4	E7014	40 (131)	FW	486

1 %) increase which promotes hydrogen embrittlement which explains the presence of microcracks in the sample welded at 40 m depth, as noted by Dias-da-Silva et al. [12]. The cooling rate is a major factor in the formation of microstructures hard and brittle [4, 6, 7, 13, 14]. Although an improvement was observed in stress tests at 20 m, this behavior was not expected based on those reported in the literature [8, 9]. Results suggest that due to the microstructure variation present, high contents of ferrite block up to 73 % in the weld metal and 48 % in the HAZ and 17 % of FA in the HAZ and 13 % filler metal are showed. The two main trends to decreases the mechanical properties are the porosity ratio and the phases ratio during solidification, obtaining the highest tensile stress at 20 m of depth.

3.4 Conclusions

Based on the experiments it is concluded:

- In the process of repairing structural components used in welding excellence in marine environment is the MMAW process due to its efficiency in time and cost.
- There is a tendency of depth-owned mechanical wet welding; with increasing depth, the tensile strength decreases, keeping properties of filler metal constant.
- It was noted that in the microstructure-depth ratio structural steels with EC $< 0.37\,\%$, the HAZ shows an increase of content of FW as the depth increases. While in the ferrite content and block FLM, no significant variation in the presence of martensite and bainite block percentage $< 1\,\%$ was observed. The matrix in both, the weld metal and the HAZ, is the ferrite block.
- In order to decreases porosity and detrimental phases, welding must be performed at less depth. However, the size of the phases is lower by increasing the depth which can promote the properties in the intermediate conditions that are higher, as it was presented in the sample at 20 m.
- The addition of alloying elements such as boron and titanium and adequate control of the oxygen content and manganese acicular ferrite formation which impact on increasing the toughness of the weld is promoted.

References

1. Verma K, Garg HK (2012) Underwater welding-recent trends and future scope. Int J Emerg Technol 3:115–1120
2. Joshi AM (2012) Underwater welding, vol 2. Indian Institute of Technology, Mumbai, pp 1–5
3. Pessoa ECP, Bracarense AQ, Zica EM, Liu S, Perez-Guerrero F (2006) Porosity variation along multipass underwater wet welds and its influence on mechanical properties. J Mater Process Technol 179:239–243
4. Johnson RL (1997) The efffect of water temperature on underbead cracking of underwater wet weldments. Naval Postgraduate School, Monterey
5. Hérnandez-Gutiérrez P (2011) Comportamiento microestructural de un acero API-5L-X52 soldados por el proceso MMAW en ambientes marinos. COMIMSA, Saltillo
6. Ballesteros-Hinojosa, A (2012) Analisis de la generacion de esfuerzos residuales en uniones soldadas en el acero API 5L-X65 aplicadas a diferentes profundidades en ambientes submarinos por el proceso de soldadura húmeda. COMIMSA, Saltillo
7. Quintana-Puchol R, Perdomo-Gonzalez L, Bracarense AQ, Pessoa ECP (2009) Thermodynamic considerations between pores formation and hydrostatic pressure during underwater wet welding. Soldagem Insp 14:161–169
8. Perez-Guerrero F, Liu S (2007) The mechanism of porosity formation in underwater wet welds. Defect Anal Mitigation 9:215–218
9. PEMEX. NRF-175-PEMEX-2013 (2013) Acero estructural para plataformas marinas, México (2013)
10. AWS (2004) Specification for carbon steel electrodes for shielded metal arc welding ANSI/AWS A5.1. American Welding Society, Miami
11. American Weilding Society (2010) Underwater welding code AWS D3.6M, 5th edn. American Welding Society, Miami
12. Dias-da-Silva WC, Ribeiro LF, Bracarense AQ, Pessoa ECP (2012) Effect of the hydrostatic pressure in the diffusible. In: Materials Technology; Polar and Arctic Sciences and Technology; Petroleum Technology Symposium, vol 6, pp 1–8
13. Babu SS (2004) The mechanism of acicular ferrite in weld deposits. Curr Opin Solid State Mater 8:267–278
14. ASTM A36 (1998) Standard specification for carbon structural steel. ASTM, United States

Part II
Characterization of Copper Alloys

This part includes three chapters related to characterization of copper alloys. The first chapter includes an investigation to determine the influence of the thermo-mechanical conditions during plastic deformation on the microstructure evolution of the brass (Cu-30%Zn), by using in-situ tension test. The mapping of polycrystalline flow of the brass was obtained, as well as the mechanisms of plastic flow phenomenon based on direct observations generated during the tensile test were determined. The analysis of the results of this investigation permitted to determine the influence of the thermo-mechanical conditions during plastic deformation on the microstructure evolution. The results obtained are vital for designing an effective thermo-mechanical processing technology for the investigated copper alloy.

The second chapter includes an investigation to determine the activation energy for plastic flow at crystalline and microscopic scale of a commercial copper during in-situ tension test at room temperature by applying the quantum mechanics and relativistic model (QM-RM). With the analysis of the microscopic direct evidences of the microstructure evolution, the true activation energy related to the cellular dislocations dynamics was determinate. The findings of this investigation are very important for designing an effective metal working processing technology at room temperature for the investigated copper.

The third chapter analyzes the effect of copper additions between 0.5 and 2 wt.% on a 15%Cr white iron on the secondary carbides precipitation during the destabilization heat treatment, carried out at temperatures of 850, 950, and 1050 °C. It was found that the copper addition resulted in an increase in discontinuity of the eutectic carbide in as-cast conditions. After the heat treatment, the number of precipitated carbides increased with the copper addition. The results suggested an increase of precipitation for lower destabilization temperatures.

The main techniques used in the characterization of these materials are:

- Scanning electron microscopy (SEM).
- Optical microscopy (OM).
- X-ray diffraction (XRD).
- Image analysis.
- Energy dispersive spectroscopy (EDS).
- Mechanical tests.

Chapter 4
Mapping of Polycrystalline Flow During Hot Deformation by In Situ Tension Test of Sheet Copper Alloy

J.D. Muñoz-Andrade, E. Garfias-García, and O. Vega-Hernández

Abstract The reason of this work is to determine the mechanisms of plastic flow of copper alloy of the type Cu-30%Zn, during an in situ tensile test in a module coupled in SEM-SUPRA equipment at 250 °C with a constant crosshead velocity, $\nu = 0.152$ mm/min. Metallographic observations of the structure were carried out on a scanning electron microscope (SEM). The mapping of polycrystalline flow of the copper alloy was obtained, and the mechanisms of plastic flow phenomenon were determined on the basis of direct observations generated during the tensile test. However, the activation energy for plastic flow was calculated on the basis of quantum mechanics and relativistic model proposed by Muñoz-Andrade. In results of tensile test of copper alloy, it has been found that the cellular dislocation dynamics is the main mechanism of plastic flow at 250 °C. On the other hand, the activation energy for five stages of deformation is in the range of 162.715–162.853 kJ/mol; these results are in a closed agreement with values reported in literature to the activation energy for the self-diffusion of Cu or Zn of 159 kJ/mol.

Keywords Hot deformation • Copper alloy • Activation energy • Mapping of granular flow • Cellular dislocation dynamics

4.1 Introduction

New methods to improve the knowledge about the phenomenology and mechanics of irreversible deformation processes in metallic materials during tension test are essential in order to get more natural direct evidences to understand the mechanical behavior of metallic materials during metal working processes [1]. In this scenery a methodical study was suggested, in the direction to obtain the mapping of granular

---

J.D. Muñoz-Andrade (✉) • E. Garfias-García • O. Vega-Hernández
Departamento de Materiales, División de Ciencias Básicas e Ingeniería, Universidad Autónoma Metropolitana Unidad Azcapotzalco, Av. San Pablo 180, Col. Reynosa Tamaulipas, 02200 D.F., Mexico
e-mail: jdma@correo.azc.uam.mx

R. Pérez Campos et al. (eds.), *Characterization of Metals and Alloys*, DOI 10.1007/978-3-319-31694-9_4

flow in the spatially extended polycrystalline system (SEPCS) of metallic materials during uniaxial tension test. This mapping allows to establish the trajectory of each crystal which submerges in the surface of the polycrystalline system. Also, it is possible to define on the surface of the sample in relation to the reference system if crystals present a displacement, rotation, deformation, and transformation of the morphology surface [1–3].

On the other hand in recent times, the quantum mechanics and relativistic model of Muñoz-Andrade were proposed, in order to obtain the activation energy for plastic flow (Q_{PF}) during axial tension test at crosshead velocity in SEPCS, which is given by the following equation:

$$Q_{\mathrm{PF}} = -kT\ln\left[\frac{\rho_\perp \nu_\perp b_\perp^2}{c}\right] = -kT\ln\left[\frac{\xi_\perp b_\perp}{c}\right] \tag{4.1}$$

Here, k is the Boltzmann constant ($k = 1.38 \times 10^{-23}\,\mathrm{J/K}$) and c is the speed of light ($c = 299{,}792{,}458\,\mathrm{m/s}$), T is the absolute temperature, $\xi_\perp$ is the strain rate associated with dislocation dynamics forming the Orowan equation for plastic deformation by gliding dislocations, and $\rho_\perp$ is the density of dislocations at several average recession velocities $\nu_\perp$ of mobile dislocations during irreversible deformation processes, where $b_\perp$ is the Burgers vector [4, 5]. Over this support, in the present paper, the main objective is to describe the phenomenology and mechanics of plastic flow during hot deformation by in situ tension test of sheet SEPCS Cu-30%Zn alloy.

4.2 Experimental

4.2.1 Materials

The material used in this investigation was a sheet of the SEPCS commercial alloy Cu-30%Zn, also named 70:30 brass, which is usually made from the purest copper and zinc. This alloy is used widely for tubes, sheets, and wires. After annealing, the alloy consists of homogeneous solid solution, and it is particularly suitable for cold-working [6].

4.2.2 Microstructural Characterization

In this work, a sample for tension test was obtained in the rolling direction, and a metallographic preparation was realized before the tension test. For metallographic preparation of the surface of the tensile test sample, SiC was used as abrasive grinding papers ranging from coarse 600 grit to very fine 1100 grit sizes, and alumina was used as a final polishing abrasive using a size particle of 0.05 μm in water solution. The sample surface was etched with a reactive solution prepared with ammonium hydroxide (NH_4OH: 60 ml.) and hydrogen peroxide (H_2O_2: 2 ml.), and the sample was cleaned and degreased with acetone. Subsequently, the coordinate system of reference was inscribed on the polished and etched surface of the center of the specimen by using a pyramid-shaped micro-Vickers indenter, and a diamond pyramidal figure was inscribed.

4.2.3 In Situ Tension Test SEM Studies

The initial dimensions of the tensile sample were gage length of 2.28 mm parallel to the rolled direction, smallest width of 1.15 mm, and thickness of 0.57 mm. The axial tensile test of this material at 250 °C was carried out in special module, Kammarth & Weiss Company, coupled in the field emission scanning electron microscopy (FESEM) with a capacity of 500 N. Also, the experiment was performed at constant crosshead velocity, $\nu = 0.152$ mm/min, and the initial strain rate was $\xi = 2.53 \times 10^{-3}\,\mathrm{s}^{-1}$, in the five stages of additive deformation for displacement in the X direction, for example, for the grain nine selected, as it is shown in Fig. 4.1a, b, the five stages of deformation are $\varepsilon_1 = 0.03$, $\varepsilon_2 = 0.113$, $\varepsilon_3 = 0.206$, $\varepsilon_4 = 0.343$, and $\varepsilon_5 = 0.448$.

4.3 Results and Discussion

4.3.1 Materials

70Cu-30Zn brass is based on solid solution, with a base crystalline structure FCC of Cu. Consequently, this metallic material has a single phase. Industrially, this alloy is typically named C26000. It is noticed that many physical properties of this alloy show obvious dependences on the Zn contents. In particular, the Zn content shows an efficient solute-strengthening effect because the tensile strength increased, but in practice the ductility of this metallic material could be reduced in anomalous behavior due to the short-range order mechanism associated with the atomic distribution in the crystalline solid solution of 70Cu-30Zn brass [6].

4.3.2 Microstructural Characterization

Figure 4.1a shows the microstructure of a single phase of the 70Cu-30Cu solid solution with a reference system inside of the surface of the sample, in order to

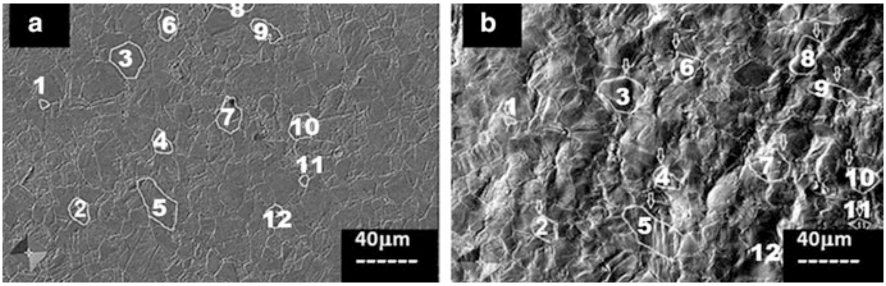

Fig. 4.1 Microstructure of Cu-30%Zn alloy at 250 °C: (**a**) previous deformation ($\varepsilon_0 = 0$) and (**b**) after deformation of $\varepsilon_5 = 0.26$

define the specific trajectory of a group of identified grains during the in situ tension test. This systematic study allows understanding with direct evidence more about the phenomenology and mechanics of the irreversible deformation process of this metallic material.

4.3.3 In Situ Tension Test SEM Studies

The total macroscopic irreversible deformation induced on the specimen was $\varepsilon_T = 0.18$. In situ, metallographic evidences of the plastic strain field were taken from the sample for each stage of deformation as it is shown in an example in Fig. 4.1b, with the proposed to obtain the mapping of the polycrystalline flow related with the microstructure evolution on the surface of the tension sample; some grains are identified with a number in order to define their trajectory during each step of the irreversible deformation process.

Physical macroscopic evidences of the tension test sheet specimen of SEPCS, Cu-30%Zn alloy at 250 °C before and after the severe irreversible deformation process under in situ tension test in FESEM, are shown in Fig. 4.2: (a) previous deformation process, $\varepsilon_0 = 0$; (b) identification of numerous lines for localized regions on the surface of the sample, before the deformation process $\varepsilon_0 = 0$; and (c) identification of numerous lines to evaluate the evolution of the true macroscopic deformation (ε_M) on the surface of the sample, as a function of displacement in the X direction with localized regions, after the severe irreversible deformation process ($\varepsilon_5 = 0.18$) under axial tension, before fracture. Directly observations allows to identify that macroscopic irreversible true deformation (ε_M) decreases exponentially from the center of the sample to the extreme of the work area, due to the particular geometry of the tension sample, which in principle induced high concentration of the stress during tension test in the central region of the work area delimited by the shoulder of the sheet tension sample for the fixed and mobile parts during tension test at constant crosshead velocity.

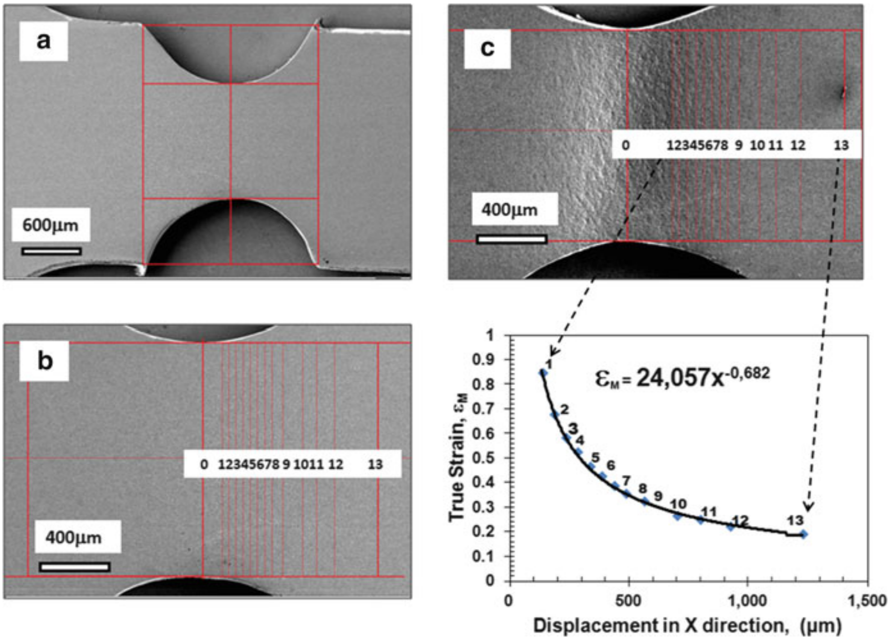

Fig. 4.2 Tension test sheet specimen of Cu-30%Zn alloy at 250 °C: (**a**) and (**b**) previous deformation, $\varepsilon_0 = 0$, and (**c**) surface evolution of macroscopic deformation until deformation of $\varepsilon_{M5} = 0.18$

Furthermore, the visual surface roughness of the sheet tension sample changes drastically from the central region to the extreme regions up to the shoulders of the tension sample. Also, it is interesting to describe that such surface roughness of the sheet tension sample is related with the appearance of the cellular dislocations defined by blocks of grains [7–12], as the main mechanisms for the macroscopic irreversible deformation process, as it is shown in Fig. 4.3a. Here, the density of cellular dislocations of 2.378×10^9 CD⊥/m^2 has been calculated under the consideration of 124 cellular dislocations inside of an area of 5215×10^{-8} m^2. Also, from Fig. 4.3b, the average size of the blocks of grains, named cellular dislocations, of 1.607×10^{-5} m, has been determinated by the mean linear intercept on localized surface associated with the microstructure evolution, and this value is considered as the magnitude of Burgers vector for cellular dislocation dynamic process ($\lambda_{CD\perp} = 1.607 \times 10^{-5}$ m) at the stage of macroscopic total deformation of $\varepsilon_{M5} = 0.18$.

Moreover, with the information obtained from Fig. 4.3 and with the average value of strain rate for cellular dislocations of $\xi_{5CD} = 1.03 \times 10^{-3}\ \mathrm{s}^{-1}$, associated with stage five of deformation ε_5, by applying Eq. (4.1), the activation energy for the irreversible deformation process induced by cellular dislocations at 250 °C was obtained: $Q_{CD\perp} = 162.783$ kJ/mol. This result is in a closed agreement with values

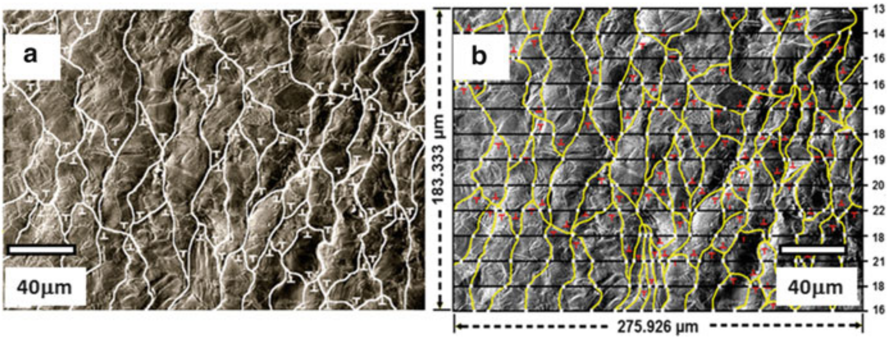

Fig. 4.3 Microstructure of Cu-30%Zn alloy at 250 °C: (**a**) identification of cellular dislocations and (**b**) determination of average value of the blocks of grains ($\lambda_{CD\perp} = 1.607 \times 10^{-5}$ m)

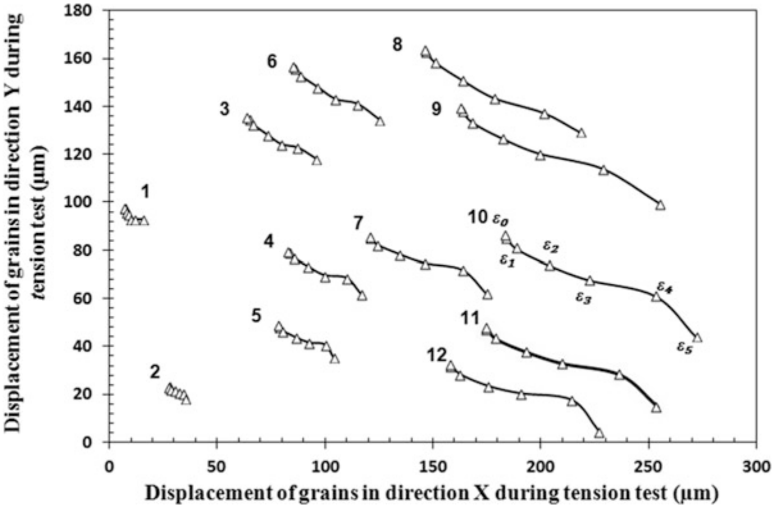

Fig. 4.4 Mapping of the granular flow of sheet Cu-30%Zn alloy at 250 °C

of $Q_{\perp} = 159$ kJ/mol reported in literature for a similar alloy in the range of temperature between 370 and 430 °C. Also, this value of the activation energy is near to the value reported for the self-diffusion of Cu or Zn [13]. In addition, for a single-phase Cu-30%Zn alpha brass, the activation energy for creep behavior reported at 300 °C is 170 kJ/mol [14]. Also, this last value is in a closed agreement with the main result obtained in this work.

The mapping of granular flow at five stages of the localized irreversible deformation process, under in situ axial tension test, at 250 °C of sheet SEPCS Cu-30%Zn alloy is shown in Fig. 4.4, where the selected grains follow a hyperbolic trajectory until stage four of the deformation process in a similar way as was reported previously for austenitic 304 stainless steel [1–3].

4.4 Conclusions

The present study by systematic mapping of granular flow during the irreversible deformation process under in situ axial tension test, at 250 °C and constant crosshead velocity of sheet SEPCS Cu-30%Zn alloy, has demonstrated that the hyperbolic motion of grains is assisted by cellular dislocation dynamics from direct evidence obtained with a different magnification from macroscopic scale to microscopic scale. Also, at macroscopic scale, deformation decreases exponentially from the center of the sheet tension sample, until their shoulders are fixed and mobile, during tension test. This important result is just couplet with changes of roughness over the surface of the sample. The local deformation of grains associated with their displacement in the *X* direction could be higher than the macroscopic deformation of the sheet tensile sample. Additionally, by applying the quantum mechanics and relativistic model proposed by Muñoz-Andrade, the activation energy for cellular dislocation dynamics could be calculated with the systematic information obtained from the methodology used to analyze the direct metallographic evidences by using the special tension module coupled with the FESEM.

References

1. Muñoz-Andrade JD (2007) Mapping of the granular flow during the irreversible deformation processes in spatially extended polycrystalline systems. Mater Sci Forum 561–565:901–904
2. Muñoz-Andrade JD (2007) On the hyperbolic flow manifested during the irreversible deformation processes in spatially extended crystalline systems. In: AIP Conference Proceedings, vol 907, pp 1283–1288
3. Muñoz-Andrade JD (2013) Systematic study of polycrystalline flow during tension test of sheet 304 austenitic stainless steel at room temperature. In: AIP Conference Proceedings, vol 1567, pp 796–799. doi:10.1063/1.4850090
4. Muñoz-Andrade JD (2007) Super plastic flow and cosmic micromechanics. Key Eng Mater 345–346:577–580
5. Muñoz-Andrade JD (2008) The activation energy for plastic flow in spatially extended polycrystalline systems during tension test. Int J Mater Form Suppl 1:81–84
6. Hong HL, Wang Q, Dong C, Liaw PK (2014) Understanding the Cu-Zn brass alloys using a short-range-order cluster model: significance of specific compositions of industrial alloys. Sci Rep 4:7065, 1–4. doi:10.1038/srep07065
7. Morral JE, Ashby MF (1974) Dislocated cellular structures. Acta Metall 22:567–575
8. Zelin MG, Dunlap MR, Rosen R, Mukherjee AK (1993) The direct observation of cooperative grain boundary sliding and migration during superplastic deformation of lead tin eutectic in shear. J Appl Phys 74:4972–4982
9. Zelin MG, Mukherjee AK (1995) Study of cooperative grain boundary sliding by using macroscopic marker lines. Metall Mater Trans A 26:747–750
10. Zelin MG, Mukherjee AK (1995) Cooperative phenomena at grain boundaries during superplastic flow. Acta Metall Mater 43:2359–2372
11. Zelin M, Guillard S, Mukherjee AK (2001) Cellular dislocations: experiment and modelling. Mater Sci Eng A 309–310:514–519

12. Muñoz-Andrade JD, Mendoza-Allende A, Torres-Villaseñor G, Montemayor-Alderete JA (2001) Cooperative grain boundary sliding at room temperature of a Zn-20.2%AI - 1.8%Cu superplastic alloy. Mater Sci Forum 357–359:551–558
13. Lee KA, Chang YW, Lee CS (2004) An internal variable approach for anomalous yield phenomena of β-CuZn alloy. Acta Mater 52:2913–2922
14. Raj SV (1991) Creep behavior of Cu-30%Zn at intermediate temperature. J Mater Sci 26:3533–3543

Chapter 5
Determination of the Activation Energy of Copper During In Situ Tension Testing by SEM

D. Morán García, E. Garfias-García, and J.D. Muñoz-Andrade

Abstract Following the polycrystalline flow study of a commercial copper during in situ tension testing was done with a special module coupled with SEM-SUPRA equipment and also by tension testing using an Instron machine. All the experiments were done with a constant crosshead velocity of $V_c = 0.19$ mm/min, at room temperature. The activation energy for plastic flow was obtained by using the quantum mechanics and relativistic model, proposed by Muñoz-Andrade. The true activation energy ($Q_\perp$) for plastic flow during axial tension testing at constant crosshead velocity, in a Universal Tension Machine, was calculated with an average value of 122.76 kJ/mol. Additionally, direct observation during five steps of deformation using a special Kammrath & Weiss Company module, coupled with SEM-SUPRA, with a total deformation of $\varepsilon = 0.0908$, establishes that the trajectory of the crystals during the irreversible deformation process follows a hyperbolic motion. It was observed that the polycrystalline irreversible deformations are promoted by two coupled mechanisms, including dislocation dynamics at inner individual crystals and granular group movement, called cellular dislocations. The true activation energy related to the cellular dislocation dynamics was determinate with a value between 100.16 and 106.55 KJ/mol.

Keywords Activation energy • Copper • Plastic flow • Dislocation dynamics • Cellular dislocation

---

D. Morán-García • E. Garfias-García • J.D. Muñoz-Andrade (✉)
Departamento de Materiales, División de Ciencias Básicas e Ingeniería, Universidad Autónoma Metropolitana Unidad Azcapotzalco, Av. San Pablo 180, Col.
Reynosa Tamaulipas, 02200 D.F., Mexico
e-mail: jdma@correo.azc.uam.mx

R. Pérez Campos et al. (eds.), *Characterization of Metals and Alloys*, DOI 10.1007/978-3-319-31694-9_5

5.1 Introduction

Determining the activation energy for plastic flow of the material is essential to identify deformation mechanisms influencing the deformation. The dislocations are a crystallographic defect, are responsible for the plastic properties in metallic materials, and constitute one of the key mechanisms in any process of plastic deformation. They do so because its nature is associated with the lowest energy state that is necessary and sufficient to initiate activation of the slip systems inside the crystals [1, 2].

In a polycrystalline system, a cooperative phenomenon of grain boundary sliding could be presented during the irreversible deformation process. This phenomenology is also known as cellular dislocation dynamics [3, 4]. In principle, the apparent activation energy for irreversible deformation processes can be determined from experimental data by applying the theoretical model proposed by Mohamed and Langdon [5]:

$$Q_a = nR\left[\frac{\partial ln\sigma}{\partial(1/T)}\right]_{\xi} \tag{5.1}$$

Where ξ is the strain rate, R is the universal gas constant, T is the absolute temperature, n is a constant, and σ is the applied stress. The limitation of this conventional model is that it only determines the apparent activation energy as it is used in a temperature range, and the result is an average value of activation energy in that range.

Nonetheless, in today's environment, using a new quantum mechanics and relativistic model recently proposed by Muñoz-Andrade, it is possible to obtain the true activation energy for the irreversible deformation process [6–8], which is presented with the follow relationship:

$$Q_{\perp} = -kT\ln\left[\frac{\xi_{\perp}\lambda_{\perp}}{c}\right] \tag{5.2}$$

Where $\xi_{\perp}$ is the strain rate, $\lambda_{\perp}$ is the Burgers vector, T is the work temperature ($T = 250\,^{\circ}\mathrm{C}$), K is the Boltzmann constant ($k = 1.38 \times 10^{-23}\,\mathrm{J\,K^{-1}}$), c is the speed of light ($c = 299,792,458\,\mathrm{ms^{-1}}$), and $Q_{\perp}$ is the activation energy for plastic deformation. With this model, the activation energy at each thermo-mechanical condition during the deformation process is obtained. The strain rate is determined from Eq. (5.3):

$$\xi = \frac{V_{\mathrm{c}}}{l_{\mathrm{inst}}} \tag{5.3}$$

Where ξ is the strain rate, V_c is the constant crosshead velocity, and l_{inst} is the instantaneous length value, which is obtained from the force—extension curve. Moreover, from the Orowan's equation for plastic flow related to dislocation dynamics in crystals, it is possible to relate the strain rate, in analogous way, with the density of cellular dislocations on the surface of polycrystalline system, according to the following expression:

$$\xi_{\perp} = \rho_{\text{CD}\perp} v_{\text{CD}\perp} \lambda_{\text{CD}\perp} \tag{5.4}$$

Where, $\rho_{\text{CD}\perp}$ is cellular dislocations density, $v_{\text{CD}\perp}$ is the average glide velocity of cellular dislocations, and $\lambda_{\text{CD}\perp}$ is the Burgers vector for cellular dislocation for cooperative grain boundary sliding. As well, the study of the mechanics of granular flow during plastic deformation could be made by the new mapping technique proposed by Muñoz-Andrade [9, 10]. This technique implements a reference system on the surface of the metallic material sample by using micro hardness indentations in order to build a set of indentation marks, which in this study is done on a commercial copper.

With this new technique, it has been demonstrated, in an austenitic stainless steel AISI 304, that the dynamics of the cooperative granular flow during plastic deformation describe a set of hyperbolic trajectories associated with the movement of self-accommodation of the crystals and to the deformation process by dislocations inside the crystals [9]. Also the study, done using type 430 stainless steel, found that the trajectory of the crystals during an irreversible deformation process also follow a hyperbolic motion [11]. In addition, the study has been done in a Pb-50%Sn sample, where the trajectory of the cooperative granular flow does not fit a curve [12].

The main objectives in this work are as follows: First, to obtain the activation energy for plastic flow during tension testing at constant crosshead velocity in a universal test machine. Second, to construct the mapping of the granular flow during tension testing at constant crosshead velocity, performed by using the tensile module of Kammrath & Weiss in the Scanning Electron Microscope (SEM). Third is to establish the deformation mechanisms by direct observations.

5.2 Experimental

The material used in this study was commercial copper in a sheet form, with thickness of 0.5 mm,with an average grain size of 262.47 μm, obtained by using the mean linear intercept technique.

The copper sheet was punched out on flat test pieces for tensile tests, as shown in Fig. 5.1. The two tensile tests were performed using different techniques.

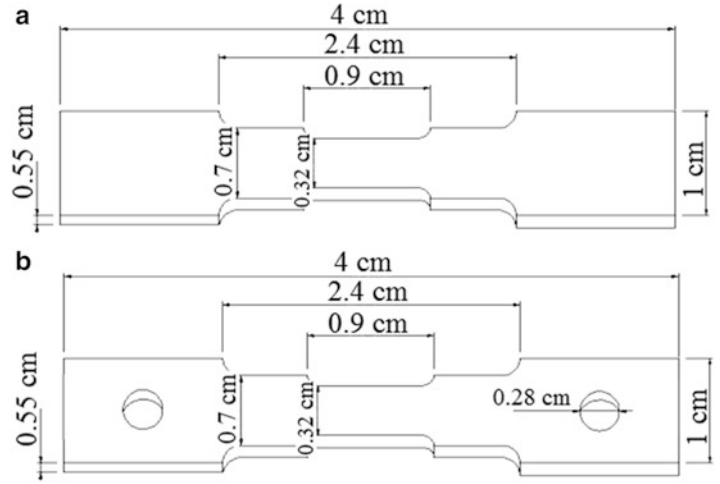

Fig. 5.1 Tensile test samples manufactured by punching (**a**) For testing in a universal tensile machine and (**b**) For testing in a Kammrath & Weiss tensile module

5.2.1 Tensile Test in a Universal Machine

The first tensile test of this material at room temperature was carried out using an Instron Universal Tensile Machine in five steps of additive deformation. The initial dimensions of the tension test sample are shown in Fig. 5.1. The experiment was performed at constant crosshead velocity, $V_c = 0.19$ mm/min with an initial strain rate of $\xi = 3.51 \times 10^{-4}\,\mathrm{s}^{-1}$. The Burgers vector value used in this work for a unitary dislocation is $\lambda_{\mathrm{Cu}} = 0.2556$ nm.

5.2.2 Tensile Kammrath & Weiss Tensile Module at SEM

The second test was carried out with a Scanning Electron Microscope (SEM) using the Kammrath & Weiss tensile module at room temperature with a constant crosshead velocity of $V_c = 0.19$ mm/min. Before conducting the test, the tensile test specimen should be performed by metallographic preparation to observe the microstructure during the deformation process. For this, the samples are polished to have a mirror finish and etched to reveal the microstructure using hydrochloric acid (2 ml), ferric chloride (5 g) and ethyl alcohol (98 ml), with an attack time of approximately 20 s.

Once upon a time, the microstructure revealed a mesoscopic coordinate system of reference that was inscribed on the polished and etched surface of the center of the specimen by using a pyramidal-shaped micro Vickers indenter, and a diamond

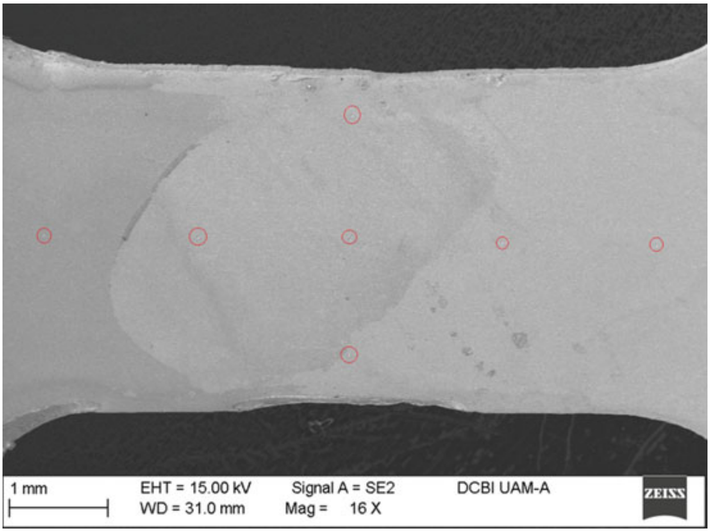

Fig. 5.2 Coordinate system of reference on the surface of the center of a tension test specimen of copper

pyramidal set of figures were inscribed as shown in Fig. 5.2. The indentations are about the size of grain and avoided having influence in the deformation process. This reference system helps to monitor the microstructure and to take photomicrographs at each step of deformation of the material until the fracture. With these photomicrographs and the mapping of granular flow obtained by using the technique developed by Muñoz-Andrade [8], it was possible to obtain the value of the Burgers vector at a mesoscopic level for cellular dislocations, which enabled the calculation of the activation energy for plastic flow by applying Eq. (5.2).

5.3 Results and Discussion

5.3.1 Tensile Test in a Universal Machine

Figure 5.3 shows the stress-strain curve from the tensile test carried out in a Universal Testing Machine at a constant crosshead velocity, $V_c = 0.19\,\text{mm/min}$, and an initial strain rate of $\xi = 3.51 \times 10^{-4}\,\text{s}^{-1}$. With this information, the true activation energy is obtained by using Eq. (5.2), $Q = 122.76\,\text{KJ/mol}$.

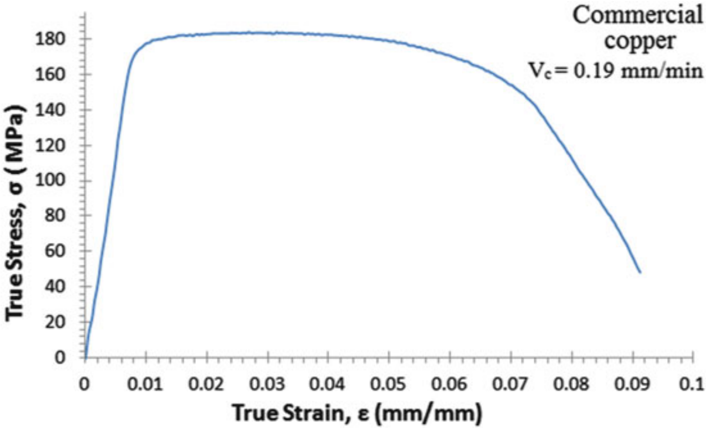

Fig. 5.3 Stress-strain curve of a tensile test made by a Universal Instron Tensile Machine in a commercial copper sheet at room temperature with $V_c = 0.19$ mm/min

5.3.2 Tensile Kammrath & Weiss Tensile Module at SEM

In Fig. 5.4, a representation of cellular dislocations is revealed for a magnification of 400×, associated with the final step of deformation under unidirectional tension, to determine the activation energy for plastic flow related to cellular dislocation ($Q_{CD\perp}$) over and done with respect to the microstructure evolution evident at the mesoscopic level.

In Fig. 5.5, horizontal lines are plotted to established the average size of blocks of grains, named cellular dislocations, the value of which is associated on the mesoscopic scale with the Burgers vector for cellular dislocations, $\lambda_{DC\perp} = 9.48097 \times 10^{-8}$ m. By applying Eq. (5.2), the activation energy for plastic flow assisted by cellular dislocations at room temperature is $Q_{CD\perp} = 106.303$ KJ/mol.

Taking the theory of Muñoz-Andrade [6, 8] as a starting point, the Burgers vector on a mesoscopic scale for cellular dislocations has been used to established the average size of blocks. Consequently, the Burgers vector is used in a mesoscopic scale at each stage of deformation during in situ tension test. From Figs. 5.6, 5.7, and 5.8, cellular dislocations are shown in yellow marked lines and are associated with the last step of deformation under unidirectional tension, with a magnification of 200× to determine the activation energy ($Q_{CD\perp}$) for plastic flow to the microstructural evolution.

Also, in Fig. 5.7, horizontal lines are plotted to establish the average size of blocks grains, using the Burgers vector for cellular dislocations, $\lambda_{DC\perp} = 8.5655 \times 10^{-8}$ m at room temperature. The activation energy is associated with the plastic

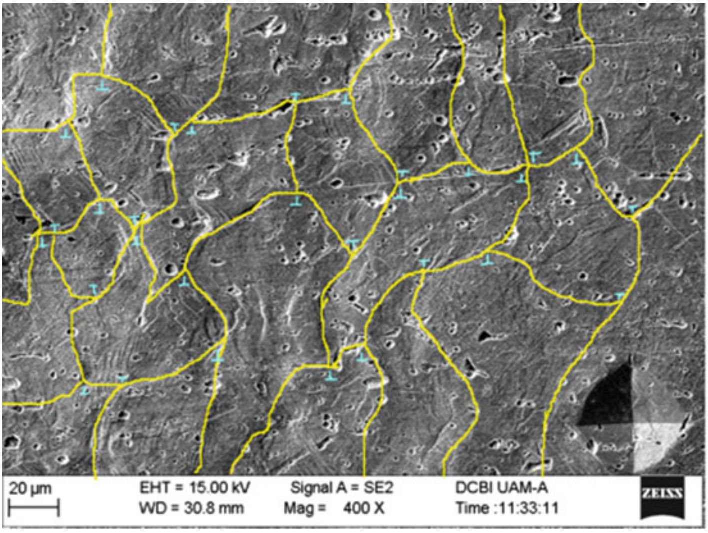

Fig. 5.4 Indication of the cellular dislocations (positive T and negative ⊥) on the surface of the sheet test sample at the last step of deformation "$\varepsilon_5 = 0.0908$" at 400×

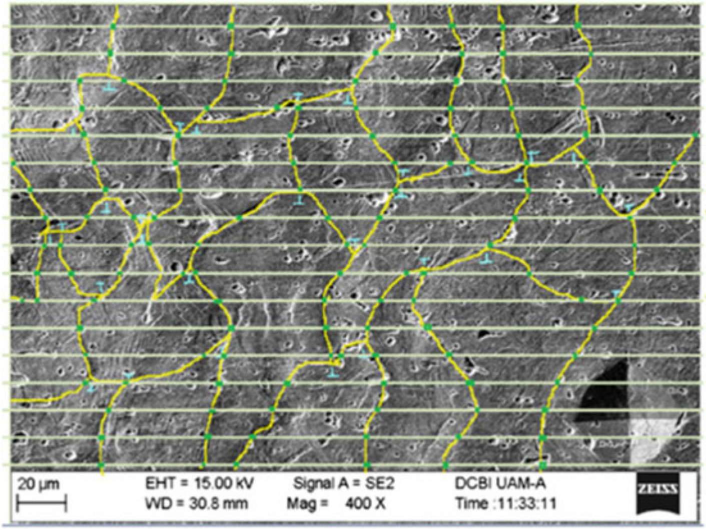

Fig. 5.5 Representation of the *horizontal lines*, to find the average size of blocks named cellular dislocations at the mesoscopic level, considered as the Burgers vector, in the last step of deformation "$\varepsilon_5 = 0.0908$" at 400×

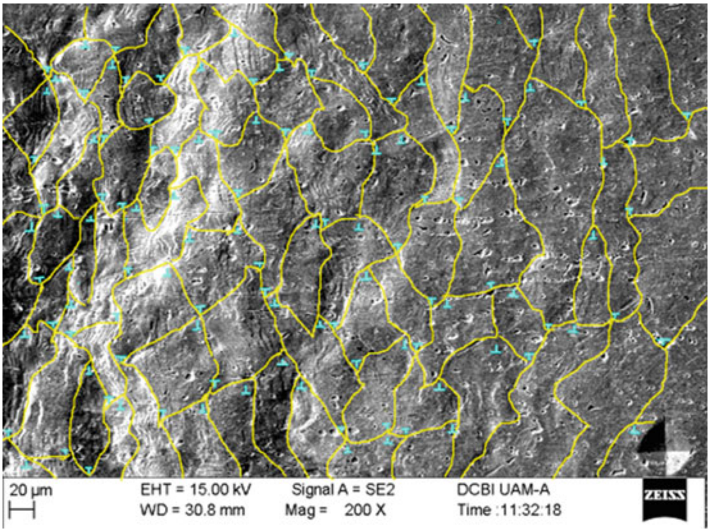

Fig. 5.6 Representation of the (positive T and negative $\perp$) cellular dislocations on the surface of the flat test piece in the last step of deformation "$\varepsilon_5 = 0.0908$" at 200×

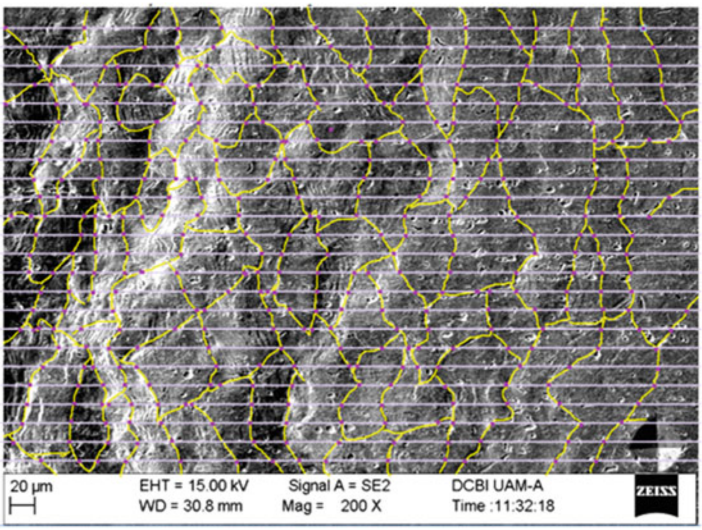

Fig. 5.7 The *horizontal lines* represent the average thickness of cellular dislocation at the mesoscopic level, called the Burgers vector, in the last step of deformation "$\varepsilon_5 = 0.0908$"

deformation assisted by cellular dislocations $Q_{CD\perp} = 106.550\,\text{KJ/mol}$. Figure 5.8 shows a micrograph with a magnification of 60×, from which an increase in cellular density dislocations is also observed.

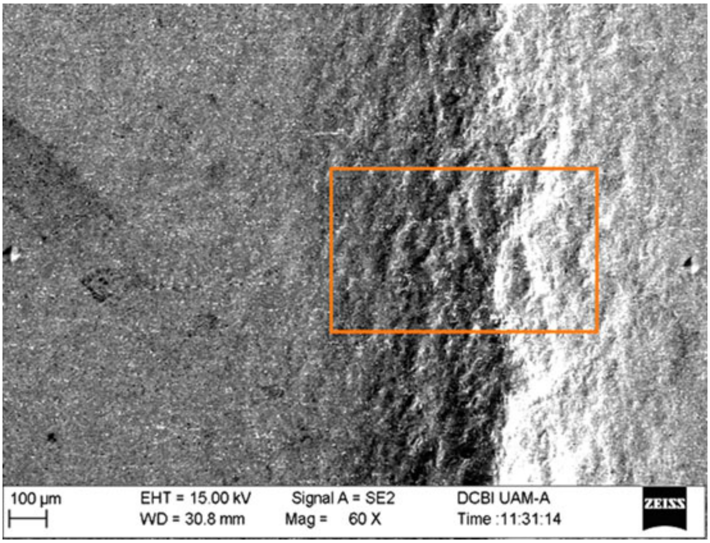

Fig. 5.8 A localized region is used to determine the Burgers vector at a mesoscopic level, on a sheet test sample in the last step of deformation "$\varepsilon_5 = 0.0908$" to 60×

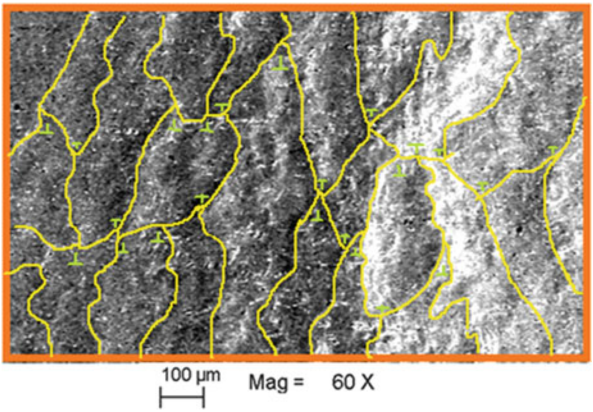

Fig. 5.9 Representation of the (positive T and negative ⊥) cellular dislocations on the sheet test sample in the last step of deformation "$\varepsilon = 0.0908$" to 60×

The calculated values of the Burgers vectors and the values of activation energy for plastic flow assisted by cellular dislocations are direct evidence of the microstructure evolution at the mesoscopic level during tension testing with the scanning electron microscope and are related for several scales in the last step of deformation prior to fracture (Fig. 5.9).

The activation energy values reported in Table 5.1 were calculated by applying Eq. (5.2), associated with the relativistic quantum mechanical model proposed by Muñoz-Andrade. Such results, on a mesoscopic scale, differ from the inner value of activation energy for plastic flow at room temperature assisted by dislocations inside

Table 5.1 Activation energy and Burgers vector values

Magnification	$\lambda_{DC}\perp$ (m)	$Q_{DC}\perp$ (KJ mol^{-1})
400×	9.48097×10^{-8}	106.30364
200×	8.5655×10^{-8}	106.5509
60×	1.1794×10^{-6}	100.1642

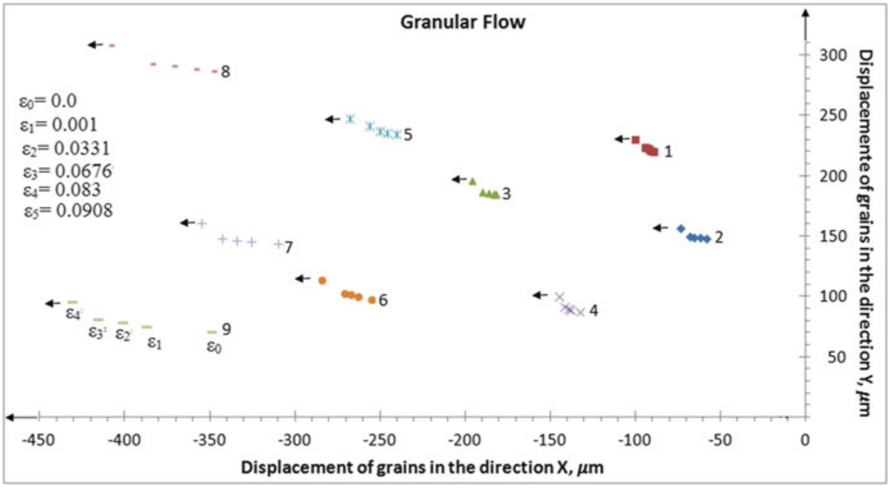

Fig. 5.10 Mapping of the granular flow during the irreversible deformation processes in copper after five stages of deformation

of copper crystals, about ≈11 %. From the metallographic evidence obtained for the five steps of the irreversible deformation processes, the mapping of the granular flow of copper was obtained, as it is shown in Fig. 5.10.

Mapping of the granular flow in this contribution suggests that the hyperbolic motion is manifested during the irreversible deformation processes in polycrystalline copper. The experimental evidence indicated that the hyperbolic granular flow is assisted by cellular dislocation dynamics and self-accommodation of grains.

5.4 Conclusions

The relevant characteristic of this work is that the polycrystalline irreversible deformation process of copper, for the tension testing conditions reported, are promoted by two coupled mechanisms that include dislocation dynamics inside of crystals and the movement of blocks of grains called cellular dislocations. Also, the activation energy obtained for both mechanisms are closer.

The relevant characteristics of this work are as follows:

1. The polycrystalline irreversible deformation process of copper, for the tension testing conditions reported are promoted by two coupled mechanisms: dislocation dynamics inside of crystals and the movement of blocks of grains called cellular dislocations.
2. The activation energy obtained for both mechanisms are closer.
3. The mapping of the granular flow indicates that the trajectories of polycrystalline flow obey a hyperbolic flow during irreversible deformation processes.

References

1. Hull D, Bacon D (2011) Introduction to dislocations. Butterworth-Heinemann, Oxford
2. Rodriguez P (1996) Sixty years of dislocations. Bull Mater Sci 12:857–872
3. Morral J, Ashby M (1974) Dislocated cellular structures. Acta Metall 22:567–575
4. Zelin MG, Dunlap MR, Rosen R, Mukherjee AK (1993) The direct observation of cooperative grain-boundary sliding and migration during superplastic deformation of lead-tin eutectic in shear. J Appl Phys 74:4972–4982
5. Mohamed F, Langdon T (1976) The determination of the activation energy for superplastic flow. Phys Stat Sol 33:375–381
6. Muñoz-Andrade JD (2008) The activation energy for plastic flow in spatially extended polycrystalline systems during tension test. Int J Mater Forum 1:81–84
7. Muñoz-Andrade JD (2007) Cosmic micromechanics connection with irreversible deformation processes in spatially extended crystalline systems. Mater Sci Forum 561:1927–1930
8. Muñoz-Andrade JD (2004) Activation energy for irreversible deformation processes in spatially extended crystalline systems. AIP Conf Proc 1601–1606
9. Muñoz-Andrade JD (2007) On the hyperbolic flow manifested during the irreversible deformation processes in spatially crystaline systems. AIP Conf Proc 907:1283–1288
10. Muñoz-Andrade JD (2007) Mapping of the granular flow during the irreversible deformation processes in spatially extended polycrystalline systems. Mater Sci Forum 561–565:901–904
11. Pérez R, Contreras A, Esparza R (2015) Materials characterization. Springer, New York
12. López-Ramírez J, Muñoz-Andrade JD, Garfias-García E, Aguilar-Sánchez M (2014) Systematic study of polycrystalline flow during in situ tension test by SEM of Pb-50%Sn at room temperature. Mater Sci Forum 793:113–118

Chapter 6
Effect of Copper Additions on Secondary Carbide Precipitation in High Chromium with Cast Iron

F.V. Guerra, A. Bedolla-Jacuinde, I. Mejía, J. Zuno-Silva, and E. Cardoso-Legorreta

Abstract This work analyzes the secondary carbide precipitation during the destabilization heat treatment of a 15 % Cr white iron and copper additions between 0.5 and 2 wt%. The destabilization heat treatments were undertaken at temperatures of 850, 950, and 1050 °C between 5 and 480 min. Characterization was carried out by X-ray diffraction (XRD), optical and electron microscopy, image analysis, and energy-dispersive spectroscopy (EDS) microanalysis; the resultant hardness was also measured. It was found that the copper addition resulted in an increase in discontinuity of the eutectic carbide in as-cast conditions. After the heat treatment, the number of precipitated carbides increased with the copper addition, and they were found smaller. There were an increase of precipitation for lower destabilization temperatures and large soaking times.

Keywords High-chromium white cast iron • Destabilization • Precipitation • Secondary carbides • Copper

6.1 Introduction

High-chromium white irons are ferrous alloys containing between 11–30 % Cr and 1.8–3.6 % C carbon, with molybdenum, manganese, copper, and nickel sometimes added as additional alloying elements. The typical as-cast microstructure of these alloys consists of primary and/or eutectic carbides (M_7C_3) in an austenitic matrix or one of its transformation products [1]. The hard eutectic carbides and matrix present

---

F.V. Guerra (✉) • J. Zuno-Silva • E. Cardoso-Legorreta
Universidad Autónoma del Estado de Hidalgo, Av. Madero 706, Doctores,
42090 Pachuca, Hgo., Mexico
e-mail: vapeani@hotmail.com

A. Bedolla-Jacuinde • I. Mejía
Instituto de Inv. Metalúrgicas y de Materiales, UMSNH. J. Múgica S/N,
58030, Morelia, Mich., México

R. Pérez Campos et al. (eds.), *Characterization of Metals and Alloys*, DOI 10.1007/978-3-319-31694-9_6

in the microstructure are responsible for the great abrasion resistance and fracture toughness of these alloys; hence, these alloys are commonly used to applications where abrasion resistance is the main required property [2]. If a high hardness is needed, the as-cast austenitic structure is submitted to destabilization heat treatment between 800 and 1000 °C to obtain small secondary carbides (SC) precipitated in the matrix. During the treatment, the matrix decreases in chromium and carbon content due to precipitation of carbides raising the temperature of martensitic start transformation resulting in a mixture of martensite and retained austenite [3]. Some alloying elements like Cr, Mo, Ni, and Cu are added to promote a good hardenability [4]. Temperature in combination with the soaking time and content of alloying elements change the kinetic of precipitation of secondary carbides. The addition of Cu contributes to hardenability but stabilizes the austenite and delays the carbon diffusion [4]. Therefore, the presence of Cu has a strong influence in the precipitation of secondary carbides modifying the time of precipitation. Time, temperature, and Cu content are the variables used in this work, to analyze their effect on distribution, velocity, and microhardness of precipitated carbides.

6.2 Experimental

The high-chromium white iron subject to experimentation was manufactured with high-purity raw materials to control impurities and chemical composition. They were melted in an induction furnace and poured in a sand mold to obtain bars of 10 in. length and 1 in. diameter. Four different compositions were obtained with 15 % Cr, 3 % C, 1 % Mo, 1 % Ni, and 0, 0.5, 1, and 2 wt% Cu, respectively. The bars were sectioned on samples of $1/2 \times 1/2 \times 1/4$ in. with an abrasive wheel in a Struers metallographic cutter (Struers, Copenhagen, Denmark) Labotom-3 using coolant to avoid overheating. The heat treatments were carried out on an electric furnace at 850, 950, and 1050 °C and soaking times of 5, 15, 30, 60, 90, 150, 300, and 480 min for each composition; the samples were quenched in water to avoid further precipitation during cooling. Samples were prepared for metallography by grinding on abrasive paper of different mesh sizes. Samples were then polished on nylon cloth with 6 μm diamond paste as the abrasive and finally with 1 μm paste. Etching was carried out with two different solutions: Vilella's etchant (5 ml HCl and 1 g picric acid in 100 ml ethanol) for 30–60 s to reveal the microstructure and a solution of 50 ml $FeCl_3$ plus 20 ml HCl in 930 ml ethanol immersed during 8 h, for a deep etching to remove part of the matrix to observe the eutectic carbides. As-cast eutectic carbide volume fraction was measured by image analysis on digitized micrographs obtained at 200× on a Nikon EPIPHOT 300 optical microscope (Nikon, Melville, NY). For this purpose, the samples were deeply etched, and 20 micrographs were processed by the SigmaScan (Jandel Scientific, San Rafael, CA) V.5 software on a PC. XRD studies were also undertaken to identify the different phases present in the alloy before and after heat treatment. Retained austenite after heat treatment was calculated from XRD data by the technique described by Kim [5]. XRD tests were carried out by using Cu-Ka radiation in a 2θ range of 30–130°. Further characterization was undertaken on a JEOL (JEOL, Peabody, MA) 6400 SEM at 20 kV for imaging and EDS microanalysis. Secondary carbide volume fraction and size were obtained by point counting measurements on SEM micrographs. Microhardness of the matrix was undertaken on metallographic samples. Twenty tests for each sample were carried out by a diamond indenter and a 100 g load for 15 s, for Vickers microhardness (HV100).

6.3 Results and Discussion

The chemical composition of the experimental irons is shown in Table 6.1.

As shown in Table 6.1, the main difference in composition is regarding the copper content. Therefore the changes in microstructure and properties are attributed to copper addition. This copper addition was made to modify the time of precipitation of secondary carbides because it is known that the copper addition can increase the hardenability and decrease the carbon diffusion [6, 7] which modifies the time, shape, and distribution of precipitated carbides.

6.3.1 *As-Cast Structure*

Figure 6.1 shows the as-cast structure of the alloy, where the eutectic M_7C_3 carbides and the austenitic matrix can be observed; however, small amounts of martensite $\acute{\alpha}$ and molybdenum M_2C carbides can be observed.

The presence of martensite can be observed in the periphery of the eutectic carbide due to the carbon and chromium depletion by diffusion to the carbide, which causes the raising of the martensite start temperature (Ms), giving place to the martensitic transformation under cooling to room temperature [3, 8, 9]. The XRD pattern of Fig. 6.2 shows the presence of austenite γ, eutectic carbides M_7C_3, and carbides type M_2C in the alloy; no ferrite/martensite peaks are observed due to the low volume content in as-cast conditions.

The presence of copper precipitate particles or segregation was not observed; as shown in Fig. 6.3, copper is distributed uniformly in the matrix.

The quantification of eutectic carbide volume fraction is shown in Table 6.2.

Table 6.1 Chemical composition of experimental irons, wt%

Alloy	C	Cr	Mo	Ni	Cu
A	2.97	15.21	1.02	1.05	0
B	3.15	14.79	1.01	0.97	0.6
C	3.13	15.47	0.97	0.96	1.1
D	2.96	15.51	0.97	1.04	2.1

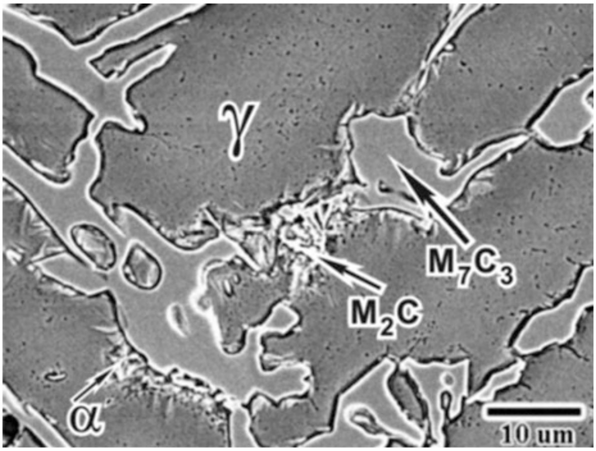

Fig. 6.1 As-cast microstructure of the as-cast experimental iron

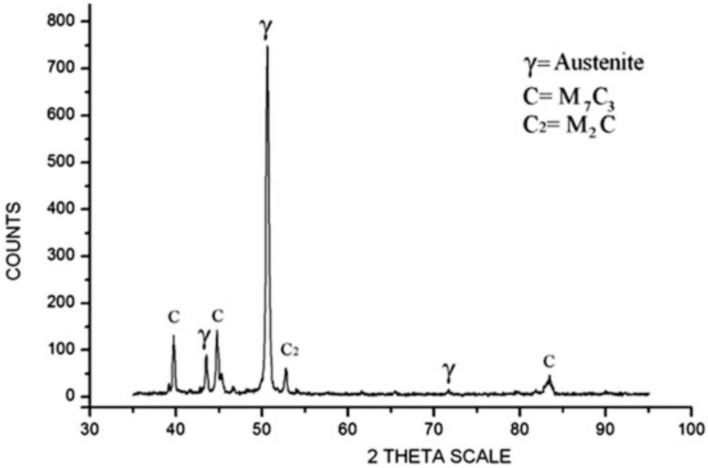

Fig. 6.2 XRD pattern of the D alloy in as-cast conditions

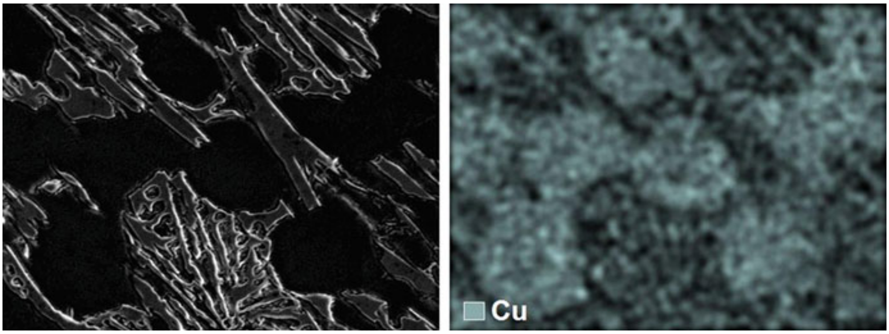

Fig. 6.3 SEM micrograph and chemical composition mapping for copper

Table 6.2 Eutectic carbide volume fraction ($ECV_{Frac.}$)

Cu Wt%	0	0.6	1.1	2.1
$ECV_{Frac.}$	26.5 %	27 %	27.5 %	26.5 %

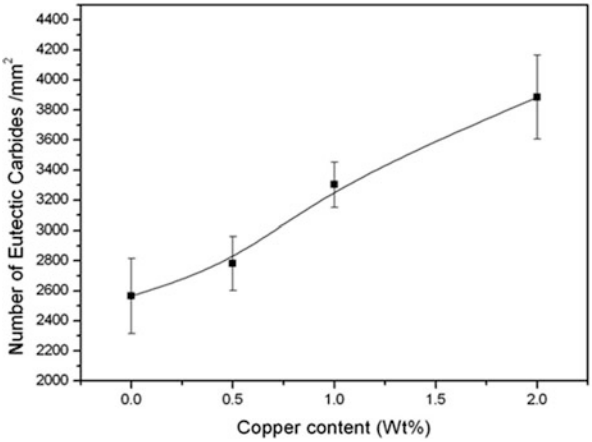

Fig. 6.4 Eutectic carbides/mm^2 as a function of copper content

There is no significant difference about the volume fraction of eutectic carbide, but there is a different distribution. Figure 6.4 shows the number of eutectic carbides per square millimeter.

As shown in Fig. 6.4, the number of carbides/mm^2 increases with increasing the copper addition, but the volume remains almost constant; this is seen as more discontinuous eutectic carbide. The above agrees with the observations of Choi et al. [10] for irons with higher content of copper. This modifying effect has been widely reported for different researchers [11–15] and is based necessarily on segregation during the solidification process, due to the lower solubility on at least one of the phases. Similar effect has been found by Liang and Su [14] in low-chromium white irons, where the addition of 5 wt% of rare earths (RE) changes the leader phase during the solidification process from austenite to cementite. They found cementite blocks instead of a common ledeburitic structure. It seems that the presence of copper limits the growth in certain directions, obtaining a higher number of eutectic carbides with a constant volume. But it not necessarily limits the precipitation; according to Qingxiang et al. [11], rare earth addition suppresses the M_3C growth in a Ni-Cr iron in the [010] direction. Also, they observed that this addition of RE promotes the growing in [100] and [001] directions helping the formation of carbides in the form of isolated blocks.

6.3.2 Structure After Destabilization Heat Treatment

The heat treatment changes the volume of phases, increasing the volume of carbide and martensite at the expense of austenite with the increase in the soaking time, except in those treated at 1050 °C where the austenite phase was overstabilized as will be shown later. The number and size of precipitated carbides are functions of temperature, time, and chemical composition.

6.3.3 Number and Average Diameter of Secondary Carbides

Figure 6.5 shows a sequence of micrographs (a–d) from the iron with 1 % of copper addition, heat treated for 15, 60, 120, and 480 min, respectively, at 850 °C.

From Fig. 6.4, we can observe an increase in precipitation with the increase of the exposure time. Figure 6.5 shows the average number of precipitated carbides per square micrometer. For the different alloys, the average number of precipitated

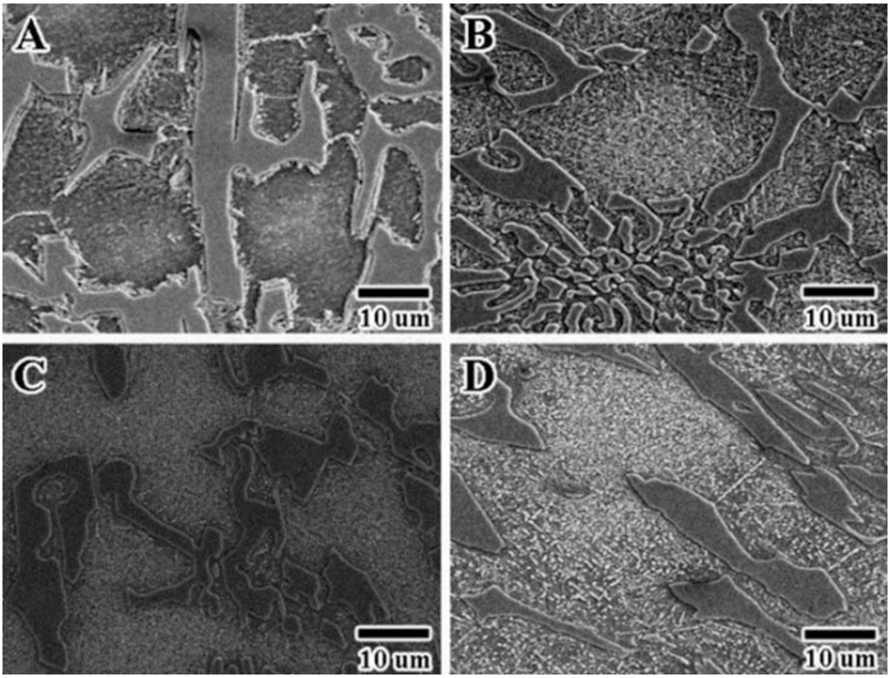

Fig. 6.5 SEM micrographs of 1 % of copper iron heat treated for 15, 60, 120, and 480 min at 850 °C

carbides increases with the holding time at 850 °C; this is because at this temperature, the rate of diffusion to reach the equilibrium is low and the precipitation continued until the longer times.

Therefore, as shown in Fig. 6.4, the microstructures of the heat-treated alloys at 850 °C show a very small-size secondary carbide distribution. Copper additions produce a delay of carbide precipitation for short periods of time as shown in Fig. 6.5 because copper stabilizes the austenite phase in accordance with Krishnadev and Sudan (see JW Choi, 1992) [10]. For holding times longer than 90 min, a remarkable increase in the number of secondary carbides on higher-copper content samples is shown. This effect is attributed to the ability of copper to reduce the diffusion of carbon in austenite; therefore, the elements which form the precipitates (Cr and C) are expelled from the matrix during the destabilization process, and due to the presence of copper, they move shorter distances. As a result, we have a greater number of particles but of smaller size as we can see on Figs. 6.6 and 6.7 with the copper addition.

As we can see, the samples with higher copper content show precipitated carbides with smaller diameter. Figure 6.6 shows that the precipitation occurs in short periods of time in the samples with lower copper content, but there are only some large particles of diameters between 0.20 and 0.25 μm. After the average diameter decreases due to precipitation of particles of smaller size, precipitation continues until 150 min. Subsequently the particles start to grow up to a diameter between 0.17 and 0.19 μm. By contrast, samples with copper contents of 1 and 2 % at longer times of 15 min have precipitated particles of very small diameters of about 0.06 μm. Precipitation occurs in uniformly throughout the matrix. These particles start to grow at times greater than 150 min; this effect is attributed to the copper's ability to decrease the carbon diffusion in austenite. Therefore carbon and chromium expelled from the matrix tend to move shorter distances. As mentioned above the case has been reported by some researchers as Choi et al. [10] in the presence of copper secondary carbides; therefore, it can be acting as nucleating since it has a greater number of smaller precipitates of smaller size.

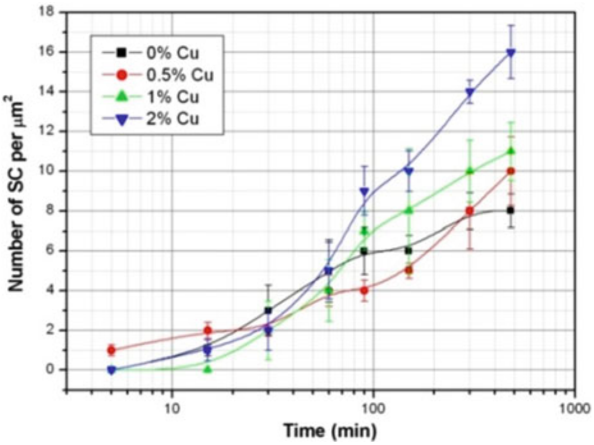

Fig. 6.6 Number of precipitated carbides as a function of soaking time at 850 °C

Fig. 6.7 Average diameter of SEC. Carbides as a function of soaking time at 850 °C

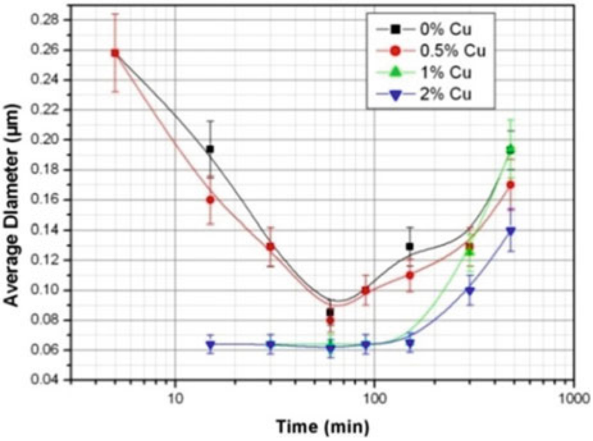

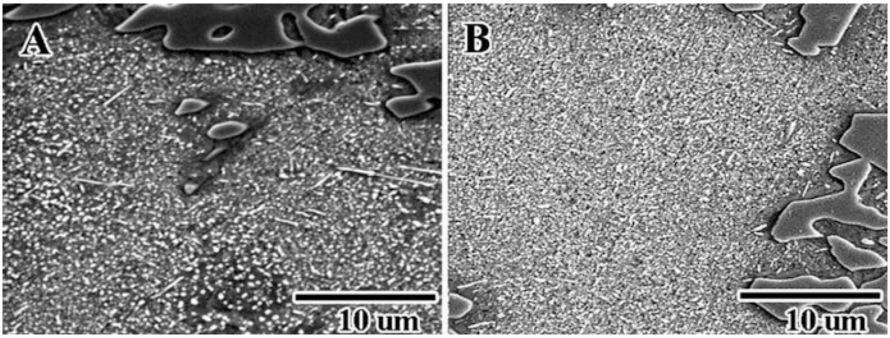

Fig. 6.8 SEM micrographs showing secondary carbide precipitation during destabilization heat treatment at 850 °C. (**a**) Base alloy, (**b**) 2 wt% of copper alloyed white iron

Figure 6.8 shows the micrographs for comparative purposes for the alloys treated for 480 min at 850 °C; we can observe a notable increment on the number of precipitated carbides and of smaller size in the 2 % of copper alloy.

Figure 6.9 shows a sequence of micrographs (A–D) from the iron with 1 % of copper addition, heat treated for 15, 60, 120, and 480 min, respectively, at 950 °C.

Figure 6.10 shows the number of secondary carbides precipitated as a function of the soaking time during destabilization at 950 °C.

As we can see, the number of precipitated carbides is lower and reaches a maximum at 90 min and subsequently decreases; this is because the precipitation is performed by nucleation and growth phenomena; at this temperature the diffusion coefficient is higher than at 850 °C. At the temperature of 950 °C, the delayed precipitation is also observed with the increase in the copper content, but as observed in the treatment at 850 °C and after 60 min of treatment, the number of precipitated particles increases notably. As the temperature increases, precipitation occurs in shorter times; this increase in temperature accelerates the diffusion of

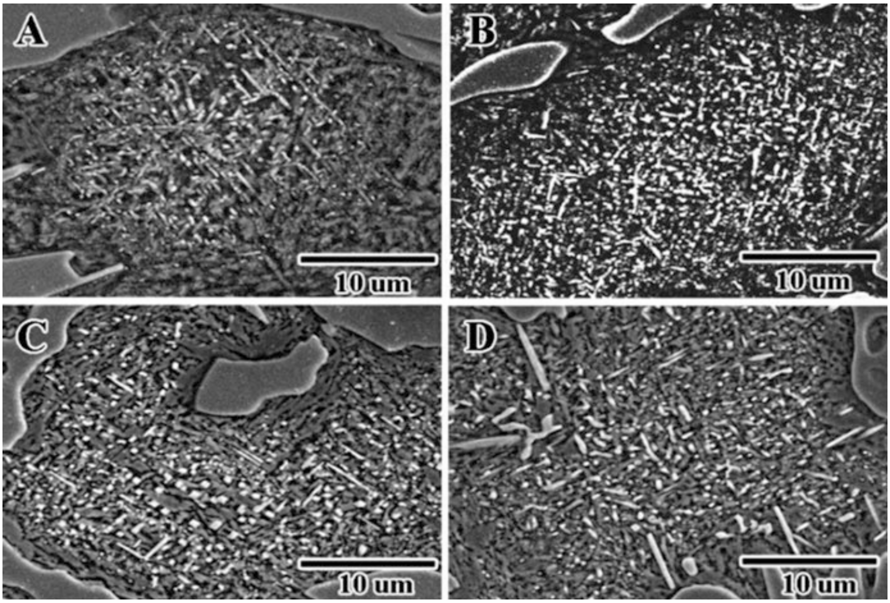

Fig. 6.9 SEM micrographs of the alloy with 1 % of copper heat treated for 15, 60, 120, and 480 min at 850 °C

Fig. 6.10 Number of secondary carbides as a function of soaking time at 950 °C

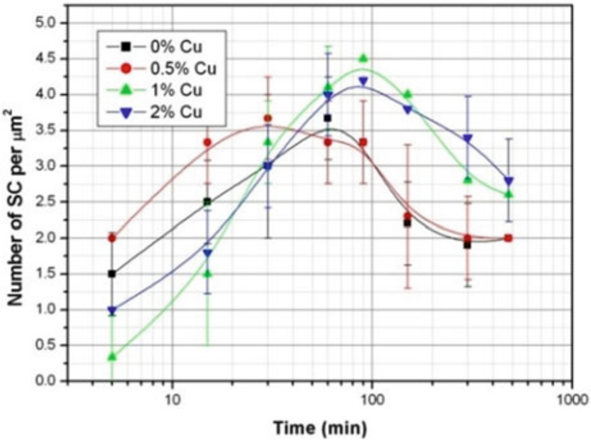

dissolved elements in the matrix. The aforementioned effect is shown in Fig. 6.11 where precipitated carbides are observed for two samples of the same composition. Figure 6.11a corresponds to the sample heat treated at 850 °C and Fig. 6.11b at 950 °C; we can observe the reduction in number of precipitates but an increase in size due to increased diffusivity. The average diameter of the precipitated carbides at 950 °C is shown in Fig. 6.12.

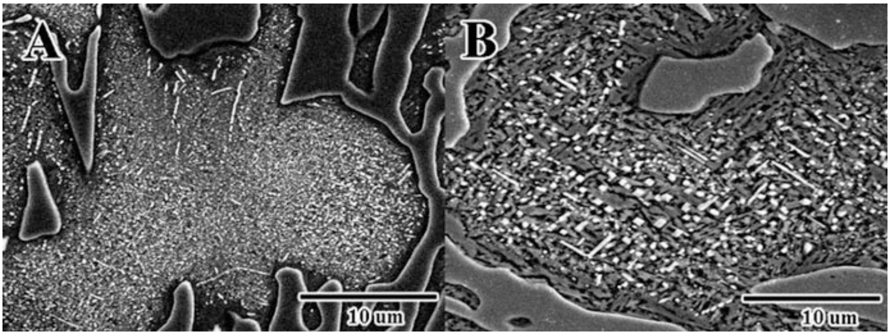

Fig. 6.11 Comparative micrographs of 1 % copper alloyed iron heat treated for 300 min. (**a**) 850 °C, (**b**) 950 °C

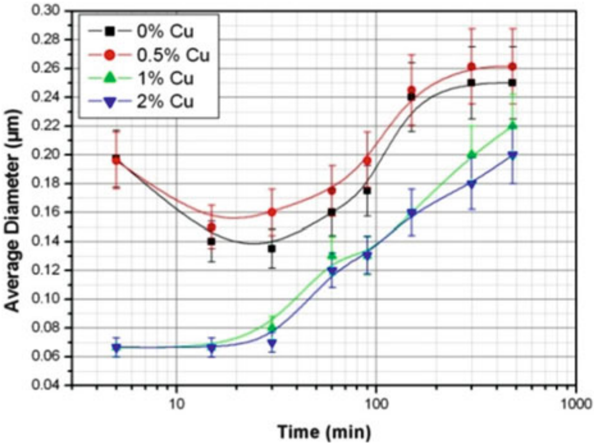

Fig. 6.12 Average diameter of precipitated carbides as a function of soaking time at 950 °C

As observed at 850 °C, in the samples with lower copper addition, the precipitation occurs in short periods of time, but there are only some large particles of diameters; after, the average diameter decreases due to the precipitation of particles of smaller size; after 30 min, the present particles start growing. In the case of the samples with copper contents of 1 and 2 %, the precipitated particles are of small diameter, precipitation continues until 90 min, and then the particles begin to grow; the average diameter is small and the particles are uniformly distributed. Compared with treatment at 850 °C, the average diameter is significantly higher; this is because, as temperature increases, the elements that precipitate from the matrix can travel longer distances and can form bigger carbides due to increased diffusion; therefore, carbides reach an average diameter of up to 0.262 µm in the longer treatment times. The average diameter is greatly increased in comparison with the treatment at 850 °C, wherein the average maximum diameter reached at

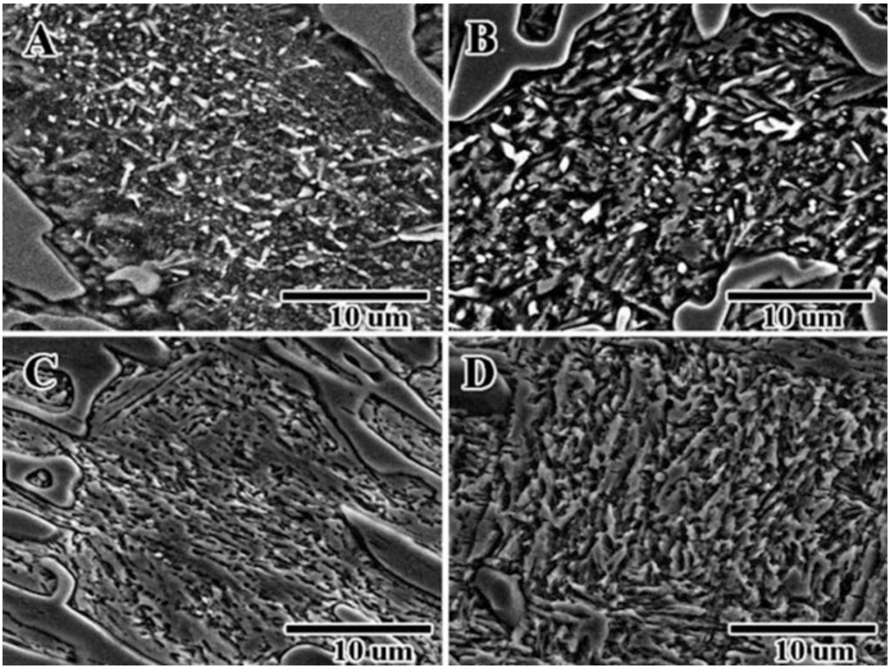

Fig. 6.13 SEM micrographs of the alloy with 1 % of copper heat treated for 15, 60, 120, and 480 min at 1050 °C

480 min was 0.19 μm. Figure 6.13 shows a sequence of micrographs (a–d) from the iron with 1 % of copper addition, heat treated for 15, 60, 120, and 480 min, respectively, at 1050 °C. We can observe the presence of secondary carbides for short times, but after 60 min, there is a decrease in the number; for exposure times longer than 90 min, the matrix is almost free of secondary carbides.

Figure 6.14 shows the quantification of a number of secondary carbides per μm^2; precipitation is observed for short times. Complementarily, Fig. 6.15 shows the average diameter of the precipitated carbides at 1050 °C; the average diameter of the precipitates found in short periods of time was significantly greater than those observed at 850 and 950 °C. However, at times over 300 min, the matrix is substantially free of precipitates, as shown in micrographs c and d of Fig. 6.13.

It is possible that the secondary carbides observed at times below 300 min are precipitated during heating, aided by the segregation product of the solidification process, but these dissolve at longer times when the equilibrium composition of carbon and chromium in the austenite is reached. It is possible that at this temperature, the equilibrium concentration of carbon in austenite can be higher than the carbon content that is dissolved in the matrix. In support of the above assertion, Fig. 6.16 is presented where the dissolution of eutectic carbides is observed, which has not been reported by other researchers; according to Tabrett [1], eutectic carbides are not affected at the destabilization temperatures.

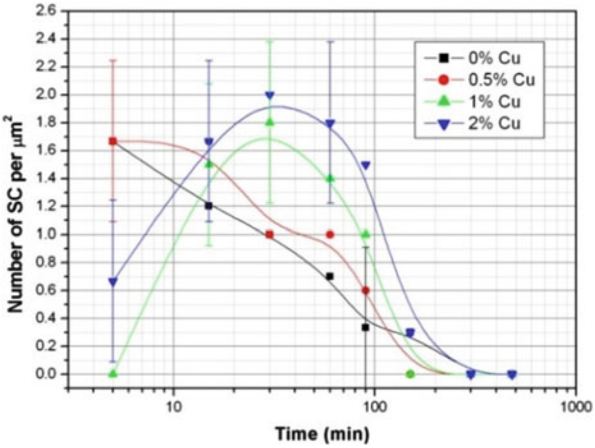

Fig. 6.14 Number of SEC carbides as a function of the soaking time at 1050 °C

Fig. 6.15 Average diameter of SEC carbides as a function of soaking time at 1050 °C

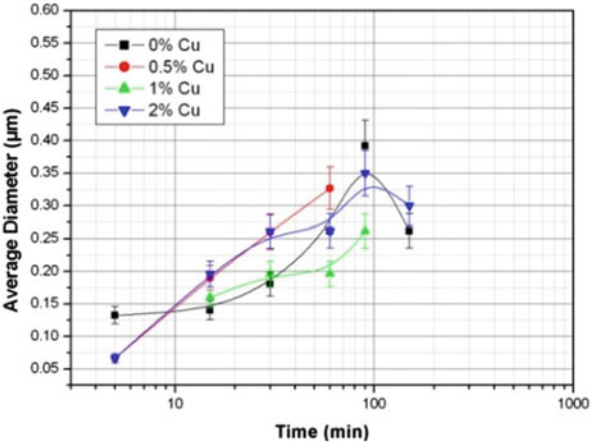

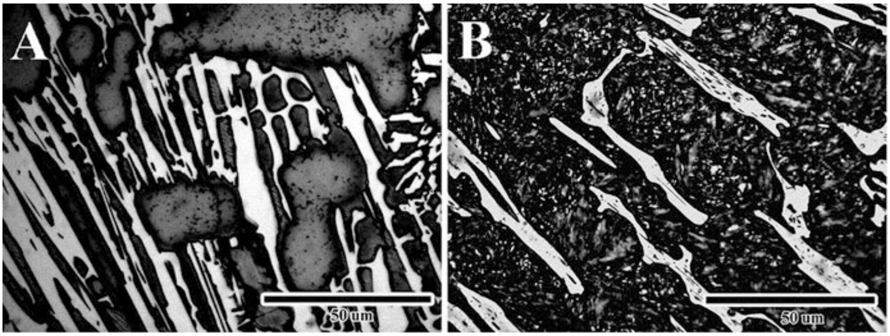

Fig. 6.16 SEM micrographs of the alloy with 2 % of copper: (**a**) as-cast conditions (**b**) heat treated at 1050 °C for 480 min. Note the decrease in volume of the iron carbides

Fig. 6.17 $SCV_{Frac.}$ as a function of the soaking time at 850 °C

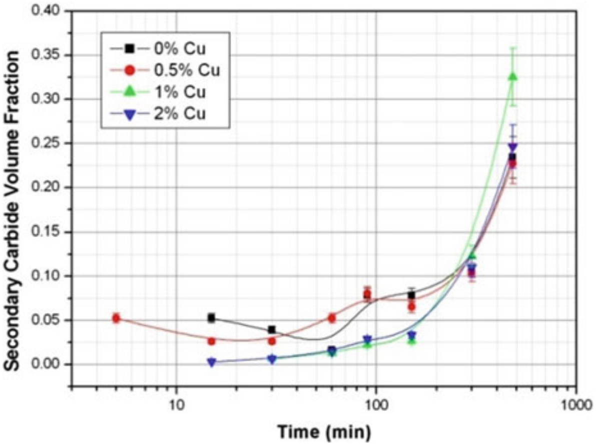

The reason why increasing the treatment temperature decreases precipitation of secondary carbides is explained by the Fe-C diagram. The austenite can dissolve a larger amount of carbon as the temperature increases until the eutectic; this decreases the amount of carbon that can be ejected to form secondary carbides.

6.3.4 *Secondary Carbide Volume Fraction ($SCV_{Frac.}$)*

From measurements of the number and diameter of precipitate carbides, precipitates, calculation of the $SCV_{Frac.}$ was performed. The results are presented below. The $SCV_{Frac.}$ for the samples thermally treated at 850 °C is shown plotted against time in Fig. 6.17.

It is noted that the volume fraction of carbide precipitates increases with exposure time in the thermal treatment for four different compositions. It is also noted that at short times, the volume of secondary carbides is lower in samples with higher copper content. For times greater than 150 min, the samples with higher copper content increase their $SCV_{Frac.}$

The maximum volume of 32.5 % was obtained by the sample with 1 % copper, which agrees with the results obtained by Bedolla et al. [16] in a white iron with 2.6 % C, 17 % Cr, 2 % Mo, and 2 % V. It is possible that the measurement results of $SCV_{Frac.}$ for the samples with lower copper content have been influenced by the carbon and chromium migration to coarsening the eutectic carbide; therefore, the $SCV_{Frac.}$ was lower for this samples.

As can be seen in the micrograph of Fig. 6.7a, there is a darker secondary carbide free region in the vicinity with the eutectic carbide; such region is depleted of chromium and carbon, which has also been observed by Duppin et al. [17] in some high-chromium irons. By contrast, in the samples with higher copper content, this phenomenon is not as evident, which is attributed to the ability of copper to

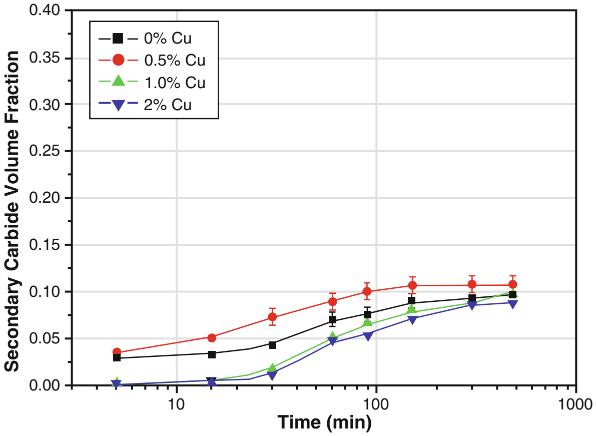

Fig. 6.18 $SCV_{Frac.}$ as a function of the soaking time at 950 °C

reduce the diffusion of carbon in austenite forming a diffusion barrier preventing the migration of carbon to the eutectic carbide during solidification. A similar phenomenon has been observed in nodular iron with the addition of copper, where this element segregates at austenite-graphite interface acting as a barrier to the diffusion of carbon into graphite nodules [18]. Figure 6.18 shows the $SCV_{Frac.}$ for the samples heat treated at 950 °C.

As was observed in the treatment at 850 °C, there is an increase in the $SCV_{Frac.}$ as the time increases. It is appreciated that the $SCV_{Frac.}$ increases faster than treatment at 850 °C; this is because the increase in temperature causes an increase in the diffusion. However, the $SCV_{Frac.}$ is much lower; this is caused by an increased solubility of carbon in austenite which decreases precipitation. Figure 6.19 corresponds to the measurement of $SCV_{Frac.}$ for the treatment at 1050 °C.

The $SCV_{Frac.}$ is diminished by the increased solubility of carbon in austenite; therefore, it is remarkably lower compared with the previous two temperatures. In addition for longer times up to 90 min, it is observed that $SCV_{Frac.}$ is almost null. Noticeably as the temperature increases, there is a lower precipitation, since according to the Fe-C diagram, the austenite phase can dissolve higher amount of carbon at higher temperatures until the eutectic. This is reflected in the decrease in volume of secondary carbides precipitated. In contrast at lower temperatures, the capacity of austenite for dissolving carbon is lower, so there is greater amount of carbon to precipitate, which is reflected in a higher volume of secondary carbides.

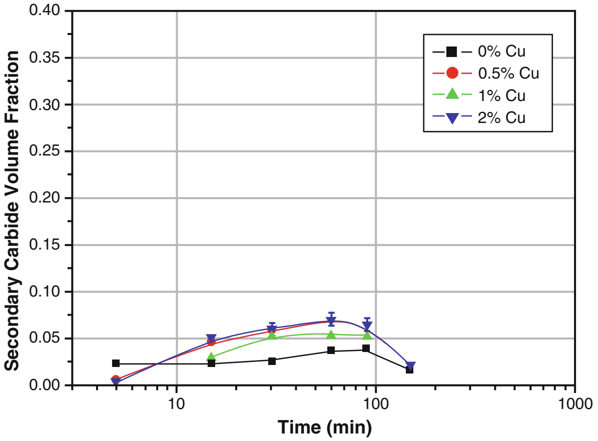

Fig. 6.19 $SCV_{Frac.}$ as a function of the soaking time at 1050 °C

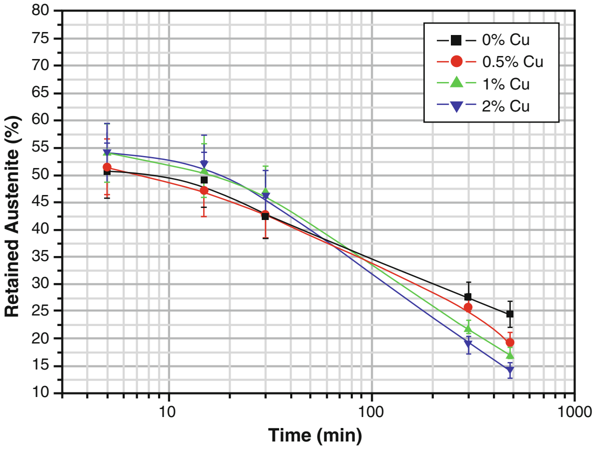

Fig. 6.20 Retained austenite volume fraction as a function of soaking time at 850 °C

6.3.5 Retained Austenite Volume Fraction

The results of the measurement of retained austenite after heat treatment are shown in Figs. 6.20, 6.21, and 6.22 heat treated at 850, 950, and 1050 °C, respectively.

In a general way, the samples treated at 850 °C for 480 min show low retained austenite values. The increase in exposure time at this temperature results in a higher precipitation of secondary carbides, thereby decreasing the volume of retained austenite, since as the treatment time increases, the matrix is reduced in dissolved alloying elements, which increases the volume of material to be transformed to martensite during subsequent cooling. As mentioned above, the precipitation of

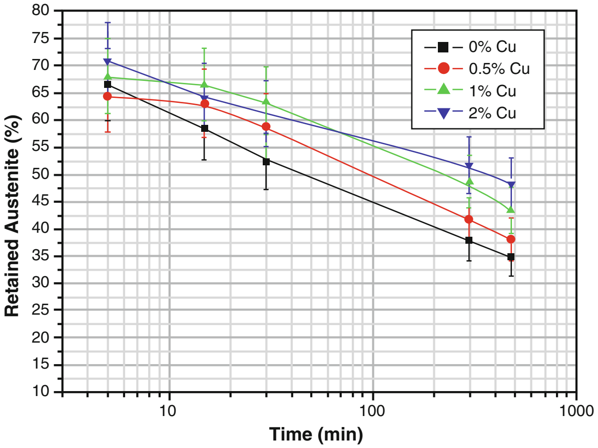

Fig. 6.21 Retained austenite volume fraction as a function of soaking time at 950 °C

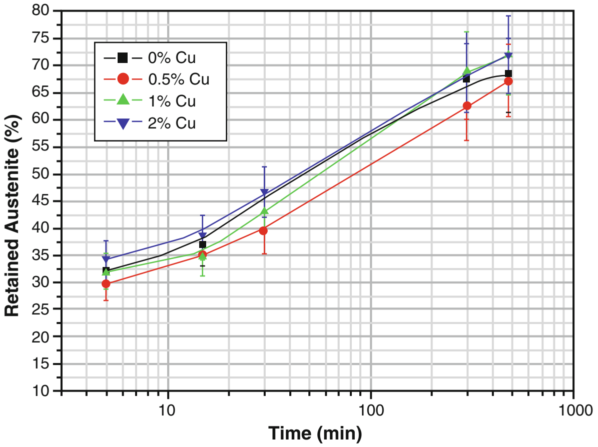

Fig. 6.22 Retained austenite volume fraction as a function of soaking time at 1050 °C

secondary carbides during heat treatment depletes the austenitic matrix in carbon and chromium mainly [5, 19]. Such depletion in dissolved alloying elements in the matrix causes an increase in the Ms temperature, so martensitic structures are present.

The same trend can be seen in Fig. 6.21, which corresponds to the thermal treatment at 950 °C. However, at this temperature, there is a greater volume of retained austenite compared to treatment at 850 °C. This is explained using the iron-carbon diagram, where at higher temperature austenite can dissolve more carbon, causing a lower precipitation of secondary carbides. Therefore, by increasing temperature, a greater amount of chromium and carbon is dissolved in the matrix, which lowers the Ms temperature, obtaining thus a larger volume of retained austenite at room temperature. It has been widely reported by several researchers [8, 16, 20, 21]. The retained austenite volume fraction decreases with increasing the exposure time for the four compositions; therefore, the minimum volume of retained austenite occurs in the maximum time of 480 min. In Fig. 6.9 that was showed above, it was observed that the number of secondary carbides decreases, but the precipitation of elements of the matrix continues to give rise to the growth of existing particles; therefore, the residual austenite decreases due to depletion of chromium and carbon matrix which raises the Ms transformation temperature, transforming the matrix to martensite during cooling. In the graph of Fig. 6.22, it shows the retained austenite volume fraction in the iron treated at 1050 °C; it is noted that the austenite volume increases with increasing the soaking time in the heat treatment. This is explained as follows: As the treatment temperature increases, there is a greater dissolution of chromium and carbon in austenite, which stabilize the matrix. Therefore, the austenitic structure is stable during cooling due to the high content of dissolved alloying according to Kim [5].

6.3.6 *Microhardness of Matrix After Destabilization*

Figure 6.23 shows the microhardness values obtained for the iron matrix after heat treatment. At a temperature of 850 °C, for a treatment time of 5 min, the four compositions practically start with a hardness value around 500 HV_{100}; microhardness for all compositions increases with increasing time. Samples with the lower copper content reach a maximum hardness at 90 min, achieving hardness between 1017 and 1030 HV_{100}. For times greater than 150 min the hardness decreases as the secondary carbides grow and begin to diminish in number. Furthermore, the samples

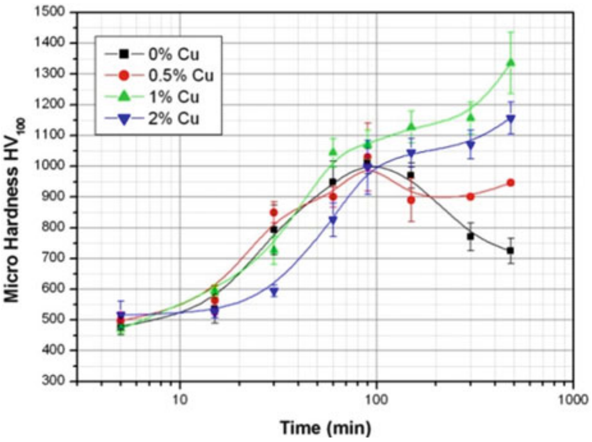

Fig. 6.23 Vickers microhardness of the iron matrix as a function of soaking time at 850 °C

with higher copper content continue to harden; this is because in these samples precipitation process starts more slowly. The carbides are of very small size and uniformly distributed; therefore, these reach values of hardness until 1336 HV_{100}.

According to the above exposed, the increase in the microhardness values as the treatment time increases is explained by the precipitation of secondary carbides which harden the matrix and the increase in the martensite content. The decrease of the hardness after 150 min in the samples with lower copper content is attributed to the coarsening of carbides, since long exposure times produce an increase in diffusion of elements, resulting in growth of carbides from the dissolution of others. Furthermore, this decrease in hardness is attributed to the formation of martensite of low carbon content due to the low solubility of carbon in austenite and the high precipitation of secondary carbides. The secondary carbides present in the samples treated at 950 °C are much larger than those observed at 850 °C, and although the precipitation decreases, the hardness is only slightly lower than that obtained at 850 °C; further to 850 °C the hardness of the matrix decreases drastically after 90 min for samples with lower content of copper due to the formation of martensite of low carbon content; this phenomenon has been reported by Maratray [22] and Karantzalis [23] (0.31 Ni, 0.47 Cu); both obtain lower hardness values at low temperatures. At 950 °C this phenomenon does not occur due to a lower precipitation; the hardness is maintained between 900 and 950 HV_{100}. In the case of samples with higher copper content, the precipitation is slower, but the precipitated particles are smaller. This precipitation continues until long times, resulting in a saturated matrix of fine secondary carbides uniformly distributed increasing the hardness of the matrix.

The described effect is attributed to the addition of copper, which, as mentioned above, reduces the diffusion of carbon in austenite, causing it to move shorter distances. Some researchers as Choi et al. [10] have reported the presence of copper in the secondary carbides, so it is believed that copper may act as nucleating causing a remarkable increase in the number of precipitates. Figure 6.24 shows the microhardness of the matrix for the treatment of 950 °C where there is a peak for samples with lower contents of copper in 60 min and 90 min for the samples with higher copper content, which coincide with the maximum values in the number of secondary carbide precipitates. Then the hardness of the matrix has a slight decrease, due to the growth of these particles. The highest values of microhardness are obtained due to the increase in the volume of martensite.

The maximum hardness value was obtained for samples with lower copper content, reaching a maximum of 975 HV_{100} for a time of 60 min in the sample with 0.5 % Cu.

The above effect at 850 °C due to copper addition is no longer observed, even when it has a greater number of precipitates in samples with higher copper content; the temperature increase produces a greater diffusion, so that the precipitated particles tend to grow rapidly, decreasing the hardness matrix. The decrease in hardness of the matrix compared to treatment at 850 °C is because the amount of precipitated carbides at 950 °C is lower, since the austenite phase can retain in solution higher quantities of carbon and chromium.

Fig. 6.24 Vickers microhardness of the iron matrix as a function of soaking time at 950 °C

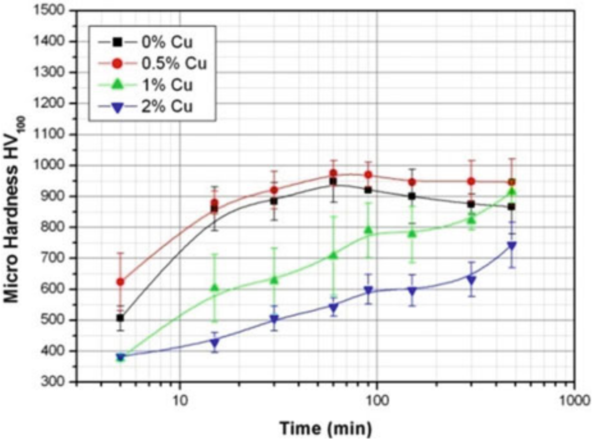

Fig. 6.25 Vickers microhardness of the iron matrix as a function of soaking time at 1050 °C

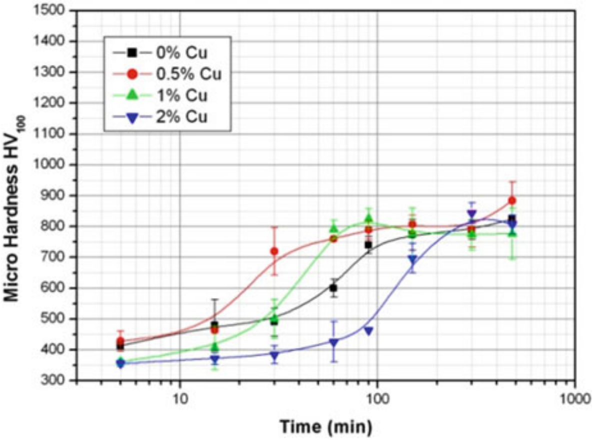

By increasing the treatment temperature, the formation of a fewer number of nuclei of larger size due to the increased diffusion was observed, allowing the atoms to travel longer distances. This causes a lower precipitation hardening, due to the morphology and distribution of these particles. The lower precipitation of secondary carbides regarding at 1050 °C implied a higher content of retained austenite in the structure reaching lower hardness values in the matrix. Figure 6.25 shows the microhardness values on the heat-treated iron matrix at 1150 °C. In this case we found a phenomenon that has not been reported before during destabilization: the matrix microhardness increased with the soaking time without secondary carbide precipitation.

Unlike the other two temperatures, the volume of residual austenite was increased with time; therefore, for long exposure times, there is not precipitation of secondary carbides and therefore decrease in hardness would be expected. However, hardening was due to solid solution of carbon and chromium, due to the dissolution of part of the eutectic carbide. At 1050 °C the maximum hardness of the matrix was of 884 HV_{100} for the sample with 0.5 % copper treated by 480 min. For short periods of time, samples with higher copper content show lower microhardness values, and on the previous temperatures, a delay in the precipitation of secondary carbides is observed. However, for long times, the difference is not significant, because all the samples show an almost fully austenitic matrix absent of secondary carbides, hardened only by solid solubility of elements such as carbon and chromium mainly. The above-explained phenomenon was showed previously in Fig. 6.15. In this case, a stabilization of the austenite phase at longer times has led to a structure free of secondary carbides, which was only hardened by solid solution with elements such as carbon, chromium, and molybdenum from the eutectic carbide dissolution.

6.4 Conclusions

Copper additions resulted in more discontinuous eutectic carbide in as-cast condition. After the heat treatment, an increase in number of precipitated particles for lower temperatures of treatment was observed. The smaller diameter of secondary carbides and a more uniform distribution of these were observed in samples with the greater contents of copper heat treated at 850 °C. The volume fraction of secondary carbides was found to increase for lower destabilization temperatures and large holding times. The volume fraction of retained austenite increased as the temperature of treatment was increased; therefore, very low carbide precipitation along with a stabilization of the austenite phase occurred for heat treatment at 1050 °C; in addition, for large soaking times, dissolution of eutectic carbides was observed. Microhardness was observed to decrease with the temperature of heat treatment due to the decrease of secondary carbides and therefore a lower transformation level of austenite to martensite.

Acknowledgements The authors acknowledge the CIC-UMSNH (grant No. 019) and CONACYT (grant No. 57197-Y) for the financial support and UAEH for the facilities obtained during the present research.

References

1. Tabrett CP, Sare IR, Gomashchi MR (1996) Microstructure-property relationships in high-chromium white iron alloys. Int. Mater Rev 41(2):59–82
2. Dogan ON, Hawk JA, Laird F II (1997) Solidification structure and abrasion resistance of high chromium white irons. Metall Mater Trans A 28(6):1315–27
3. Laird G II, Powell GLF (1993) Solidification and solid-state transformation mechanisms in Si alloyed high-chromium white cast irons. Metall Trans A 24(2):981–988
4. Laird G, Gundlach R, Rohrig K (2000) Abrasion resistant cast iron handbook. American Foundry Society, Des. Plaines

5. Kim C (1979) X-Ray method of measuring retained austenite in heat treated white cast irons. J Heat Treat 1(2):43–51
6. Babu SS, Bhadeshia HKDH (1995) Diffusion of carbon in substitutionally alloyed austenite. J Mater Sci Lett 14:314–316
7. Silman GI, Kamynin VV, Goncharov VV (2007) On the mechanisms of copper effect on structure formation in cast iron. Met Sci Heat Treat 49:387–393
8. Powell GLF, Laird G II (1992) Structure, nucleation, growth and morphology of secondary carbides in high chromium and Cr-Ni white cast irons. J Mater Sci 27:29–35
9. Laird G II (1991) Microstructures of Ni-Hard I, Ni-Hard IV and High-Cr White Cast Irons. AFS Trans 99:339–357
10. Choi JW, Chang SK (1992) Effects of molybdenum and copper additions on microstructure of high chromium cast iron rolls. ISIJ Int 32(11):1170–1176
11. Qingxiang Y, Bo L, Jianhua L, Mei Y (1998) Effect of rare earth elements on carbide morphology and phase transformation dynamics of high Ni-Cr alloy cast iron. J Rare Earths 16:36–40
12. Shen J, Zhou QD (1988) Solidification behavior of boron-bearing high-chromium cast iron and the modification mechanism of silicon. Cast Met 2:79–85
13. Li J, Smith RW (1997) Growth modification of austenite-(Fe,Cr)3C pseudo-binary eutectic. In: Proceedings IV Decennial International Conference on Solidification Processing, pp 481–488
14. Liang GY, Su JY (1992) The effect of rare earth elements on the growth of eutectic carbides in white cast irons containing chromium. Cast Met 4(2):83–88
15. Fusheng H, Chaochang W (1989) Modifying high Cr-Mn cast iron with boron and rare earth-Si alloy. Mater Sci Technol 5:918–924
16. Bedolla-Jacuinde A, Arias L, Hernández B (2003) Kinetics of secondary carbides precipitation in a high-chromium white iron. J Mater Eng Perform 12(4):371–382
17. Duppin P, Saverna J, Schissler JM (1982) A structural study of chromium white cast iron. AFS Trans 90:711–718
18. Yu SK, Loper Cr Jr (1988) The effect of molybdenum, copper, and nickel on the pearlitic and martensitic hardenability of ductile cast irons. AFS Trans 96:811–822
19. Cias WW (1974) Austenite transformation kinetics and hardenability of heat treated 17.5%Cr white cast irons. AFS Trans 82:317–28
20. Kuwano M, Ogi K, Sawamoto A, Matsuda K (1990) Studies on precipitation process of secondary carbides in high-chromium cast iron. AFS Trans 98:725–734
21. Powell GLF, Bee JV (1996) Secondary carbide precipitation in an 18 wt%Cr-1 wt%Mo white iron. J Mater Sci 31:707–711
22. Maratray F, Poulalion A (1982) Austenite retention in high chromium white irons. AFS Trans 90:795–804
23. Karantzalis AE, Lekatou A, Diavati E (2008) Effect of destabilization heat treatments on the microstructure of high-chromium cast iron: a microscopy examination approach. J Mater Eng Perform 18(8):1078–1085

Part III
Characterization of Steels Applying Heat Treatment

This part includes two chapters related to characterization of steels applying different heat treatments. The first chapter presents a study of the thermal behavior and its effect on phase transformations in the heat affected zone (HAZ), with different cooling rates (0.1–200 °C/sec) in order to obtain continuous cooling transformation (CCT)curves for an API X70 steel. With the CCT curves obtained in this study, it is possible make predictions in the HAZ of welded joints, about the formation of brittle structures, such as the martensite. The results showed that it will be possible to control the microstructure to optimize the pipe fabrication with submerged arc welding process (SAW) in industrial plants.

The second chapter presents the experimental numeric-study to determine the influence of induction of hydrogen in an API X60 microalloyed steel with conventional heat treatment. The production and transportation of oil and gas have problems with hydrogen embrittlement. The hydrogen generated failures and critical deterioration of low carbon steels. Thus, analysis of influencing microstructure obtained on hydrogen induction is carried out. Finite element method (FEM) is presented to simulate the behavior of hydrogen diffusion on the dimensions of the specimens studied. Using finite element method, it is possible to determine the phenomenon of movement hydrogen on X60 steel.

The main techniques used in the characterization of these steels are:

- Scanning electron microscopy (SEM).
- Optical microscopy (OM).
- Energy dispersive spectroscopy (EDS).
- Mechanical tests.
- Finite element method (FEM).

Chapter 7
Thermal Behavior of an HSLA Steel and the Impact in Phase Transformation: Submerged Arc Welding (SAW) Process Approach to Pipelines

P.S. Costa, F.A. Reyes-Valdés, R. Saldaña-Garcés, E.R. Delgado, and A. Salinas-Rodríguez

Abstract Heat input during welding metal fusion generates different transformations, such as grain growth, hydrogen cracking, and the formation of brittle structures, generally associated with the heat-affected zone (HAZ). For this reason, it is very important to know the behavior of this area before welding. This paper presents a study of the thermal behavior and its effect on phase transformations in the HAZ, depending on cooling rates (0.1–200 °C/s) to obtain continuous cooling transformation (CCT) curves for an high-strength low-alloy (HSLA) steel. In order to determine the formed phases, optical microscopy and Vickers microhardness measurement were used. The experimental CCT curve was obtained from an HSLA steel, and the results showed that, with the used cooling conditions, the steel did not provide formation of brittle structures. Therefore, it is unlikely that welds made by submerged arc welding (SAW) may lead to hydrogen embrittlement in the HAZ, which is one of the biggest problems of cracking in gas conduction pipelines. In addition, with these results, it will be possible to control the microstructure to optimize the pipe fabrication with SAW process in industrial plants.

Keywords Phase transformations • Heat-affected zone (HAZ) • Dilatometry • Welding metallurgy • CCT curve

---

P.S. Costa (✉) • F.A. Reyes-Valdés • R. Saldaña-Garcés
Corporación Mexicana de Investigación en Materiales (COMIMSA), Posgrado en Tecnología de la Soldadura Industrial, Ciencia y Tecnología # 790, C.P. 25290 Saltillo, Coahuila, México
e-mail: patricia_sheilla@hotmail.com

E.R. Delgado
TUMEX Grupo ITISA, Carretera México - Pachuca Km 48.4, Parque Industrial, C.P. 55755, Tecámac, Mexico

A. Salinas-Rodríguez
Centro de Investigación y de Estudios Avanzados del Instituto Politécnico Nacional (CINVESTAV), Zona Industrial, 25903 Ramos Arizpe, Coahuila, Mexico

R. Pérez Campos et al. (eds.), *Characterization of Metals and Alloys*, DOI 10.1007/978-3-319-31694-9_7

7.1 Introduction

The high demand and competitiveness in the industry led to the need to develop new steels with the aim of meeting the stringent requirements of strength, toughness, and weldability. Examples of this development are the high-strength low-alloy steels or HSLA steels. These steels can be used in the manufacture of large-diameter pipes for oil extraction, offshore platforms, shipbuilding, automotive industry, and metal structures; such applications involve severe operating conditions, high-security requirements, and competitive cost [1].

The steels from American Petroleum Institute (API) are examples of HSLA steel applied in the oil industry as tubes for oil and gas extraction. With the growth of this sector, investments are directed to the construction of new pipelines, which implies an increase in the amount of fuel transported to ever higher pressures, and yet more economical operation of transport is required [2].

There is therefore the need to use steel tubes with high mechanical strength, making investigations to focus on the HSLA steels types API 5L X70, X80, X100, and X120, [3]. The balance of high strength and good toughness achieved in the HSLA steels, such as API 5L X70, can be lost by the thermal cycles during welding operations, generating low toughness in the heat-affected zone (HAZ). High rates of cooling, the hydrogen content in the weld metal, and high residual stress levels favor the formation of cracks. Furthermore, accelerated cooling rates affect the microstructure in the HAZ and can increase the hardness due to the formation of brittle microstructures in this region [3], which leads to increased susceptibility to cracking because this region is traditionally the critical area for hydrogen embrittlement [4].

Hydrogen-induced cracking is one of the problems occurring in the pipes for transporting sour gas and is responsible for premature fail in service pipe [5]. This phenomenon is related to hydrogen diffusion, and its trapping at the metal [6], as in the inner walls of the pipes, can occur following corrosion reaction [7]:

$$\mathrm{Fe} + \mathrm{H_2S} \rightarrow \mathrm{FeS} + \mathrm{H_2}\uparrow(\mathrm{gas}) \tag{7.1}$$

The hydrogen gas coming from the previous reaction dissociates and diffuses into the tube. Hydrogen atoms that dissolved in the steel tend to recombine into hydrogen molecules which caused the problem of embrittlement and cracking [7].

The HIC is likely to happen when steel structure is martensitic or there is a mixture of ferrite and high carbon martensite or bainite, which can be decreased by minimizing the formation of these structures in the weld metal and the HAZ [8]. Huang et al. [5] showed that an increase in the amount of inclusions and granular bainite phase and microconstituent martensite-austenite (MA) increase susceptibility to hydrogen cracking in HSLA steel for manufacturing X120 pipe at H_2S environment. Arafin and Szpunar [9] investigated the effect of bainite on susceptibility to hydrogen-induced cracking in steel grades X80 and X100. As one result, the X100 steel is more susceptible to cracking than the X80, also, the microstructure composed by bainite lath is more vulnerable to hydrogen cracking than ferrite and granular bainite.

In this context, to reduce the probability of hydrogen cracking in the HAZ of welded pipes, it is necessary to have a strict control of the microstructures in these regions [8]. Thus, this paper aims to provide information regarding the phase transformations that occur in API 5L X70 steel when subjected to thermal cycles with different continuous cooling speeds. These transformations can be compared to those that occur in the HAZ of the steel when it passes through welding processes, and, once this is known, the microstructures can be controlled during the manufacturing process of pipes with helical welding to conduct wet sour gas.

Thus, the scientific contribution of this research relates with the obtainment of a methodology to obtain and interpret the CCT curves in order to control the microstructure of the HAZ in the welding of HSLA steels.

7.2 Experimental

For this study, tests were performed on a quenching dilatometer Linseis L78 RITA, applying thermal cycles in nine steel samples of 3 mm in diameter and 10 mm in length. The thermocouples used were of type K and the atmosphere was controlled by helium gas. Table 7.1 shows the parameters used in thermal cycles, and Fig. 7.1 presents the equipment used.

After dilatometric tests, the samples were prepared with conventional metallographic preparation techniques and analyzed by optical microscopy to aid in the identification of microconstituents. Vickers microhardness measurements were performed on samples using the equipment Wilson Hardness Tukon 2500, applying loading of 500 g for 10 s.

Table 7.1 Parameters used in the dilatometry tests

Sample	Heating temperature (°C)	Heating speed (°C/s)	Residence time (min)	Cooling rate (°C/s)
X70_0.1Cs	1100	5	5	0.1
X70_1Cs	1100	5	5	1
X70_5Cs	1100	5	5	5
X70_10Cs	1100	5	5	10
X70_30Cs	1100	5	5	30
X70_50RCs	1100	5	5	50
X70_70Cs	1100	5	5	70
X70_100Cs	1100	5	5	100
X70_200Cs	1100	5	5	200

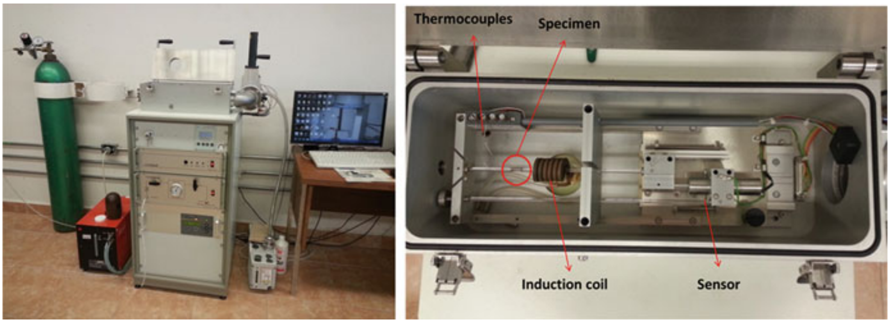

Fig. 7.1 (**a**) Dilatometer L78 RITA; (**b**) internal part details

Table 7.2 Chemical composition of steel API 5L X70 under study (wt. %)

%C	%S	%Mn	%P	%Si	%Cr	%Ni	%Mo
0.07	0.002	1.5	0.005	0.28	0.19	0.04	0.22
Cu	V	Nb	Ti	W	CE_{IIW}	CE_{Pcm}	Nb+V+Ti
0.014	0.04	0.068	0.009	0.002	0.413	0.183	0.117

Note: $CE_{IIW} = C + (Mn/6) + [(Cr + Mo + V)/5] + [(Ni + Cu)/15]$
$CEP_{cm} = C + (Si/30) + (Mn/20) + (Cu/20) + (Ni/60) + (Cr/20) + (Mo/15) + (V/10) + 5B$

Table 7.3 Mechanical properties of steel API 5L X70 under study

Record COMIMSA	Area (mm^2)	Load máx. (kgf)	Yield load (kgf)	Tensile strength (MPa)	Yield strength (MPa)	Elongation (%)
14 PM0817 T1 longitudinal	155.1	11,100	8580	702	542	31

7.3 Results and Discussion

7.3.1 *Characterization of API 5L X70 Steel*

The chemical composition and mechanical properties of steel in study are presented in Tables 7.2 and 7.3, respectively. The chemical composition results indicate that, according to standard API 5L [10], the steel meets the requirements for manufacturing of pipes types API 5L X70 to PSL2. This type of pipe is used in transportation systems in the industries of oil and natural gas [10].

Importantly, the carbon equivalent results indicate that in welding this steel, preheating and care as post-weld heat treatment is not necessary, because steels with carbon equivalent lower to 0.45 are considered to have good weldability. Moreover, the sum of the percentages of vanadium (V), niobium (Nb), and titanium (Ti) is less than 0.15 %, which also meets the specifications of standard API 5L [10].

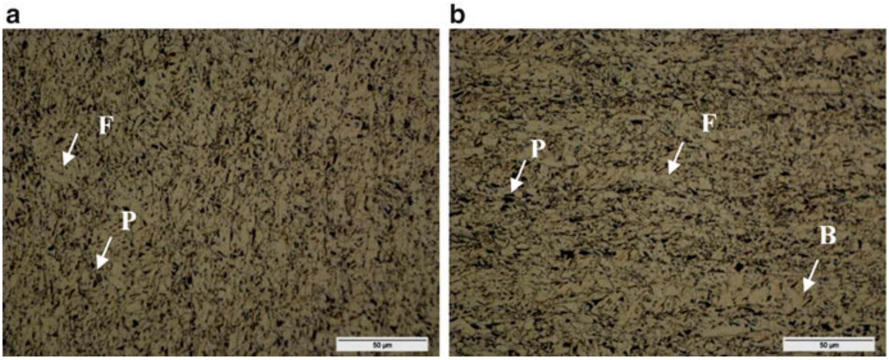

Fig. 7.2 Micrographs of the base metal. (**a**) Cross section; (**b**) longitudinal section. Attack Nital 2 %. 500× magnification. P, perlite; F, ferrite; B, bainite

Regarding the mechanical properties, the API 5L [10] standard specifies that the yield strength limit should be between 485 and 635 MPa and that the limit of tensile strength should be at least 570 and at most 760 MPa, so thus the results indicate that the steel study complies with the requirements of mechanical properties for application as API 5L X70 PSL2 grade.

Analyzing the micrographs of API 5L X70 steel in laminated state as presented in Fig. 7.2, it can be said that the microstructure is composed of a ferritic matrix with areas of perlite and small bainite. This microstructure is consistent with hardness measurements of material (237 HV0.5) and with the literature [3, 8, 9, 11, 12].

In addition to the abovementioned phases, the steel has a medium level of inclusions, and these relate mainly to inclusions of oxides of aluminum and manganese sulfide that can be visualized in the micrograph and the microanalysis for energy-dispersive X-ray analysis (EDX) in Fig. 7.3.

The alumina inclusions are formed during the refining process of steel because of the addition of aluminum for deoxidation of the same in the steelworks of steel, and inclusions of manganese sulfide are also formed in this process because of the presence of sulfur and manganese from raw materials used in the manufacturing process [13]. These inclusions may promote hydrogen-induced cracking as in the literature [12, 14] it is reported that large inclusions of manganese sulfide and oxide inclusions increase susceptibility to HIC. This is because the hydrogen absorbed by the steel may be trapped in interfaces such as those between the metal matrix and inclusions producing the generated stress field increase by the pressurization consequence of hydrogen embrittlement [15].

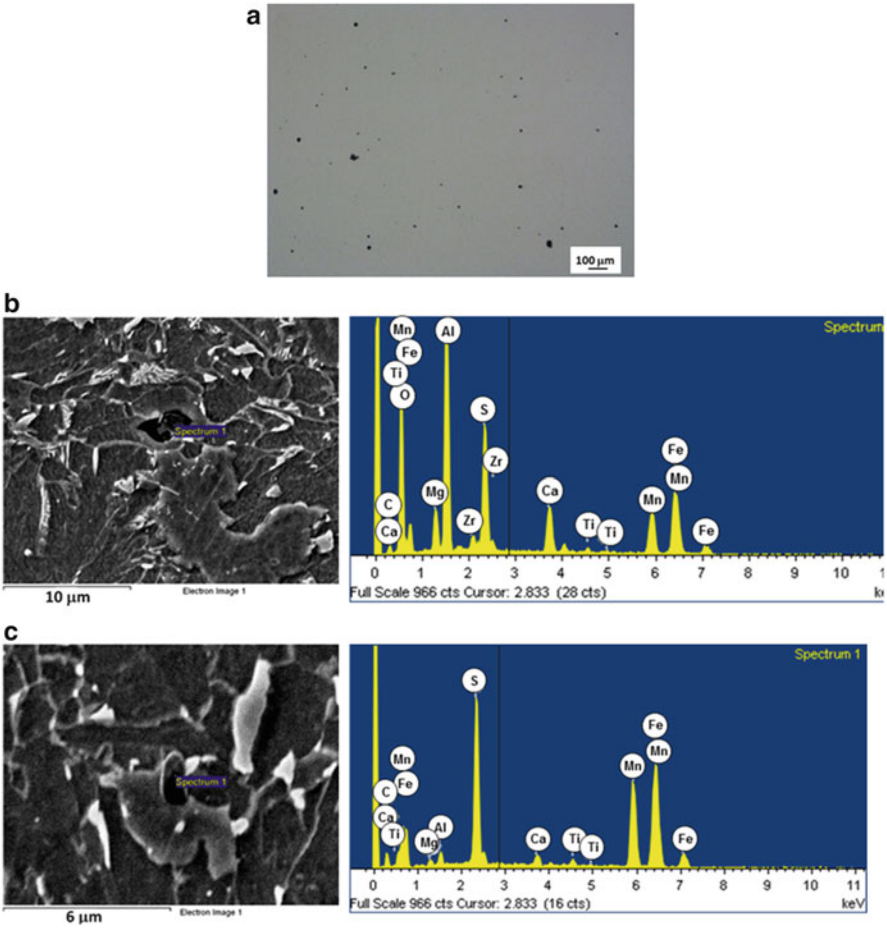

Fig. 7.3 Analysis of inclusions. (**a**) MO micrograph without attack at 100× magnification; (**b**) SEM micrograph showing the inclusion basically composed of aluminum oxide; (**c**) SEM micrograph showing inclusion basically composed of manganese sulfide. Attack Nital 2 %

7.3.2 *Dilatometry Curves*

With the results of the dilatometric curves and the metallographic characterization of the samples, it was possible to construct the curve of continuous cooling transformation or continuous cooling transformation (CCT) curves for API 5L X70 steel. With this curve, the behavior phase transformations that may occur in the material when it passes through different temperature cycles are known. This technique is used because phase transformations cause expansion or contraction of material because the density of a new phase is generally different from the original phase [13]. These transformations of phases obtained by dilatometry are

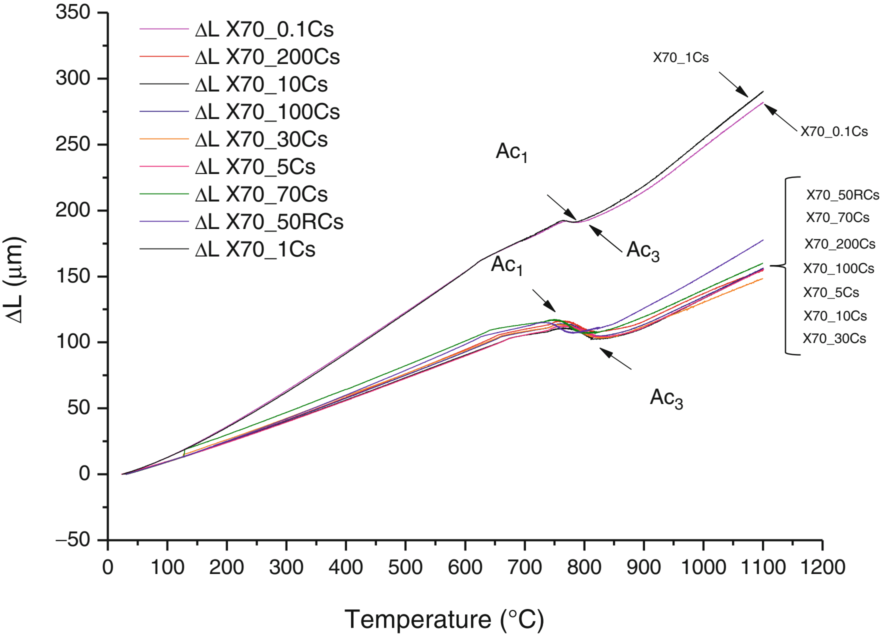

Fig. 7.4 Heating curves of dilatometry testing

compared to those that occur in the HAZ when steel passes welding processes. This is because the HAZ is the region of the base metal suffering microstructural alterations due to temperature variations during welding. These changes can cause embrittlement at the weld joint which is not desirable in most applications [16]. The heating temperature in dilatometric tests was 1100 °C to make it possible to simulate the grain growth that occurs in the HAZ. According to the literature, the peak temperature in the region of the HAZ grain growth can reach 1200 °C [17].

Figures 7.4 and 7.5 show the dilatometric curves of heating and cooling, respectively, for the conditions presented in Table 7.1. These curves are used to find the points of phase transformations that are used in the construction of the CCT curve.

As all samples were heated at the same temperatures and speeds, with the curves of Fig. 7.4, an average value for Ac1 and Ac3 temperatures for API 5L X70 steel can be obtained, being 753 °C and 848 °C, respectively. These results show the start and end temperatures of austenite formation of this material.

With regard to the cooling curves in Fig. 7.5, each sample has its start and end points of phase transformation, and that is because the cooling rates were different for each sample. When the steel is slowly cooled from the austenite field, the environment temperature will present one or more phases which may be ferrite, cementite, and pearlite. However, if the cooling of the steel from the austenitic region is very fast, other microconstituents called metastable bainite and martensite

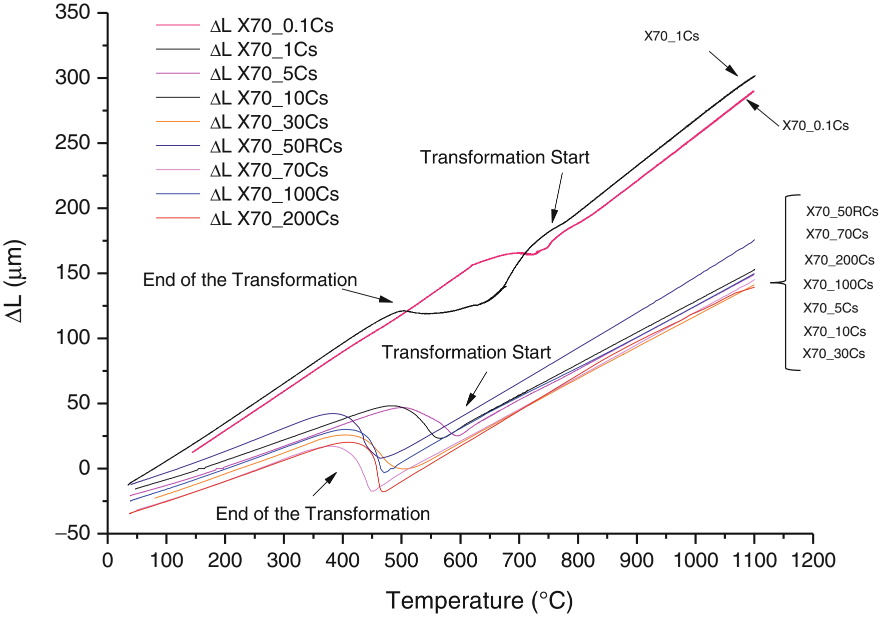

Fig. 7.5 Cooling curves of dilatometry testing

are not foreseen in the binary phase diagram, and iron-cementite will appear. To accompany the formation of the microconstituents, the CCT curves are used [13].

Importantly, the hardness can provide an estimate of the embrittlement of the different subregions of the steel HAZ. For high-strength low-alloy steels, hardness greater than 350 HV (Vickers hardness) can be considered excessive and lead to embrittlement and cracking sensitivity in this area [18]. As the microhardness results presented in Fig. 7.6 do not exceed 350 HV, it can be said that even the cooling during the welding process is fast, and the steel under study is not susceptible to the formation of brittle structures in the HAZ.

7.3.3 Microhardness

Figure 7.6 shows the results of Vickers microhardness for the samples studied. It verified that with increasing cooling rates the hardness value increase. These results are consistent with those reported in the literature [19], because when the cooling rate of the austenite is increased, there will not be enough time for the complete atomic mobility and the phase transformation reactions are modified and hence the mechanical properties too [13].

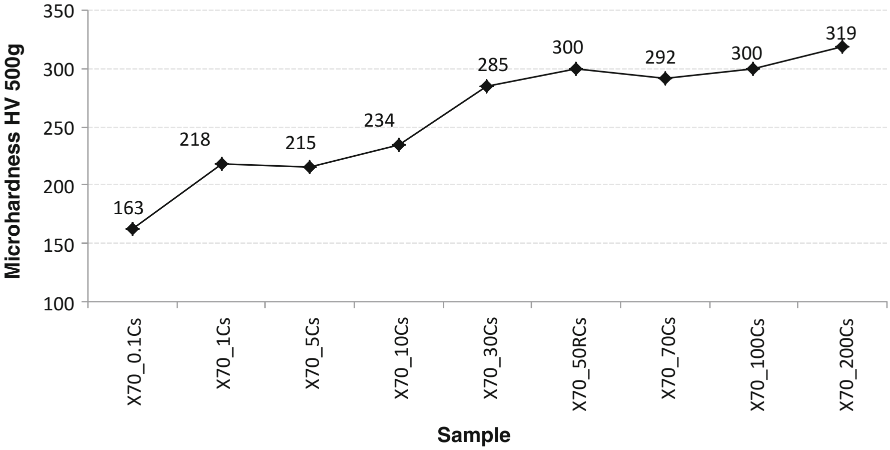

Fig. 7.6 Microhardness HV for different thermal cycles applied to API X70 steel in dilatometry tests

7.3.4 Optical Microscopy

The samples studied were characterized by metallography, and the micrographs are presented in Fig. 7.7. It is verified that for low cooling rates (0.1 °C/s, 1 °C/s, and 5 °C/s), the steel microstructure consists of a ferritic matrix with aggregates of ferrite and carbides. The sample with cooling rate 0.1 °C/s is verified with high growth of grain, and the few aggregates of ferrite and carbide are perlite, which explains the low hardness for this sample (163 HV).

Samples with rate of 1 °C/s and 5 °C/s are not verified since the difference is not significant between their microstructures, being those composed of ferrite, pearlite, and bainite strokes. The less difference between the microstructures explains the proximity of the results presented by hardness of these samples (218 HV and 215 HV, respectively).

In the sample cooling rate of 10 °C/s, a microstructure is mainly composed of bainite, this being both lower bainite and higher bainite. The difference between the two forms of bainite is related to the diffusion of carbides during cooling. The forms of upper bainite occurs at higher temperatures, and carbides (cementite basically) are distributed in the grain boundaries. Meanwhile, lower bainite is formed at lower temperatures, and there is no time for the complete diffusion of the carbides, and these remain in and ferrite grain boundary doing lower bainite is the hardest [13].

For samples with cooling rates at or above 30 °C/s, the microstructure is composed primarily of bainite. However, there are traces of martensite in the samples X70_50RCs, X70_70Cs, X70_100Cs, and X70_200Cs due to the hardness value in the graph presented in Fig. 7.6, but this microconstituent is not present in sufficient quantities to embrittle the steel.

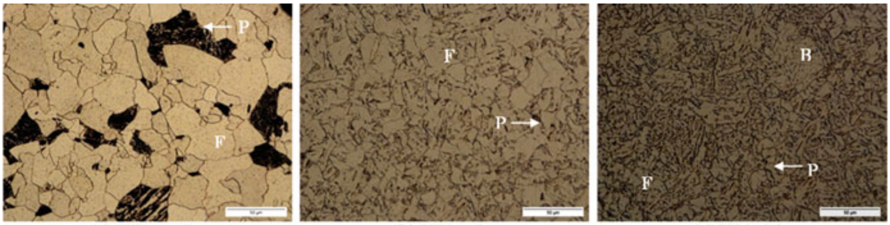

(a) X70_0.1Cs (b) X70_1Cs (c) X70_5Cs

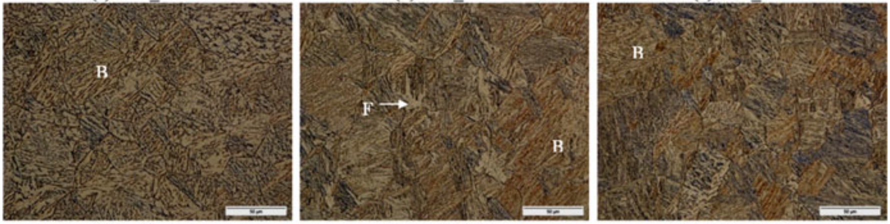

(d) X70_10Cs (e) X70_30Cs (f) X70_50RCs

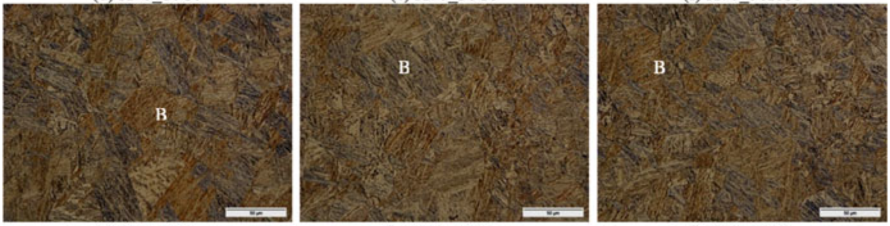

(g) X70_70Cs (h) X70_100Cs (i) X70_200Cs

Fig. 7.7 Micrographs of the samples under study

Using scanning electron microscopy (SEM) for samples cooled to 1 °C/s and 50 °C/s, it is possible to confirm the presence of perlite and bainite (Fig. 7.8). Figure 7.8a presents the microstructure that consists of ferrite and pearlite (intercalated lamellae of ferrite and cementite) grains, and in Fig. 7.8b finely distributed carbides in the ferrite grain characterizing bainite are verified.

It is noteworthy that in addition to the inclusions, steel microstructure affects directly the hydrogen cracking because hard microstructures such as martensite and untempered bainite are more susceptible to HIC because the lower toughness and ductility of these microstructures reduce the ability to accommodate the stresses in the region of the weld. Thus, a more ductile microstructure is able to tolerate, without cracking, a greater amount of hydrogen [18].

In addition, since the grain size of the steel X70, before dilatometric tests, is about 12 μ [20], it is possible to visualize the significant growth of grain, since the dilatometry tests were carried out with a heating temperature of 1100 °C. With these results it is expected that in the HAZ of a weld using the submerged arc process, similar or greater grain growth occurs when compared with dilatometry samples, which can affect the impact resistance of this region. In earlier work [21], it was shown that with the increase of grain size in the HAZ of welds made with

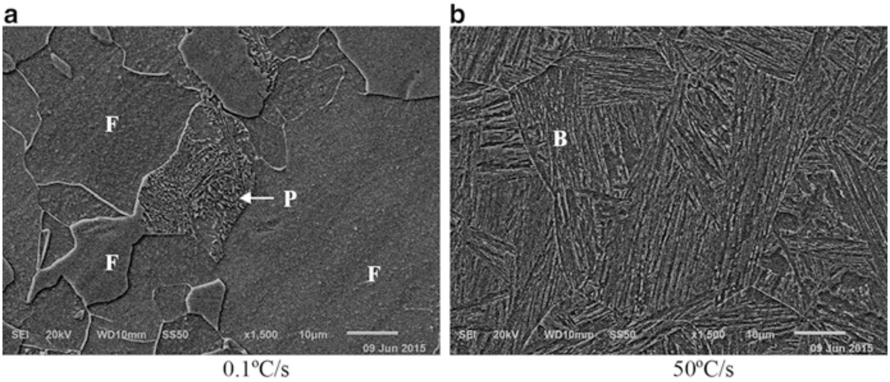

Fig. 7.8 SEM micrographs of the samples: (**a**) X70_0.1Cs; (**b**) X70_50Cs. Attack Nital 2 %

high heat input (2470 J/mm), the impact strength at −20 °C and −40 °C decreases considerably and, therefore, grain size in this region must be controlled to avoid embrittlement of the welded joint.

7.3.5 CCT Experimental Curve

With the results presented in the dilatometric curves, microhardness measurements, and the microstructural analysis of the samples, it can propose the experimental CCT curve for the API 5L X70 steel which is presented in Fig. 7.9.

It is verified in Fig. 7.9 that in cooling rates greater than 30 °C/s, the bainite formation begins to occur as was displayed in the micrographs of Fig. 7.5. However, to build the martensite start (Ms) line, it was necessary to support the theoretical CCT curve (Fig. 7.10) for the steel that was calculated based on the chemical composition using the modeling software JmatPro 7.0.

Comparing the two graphs, it is visualized that the microstructures provided in the theoretical diagram were the same presented in the experimental curve. Due to the amount of alloying elements in steel, the bainite formation is favored, and there is very little amount of pearlite formed in the samples. For the formation of pearlite in larger amounts, very slow cooling rates are required (e.g., 0.01 °C/s).

7.4 Conclusions

With the CCT curve obtained in this study, it is possible to predict that in the HAZ of welded joints by the SAW process of API 5L X70 steel, the formation of brittle structures, as the martensite, is not expected, but according to metallographic

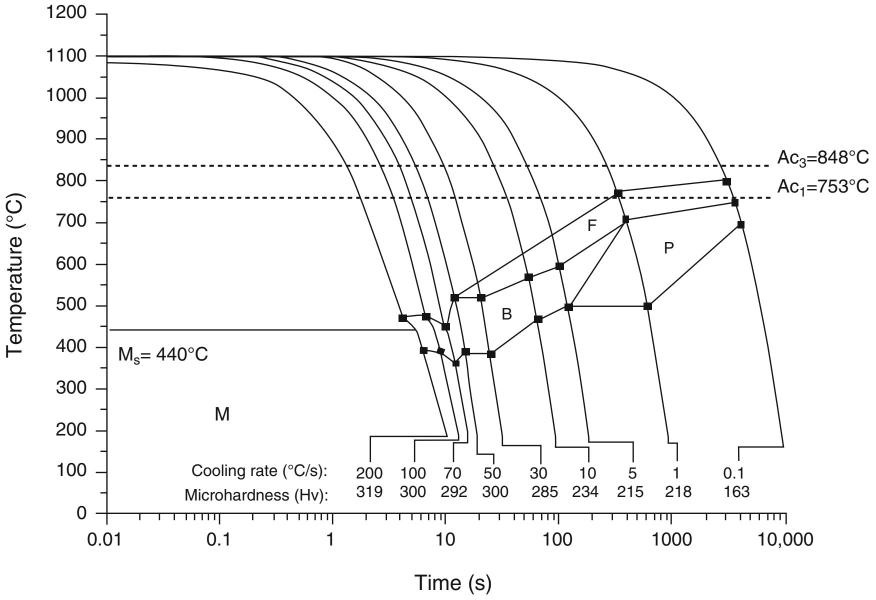

Fig. 7.9 CCT experimental curve proposed for API 5L X70 steel

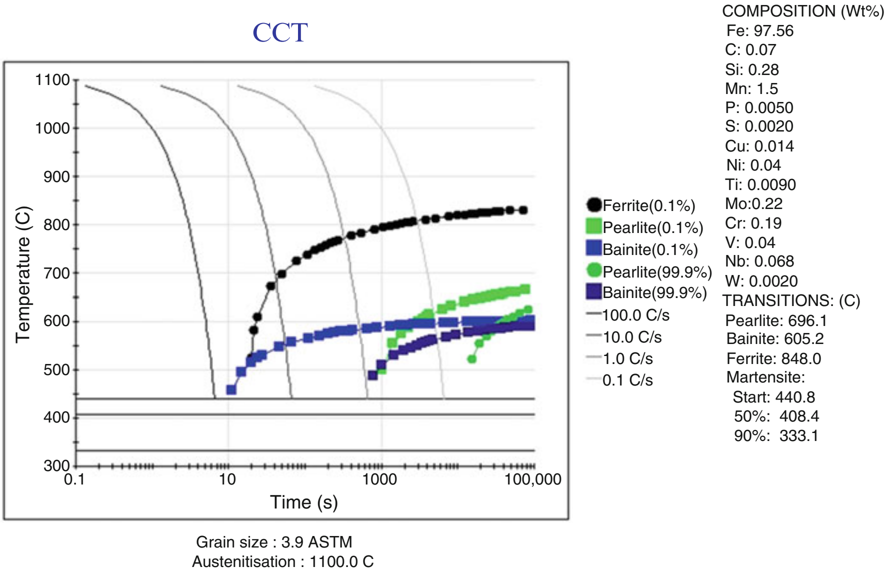

Fig. 7.10 CCT theoretical curve proposed for API 5L X70 steel

analysis, the grain growth can be a problem. These diagrams can be applied to any welding process because the phase transformations in the HAZ basically depend on the maximum temperature, cooling rate, and chemical composition of this region.

Furthermore, with the CCT the behavior of phase transformations in the weld regions was discovered, allowing more control in the manufacturing process of pipes avoiding the formation of phases that make susceptible the hydrogen damage in the pipelines.

It is also important to note that to study the phase transformations that occur due to the heat input applied to the weld metal, it is advisable to first obtain the CCT curves to optimize the experimental design with welding application.

Further work is necessary to perform welds in X70 steel with the SAW process and evaluate the impact resistance of the HAZ and the microstructural behavior under different process parameters.

Acknowledgements The authors thank the Consejo Nacional de Ciencia y Tecnología (CONACYT) of Mexico and the Corporación Mexicana de Investigación en Materiales (COMIMSA) for granting support for this project. The authors also thank the Centro de Investigación y de Estudios Avanzados del Instituto Politécnico Nacional (CINVESTAV) of Saltillo for the technical support provided for part of this research.

References

1. Gorni AA, de S. Reis JS (2010) Metalurgia dos aços microligados usados em tubos soldados de grande diâmetro. Corte e Conformação de Metais 57:50–63
2. de S. Bott I (2013) Corrosão na indústria do petróleo. Revista ABM 69(621):53–57
3. Li C, Wang Y, Han T, Han B, Li L (2010) Microstructure and toughness of coarse grain heat-affected zone of domestic X70 pipeline steel during in-service welding. J Mater Sci 46:727–733
4. Skjellerudsveen M, Akselsen OM, Olden V, Johnsen R, Smirnova A (2010) Effect of microstructure and temperature on hydrogen diffusion and trapping in X70 grade pipeline steel and its Weldments, Norwegian University of Science and Technology, pp 1–13
5. Huang F, Liu J, Deng ZJ, Cheng JH, Lu ZH, Li XG (2010) Effect of microstructure and inclusions on hydrogen induced cracking susceptibility and hydrogen trapping efficiency of X120 pipeline steel. Mater Sci Eng 527:6997–7001
6. Frappart S, Feaugas X, Creus J, Thebault F, Delattre L, Marchebois H (2010) Study of the hydrogen diffusion and segregation into Fe – C – Mo martensitic HSLA steel using electrochemical permeation test. J Phys Chem Solids 71:1467–1479
7. Reyes AM (2004) Análisis de Estabilidad Mecánica de Laminaciones Escalonadas en Recipientes Cilíndricos con Presión Interna Aplicando el Método del Elemento Finito, INSTITUTO POLITÉCNICO NACIONAL
8. Oates WR, Saitta AM (1998) Materials and applications – part 2. In: AWS Welding Handbook, 8th edn. AWS, Miami
9. Arafin MA, Szpunar JA (2011) Effect of bainitic microstructure on the susceptibility of pipeline steels to hydrogen induced cracking. Mater Sci Eng 528:4927–4940
10. American Petroleum Institute (2013) API 5L 2013. Estados Unidos
11. Júnior EH (2004) Investigação experimental do comportamento dúctil de aços API-X70 e aplicaçoes de curvas de resistência J-Da para previsão de colapso em dutos, Escola Politécnica da Universidade de São Paulo

12. Mohtadi-Bonab MA, Szpunar JA, Razavi-Tousi SS (2013) A comparative study of hydrogen induced cracking behavior in API 5L X60 and X70 pipeline steels. Eng Fail Anal 33:163–175
13. da Costa e Silva ALV, Mei PR (2010) Aços e ligas especiais, 3rd edn. Blucher, São Paulo
14. Kim WK, Koh SU, Yang BY, Kim KY (2008) Effect of environmental and metallurgical factors on hydrogen induced cracking of HSLA steels. Corros Sci 50:3336–3342
15. Alvisi PP (2010) Nota sobre a seleção do aço para o serviço com H2S. Tecn Metal Mater Miner 6:192–200
16. Sperko WJ (2005) Exploring temper bead welding. Weld J 84(7):37–40
17. Modenesi PJ, Marques PV, Santos DB (2012) Introdução à. Metalurgia da Soldagem, UFMG, Belo Horizonte
18. Modenesi PJ (2012) Soldabilidade dos Aços. Transformáveis, Belo Horizonte
19. da C. Santos IM (2013) Elaboração de um Diagrama TAC para um Aço de Alta Tenacidade API X-70, Universidade Nova de Lisboa
20. Arámburo G, García S, Pérez R, Juárez JA (2004) Impacto tecnológico de aceros grado API 5L X-70 para la fabricación de ductos de 36" de diámetro resistentes al gas amargo. Ing Invest Technol 1:17–26
21. Chilque ARA, de S. Jardim MV, Gonçalves PN, Tavares SS (2014) Determinação da resistência ao impacto da região de grão grosseiro da ZTA do aço API5L X80 soldado em condições de alta energia, Congresso Nacional Soldagem, Brasil

Chapter 8
Effect of Hydrogen on a Microalloyed Steel Permeate

D.C. Rojas Olmos, S.C. Carranza Florida, J.A. Ortega Herrera, M.A. Doñu Ruiz, N. López Perrusquia, and M. Arredondo Ramírez

Abstract In this work, we examined the influence of hydrogen into microstructure in a steel API-X60, with different heat treatments. First, all plate samples undergo heat treatment at a temperature of 1000 °C for 30 min. The formation of microstructures are obtained at temperatures of 204, 315, 426, 538, and 650 °C for 30 min and cooled in water. The permeation tests were carried out according to the modified Devanathan-Starchurski setup. Microstructural observation involved use of an optical microscope (OM) with and without hydrogen. The phases predominantly after heat treatment are bainite-ferrite, ferrite-martensite, Widmanstatten ferrite, and globular bainite. The result obtained at the condition of 204 °C and 315 °C decrease the hydrogen diffusion due to the formation of different phases. In addition, the finite element method (FEM) was used to evaluate the hydrogen diffusion on the specimens.

Keywords Finite element • Heat treatment • Hydrogen • Microstructure

8.1 Introduction

The production and transportation of oil and gas have problems with hydrogen. The hydrogen generated failure and critical factors in the deterioration of low-carbon steels [1, 2]. In the oil industry, failure and replacement of millions of pipes occur each year caused by processes of degradation of the mechanical properties of the steel associated with the environment of these structures.

D.C. Rojas Olmos (✉) • S.C. Carranza Florida • M.A. Doñu Ruiz • N. López Perrusquia • M. Arredondo Ramírez
Grupo Ciencia e Ingeniería de Materiales, Universidad Politécnica del Valle de México,
Av. Mexiquense, Tultitlán. Edo, México
e-mail: citlallirojas@hotmail.com

J.A. Ortega Herrera
Grupo de Ingeniería Mecánica Computacional Adolfo López Mateos, SEPI-ESIME,
Instituto Politécnico Nacional, Zacatenco, México, D.F. 07738, Mexico

R. Pérez Campos et al. (eds.), *Characterization of Metals and Alloys*, DOI 10.1007/978-3-319-31694-9_8

Hydrogen has the smallest atomic size among all the elements and diffuses rapidly even at room temperature and accumulates at the microstructural defects such as voids, dislocations, grain boundaries, precipitates, and triple junctions [3]. Diffusion of hydrogen is affected by the presence in the microstructure of various defects attracting the hydrogen and trapping it. The hydrogen trapping sources in metals are categorized into two groups: chemical and physical trapping sources [4].

Hydrogen embrittlement adsorption (HEA) occurs by adsorption of molecular hydrogen in a hydrogen atmosphere generated, or by a corrosion reaction, and absorption into the crystal lattice after their dissociation to atomic form [5]. Hydrogen embrittlement induced (HEI) occurs in the absence of a hydrogenated atmosphere and is caused by the hydrogen entering the cross linked section during the production of steel and in some manufacturing processes of structures, such as welding, before testing or the start of service [6–8].

The HEA induces ductile fracture morphology in AISI 304L stainless steel, additionally the HEI cleavage fracture presented in Kuromoto [9] and the work of Gao and Hu [10] observed a mixed mode of fracture (ductile and cleavage) in Ni_3 al alloy low effect gives HEA while under HEI behavior was ductile or mixed, depending on the hydrogen concentration.

The heat treatment is important for modifying the phases on steels through microstructure, with the type of cooling controlling the size to grain. The finer the size, the greater is the resistance and fracture toughness. The small grain size produces improved mechanical properties and the heat treatment is employed to improve the material properties, such as resistance to hydrogen embrittlement that results from defects in materials as impurities or mechanical deterioration and diffusion of hydrogen varies as to the time exposition [11, 12].

The work in Haq and Muzuka [13] described that different grain sizes derived by the heat treatment, the diffusivity of hydrogen in the steel microstructure and the phases observed, and the detected cracking in steel. These grain sizes or phases may increase or decrease the mobility of hydrogen in the steel interaction; the low diffusivity is shown due to the combination of finer grain size.

This study evaluates the effect of hydrogen on API-X60 steel with different thermal treatment and obtaining different phases in the steel, so creating trapped hydrogen and reducing the formation of blistering and the generation of cracks. Therefore, a symmetric model of FEM was used with 2D diffusion of hydrogen to evaluate hydrogen saturation in the specimens.

8.2 Developed Experimental

8.2.1 Materials

A plate of API-X60 steel was used as a specimen with the dimension of 37.5 × 7.5 with a thickness of 2.5 mm and the chemical composition show in Table 8.1.

Table 8.1 Chemical composition API-X60 steel

Steel	C	Mn	Si	P	S	Al	Nb	Cu	Cr	Ni	V	Ti	Mo
X60	0.04	1.57	0.14	0.013	0.002	0.046	0.04	0.30	0.26	0.17	0.0065	0.014	0.05

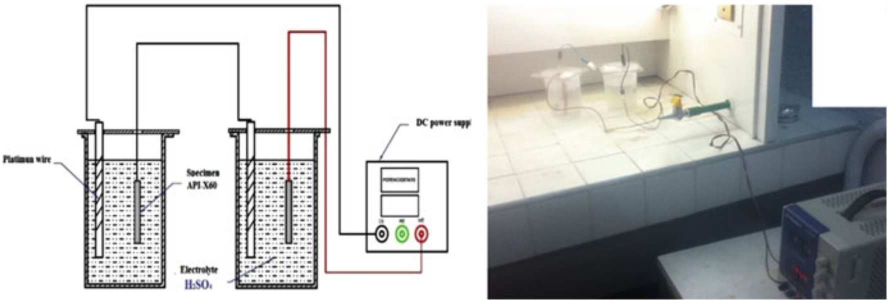

Fig. 8.1 Construction of the hydrogen permeation cell

8.2.2 *Heat Treatment*

All specimens were given a heat treatment at a temperature of 1000 °C for 30 min. After the heat treatment, six specimens were introduced on the furnace at five temperatures of 204, 315, 426, 538, and 650 °C during 30 min for each condition and cooled in water.

8.2.3 *Metallography*

Metallography of the specimens was performed at tree treatment temperature, the specimens were first ground up to 2000 grit SiC paper, then polished. They were then etched with a solution containing 5 % of concentrated nitric acid and 95 % methanol. An optical microscope (OM) was used for microstructure observation.

8.2.4 *Hydrogen Permeation*

Fig. 8.1 shows the permeation tests according to setup using standard ASTM G148-97. In this test,tree specimens were prepared, and the hydrogen cathodic charging is carried out in a 0.5 M of sulfuric acid electrolyte solution at the room temperature using a current density of 50 mA/cm^2 with v.10.02 EC-LAB. The time was selected on the hydrogen diffusivity according to Shrier et al. [14] and was permeated for 4.6 h. After the test, each specimen was sectioned along the side. Then, the cross section was polished and observed on OM without being etched.

8.2.5 Simulation of Diffusion Hydrogen

The FEM simulation was used to evaluate the development of monatomic hydrogen concentration inside the specimen as a function of time. It is considered an isothermal system in which the diffusion coefficient is constant, the flow cross-sectional area is constant, and the borders of the specimen instantly reach the hydrogen concentration defined by each of the aqueous solutions. The possible presence of hydrogen trap boundary conditions is ignored.

The diffusion is assumed to be driven by a chemical potential gradient. The main equation given by ABAQUS 6.12, the problem is one-dimensional with only the gradient along the *x* direction specimen, therefore, a 2D mesh with DC2D8 element (rectangular eight nodes) contains nodes with 756 and 700 elements. The mesh is refined near the edge of the specimen where the concentration gradient is on the surface.

8.3 Results and Discussion

The effect of heat treatments in each condition of the microstructure is shown in Fig. 8.2.

Microstructure observed by OM at the temperature of 204–650 °C, reveals morphology of ferrite mixed grains with the distribution of dark phases at the ferrite grain boundaries with featureless appearance, acircular ferrite (AF), polygonal ferrite (PF), bainite-ferrite (BF), ferrite-martensite (MA), ferrite Widmanstatten

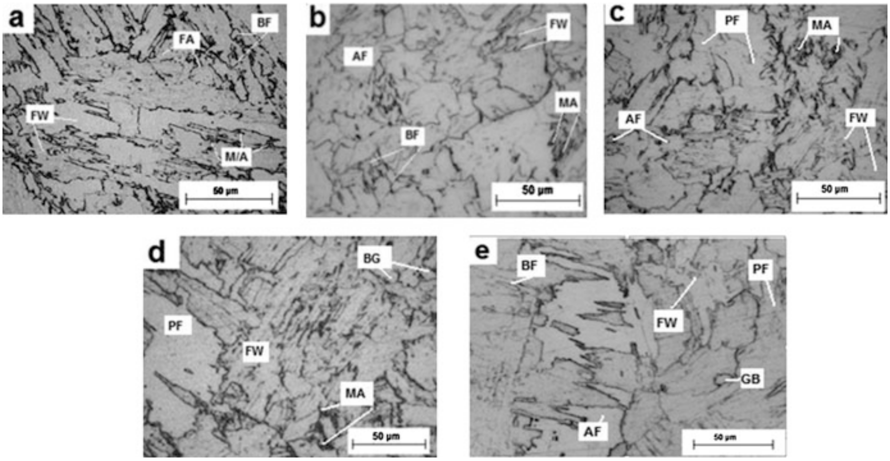

Fig. 8.2 Micrographs of steel API-X60 with heat treatments at temperatures; (**a**) 204 °C, (**b**) 315 °C, (**c**) 426 °C, (**d**) 538 °C, and (**e**) 650 °C

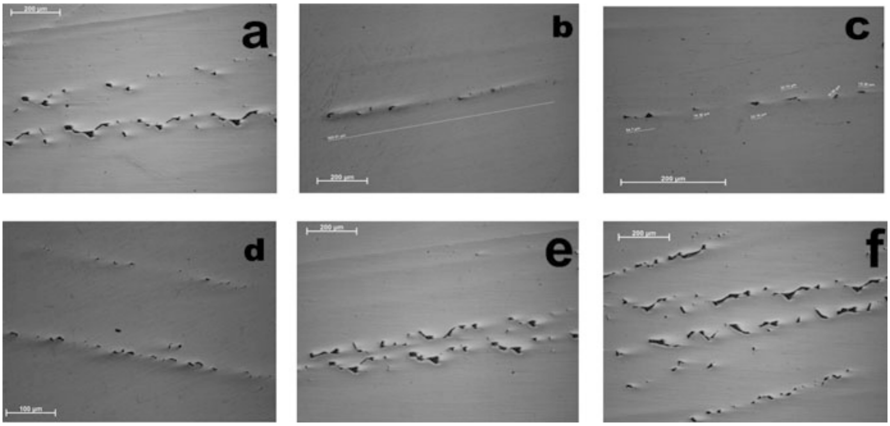

Fig. 8.3 Micrographs API-X60 steels with permeated of hydrogen (**a**) without hydrogen; (**b**) 204 °C, (**c**) 315 °C, (**d**), 426 °C, (**e**) 538 °C and (**f**) 650 °C

(FW), and globular bainite (GB). The effect of materials give in to cooling and tend to be transformed to martensite or bainite with other micro constituents, as it presented in the microstructure in Fig. 8.2, about ferrite microstructures classified as PF or AF, so they consist essentially of products of FW processing.

One possible reason for PF is that it requires relatively high temperatures for formation compared with AF. Besides, there is the presence BF representing high bainite, which has a different mechanism of formation, so the effect of the microstructure in the micro alloyed steels, establishing equiaxed grains by heat transfer with lower diffusivity [15, 16].

Moreover, from the hydrogen diffusion into sample X60 with heat treatment, the cross sections on each condition were observed and show in Fig. 8.3.

The condition of the heat treatment of 426, 538, and 650 °C show a significant crack region of the the cross sections. The condition of the heat treatment of 204 and 315 °C show a decreased crack region due to the formation of phases cracks stemming from hydrogen permeation after 4.5 h. The formation of cracks is due to hydrogen that is concentrated in a particular region, and cracks are formed randomly, where the effect of hydrogen on the microstructures with ferrite phase is evident. According to the work of Gau and Hu, Doñu Ruiz et al., and Lopez-Perrusquia et al. [17–19], the microstructures reduce the effect of hydrogen in the material using a hydrogen permeation showing a low embrittlement.

The diffused hydrogen was modeled for 5 h and the analysis was performed in three stages in order to compare the results at specific times during the transition. The variation of concentration with time was determined by the FEM (phenomenon finite element) and was shown in Fig. 8.4.

The concentration profile for the size of specimen thickness is observed and different time values are shown in Fig. 8.5, so that the hydrogen flow reaches a steady state in order to saturate the full sample of hydrogen.

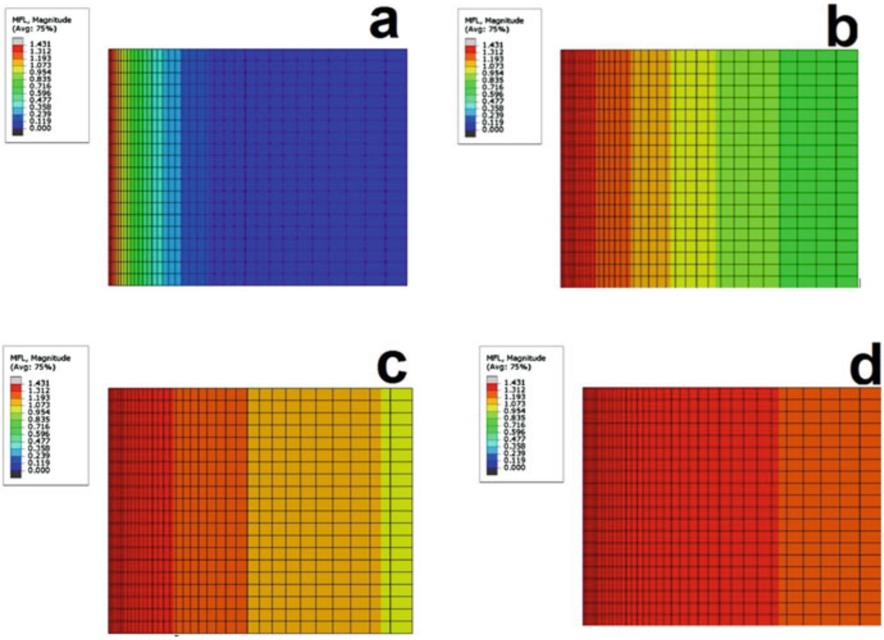

Fig. 8.4 Contour standardized the API-X60 steel with FEM hydrogen concentration, with time; (**a**) 9 min, (**b**) 2 h, (**c**) 4 h, and (**d**) 5 h

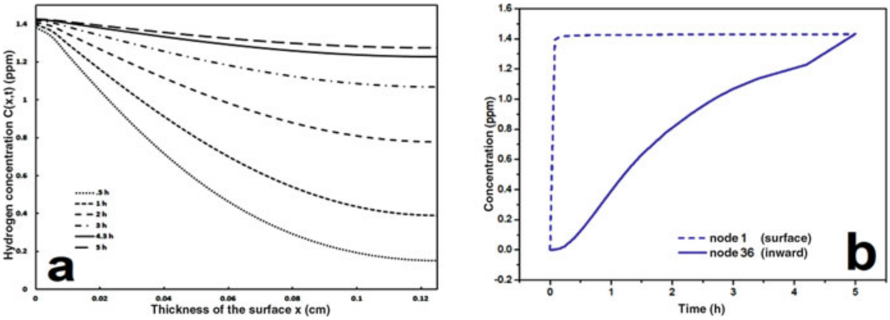

Fig. 8.5 Hydrogen concentration profile at (**a**) different times along the thickness of 0.12 cm specimen and (**b**) surface node 1 and inside node 36

The effect of diffusion of hydrogen in the material from API-X60 simulation part is presented in the results, which reflect no doubt that cracks tend to form due to the diffusion of hydrogen, which are presented in the study material with heat treatment as they were presented in the experimental section, showing a relationship in the numerical data (Fig. 8.5).

With the effect of hydrogen in a special type of degradation known as hydrogen embrittlement (HE), the metallographic study revealed the effect of microstructure, high temperature heat treatment (>426 °C) showed region cracks, and temperatures (<315 °C) showed the presence of microstructure, like BF and PF, as factors to reduce the hydrogen diffusion in material acting as H-traps [20].

8.4 Conclusions

The heat treatment on API-X60 shows the effect of hydrogen diffusion, the condition at temperatures of 204 and 315 °C evidences a decrease of the cracked region due to the formation of microstructures of bainite-ferrite, ferrite Widmanstatten, and ferrite-martensite. The conditions of 426, 538, and 650 °C have a crack region growth with microstructure formation of polygonal ferrite and acircular ferrite. The optimal conditions to reduce the diffused hydrogen are at condition <315 °C with formation of traps like bainite, globular bainite, and martensite. The model of finite element is possible to observe the phenomenon of hydrogen diffusion with steady state on steel API-X60. Based on the experimental results of permeated hydrogen, it was proposed to observe the behavior and concentration gradient of hydrogen on the specimen.

References

1. Xu LY, Cheng YF (2012) Development of a finite element model for simulation and prediction of mechano electrochemical effect of pipeline corrosion. Comput Mater Sci 56:49–57
2. Yazdipour N, Haq AJ, Muzaka K, Pereloma EV (2012) 2D modelling of the effect of grain size on hydrogen diffusion in X70 steel. Comput Mater Sci 56:49–57
3. Oriani RA (1978) Hydrogen embrittlement of steels. Annu Rev Mater Sci 8(1):327–357
4. Wert CA (1978) Trapping of hydrogen in metals. In: Hydrogen in metals II. Springer, Berlin
5. Yazici M, Durmus A, Bayram A (2000) Influence of morphology of martensite on tensile and strain hardening properties of dual phase steels. Materialprüfung 45:214–219
6. Abdur Razzak M (2011) Heat treatment and effects of Cr and Ni in low alloy steel. Bull Mater Sci 34:1439–1445
7. Maleque MA, Poon YM, Masjuki HH (2004) The effect of intercritical heat treatment on the mechanical properties of AISI 3115 steel. J Mater Process Technol 153:482–487
8. Hayat F, Uzun H (2011) Effect of heat treatment on microstructure mechanical properties and fracture behaviour of ship and dual phase steels. J Iron Steel Res Int 18:65–67
9. Kuromoto NK, Guimarães AS, Lepienski CM (2004) Surface and internal hydrogenation effects on the fatigue life of austenitic steels. Mater Sci Eng 381:216–222
10. Gao SJ, Hu ZQ (2000) Environmental and internal hydrogen embrittlement of a directionally solidified Ni-rich Ni3Al intermetallics. Mater Sci 35:1433–1438
11. Pereira PAS, Franco CSG (2015) Hydrogen effects on the microstructure of a 2.25 Cr-1Mo-0.25V steel welded joint. Int J Hydrog Energy 40:17136–17143
12. de Jesús SAM, Facundo RG, Raúl C-PF, Fernando G-G, Humberto A-J, Antonio S-GL (2015) Effect of heat treatment on the mechanical properties and microstructure of a API 5CT J55 pipeline steel. Eng Res Technol 16:539–550
13. Haq AJ, Muzuka K (2015) Effect of microstructure and composition on hydrogen permeation in X70 pipeline steel. Int J Hydrog Energy 40:2544–2556
14. Shreir LL, Jarman RA, Burstein GT (1994) Corrosion metal environment reactions, vol 1. Butterworth-Heinemann, Oxford, pp 4–44

15. Dong CF, Liu ZY, Li XG, Cheng YF (2009) Effects of hydrogen charging on the susceptibility of X100 pipeline steel to hydrogen-Induced cracking. Int J Hydrog Energy 34:799–884
16. Koh SU, Kim JS, Yang BY, Kim KY (2004) Effect of line pipe steel microstructure on susceptibility to sulfide stress cracking. Corros Sci 60:244–254
17. Gao SJ, Hu ZQ (2000) Environmental and internal hydrogen embrittlement of a directionally solidified Ni-rich Ni3Al Intermetallics. J Mater Sci 35:1433–1438
18. Ruiz MAD, López Perrusquia N, Ortega Herrera JA, Urriolagoitia Calderón G, Cortés Suárez VJ, Rodriguez Gonzales S (2014). API X70 Bending test embrittlement index fracture. Defect Diffus Forum 353:159–164
19. Lopez-Perrusquia N, Doñu-Ruíz MA, Ortega-Herrera JA, Urriolagoitia-Calderón G, Vargas-Oliva YE (2014) Study of hydrogen permeation in a micro-alloyed heat treated steel. Defect Diffus Forum 353:165–170
20. Oriani RA (1970) The diffusion and trapping of hydrogen in steel. Acta Metall 18:147–157

Part IV
Characterization of Thin Layers and Coatings

This part includes two chapters related to characterization of coatings and nanolayers applied on different substrates. The first chapter presents a study to solve corrosion damage on metallic substrates, which causes large economic losses as well as security problems, therefore, great efforts to combat these issues have been reported in this research. The aim of this work is to produce monolayers of silicon oxide on 304 stainless steel sheets by means of the sol-gel and dip-coating process, which has been widely used due to its low production cost and simplicity producing uniform thin films and coatings.

The second chapter presents the synthesis and structural and optical characterization of $CdSe_{1-y}S_y$ deposited by chemical bath deposition (CBD) technique on corning glass at room temperature. The sulfur molar fraction was varied by varying the thiourea volume added to the growth solution. X-ray diffraction results and Raman spectroscopy vibrational showed that obtained nanocrystals present hexagonal wurtzite crystal systems. Thiourea showed an effective substrate protection against corrosion revealed by the potentiodynamic polarization curves. Because of excellent properties of Cd(S,Se), it is used in optoelectronic devices, photoconductors, gamma ray detectors, visible-light emitting diodes, lasers, and solar cells.

The main techniques used in the characterization of these steels are:

- Potentiodynamic polarization curves.
- Optical microscopy (OM).
- Mechanical tests.
- X-ray diffraction.
- Energy dispersive spectroscopy (EDS).
- High Resolution transmission Electron Microscopy (HRTEM).
- Raman spectroscopy.
- Photoluminescence (PL).
- Transmittance.

Chapter 9
Mechanical Properties of SiO_2 Coatings for Corrosion Protection of 304 Stainless Steel

J. Reyes Miranda, M. Aguilar Sánchez, E. Garfias García, D.Y. Medina Velazquez, and Á. de J. Morales Ramírez

Abstract Corrosion damage on metallic substrates causes large economic losses as well as security problems. Fortunately, great efforts to combat these issues have been reported in all kinds of metals and their alloys, but until now the effect of corrosion has had no a real solution. The aim of the present is to produce monolayers of silicon oxide on 304 stainless steel sheets using the sol-gel and dip-coating processes, which have been widely employed due to low production costs, simplicity, and the ability to produce uniform thin films and coatings. Focusing the work on organic–inorganic hybrid coatings, tetraethilorthosilicate (TEOS) and 3-(Trimethoxysilyl)propyl methacrylate are used as precursors for the SiO_2 layers formation. The mechanical properties of the SiO_2 coating were evaluated by tensile and Vickers microindentation hardness tests, while corrosion resistance is characterized by potentiodynamic measurements.

Keywords Hybrid materials • Sol-gel • Corrosion • Thiourea • Dip-coating

9.1 Introduction

The sol-gel method has emerged as a very promising technique for the synthesis of organic–inorganic hybrid materials [1]. It is promising because it can be identified in the molecular scale homogeneity of the starting solutions, the low processing temperatures, chemical homogeneity, the possibility of incorporating many different metal dopants into different matrixes, and the capability for using coating substrates of any shape [2]. Moreover, these materials can be easily deposited on metallic

---

J.R. Miranda (✉) • M.A. Sánchez • E.G. García • D.Y.M. Velazquez
Departamento de Materiales, Ciencias Básicas e Ingeniería, Universidad Autónoma Metropolitana-Azcapotzalco, Av. San Pablo No 180, Col. Reynosa-Tamaulipas, C.P. 02200, México D.F., Mexico
e-mail: joremi@live.com.mx

Á. de J. Morales Ramírez
Instituto Politécnico Nacional-CIITEC, Cerrada de CECATI S/N Col. Santa. Catarina, Del. Azcapotzalco, México D.F. 02250, Mexico

R. Pérez Campos et al. (eds.), *Characterization of Metals and Alloys*, DOI 10.1007/978-3-319-31694-9_9

substrates by spraying, dipping, and spinning techniques. Hybrid coatings have been prepared to improve the corrosion resistance properties of steel, zinc, aluminum, and magnesium substrates and designed to offer environmentally friendly alternatives in pre-treatment coating [3, 4]. Hybrid coatings are mainly prepared from the sol of alkoxide mixed with organic polymers or organoalkoxysilanes. R'-Si(OR)3 bearing R'= various organic functional groups, which are the most used organic molecules to form strong chemical interactions with inorganic sols [5, 6]. The presence of organic components in sols forms dense films and reduces coating porosity, which makes the gel network more flexible and less prone to cracking during further drying processes [7]. The hydrophobicity and adhesive strength as well as the anticorrosion properties of inorganic–organic sol-gel hybrid coatings suggest their potential utility as technologically compatible alternatives to conventional coating [8]. In this work, the effect of organic precursors is reported. SiO_2 organic–inorganic hybrids were coated on type 304 stainless steel by dip-coating technique using tetraetylorthosilicate and 3-(trimethoxysilyl) propyl methcrylate as precursors, with molar ratio TEOS/MAPTS = 1:0.5, 1:1 and 1:1.5. Moreover, the behavior of Thiourea on corrosion resistance was studied.

9.2 Experimental

9.2.1 Sol-Gel Synthesis of SiO_2 Organic–Inorganic Hybrids

The SiO_2 organic–inorganic hybrid was synthesized by sol-gel method using tetraethyl orthosilicate ($Si(OC_2H_5)_4$, 98 %, Aldrich), TEOS, and 3-(trimethoxysilyl) propyl methcrylate ($C_{10}H_{20}O_5Si$) MAPTS, 98 %, Aldrich, ethanol (CH_3CH_2OH, 99.9 %, Fermont), hydrocloric acid (HCl 37.1 %, Fermont), and distilled water as precursors. In this procedure, the hybrid sol was obtained by hydrolysis and condensation of TEOS and MAPTS. A solution of ethanol/TEOS was prepared with a molar ratio of 4:1, according to Klein's diagram [8]. The solution was stirred continually for 1 h. Later, a solution of distilled water and hydrochloric acid was added to the ethanol/TEOS solution and kept stirred for 1 h, fixing a water/TEOS molar ratio of 6:1. Afterwards, the MAPTS was added to the solution varying the molar ratios of TEOS/MAPTS = 1:0.5, 1:1 and 1:1.5 and thiourea with molar ratios of TEOS/thiourea of 1:0.04 and 1:0.08. Finally, the sols were stirred continuously for 20 h.

9.2.2 Coatings Deposition

The SiO_2 organic–inorganic hybrids coatings were deposited on 304 stainless steel by the dip-coating technique. The rate used was 0.36 cm/s. Before the deposition of the films, the substrates were perfectly cleaned in an ultrasound bath in distilled water with soap for 10 min, and then washed with distilled water. Once the first SiO_2 layer was formed, the films were dried for 10 min at 100 °C, then an annealing treatment was carried out at 180 °C for 10 min. The temperature ramp (100–180 °C) was chosen to avoid crack formation and organic evaporation. The cycle was repeated three times to increase the film thickness.

9.3 Results and Discussion

9.3.1 Corrosion Testing

For the corrosion testing, a three-electrode cell was employed using 304 stainless steel as a counter electrode and a silver–silver chloride as the reference electrode. Potentiodynamic polarization measurements were conducted from -1.1 to 1.9 V, with a scan rate of 0.005 V s^{-1}. The tests were performed in a saline solution containing chloride ions (3.5 wt % NaCl).

Figure 9.1 shows the corrosion resistance of SiO_2 hybrid coatings on 304 stainless steel, keeping the 1TEOS:0.5MAPTS molar ratio and varying the thiourea concentration. As can be seen, the bare metal has poor corrosion resistance, since the corrosion current density is about 5.5 μA-cm^{-2}. However, once the

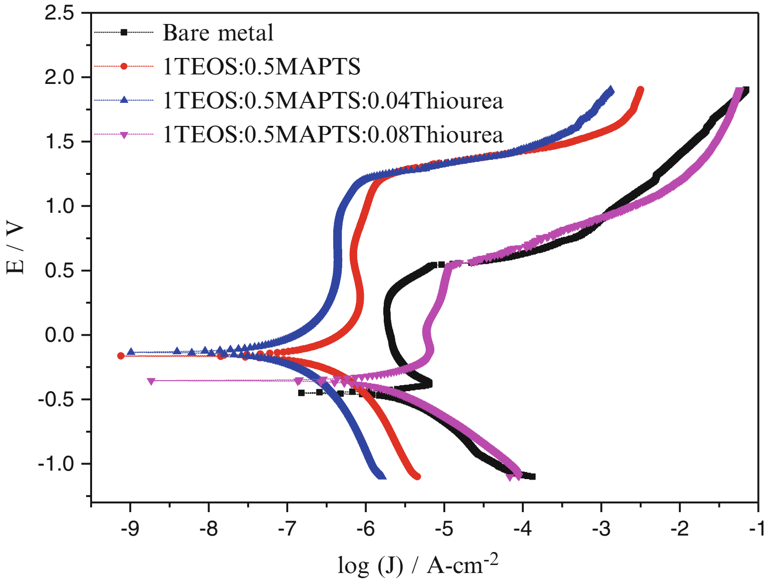

Fig. 9.1 Potentiodynamic polarization curves for hybrid coating 1TEOS:0.5MAPTS varying thiourea concentration in a saline solution (3.5 wt % NaCl)

steel has a SiO_2 coating with a 1TEOS:0.5MAPTS ratio, the corrosion current density decreases to 0.58 μA-cm^{-2}. The addition of 0.69 mmol of thiourea (sample 1TEOS:0.5MAPTS:0.04thiourea) on the hybrid sol favored the protection of the steel substrate with a corrosion current density of 0.234 μA-cm^{-2}. However, when the concentration of thiourea increases to 1.42 mmol (sample 1TEOS:0.5MAPTS:0.04thiourea), the corrosion current density increases to 3.01 μA-cm^{-2}. With a bigger concentration of thiourea, the quality of the coatings was not homogeneous. One possible explanation is the increasing of internal stresses accompanying crack formation impeding the interaction of the NaCl solution with the steel substrate 304. Figure 9.1 also shows an interesting passivation response for the samples 1TEOS:0.5MAPTS and 1TEOS:0.5MAPTS:0.04thiourea until a potential of 1.15 V; afterwards, the current density increases again.

With the aim to observe the effect of the saline solution on the stainless steel substrate, some micrographs at 5× were obtained with an Olympus microscope, model PMG3. Figure 9.2 shows some micrographs of the samples (1) 1TEOS:0.5MAPTS, (2) 1TEOS:0.5MAPTS:0.04thiourea, and (3) 1TEOS:0.5MAPTS:0.08MAPTS, before and after the corrosion test. As can be seen, the addition of thiourea enhances the substrate protection, but an excess on the thiourea concentration produces defects on the coating, reducing the substrate protection.

Figure 9.3 shows the corrosion response of the hybrid coating of the samples 1TEOS:1MAPTS:0.04 and 1TEOS:1MAPTS:0.08. The same behavior is observed when the thiourea concentration is high, i.e., the corrosion current density increases obtaining a corrosion rate bigger.

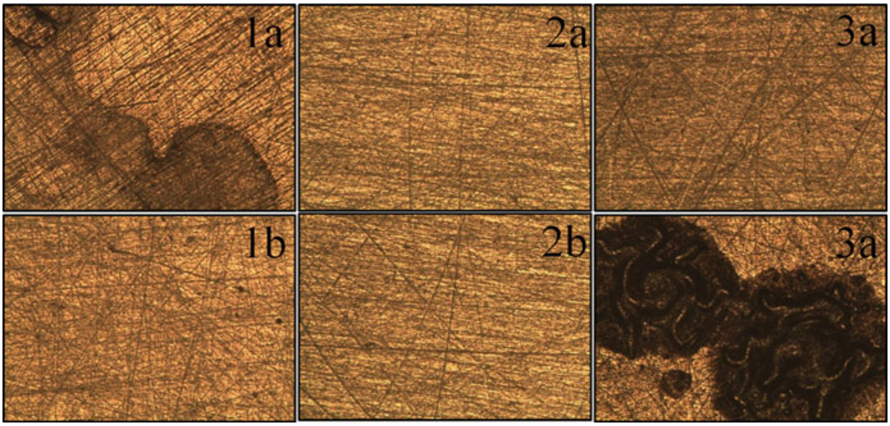

Fig. 9.2 Optical microscopy observation of 1TEOS:0.5MAPTS (*1a*) before and (*1b*) after corrosion testing; 1TEOS:0.5MAPTS:0.04thiourea (*2a*) before and (*2b*) after corrosion testing; 1TEOS:0.5MAPTS:0.08thiourea (*3a*) before and (*3b*) after corrosion testing

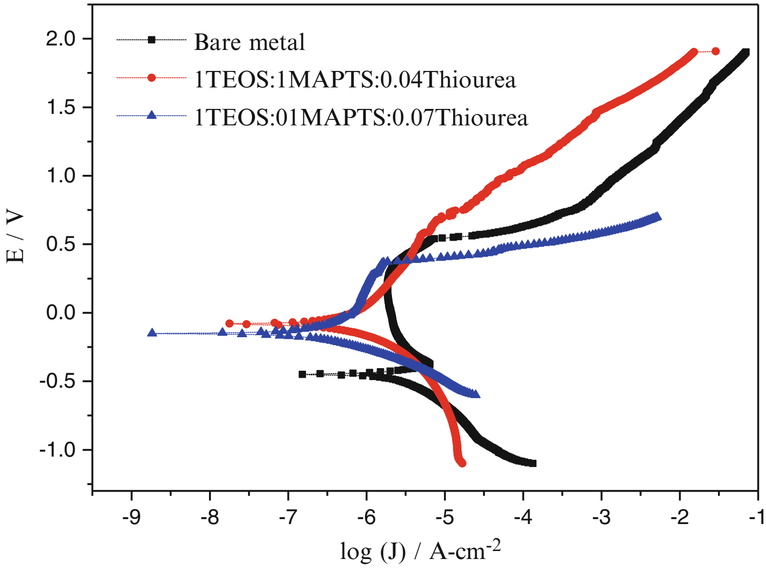

Fig. 9.3 Potentiodynamic polarization curves for hybrid coating 1TEOS:1MAPTS varying thiourea concentration in a saline solution (3.5 wt % NaCl)

Figure 9.4 shows the results obtained of the sample 1TEOS:1.5MAPTS:0.04. In this case, the coating does not have a significant corrosion protection because the coating was not homogeneous and the NaCl solution has contact with the substrate.

Figure 9.5 shows a comparison of the 3 TEOS/MAPS/thiourea molar ratios: 1:0.5:0.04, 1:1:0.04 and 1:1.5:0.04. The best substrate protection was obtained with the coating of the sample 1TEOS:0.5MAPTS:0.04thiourea.

9.3.2 Microhardness Testing

The microhardness test of the samples was carried out in a Tukon Wilson apparatus, model 11.02. Figure 9.6 shows the microhardness results obtained for the hybrid coatings under different conditions. As can be seen, the 304 steel hardness is about 231.44 ± 13.63 HV, the sample 1TEOS:0.5MAPTS showed an increase in hardness 250.22 ± 15 HV. However, the addition of thiourea into the hybrid sol produced a reduction of hardness to 62.74 ± 4.14 HV. The same happens with a high MAPTS and thiourea concentration. Interestingly, the hardness ratio of the samples 1TEOS:0.5MAPTS:0.04thiourea and 1TEOS:0.5MAPTS is four times lower only with the addition of thiourea.

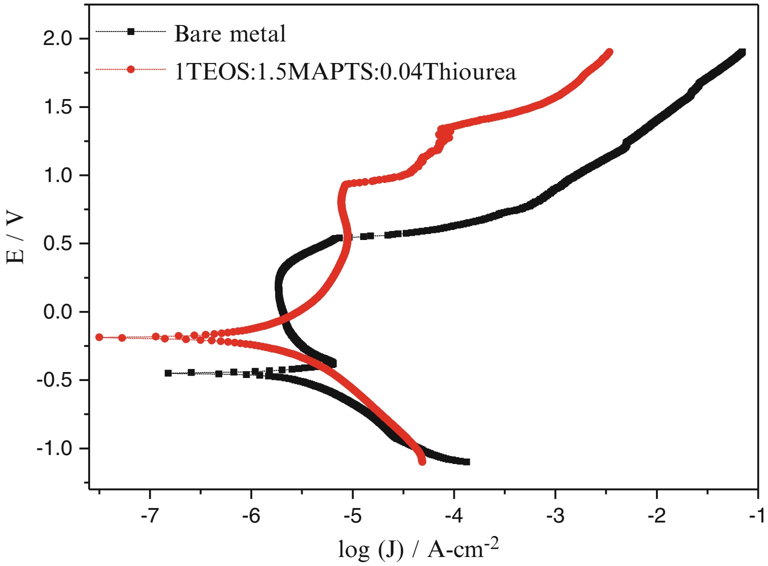

Fig. 9.4 Potentiodynamic polarization curves for hybrid coating 1TEOS:1.5MAPTS:0.04 thiourea in a saline solution (3.5 wt % NaCl)

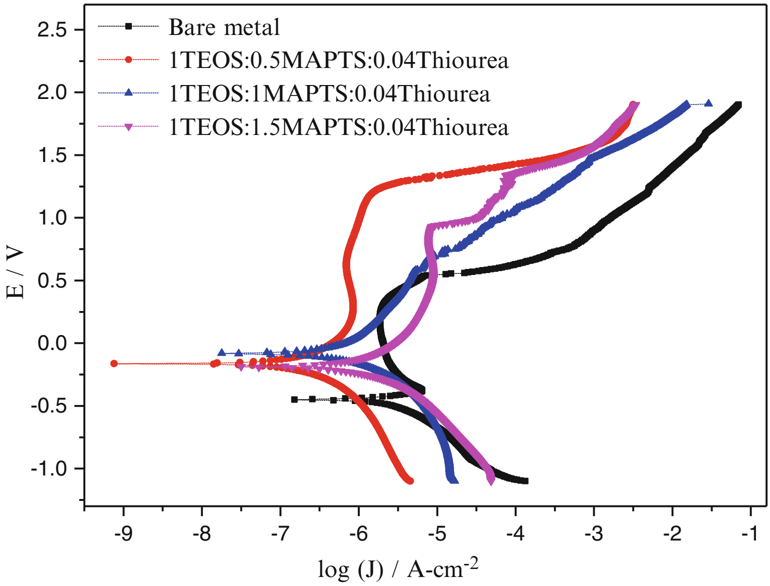

Fig. 9.5 Comparison of potentiodynamic polarization curves for hybrid coating in a saline solution (3.5 wt % NaCl)

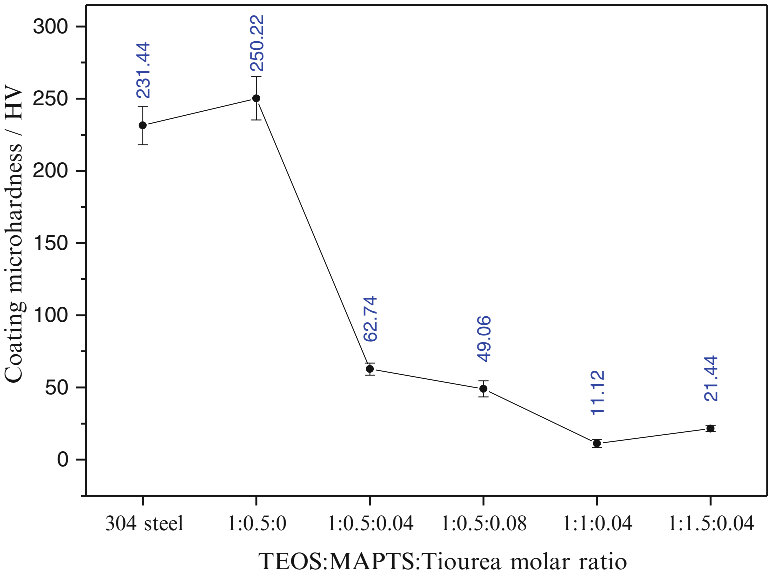

Fig. 9.6 Influence of MAPTS and thiourea concentration on coating microhardness

9.3.3 *Tensile Testing*

The tensile test was carried out with an Instron 5500R, model 1125. The specimens have a rectangular shape with a $l_0 = 6.3\,\text{mm}$, $w_0 = 3.6\,\text{mm}$ and $t_0 = 0.7\,\text{mm}$. The loading speed was 0.25 mm/min. The loads chosen to test the specimens were 70 kg_f corresponding to the yield stress of the substrate.

The specimens have a rectangular shape with the following work dimensions: $\text{l}_0 = 6.3\,\text{mm}$, $\text{w}_0 = 3.6\,\text{mm}$ and $\text{t}_0 = 0.7\,\text{mm}$. The loading speed was 0.25 mm-min^{-1}. Figure 9.7a shows a tensile test of the bare metal. The yield stress is located at 330 MPa. For that reason, the sample 1TEOS:0.5MAPTS:0.04thiourea was tested until a stress of 300 MPa (70 kg_f) and Fig. 9.7b shows a micrograph after the tensile test. As can be seen, neither cracking nor blasting off of the coating occurs with this load.

9.4 Conclusions

The sample 1TEOS:0.5MAPTS showed the best molar ratio for corrosion protection of 1TEOS:1MAPTS, 1TEOS:1.5MAPTS. Besides, thiourea showed an effective substrate protection of corrosion as evidenced with potentiodynamic polarization curves. The effect of thiourea on the microhardness coatings is very interesting, as there was a microhardness reduction in a ratio of 4 as compared with the sample

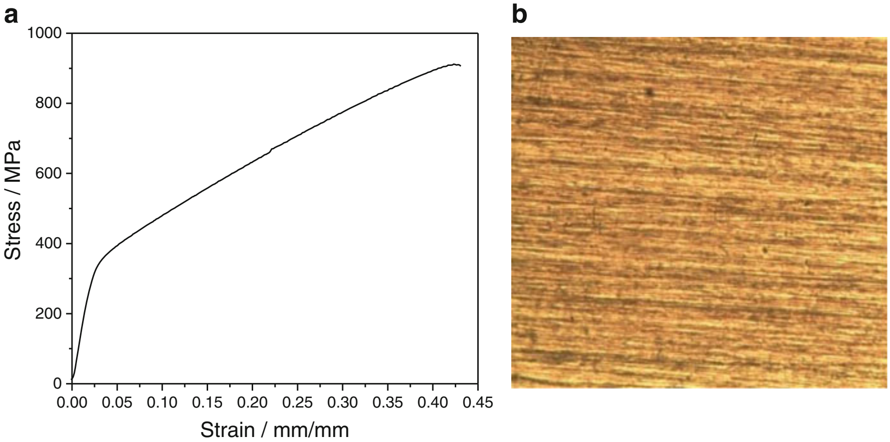

Fig. 9.7 (**a**) Stress–strain curves for tensile bare metal, (**b**) micrograph after the tensile test of sample 1TEOS:0.5MAPTS:0.04thiourea

without thiourea. Finally, no cracking was produced after tensile testing with a load of $70\,\mathrm{kg_f}$, which indicates that the mechanical properties of the coatings are suitable for those loads.

Acknowledgements The authors would like to thank the financial support giving for the Materials Department UAM Azcapotzalco.

References

1. Metroke TL, Parkhill RL, Knobbe ET (2001) Passivation of metal alloys using sol–gel-derived materials - a review. Prog Org Coat 41:233–238
2. Kirtay S (2014) Preparation of hybrid silica sol–gel coatings on mild steel surfaces and evaluation of their corrosion resistance. Prog Org Coat 77:1861–1866
3. Wang D, Bierwagen GP (2009) Sol–gel coatings on metals for corrosion protection. Prog Org Coat 64:327–338
4. Zheng S, Li J (2010) Inorganic–organic sol gel hybrid coatings for corrosion protection of metals. J Sol-Gel Sci Technol 54:174–187
5. Figueira RB, Silva CJR, Pereira EV (2015) Organic–inorganic hybrid sol–gel coatings for metal corrosion protection: a review of recent progress. J Coat Technol Res 12:1–35
6. Balgude D, Sabnis A (2012) Sol–gel derived hybrid coatings as an environment friendly surface treatment for corrosion protection of metals and their alloys. J Sol-Gel Sci Technol 64:124–134
7. Nasr-Esfahani M, Pourriahi M, Ashrafi A, Motalebi A (2014) Corrosion Performance of Rosemary-Extract-Doped TEOS:TMSM SolGel Coatings on 304L Stainless Steel. Sur Eng Appl Elect 15:337–345
8. Klein LC (1985) Sol–gel processing of silicates. Annu Rev Mater Sci 15:227–248

Chapter 10

Synthesis and Physical Properties Characterization of $CdSe_{1-y}S_y$ Nanolayers Deposited by Chemical Bath Deposition at Low-Temperature Treatment

J.E. Flores-Mena, J.I. Contreras-Rascón, J. Diaz-Reyes, and R.S. Castillo-Ojeda

Abstract In this work, we present the synthesis and structural and optical characterizations of $CdSe_{1-y}S_y$ deposited by chemical bath deposition (CBD) technique on corning glass at a temperature of $20 \pm 2\,°C$. The sulfur molar fraction was varied from 0 to 42.13 %, which was realized by varying the thiourea volume added to the growth solution in the range from 0 to 30 mL. The chemical stoichiometry was estimated by energy dispersive spectrometry (EDS). The $CdSe_{1-y}S_y$ showed hexagonal wurtzite crystalline phase that was found by X-ray diffraction (XRD) analysis and Raman spectroscopy. The average grain size range of the films was 1.48–1.68 nm that was determined using the Debye–Scherrer equation W(002) direction and was confirmed by high-resolution transmission electron microscopy (HRTEM). Raman scattering shows that the lattice dynamics is characteristic of bimodal behavior and the multipeaks adjust to the first optical longitudinal mode for the CdSeS, in all cases, Raman spectra show two dominant vibrational bands about 208 and 415 cm^{-1} associated at CdSe-1LO-like and CdSe-2LO-like. $CdSe_{1-y}S_y$ band gap energy can be varied from 1.86 to 2.16 eV by varying the thiourea volume added in growth solution in the investigated range obtained by transmittance

---

J.E. Flores-Mena
Benemérita Universidad Autónoma de Puebla, Facultad de Ciencias de la Electrónica, Av. San Claudio y 18 sur, Ciudad Universitaria, Puebla, Puebla 72500, Mexico

J.I. Contreras-Rascón
Universidad de Sonora, División de Ciencias Exactas y Naturales, Col. Centro, Hermosillo, Sonora 83000, Mexico

J. Diaz-Reyes (✉)
Instituto Politécnico Nacional, Centro de Investigación en Biotecnología Aplicada, Ex-Hacienda de San Juan Molino Km 1.5, Tepetitla, Tlaxcala 90700, Mexico
e-mail: joel_diaz_reyes@hotmail.com

R.S. Castillo-Ojeda
Universidad Politécnica de Pachuca, Km. 20, Rancho Luna, Ex-Hacienda de Sta. Bárbara, Zempoala, Hidalgo 43830, Mexico

R. Pérez Campos et al. (eds.), *Characterization of Metals and Alloys*, DOI 10.1007/978-3-319-31694-9_10

measurements at room temperature. The room temperature photoluminescence shows a dominant radiation band at about 3.0 eV that can be associated with exciton bonded to donor impurity and the quantum confinement because of the grain size is less than the Bohr radius.

Keywords CBD • HRTEM • X-ray diffraction • Photoluminescence • Raman spectroscopy

10.1 Introduction

The development of next-generation solar cells including sensitized inks solar cells (dye solar cells), that make use of the concept of the intermediate band cells and nanostructures, exceed the limit Shockley–Queisser efficiency for a single absorption, 31 %, this is one of the most fascinating challenges in research on sustainable energy. In this regard, semiconductor quantum dots (QDs) have shown properties very attractive for the development of solar cells that exceed the current limitations. The demonstration of efficient processes, multiple exciton generation (MEG) in colloidal quantum dots, has aroused great interest in the use of these materials in photovoltaic devices. In particular, the mixed semiconductor $CdSe_{1-y}S_y$ in semiconductor quantum dot technology from binary materials, cadmium sulfide (CdS) and cadmium selenide (CdSe). The cadmium chalcogenide $CdSe_{1-y}S_y$ semiconducting alloy is characterized by a variable direct band gap which can be tuned by alloying, from 1.72 eV for CdSe to 2.44 eV for CdS at room temperature. Because of excellent properties of Cd(S,Se), it is used in optoelectronic devices, photoconductors, gamma ray detectors, visible-light emitting diodes, lasers and solar, cells [1]; and the references cited therein. $CdSe_{1-y}S_y$ solid solutions have attracted great interest in recent years from both experimental and theoretical points of view [1, 2].

The CdS known as material optical window also acts as a passivating agent which forms an enveloping film relatively inert on the absorbent material (CdSe), which masks against the action of external agents. Although the reaction between the material and the external agent is thermodynamically feasible macroscopically, the layer or passivation film does not allow them to interact. There have been many efforts to find better agents that allow to passivate the surface of the nanoparticle, such as thiourea organic agent [3]. This mixed semiconductor offers one of the best alternatives for the performance of photovoltaic devices. Expectations for the semiconductor solar cell $CdSe_{1-y}S_y$ with an irradiance of 100 mW/cm^2 are: current density (Jsc) estimated at 29 mA/cm^2 [4], open circuit voltage estimated at 1.0 V [4], and an expected quantum efficiency at 17.5 % [5, 6].

Deposition by chemical bath technique of thin films consists of moderate release of metal ions into alkaline solution [7]. This technique has become important for the development of thin film solar cells, since the synthesis of CdS by this method offers a better efficiency than traditional evaporation method [8–10]. In the formation of the film exhibit two different mechanisms: The first mechanism is that involving the reaction of atomic species on the surface, this mechanism is called ion-to-ion [11–13]. The second mechanism is associated with the agglomeration of colloids formed in the solution, which can be regarded as an increase in grouping or cluster by cluster. For practical purposes, the formation of the core, which leads to the formation of the film, can occur by a process of heterogeneous nucleation on the substrate or through a process of homogeneous nucleation in the volume of the solution.

In this work we report the synthesis and characterization of $CdSe_{1-y}S_y$ nanocrystals in one step by chemical bath deposition on glass substrate at low temperature. In particular, the effects of the chemical composition on structural and optical properties of the $CdSe_{1-y}S_y$ alloy were studied by X-ray diffraction, HRTEM, EDS, Raman scattering, transmittance, and photoluminescence (PL).

10.2 Experimental

$CdSe_{1-y}S_y$ was deposited by chemical bath deposition (CBD), technique which requires no a special growth atmosphere, the used deposition temperature is low. With this technique it is possible to obtain large areas of film, thickness control, and also highly reproducible results [14]. The growth technique requires during the reactions: control of physical and chemical parameters such as mechanical stirring, temperature, concentration of chemical reagents, pH, and adequate volume ratio. With these experimental conditions it is possible to obtain polycrystalline thin films on different substrate types. The feasibility of this technique for its environment is: deposit short time, it does not require high temperatures, there is no emission of toxic gases and the preparation of the solutions is carried out on micro scale. The nanofilms were deposited on substrates of corning glass at a temperature (T_d) of $20 \pm 2\,°C$ and the deposit time was 30 min. Deionized water of 20 MΩ-cm was utilized to prepare the aqueous solutions that are composed by C_dCl_2 [0.01 M], KOH [0.1 M], $SeC(NH_2)_2$ [0.1 M], and NH_4NO_3 [0.1 M]. Systematically, it was adding thiourea ($SC(NH_2)_2$) [0.2 M]. The selenourea ($SeC(NH_2)_2$) solution was prepared in an argon inert atmosphere, because it is unstable under laboratory conditions and should be maintained at a temperature of 4 °C to avoid chemical decomposition. For carrying out the intentional doping by sulfur of the deposited layers are added small thiourea volumes to the growth solution in the range of 0 to 30 mL to obtain different sulfur concentrations in the nanostructures, which are presented in Table 10.1. The Cd, Se, and S concentrations in $CdSe_{1-y}S_y$ samples were estimated by means of energy dispersive spectroscopy (EDS).

The $CdSe_{1-y}S_y$ films chemical stoichiometry was obtained by energy dispersive spectrometry (EDS) that was carried out in a System LEO 438VP, with W.D. of 26 mm using a pressure of 20 Pa. The crystalline phase and structure of the films were determined with a Bruker D8 Discover diffractometer using the copper Kα radiation ($\lambda = 1.5406$ Å) at 40 kV and 40 mA with parallel beam geometry.

Table 10.1 Summary of the $CdSe_{1-y}S_y$ samples grown and studied in this work and the doping volume added to each one

Sample	$SC(NH_2)_2$ added volume (mL)	Cd molar fraction	Se molar fraction	S molar fraction
M100	00	49.11	50.89	0.00
M205	05	56.40	26.96	16.64
M310	10	57.76	20.20	22.08
M415	15	55.54	18.23	26.23
M520	20	53.76	12.62	33.62
M625	25	55.76	4.46	39.78
M730	30	55.48	2.39	42.13

High-resolution transmission electron microscopy (HRTEM) studies were carried out in a JEOL JEM200 of 80–200 kV, the obtained image is recorded with a CCD camera in real time. The Gatan Digital Micrograph software was used for the analysis of HRTEM images. Raman scattering experiments were performed at room temperature using the 6328 Å line of a He–Ne laser at normal incidence for excitation. The light was focused to a diameter of 6.0 μm on the sample using a 50× (numerical aperture 0.9) microscope objective. The nominal laser power used in these measurements was 20 mW. Scattered light was analyzed using a micro-Raman System (Labram model of Dilor), a holographic notch filter made by Kaiser Optical System, Inc. (model superNotch-Plus), a 256 × 1024-pixel CCD used as detector cooled to 140 K using liquid nitrogen, and two interchangeable gratings (600 and 1800 g/mm). Typical spectrum acquisition time was limited to 60 s to minimize the sample heating. Room temperature photoluminescence was taken with a solid-state laser (325 nm) with 60 mW as excitation source and a SCIENCETECH 9040 monochromator was used to perform the sweep of wavelength at room and low temperature in a CRYOGENICS cryostat.

10.3 Results and Discussion

10.3.1 X-ray Microanalysis (EDS)

The chemical composition of the $CdSe_{1-y}S_y$ samples was estimated by EDS, which besides allows to know the presence of any unintentional impurities. Figure 10.1 shows the EDS spectra of typical samples, M100 and M730, which indicate the presence of oxygen in the samples along with cadmium, selenium, and sulfur.

The EDS spectra indicate that besides Cd, Se, and S, the samples contain a significant amount of silicon, potassium, calcium, sodium, and oxygen, and other residual impurities, which come from the substrate. By XPS analysis, in other materials such as ZnS, it has been showed that oxygen ions are present in the

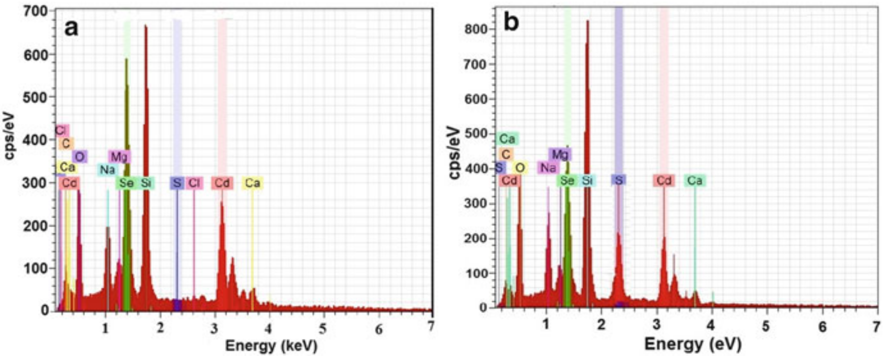

Fig. 10.1 EDS spectra of two CdSeS typical samples, M100 and M730. The spectra indicate that the samples contain a significant amount of residual impurities come from the substrate

samples in the form of O^{2-} ions that may produce CdO in the sample [15]. Since the temperature during synthesis and air drying in the present case is low, this conversion may have happened only at a very low percentage so that the presence of CdO could not be detected by XRD measurements, as will be seen below. However, these oxygen ions can form trap levels in the band gap, resulting in several transitions contributing to luminescence. Thus, it appears that oxygen has replaced sulfur or selenium at a few random points of the CdSeS lattice. The results of such measurements for the cadmium, selenium, and sulfur are shown in Table 10.1. From these results it is observed that the samples do not have a good stoichiometry and that they have a greater presence of cadmium in the material and an absence of sulfur and selenium. Considering that each unit cell contains two Cd atoms and two sulfur and selenium atoms, then when a stoichiometric deviation of ideal unit cell occurs it could establish a correspondence between vacancies or interstices of some of the elements (V_{Cd}, V_{Se}, V_S, Cd_i, Se_i, S_i). From Table 10.1 one can observe that the samples contain lower sulfur and selenium concentrations, which indicate that they have a higher structural defects concentration as is this case of the present work, where there are excess of II element and lack of VI elements.

10.3.2 X-ray Diffraction

Figure 10.2a shows the XRD diffractograms of the $CdSe_{1-y}S_y$ nanostructures deposited with different sulfur molar fractions, which have similar diffractograms. Figure 10.2b shows the deconvolution into individual components (Gaussian shape) of two typical polycrystalline films that are the extreme cases for sulfur molar fractions, M100 and M730 samples, which present five peaks that will be discussed below. It is observed from XRD patterns that $CdSe_{1-y}S_y$ deposited films are in nature polycrystalline whose crystalline phase is hexagonal wurtzite, which shows

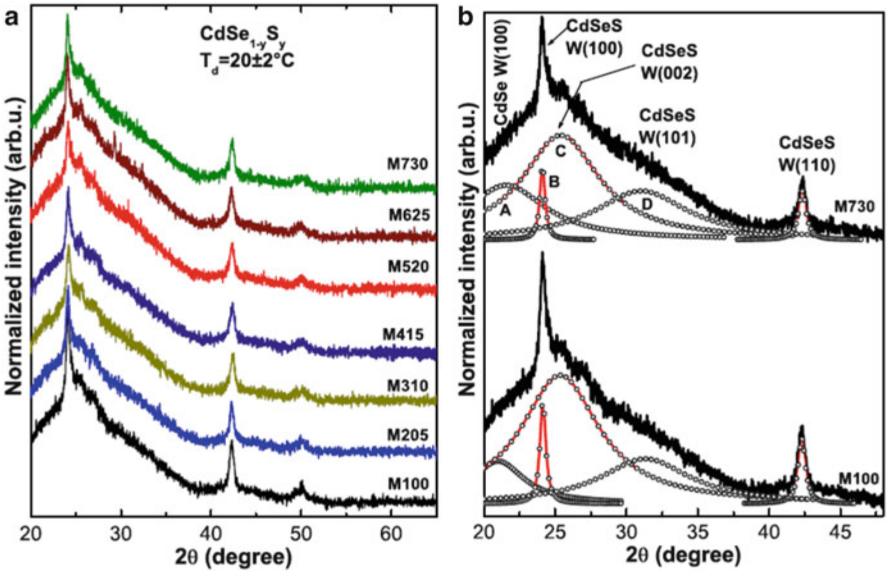

Fig. 10.2 (**a**) X-ray patterns of $CdSe_1{-}yS_y$ nanofilms with different S concentrations. (**b**) It shows the deconvolution of X-ray diffractograms of two typical samples: M100 and M730

a preferential growth in the (002) direction, besides there are other important peaks in the (110) and (112) directions. The X-ray patterns of deposited $CdSe_{1-y}S_y$ thin films are described in the *P63mc* (*186*) and whose lattice parameters were calculated using the software DICVOL04, obtaining the following average lattice constant values CdSe: $a = 4.178$ Å and $c = 6.972$ Å, which are in agreement with the reported values [16, 17].

All of the products displayed the XRD peaks corresponding to wurtzite (JCPDS-ICDD X-ray diffraction cards numbers 19-191 and 8-459, for cubic and hexagonal phases of CdSe, respectively) and no characteristic diffraction peaks arising from the possible impurity phases such as S and CdO were observed, indicating the preparation of pure wurtzite samples. In all cases the diffractograms present the same X-ray diffractions and some of them can be assigned as shown in Fig. 10.2b.

Besides, it is observed a widening at the peak of the preferential W(002) direction, which could be caused by undergoing stress, size of small crystalline domain, or fluctuations in concentration. The first case does not happen since the used substrates are amorphous and they do not produce a mismatch in the lattice constants. The variation in the size of the average domain crystalline is responsible for this widening. The mean grain size was calculated from hexagonal wurtzite (002) diffraction of $CdSe_{1-y}S_y$ for all the studied samples, which are shown in Table 10.2. Figure 10.2b shows the deconvolution of X-ray diffractograms of the samples M100 and M730 that were deposited with 0 and 30 mL of thiourea in the growth solution. The crystallite sizes ($D_{(hkl)}$) were calculated from the line broadening of the X-ray

Table 10.2 Mean grain sizes of the nanostructures obtained by Debye–Scherrer equation and the distance interplanar and optical band gap energies obtained by transmittance

Sample	a (Å)	c (Å)	$d_{(002)}$(Å)	$d_{(100)}$(Å)	Grain Size (nm)	Band gap (eV)
M100	4.173	6.971	3.510	3.720	1.48	1.87
M205	4.195	6.983	3.438	3.661	1.21	2.05
M310	4.191	7.025	3.501	3.708	1.20	1.91
M415	4.120	6.942	3.485	3.690	1.41	1.89
M520	4.172	6.776	3.469	3.708	1.68	1.89
M625	4.186	6.773	3.469	3.672	1.56	2.06
M730	4.134	6.801	3.485	3.708	1.59	2.16

diffraction peaks at 2θ using the Debye–Scherrer equation, $D_{(\mathrm{hkl})} = n\lambda/\beta\cos\theta$ [18, 19]. In a tetragonal structure, there are two parameters, $a = b$ and c, that have to be calculated. The lattice parameters of $\mathrm{CdSe}_{1-y}\mathrm{S}_y$ and the grain sizes calculated using the Debye–Scherrer equation are presented in Table 10.2. As is observed in Table 10.2, as shown in Table 10.2, there is little variation in the grain size despite the wide variation in the S mole fraction, having an average grain size of 1.41 nm for the first five samples and the last two are increased slightly. These values indicate that there is a high quantum confinement because the grain sizes are smaller than the Bohr radii of binary compounds, Bohr radii of CdS (2.8 nm) and CdSe (4.9 nm). Table 10.2 shows the mean grain sizes of the nanostructures obtained by the Debye–Scherrer equation for the direction W(002), which shows the dependence of the grain size of the average crystalline domain based on the increase of sulfur molar fraction for the $\mathrm{CdSe}_{1-y}\mathrm{S}_y$ system. Additionally, it is shown the distance interplanar and optical band gap energies obtained by transmittance.

10.3.3 High-Resolution Transmission Electron Microscopy

Figure 10.3 illustrates the images obtained by high-resolution transmission electron microscopy (HRTEM) for two typical samples, M625 and M730, and insets are the results of the processing of the HRTEM images using filters in Fourier space. There is a crystal structure of nearly spherical shape of the material with an average size of 6.3 and 7.16 nm, in addition in the insets can see clearly the distance interplanar of material, about 0.371 nm, which corresponds to the direction of the hexagonal phase of the CdSeS (100).

As can be seen, the results obtained by HRTEM are in good agreement with the results calculated from X-ray diffraction for grain size and interplanar distance and the differences are due to the used approximations and the equipment limitations.

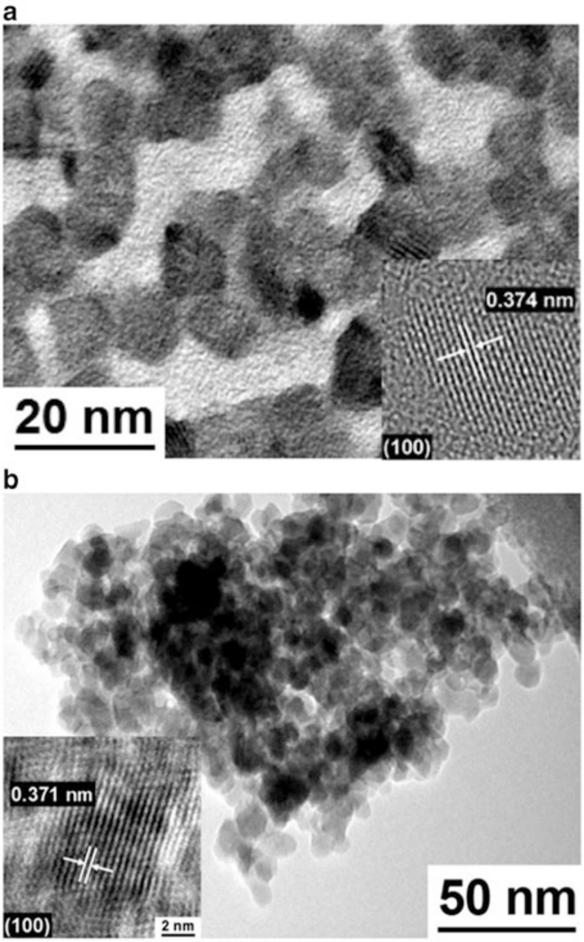

Fig. 10.3 HRTEM micrographs of typical $\mathrm{CdSe}_y\mathrm{S}_{1-y}$ samples for two: (**a**) M625 and (**b**) M730

10.3.4 Raman Spectroscopy

Back scattering geometry has been used to record the Raman spectra of all $\mathrm{CdSe}_{1-y}\mathrm{S}_y$ samples, which are shown in Fig. 10.4. As can be observed in figure all Raman spectra are similar, i.e., the Raman spectra do not depend strongly on the sulfur concentration in the layer. Figure 10.5 shows the Raman spectra of three samples: M100, M205, and M730, which were grown with zero, the lower and higher thiourea volume in the growth solution. Raman spectrum of the sample M730 features an asymmetric fundamental Raman band at around 208 cm^{-1}. The spectrum can be deconvoluted in six Lorentzian line shape signals, which are observed at 187, 209, 272, 377, 417, and 601 cm^{-1}. The dominant mode at 209 cm^{-1} is observed nearly at frequency of 1LO-CdSe, see Fig. 10.5a, by which is associated to the first order CdSe longitudinal optical phonon like (CdSe-1LO-like) in hexagonal wurtzite

Fig. 10.4 Raman spectra of the $CdSe_{1-y}S_y$ films by adding different sulfur volumes deposited at the temperature of 20 ± 2 °C

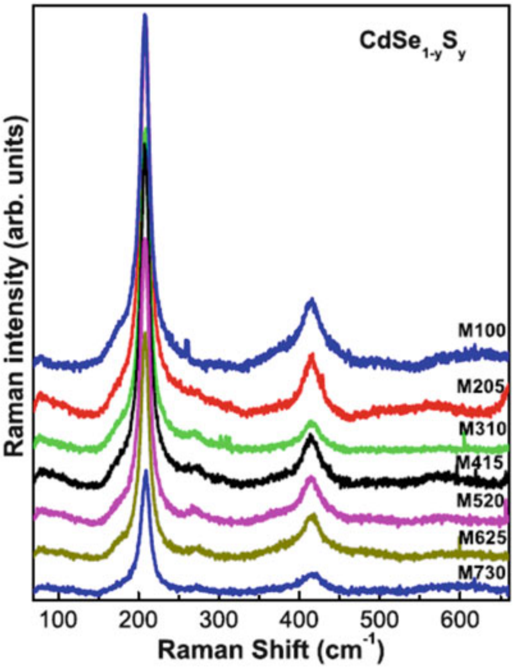

Fig. 10.5 Decomposition of the Raman spectra into individual components for three samples: (**a**) M100, (**b**) M205, and (**c**) M730. The *dashed lines* are their respective fitting

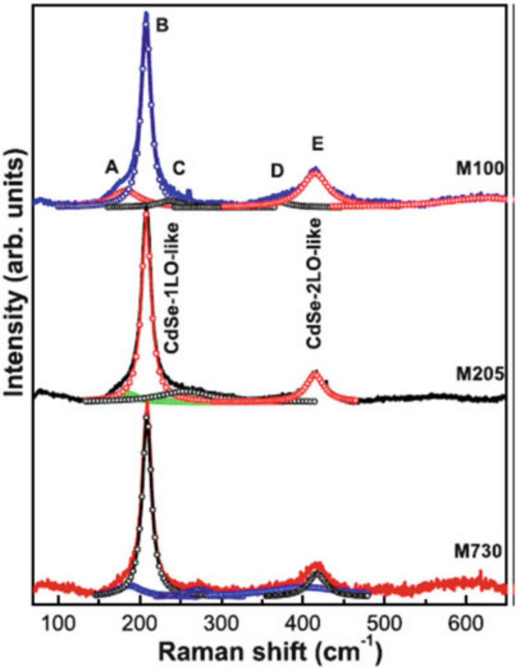

phase [16, 20]. In the same way, the Raman mode corresponding to the low-energy shoulder (187 cm^{-1}) originates from surface optical phonon modes (SO) [21, 22]. The feature at the high-energy shoulder, observed at 272 cm^{-1}, is the subject of a recent study by Dzhagan et al. [23], who suggest that it is resulted from the participation of acoustic phonons to the scattering process but is notorious for its Raman shift at higher frequencies. The Raman band at 417 cm^{-1} is associated with the second longitudinal optical mode like of the CdSe (CdSe-2LO-like) [16]. On the other hand, the bands observed around 400 and 600 cm^{-1} are overtones of the fundamental Raman band. Finally, the modes observed at 377 and 601 cm^{-1} correspond to the second and third phononic replica of the SO mode, 2SO and 3SO, respectively. The Raman intensity of the CdSe-1LO-like and CdSe-2LO-like bands decreases with the increase of thiourea compound concentration in growth solution, as can see in Fig. 10.5. From Fig. 10.5 it is observed that the CdSe-1LO-like Raman line is not only broadened, but it also shows an asymmetric broadening towards the low frequency side. Besides, the frequency of the 1LO-like peaks does not undergo any Raman shift by the thiourea volume increase in the samples but their FWHMs have decreased noticeably compared to that of the M205 (M100) sample FWHM. It is now well known that confinement of phonons, optical as well as acoustic, influences the phonon spectra conspicuously when the grain size falls to a few nanometers. Confinement of optical phonons causes an asymmetry in the line shape and a shift towards the low frequency side compared to that for bulk CdSe.

10.3.5 Transmittance

The transmittance spectra in the visible and infrared ranges are recorded for the $\text{CdSe}_{1-y}\text{S}_y$ films in the wavelength range of 400–1100 nm, which were measured at room temperature. The effect of sulfur added in the nanolayers on the optical properties including percentage of transmittance (% of T) and band gap energy (E_G) was studied in detail. The transmittance observed of the CdSe film in the visible range varies from about 0 up to nearly 60 % (without considering the substrate contribution) and it is higher of all shown transmittance spectra. The sharp reduction in the transmittance spectra at the wavelengths lower than 600 nm is due to the fundamental absorption edges of the different films. The $\text{CdSe}_{1-y}\text{S}_y$ transmittance decreases lightly as the sulfur molar fraction is increased, see Fig. 10.6. This causes the slight blue shift in optical band gap energy, which confirms the formation of $\text{CdSe}_{1-y}\text{S}_y$ with increasing y. It is observed from the transmittance spectra that the absorption edges are also slightly shifted towards the higher energy region for the films with higher sulfur molar fraction. The optical band gap (E_G) of a semiconductor is related to the optical absorption coefficient (α) and the incident photon energy ($h\nu$). The absorption coefficient α for a film of thickness d and reflectance R is determined near the absorption edge using the simple relation: $\alpha = \ln\left\{(1-R)^2/T + \left[\left(\left(1-R^2\right)/2T\right)^2/+R^2\right]^{1/2}\right\}/d$, where multiple reflections are

Fig. 10.6 Transmittance spectra of $CdSe_{1-y}S_y$ nanofilms measured at room temperature

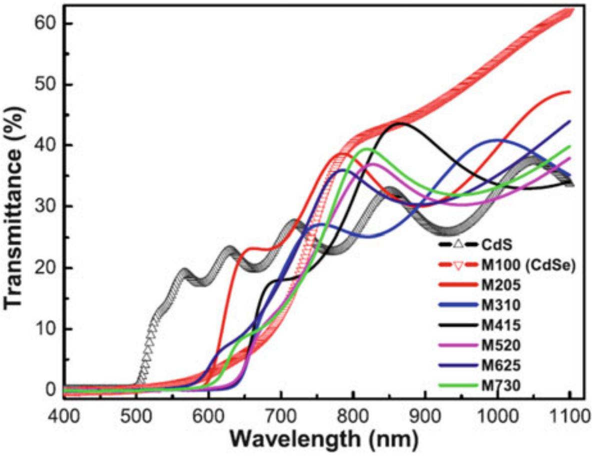

taken into, but interference neglected. Actually a transmission interference pattern could be observed in most samples, and was used to obtain an accurate value for the thickness d. The optical band gap of CdSeS has been evaluated from the transmittance spectrum using the Tauc relation [18, 19, 24]: $\alpha h\nu = (E_G - h\nu)^n$, where n depends on the kind of optical transition that prevails. Specifically, n is 1/2 and 2 when the transition is directly and indirectly allowed, respectively. The CdSeS film is known to be a semiconductor with a directly allowed transition, therefore $n = 1/2$. The $CdSe_{1-y}S_y$ average band gaps, which were estimated from the linear portion of the $(\alpha h\nu)^2$ vs $h\nu$ (see inset of Fig. 10.7), are shown in Table 10.2 and Fig. 10.7. The band gap energies were higher than the value of bulk wurtzite CdSe (1.74 eV) [25] due to quantum confinement of CdSe nanocrystals. The optical band gap of the CdSe film is of 1.86 eV that corresponds to pure CdSe and is 140 meV higher than band gap in CdSe bulk. This discrepancy is associated with the average grain size [19, 24]. For sample M730 its optical bandgap is increased slightly about 300 meV compared to the bandgap of the sample M100, which can be related to sulfur incorporation to the molecule and the average grain size, as can see in Fig. 10.7. This band gap increase can be explained due to the substitution in the lattice of selenium atoms (ionic radii ~1.98 Å) by sulfur atoms that are smaller (ionic radii ~1.84 Å).

10.3.6 Room Temperature Photoluminescence

Figure 10.8 illustrates the room temperature photoluminescence spectra of the $CdSe_{1-y}S_y$ films studied. Figure 10.9 shows the room temperature photoluminescence spectra of three typical $CdSe_{1-y}S_y$ samples: M100, M205, and M730. The photoluminescence spectrum of the M100 sample shows two dominant broad bands,

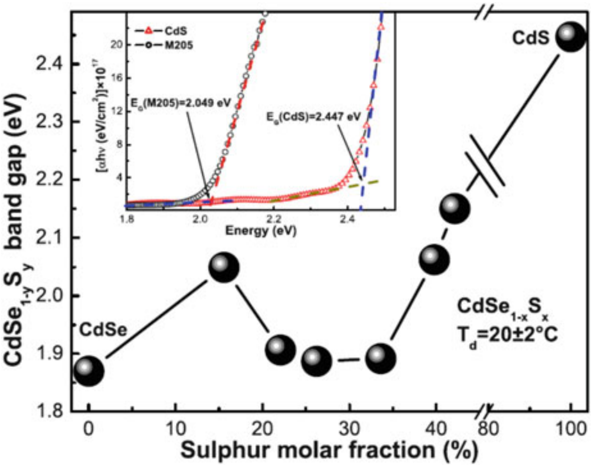

Fig. 10.7 It shows the band gap energy as a function of the sulfur molar fraction. The inset shows Tauc plot of CdSeS samples to two different molar fractions: (**a**) $x = 21.54\,\%$ and (**b**) $x = 100\,\%$

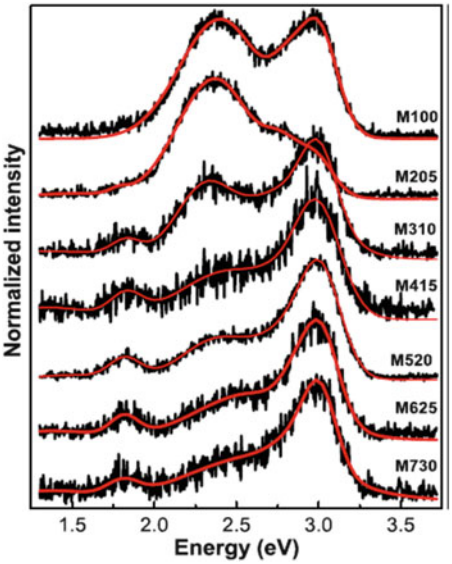

Fig. 10.8 It illustrates the room temperature photoluminescence spectra of the $CdSe_{1-y}S_y$ samples grown with different S molar fractions

which through a standard fitting procedure performed in the interval 1.3–3.75 eV, such bands can be deconvoluted in three Gaussian line shape signals as are shown in Fig. 10.9 observed at 2.99, 2.80, and 2.40 eV. As is observed in Figs. 10.8 and 10.9 the radiative bands depend strongly on the sulfur concentrations incorporated in the layers. The main radiative band at 3.00 eV is associated with an exciton bound to a donor level [26]. The others are wide bands, observed in the violet, blue, and red regions of the visible spectrum at 2.80 and 2.40 eV and are associated with emissions due to impurity levels. The broad bands indicate that these defect-related luminescence peaks are caused by radiative transitions between selenium (sulfur) vacancies or Cd interstitials acting as shallow donors and Cd vacancies

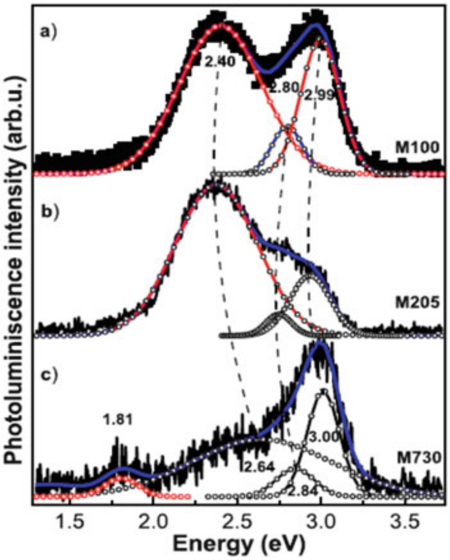

Fig. 10.9 Deconvolution of the photoluminescence spectra into individual components for three sulfur molar fractions. The *dashed lines* are merit-figures to follow the behavior of the radiative bands

acting as deep acceptors. This recombination mechanism competes with the exciton-related luminescence and seems to depend on the stoichiometry and the preparation conditions of the CdSeS films rather than on their microstructure [27, 28] as is shown in Fig. 10.9. Starting from the photoluminescence spectrum of the M100 sample (CdSe), which shows that the main radiation bands depend strongly on the sulfur molar fraction in the layers, because with its increase excitonic band becomes dominant and shifts slightly at higher energies. Violet emission observed at 2.80 eV for low molar fraction shifted at 2.84 eV for high molar fraction and the green band at 2.40 eV is displaced to blue by 24 meV. Finally, the red emission band at 1.81 eV shifted to blue with increase of sulfur molar fraction in layers. As is observed in Fig. 10.7, the band gap energy of $CdSe_{1-y}S_y$ is between 1.86 and 2.16 eV, and radiative transitions are observed at higher energies, therefore these are associated with the grain size and the quantum confinement. The band gap values were higher than the value of bulk $CdSe_{1-y}S_y$ due to quantum confinement of $CdSe_{1-y}S_y$ nanocrystals [19]. As is observed in Fig. 10.8, excitonic band is lightly blue shifted for all samples. This phenomenon was likely due to the quantum confinement effect of the CdSeS nanocrystals [29], whose diameters are several nanometers,

This quantum confinement effect can be clearly explained using the particle energy relation of the three dimensional single-particle box [24]: $E = \mathrm{D}\left(n_x^2/x^2 + n_y^2/y^2 + n_z^2/z^2\right)$, where D is a constant; n_x, n_y, n_z are the quantum number and x, y, z are the scales in each dimension. Apparently, a decreased x, y, z values (the diameters of $CdSe_{1-y}S_y$ particles) leads to an increased energy E. The reduction of diameters of the particles produces a blue shift of the band edge. This is a good demonstration of the quantum confinement effect in the nanoparticles and other 0D nanostructure [30, 31]. Hence, it is critically important to synthesize the $CdSe_{1-y}S_y$ nanoparticles of a size comparable with Bohr radius and of a narrow size distribution in order to ensure the occurrence of the quantum confinement [31]. Cadmium selenium has a low exciton Bohr radius (4.9 nm) and cadmium sulfide has a low exciton Bohr radius (2.8 nm). These values are comparable to grain size of the nanoparticles, whose values were estimated by X-ray diffraction.

10.4 Conclusions

Heat-treating an API 5L X-65 pipe steel to 1050 °C for 30 min following water cooling yields an acicular ferrite microstructure with a mechanical strength 200 MPa larger than the as-received steel. Although hardness also increases, the average value is below the recommended to avoid susceptibility to SSC. The results obtained with the non-conventional heat treatment yield similar properties to an API 5L X-80 steel, however the high hardness of this steel prevents its use with sour hydrocarbons. The findings of this study imply that it is possible to reduce the wall thickness of pipelines to transport crude oil while maintaining its resistance to SSC.

Acknowledgements The authors would like to thank CONACYT for financial support and the IIM-UMSNH for technical support.

References

1. Xu F, Ma X, Kauzlarich SM, Navrotsky A (2009) Enthalpies of formation of CdSxSe1–x solid solutions. J Mater Res 24:1368–1374
2. Mujica A, Rubio A, Muñoz A, Needs RJ (2003) High-pressure phases of group-IV, III–V, and II–VI compounds. Rev Mod Phys 75:863–912
3. Pattabi M, Uchil J (2000) Synthesis of cadmium sulphide nanoparticles. Sol Energy Mater Sol Cell 63:309–314
4. Ullal HS, Stone JL, Zweibel K, Surek T, Mitchell RL (1992) Polycrystalline thin-film solar cells and modules. In: 6th International photovoltaic science & engineering conference, New Delhi, India 10–14 February 1992
5. Morales-Acevedo A (2006) Can we improve the record efficiency of CdS/CdTe solar cells? Sol Energy Mater Sol Cells 90:2213–2220
6. Gordillo G (1995) Preparation and characterization of CdTe thin films deposited by CSS. Sol Energy Mater Sol Cells 37:273–281
7. Switzer JA, Hodes G (2010) Electrodeposition and chemical bath deposition of functional nanomaterials. MRS Bull 35:743–749
8. Kozhevnikova NS, Vorokh AS, Uritskaya AA (2015) Cadmium sulfide nanoparticles prepared by chemical bath deposition. Russ Chem Rev 84:225–250
9. Hodes G (2003) Chemical solution deposition of semiconductor films. Marcel Dekker, Inc. New York
10. Kaur I, Pandya DK, Chopra KL (1980) Growth kinetics and polymorphism of chemically deposited CdS films. J Electrochem Soc 127:943–948

11. Froment M, Lincot D (1995) Phase formation processes in solution at the atomic level: metal chalcogenide semiconductors. Electrochim Acta 40:1293–1303
12. Ó Brien P, McAleese J (1998) Developing an understanding of the processes controlling the chemical bath deposition of ZnS and CdS. J Mater Chem 8:2309–2314
13. Nakada T, Mizutani M (2002) 18% Efficiency Cd-free Cu(In, Ga)Se2 thin-film solar cells fabricated using chemical bath deposition (CBD)-ZnS buffer layers. Jpn J Appl Phys 41:L165–L167
14. Nair MTS, Nair PK, Zingaro RA, Meyers EA (1993) Enhancement of photosensitivity in chemically deposited CdSe thin films by air annealing. J Appl Phys 74:1879–1884
15. Radhu S, Vijayan C (2011) Observation of red emission in wurtzite ZnS nanoparticles and the investigation of phonon modes by Raman spectroscopy. Mater Chem Phys 129:1132–1137
16. Beserman R, Balkanski M (1970) Vibrational properties of mixed CdSxSe1-x. Phys Rev B 1:608–613
17. Kandasamy K, Singh HB, Kulshreshtha SK (2009) Synthesis and characterization of CdS and CdSe nanoparticles prepared from novel intramolecularly stabilized single-source precursors. J Chem Sci 121:293–296
18. Loghman-Estarki MR, Hajizadeh-Oghaz M, Edris H, Razavi RS (2013) Comparative studies on synthesis of nanocrystalline Sc2O3–Y2O3 doped zirconia (SYDZ) and YSZ solid solution via modified and classic Pechini method. Cryst Eng Comm 15:5898-5909
19. Mohammadikish M, Davar F, Loghman-Estarki MR (2013) Low temperature preparation of 3D solid and hollow ZnS nanosphere self-assembled from nanoparticles by varying sulfur source. J Clust Sci 24:217–231
20. Hayek M, Brafman O (1971) In: International conference on light scattering in solids, París, p 76
21. Comas F, Studart N, Marques GE (2004) Optical phonons in semiconductor quantum rods. Solid State Commun 130:477–480
22. Lange H, Artemyev M, Woggon U, Thomsen C (2009) Geometry dependence of the phonon modes in CdSe nanorods. Nanotechnology 20:045705 (5pp)
23. Dzhagan VM, Lokteva I, Valakh MY, Raevska OE, Kolny-Olesiak J, Zahn DRT (2009) Spectral features above LO phonon frequency in resonant Raman scattering of small CdSe nanoparticles. J Appl Phys 106:084318–084318-6
24. Davar F, Loghman-Estarki MR, Ashiri R (2015) From inorganic/organic nanocomposite based on chemically hybridized CdS–TGA to pure CdS nanoparticles. J Ind Eng Chem 21:965–970
25. Madelung O (2004) Semiconductors data handbook. Springer, Berlin, pp 815–835
26. Ju Seo D (2004) Structural and optical properties of CdO films deposited by spray pyrolysis. J Korean Phys Soc 45:1575–1579
27. Jin BJ, Woo HS, Im S, Bae SH, Lee SY (2001) Relationship between photoluminescence and electrical properties of ZnO thin films grown by pulsed laser deposition. Appl Surf Sci 169–170:521–524
28. Riehl N (1981) Intrinsic defects and luminescence in II–VI-compounds. J Lumin 24–25(Part 1):335–342
29. Zeng JY (1991) Introduction to quantum mechanics. Peking University Press, Beijing
30. Wolf EL (2004) Nanophysics and Nanotechnology: An Introduction to Modern Concepts in Nanoscience, Wiley, Weinheim, p 63
31. Jiang Z, Sun H, Qin Z, Jiao X, Chen D (2012) Synthesis of novel ZnS nanocages utilizing ZIF-8 polyhedral template. Chem Commun 48:3620–3622

Part V
Characterization of Materials Obtained by Mechanical Milling

This part includes two chapters related to the characterization of materials obtained by mechanical milling technique.

The first chapter presents a study to characterize magnetic properties and kinetics of crystallization in amorphous $Sm_xGd_{1-x}Co_5$ alloys obtained by mechanical milling. Johnson–Mehl–Avrami model was used to study the kinetics of crystallization in the transformation of phase amorphous-crystalline by the amorphous $Sm_{0.6}Gd_{0.4}Co_5$ alloys obtained by mechanical milling. The results showed that magnetic properties of $Sm_{0.6}Gd_{0.4}Co_5$ alloys in amorphous state are better than crystalline alloys due to the rapid grain size refinement. The results of this work demonstrate that nanocrystalline alloys of rare earth and transition metals have greatly attracted attention for use as permanent magnets due to their good magnetic properties.

The second chapter presents the synthesis of nanopowders obtained from a binary mixture of powders of Pb (50 μm) and Sn (50 μm), which were prepared by mechanical milling. The study of mechanical milling mechanism in eutectic nanopowders was analyzed. The chemical reactions traced during both high-energy milling (HEM) and thermal annealing present significant changes. These results reveal that different chemical reaction paths, HEM and thermal-process, drive the eutectic nucleation. The eutectic behavior as a function of milling time and the size of nano-heterogeneities allow the possibility of studying the mechanisms of eutectic nucleation. This study is an attempt to discern the nano-heterogeneities role to promote a rapid eutectic nucleation.

The main techniques used in the characterization of these materials are:

- X-ray diffraction.
- Differential scanning calorimetry (DSC).
- Scanning electron microscopy (SEM).
- Energy dispersive spectroscopy (EDS).

Chapter 11

Magnetic Properties and Kinetic of Crystallization in Amorphous $Gd_xSm_{1-x}Co_5$ Alloys Obtained by Mechanical Milling

J.L. Hidalgo, J.T. Elizalde, and J.A. Matutes

Abstract Alloys with nominal $Gd_{0.4}Sm_{0.6}Co_5$ composition were prepared by arc melt. X-ray diffraction patterns from the as-cast ground alloy were indexed with a $CaCu_5$-type hexagonal structure. Later the alloys were milled using different milling times, and after of 240 min of mechanical milling, the amorphous state of $Gd_{0.4}Sm_{0.6}Co_5$ was reached. The Johnson–Mehl–Avrami model is used in the study of kinetics of crystallization in the transformation of phase amorphous-crystalline by the amorphous $Gd_{0.4}Sm_{0.6}Co_5$ alloys obtained by mechanical milling. The partial substitution of Sm by Gd in nanocrystalline and/or amorphous $Sm_xGd_{1-x}Co_5$ obtained by mechanical milling technology is of vital importance as to partially or completely replace the Gd-Sm alloys $Sm_xGd_{1-x}Co_5$ is possible to increase the magnetization of saturation which is very important for their possible application as a permanent magnet. The magnetic properties were measured using a vibrating sample magnetometer and the magnetic properties by the alloys of $Gd_{0.4}Sm_{0.6}Co_5$ in the amorphous state are better than crystalline alloys due to the rapid grain size refinement.

Keywords Magnetic • Crystallization • Mechanical milling • Kinetic • Nucleation

---

J.L. Hidalgo (✉)
Instituto Tecnológico Superior Poza Rica, Luis Donaldo Colosio S/N. Arroyo del Maíz, 92330
Poza Rica, Veracruz, México
e-mail: hidalgogonzalezjoseluis@gmail.com

J.T. Elizalde
Departamento de Ciencias Básicas, Instituto de Ingeniería y Tecnología, Universidad Autónoma de Ciudad Juárez, Av. Del Charro #460 Norte, 3231 Cd. Juárez, Chihuahua, Mexico

J.A. Matutes
Centro de Investigación en Materiales Avanzados, S. C., Miguel de Cervantes 120, Complejo Industrial Chihuahua, 3112 Chihuahua, Mexico
e-mail: jose.matutes@cimav.edu.mx

R. Pérez Campos et al. (eds.), *Characterization of Metals and Alloys*, DOI 10.1007/978-3-319-31694-9_11

11.1 Introduction

Nanocrystalline alloys of rare earth and transition metal have greatly attracted attention for use as permanent magnets due to their good magnetic properties such as high anisotropy field and high Curie temperature in alloys $SmCo_5$ [1]. This kind of alloy has a hexagonal close-packed crystal structure of $CaCu_5$ type in which rare earth elements are surrounded by a hexagon of cobalt atoms [2]. Some researchers have studied the magnetic and structural properties of alloys of the $CaCu_5$ type where Sm is partially replaced by other rare earth elements, such as Pr, obtaining high coercivities (0.95 MA/m). However, few studies have been made regarding the partial substitution of Sm by Gd [3]. Also $GdCo_5$ alloys are of great scientific interest because nocolinearidades induced field can be directly observed magnetization curves and ferrimagnetic structure is broken in spin flop field of 67 T [4]. In this type of single-phase nanocrystalline alloy, some interesting phenomena include the increase of the remanence due to exchange interactions [5], the behavior of the magnetic properties versus temperature [6], and the enhancement of the Curie temperature due to the exchange interaction [7]. In some other occasions, this type of alloy is used for formation of nanocomposites composed of two phases, one hard phase and one soft magnetic phase, in which the behaviorcommonly known as spring magnet is studied by measuring recoil curves [8]. These phenomena mentioned above are very interesting; however, to study this type of alloy, it is necessary to start with a nanocrystalline alloy, often one that is in an amorphous state and will subsequently be nanocrystallized through the implementation of various heat treatments [9]. Interestingly, this type of alloy is not well studied from the amorphous state, which is very important because, for example, the properties of a material in the crystalline state are very different from the properties of a material in a nanocrystalline state and/or amorphous state. For example, an amorphous alloy exhibits high corrosion resistance, high electrical resistivity, high resistance to plastic deformation, and an increase in magnetization [10]. Such alloys are obtained through different methods like sintering, melt spinning, and mechanical milling [11–14]. Interestingly, most of the aforementioned studies have not examined the effects of structural disorder on the properties of teh solid state. Such studies can be performed using crystallization kinetics, for which the technique of differential scanning calorimetry (DSC) can be used to know the temperature of crystallization and to obtain the activation energy [15]. Moreover, through this technique, studies of the kinetics of crystallization of amorphous materials can be performed by applying the equation of Johnson, Mehl, and Avrami (JMA) in which the exponent "n" of the JMA is determined and normally provides information related with the nucleation process and growth of the studied transformation, which is important because the nanocrystallization of an amorphous alloy can have different forms of crystallization, such as polymorphic, eutectic, or primary. The different forms of crystallization are important because, in all three cases, it is necessary to begin with an amorphous alloy of one phase, and then crystallize in alloy of one or two phases with the same starting composition or a different starting composition. This work studies the kinetics of crystallization and magnetic properties of crystalline alloys and of amorphous $Gd_xSm_{1-x}Co_5$ obtained by mechanical milling.

11.2 Experimental

11.2.1 Materials

Alloys of $Gd_{0.4}Sm_{0.6}Co_5$ with nominal composition were prepared by melting in an electric arc furnace with a controlled atmosphere of argon (99.9 %). The starting materials were pieces of Gd (Alfa Aesar, 99.9 %), pieces of Sm (Alfa Aesar, 99.9 %), and Co pieces of (Alfa Aesar, 99.5 %). The milling process of the alloys was performed under an atmosphere of argon in a high-energy mill with a Spex 8000 powder ratio balls 1:8. To achieve the amorphous state of the alloy, mechanical milling was conducted for 240 min.

11.2.2 Microstructural Characterization

The X-ray diffraction studies were performed on a Siemens model D5000 Diffractometer with a Cu-radiation Cu-Kα ($\lambda = 1.5406$ Å). Differential scanning calorimetry was carried out on a TA Instruments DSC-2920 with three different heating rates used (4.585, 4.635, and 4.719 K/s). The measure were performed under an atmosphere of argon. The magnetic properties were measured with a vibrating sample magnetometer (VSM) with a maximum applied field of 1.19 MA/m.

11.3 Results and Discussion

11.3.1 Microstructural Characterization

Figure 11.1 showing the X-ray diffraction patterns for the alloy of $Gd_{0.4}Sm_{0.6}Co_5$: (a) as cast and (b) after 240 min of mechanical milling. In order to make a superior characterization, it is necessary to determine some important parameters such as the lattice parameters, unit cell volume, interplanar spacing, space group, and the crystalline structure [16]. Hence, all peaks in the as-cast alloys were indexed with a structure compact hexagonal of type $CaCu_5$ with unit cell (ICSD #102670) and a space group P 6/mmm. The lattice parameters were determined with the following equation:

$$\sin^2\theta = \frac{\lambda^2}{4}\left[\frac{4}{3}\frac{\left(h^2 + hk + k^2\right)}{a^2} + \frac{l^2}{c^2}\right] \tag{11.1}$$

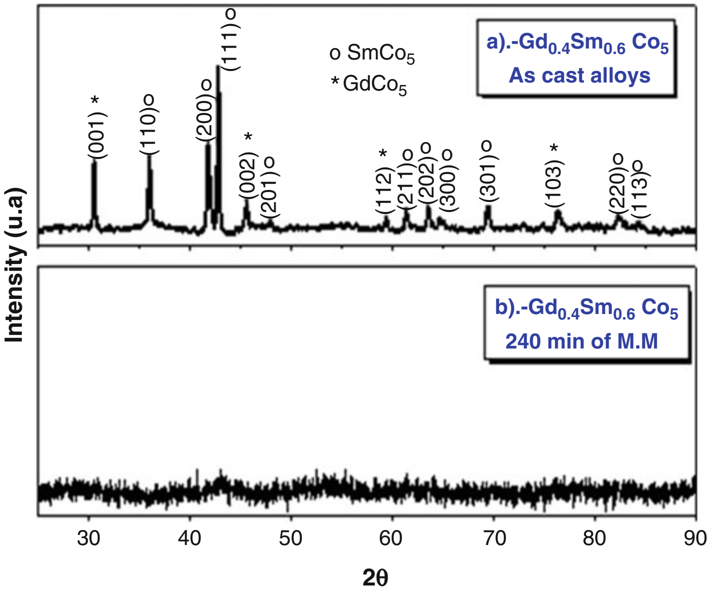

Fig. 11.1 XRD diffraction patterns for the alloy of. $Gd_{0.4}Sm_{0.6}Co_5$: (**a**) as cast; (**b**) after 240 min of mechanical milling

For the packed hexagonal crystal structure of $CaCu_5$ type for the planes {111} and {200} by simultaneous solution of the two normal equations with lattice parameters $a = 0.5039\,\text{nm}$ and $c = 0.3860\,\text{nm}$, the unit cell volume was determined with following equation:

$$\mathrm{V} = \frac{\sqrt{3}}{2}a^2c \tag{11.2}$$

And a value of 84.88 Å was determined; afterward the interplanar spacing was determined to know whether it is a single-phase or two-phase material. The interplanar spacing for each peak was determined with following equation:

$$\frac{1}{d^2} = \left[\frac{4}{3}\frac{\left(h^2 + hk + k^2\right)}{a^2} + \frac{l^2}{c^2}\right] \tag{11.3}$$

It is concluded that the samples obtained for arc melting are samples that have two phases, one for the $GdCo_5$ phase and the other for the $SmCo_5$ phase, indexed with unit cell (ICSD # 43-1382) and (ICSD # 17-0078) respectively. However, to confirm this it is necessary to make a Rietveld refinement of the X-ray powder diffraction pattern. In Fig. 11.1b it is shown that after 240 min of mechanical milling for the as cast $Gd_{0.4}Sm_{0.6}Co_5$ alloy show a characteristic behavior of an amorphous alloy. The size crystal cannot determined of the X-ray diffractions patterns and in order to determine the size crystal it would be necessary to obtain an image of dark field by electron microscopy transmission.

11.3.2 Measurement of Crystallization Temperature

In order to confirm the amorphous state for the $Gd_{0.4}Sm_{0.6}Co_5$ alloy after 240 min of mechanical milling was realized a study of differential scanning calorimetry. Figure 11.2 shows the change in heat flow during the continuous heating for the amorphous $Gd_{0.4}Sm_{0.6}Co_5$ alloy after 240 min of mechanical milling, using a heating rate of 4.5 K/s. A broad peak exothermic is observed with a temperature of 866 K which indicates the nanocrystallization for the amorphous $Gd_{0.4}Sm_{0.6}Co_5$ alloy. The crystallization temperature increases with the increasing heating rate as shown in Table 11.1. For the study of the kinetics of crystallization, DSC was

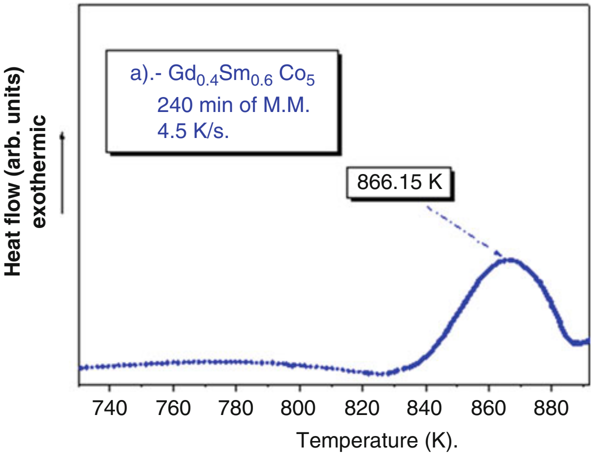

Fig. 11.2 Change in heat flow during the continuous heating for the amorphous of $Gd_{0.4}Sm_{0.6}Co_5$ alloy after 240 min of mechanical milling

Table 11.1 Increases of the crystallization temperature with the increasing heating rate for the amorphous $Gd_{0.4}Sm_{0.6}Co_5$ alloys after 240 min of mechanical milling

Tp (K)	β (K/s)
863.15	4.58
866.15	4.63
873.15	4.71

used by applying the Johnson–Mehl–Avram equation, which is described by the following expression:

$$\tau(t) = 1 - \exp\left(-g \int^{t} \dot{P}(x)\,[\Phi\,(t - x)]^{-q}\,dx\right) \tag{11.4}$$

Where g is a geometric factor, $\dot{P}(x)$ is the nucleation rate of the process, $\Phi(t)$ is the growth rate, and q represents the value of growth type. The previous equations are solved by the Avrami–Erofeev equation that is described by:

$$\tau = 1 - \exp\left(-kt^{\mathrm{n}}\right) \tag{11.5}$$

Where τ represents the value of the fraction transformed, k a rate constant, t the annealing time period, while the exponent "n" of the JMA equation normally provides information related to the nucleation and growth processes of the transformation studied. In this case, a constant random nucleation rate exists and the grow rate is typically not considered because a constant temperature is required through time and space [17, 18]. In this way, the Fig. 11.3 shows the graphical representation of the transformed fraction (τ) versus time for the amorphous $Gd_{0.4}Sm_{0.6}Co_5$ alloys measured with a heating rate of 4.5 K/s. The behavior of the plot (τ) versus time for the amorphous $Gd_{0.4}Sm_{0.6}Co_5$ alloy is a sigmoidal type that is a behavioral characteristic of the transformation kinetics. In this plot, the first part of the transformation is shown when $\tau = t$, where the transformation is dominated by the nucleation process. The second part of the transformation occurs when $t = t^{1/2}$,

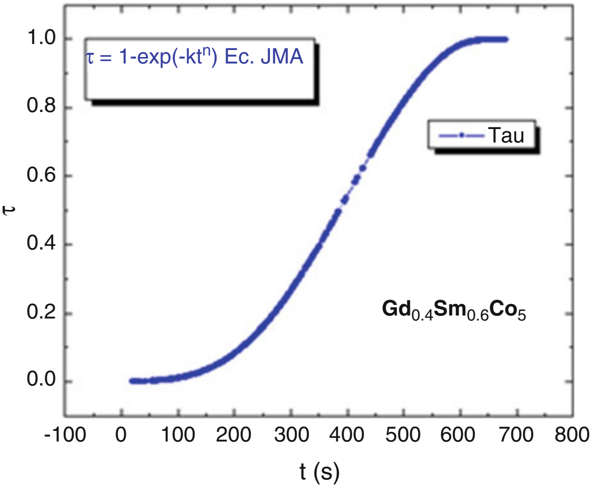

Fig. 11.3 Graphical representation of the transformed fraction (τ) versus time for the amorphous $Gd_{0.4}Sm_{0.6}Co_5$ alloys measured with a heating rate of 4.5 K/s

Fig. 11.4 "Linearize" the JMA equation, for the amorphous $Gd_{0.4}Sm_{0.6}Co_5$ alloys obtained with a heating rate of 4.5 K/s

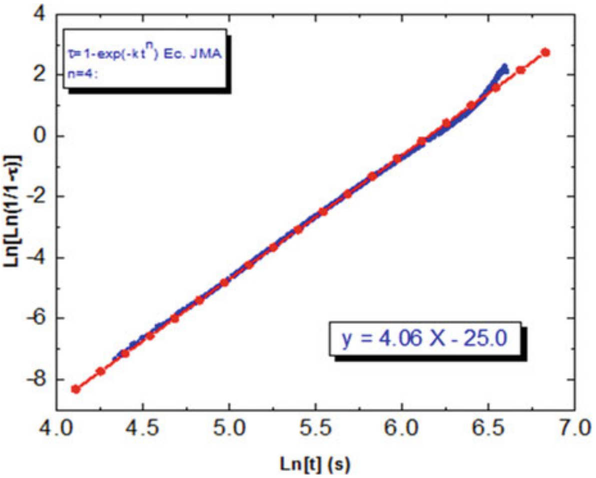

where the process is controlled by the growth. The third par of the transformation is in the range $0.5 < \tau < 1$, which is a deduction of the destruction of the growth. The final part occurs when $\tau = 1$, where the transformation was completed [19].

Meanwhile, Fig. 11.4 shows the method to "linearize" the JMA equation, for the amorphous $Gd_{0.4}Sm_{0.6}Co_5$ alloys obtained with a heating rate of 4.5 K/s. In this treatment of "linearize," the JMA equation is necessary to plot ln [ln 1/(1-τ)] versus ln t to find the value of the exponent "n" in the JMA equation by adjusting to the straight line. For these alloys, a value of the exponent "n" equal to 4 was obtained, this value is characteristic of a constant nucleation [20]. Data shown in Fig. 11.4 for the alloys $Sm_{0.6}Gd_{0.4}Co_5$ amorphous can be adjusted to a behavior straight line type, showing that the isothermal crystallization kinetics can be modeled by the equation JMA. From experimental data were estimated the values k equal to 25.0 and a value for the exponent n equal to 4, the coefficient k is important in phase transformations because it includes the nucleation rate and the rate of growth. The value of $n = 4$ is also very important because this value helps to understand the mechanism of phase transformation for a given temperature [21]. As mentioned J. W. Christian when n is in the range $3 \leq n \leq 4$ are said the nucleation and growth processes are in three dimensions and the nucleation rate is declining with time, while when n are outside this range it is said that the nucleation rate is constant as shown in this case [22].

Figure 11.5 shows the initial magnetization curve and a minor hysteresis loop for the as-cast alloys of $Gd_{0.4}Sm_{0.6}Co_5$ and after 240 min of mechanical alloying, measured in a VSM applying a maximum magnetic field of 1.19 MA/m and corrected for the demagnetizing field. The amorphous $Gd_{0.4}Sm_{0.6}Co_5$ alloys have a maximum magnetization of 58.25 J/Tkg and a developed coercivity $H_C = 113.73$ kA/m higher than that of the as-cast $Gd_{0.4}Sm_{0.6}Co_5$ alloys. It is observed that the as-cast $Gd_{0.4}Sm_{0.6}Co_5$ alloys reach a saturation state for the maximum applied field, while the amorphous $Gd_{0.4}Sm_{0.6}Co_5$ alloys show a minor hysteresis loop. The magnetic properties for the alloys of $Gd_{0.4}Sm_{0.6}Co_5$ in the

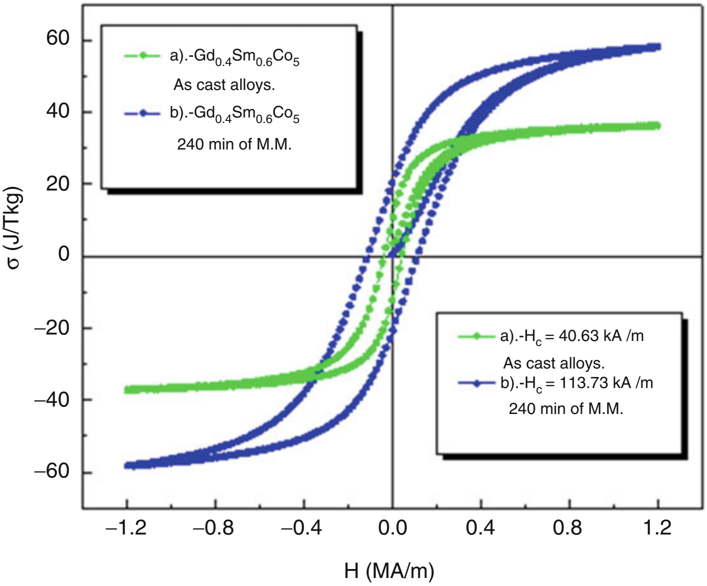

Fig. 11.5 Initial magnetization curve and a minor hysteresis loop for the as-cast $Gd_{0.4}Sm_{0.6}Co_5$ alloys and amorphous $Gd_{0.4}Sm_{0.6}Co_5$ alloys after 240 min of mechanical milling, measured in a vibrating sample magnetometer with an applying magnetic field of 1.19 MA/m

amorphous state are better than crystalline alloys due to the rapid grain size refinement and to an accumulation of defects caused by the mechanical milling process [22, 23]. Not is noting a knee in the demagnetization curve that shown in the second quadrant of the hysteresis loop for amorphous alloys of $Sm_{0.6}Gd_{0.4}Co_5$ characteristic of alloys of two phases present that are not magnetically coupled. These amorphous $Sm_{0.6}Gd_{0.4}Co_5$ alloys show a radius of remanence of 0.35 that is characteristic in alloys where there are not magnetic interactions.

11.4 Conclusions

Alloys with nominal $Gd_{0.4}Sm_{0.6}Co_5$ composition were prepared by arc melt. X-ray diffraction patterns of the as-cast ground alloy were indexed as $CaCu_5$-type hexagonal structure. Amorphous $Gd_{0.4}Sm_{0.6}Co_5$ powders were obtained after 240 min of mechanical milling. The X-ray diffraction shows that, after 240 min of mechanical milling of the alloys, $Gd_{0.4}Sm_{0.6}Co_5$ show a characteristic behavior of an amorphous alloy. The size of the crystal cannot be determined by the X-ray diffraction patterns for the amorphous $Gd_{0.4}Sm_{0.6}Co_5$ powders, which is very interesting because a crystal around 5 nm in size should present a different structure that changes some of the properties of the electronic structure. The exothermic broad peak was observed in DSC measurements for alloys of $Gd_{0.4}Sm_{0.6}Co_5$ amorphous due to the nanocrystallization of the alloy. An analysis of the kinetics of crystallization of amorphous alloys obtained by mechanical milling for the amorphous $Gd_{0.4}Sm_{0.6}Co_5$ alloys was presented. For these alloys, a value of the exponent "n" equal to 4 was obtained, which is characteristic of a constant nucleation. On the other hand, the maximum magnetization (58.25 J/Tkg) of the amorphous $Gd_{0.4}Sm_{0.6}Co_5$ alloys is caused by the progressive destruction of the magnetocrystalline anisotropy of the as-cast $Gd_{0.4}Sm_{0.6}Co_5$ alloys. The synthesis of such alloys is of vital importance from a scientific point of view as the partial substitution of Sm by Gd could also help one understand better the nature of the coupling between rare earth elements and transition metals as alloys $GdCo_5$ in the magnetic moment of Co is aligned antiparallel to the moment of Gd, whereas the alloys $SmCo_5$ Sm ferromagnetically coupled to the magnetic moment of magnetic Co [11, 24, 25].

References

1. Saito T, Nishio-Hamane D (2014) Magnetic properties of $SmCo_{5-x}Fe_x$ ($x = 0$–4) melt-spun ribbon. J Alloys Compd 585:423–427
2. Hou Y, Xu Z, Peng S, Rong C, Liu JP, Sun S (2007) A Facile Synthesis of $SmCo_5$ Magnets from Core/Shell Co/Sm_2O_3 Nanoparticles. Adv Mater 19:3349–3352
3. Wang F, Hu X, Li X, Huang G, Zhang Y, Zhang X (2014) Anisotropic $(Sm,Pr)_1Co_5$ based nanoflakes fabricated by high-energy ball milling in polar milling medium. J Alloys Compd 589:283–287
4. Coey JMD (1996) Rare-earth iron permanent magnets. Clarendon Press, Oxford
5. Dahlgren M, Grössinger R (1999) Physics of nanocrystalline magnetic materials. Mater Sci 180:302–303, 263–272
6. Al-Omari IA, Skomski R, Thomas RA, Leslie-Pelecky D, Sellmyer DJ (2001) High-temperature magnetic properties of mechanically alloyed $SmCo_5$ and YCo_5 magnets. IEEE Trans Magn 37:2534–2536
7. Hadjipanayis GC (1999) Nanophase hard magnets. J Magn Magn Mater 200:373–391
8. Panagiotopoulos I, Withanawasam L, Hadjipanayis GC (1996) Exchange spring behavior in nanocomposite hard magnetic materials. J Magn Magn Mater 152:353–358
9. Tang N, Chen Z, Zhang Y, Hadjipanayis GC, Yang F (2000) Nanograined YCo_5-based powders with high coercivity. J Magn Magn Mater 219:173–177
10. O'Handley RC (2000) Modern magnetic materials. Principles and applications. Wiley-Interscience. Wiley, New York
11. Szmaja W (2006) Study of domain structure of anisotropic sintered $SmCo_5$ permanent magnets. J Magn Magn Mater 10:1016–1021
12. Elizalde-Galindo JT, Matutes-Aquino JA, Davies HA, Liu Z (2005) Magnetic and structural study of melt-spun YCo_5 ribbons. J Magn Magn Mater 294:e137–e140
13. Elizalde-Galindo JT, Matutes-Aquino JA, Sanchez JL, Sanchez-Valdez CF, Santana Gil A (2005) Hard magnetic properties of isotropic nanostructured $Y_{0.5}Pr_{0.5}Co_5$ powders. J Magn Magn Mater 294:226–231
14. Rai BK, Mishra SR (2013) Magnetically enhanced hard–soft $SmCo_5$-FeNi composites obtained via high energy ball milling and heat treatment. J Magn Magn Mater 344:211–216
15. Sun DZ, Cheng LZ, Zhang YM, He KY (1992) Calorimetry study about $Ni_{50}Ti_{50}$ ball milled powders. Mater Sci 88–90:321–324

16. Cullity BD, Stock SR (2001) Elements of X-ray diffraction, 3rd edn. Prentice-Hall Inc., Upper Saddle River
17. Li HX, Gao JE, Wu Y, Jiao ZB, Ma D, Stoica AD, Wang XL, Ren Y, Miller MK, Lu ZP (2013) Enhancing glass-forming ability via frustration of nano-clustering in alloys with a high solvent content. Nature/Scientific Reports 1983, pp 1–7
18. Song SJ, Seok JY, Yoon JH, Kim KM, Kim GH, Lee MH, Hwang CS (2103) Real-time identification of the evolution of conducting nano-filaments in TiO_2 thin film RAM. Nature/Scientific Reports 3, 3443, pp 1–4
19. Rolando MA, Malherbe R (2009) The physical chemistry of materials: energy and environmental applications. CRC Press, Boca Raton
20. Schmelzer JWP (2005) Nucleation theory and applications. Wiley VCH, New York
21. Christian JW (1975) Theory of transformations in metals and alloys. Pergamon Press Ltd, Oxford
22. Chen Z, Meng-Burany X, Hadjipanayis GC (1999) J Appl Phys Lett 75:3165–3167
23. Sanchez JL, Elizalde-Galindo JT, Matutes-Aquino JA (2003) High coercivity noncrystalline YCo_5 powders produced by mechanical milling. Solid State Commun 127:527–530
24. Coey JMD (2009) Magnetism and magnetic materials. Cambridge University Press, Cambridge
25. Chikazumi S (1997) Physics of ferromagnetims. Oxford University Press, Oxford

Chapter 12
Metallurgical Study of Mechanical Milling Mechanism in Eutectic Nanopowders: The Role of Heterogeneities

H. Rojas-Chávez, M.L. Mondragón-Sánchez, J.A. Andraca-Adame, and D. Jaramillo-Vigueras

Abstract A study of the addition of Pb–Sn nanoparticles, as heterogeneities, during the high-energy milling (HEM) process to achieve eutectic nucleation was carried out using chemical arguments, as well as X-ray powder diffraction and microscopy techniques. In addition to a change of energy source input, growth of eutectic alloys with the addition of Pb–Sn nano-heterogeneities promotes a more refined microstructure. The conventional melting/solidification method produced coarser microstructure than that of the high-energy milling process. To determine the mechanism responsible, eutectic nucleation in high-purity Pb–Sn mixtures, with and without the addition of Pb–Sn nano-heterogeneities, was studied. It was found that the addition of nano-heterogeneities exerts a positive effect on the nucleation process, while nucleation was not detected in the unmodified powder mixture. It was concluded that mixtures with the addition of nano-heterogeneities contain a large number of potent supersaturated nuclei that are susceptible to promote eutectic nucleation.

Keywords High-energy milling • Eutectic • Heterogeneities • Nuclei • Nanopowders

---

H. Rojas-Chávez (✉)
Instituto Tecnológico de Tláhuac II, Tecnológico Nacional de México, Camino Real 625, Col. Jardines del Llano, San Juan Ixtayopan, Del. Tláhuac, CDMX. 13508, Mexico
e-mail: rojas_hugo@ittlahuac2.edu.mx

M.L. Mondragón-Sánchez
Instituto Tecnológico de Morelia, Tecnológico Nacional de México, Av. Tecnológico 1500, Col. Lomas de Santiaguito, Morelia, Mich. 58120, Mexico

J.A. Andraca-Adame
Centro de Nanociencias y Micro y Nanotecnologías, Instituto Politécnico Nacional, Av. Luis Enrique Erro s/n, U.P.A.L.M. CDMX. 07738, Mexico

D. Jaramillo-Vigueras
Centro de Investigación e Innovación Tecnológica, Instituto Politécnico Nacional, Cerrada de CECATI s/n, Del. Azcapotzalco, CDMX. 02250, Mexico

R. Pérez Campos et al. (eds.), *Characterization of Metals and Alloys*, DOI 10.1007/978-3-319-31694-9_12

12.1 Introduction

Currently, eutectic alloys for the production of engineering materials are prepared by the conventional method, melting/solidification. When the alloy solidifies, thermal and solutal gradients develop in the liquid [1]. The temperature gradients develop from differences in cooling rates caused by extraction of heat from the system as well as the evolution of latent heat within the mushy region. The concentration gradients are caused by the rejection of solute at the solid–liquid interface, and its transport by diffusion (microsegregation) and convection (macrosegregation) in the liquid and the mushy region [2, 3]. This method produces a coarse microstructure, and the compositional heterogeneity of the cast structure induces non-uniformity of mechanical properties [1, 2].

Nonetheless, extensive theoretical and experimental studies have led to a reasonable understanding of the melting/solidification behavior as well as the morphological evolution of eutectic alloys [4]. Nowadays, the conventional method requires a careful control process parameter for maintaining satisfactory control over the casting process [5, 6].

Several technological areas as well as engineering materials disciplines make use of submicron particles to improve mechanical properties. It is well known that the manufacturing of fine particles may be effectively achieved by means of grinding processes, such as the high-energy milling (HEM) process [7].

Much attention has focused recently on the processing of intermetallic compounds, composites, non-equilibrium, equilibrium, metastable, and several kinds of alloys using HEM [8, 9]. HEM is a processing technique with the capability to produce nanoparticles. As-milled powders obtained by HEM possessing a greater specific surface area exhibit unique properties and reveal reactivity parameters better than those for micron-sized powders [10–12]. The HEM process is one of the favorable solid-state nanopowder fabrication techniques featured with economical and simple operations for mass production.

Other studies have reported evidence of milling processes applied to conventional powders, explaining powder behavior (mechanism) and formation of phases during milling [13, 14]. Eutectic alloy obtained from the HEM process is an attractive topic because it is the basis of most casting alloys, which has led to the extensive theoretical and experimental study of them [2, 4, 5, 15]. Moreover, these alloys are the basis of many engineering materials, because the vast majority of technically important eutectic alloys are composed of two phases.

In this paper, we present the results and a first experimental approach of eutectic evolution by X-ray powder diffraction as a function of two kinds of energy sources, namely, mechanical and thermal. The eutectic behavior as a function of milling time and the size of nano-heterogeneities allow the possibility of studying the mechanisms of eutectic nucleation. The purpose of this study is to discern the nano-heterogeneities role to promote a rapid eutectic nucleation. We have chosen the lead–tin system as a case of study because it is straightforward and much is already known about it.

12.2 Experimental

12.2.1 Materials and Methods

Samples of a binary mixture of powders of Pb (50 μm, 99.9 mass %) and Sn (50 μm, 99.9 mass %) from Aldrich were prepared. Powders were mixed in the appropriate mass ratio. The samples were sealed together with several ZrO_2-spheres into a cylindrical nylamid vial (with hemispheric faces to prevent the formation of stagnant zones) under composition, pressure, and temperature (*c-P-T*) vial conditions [16]. The ball-to-powder weight ratio was fixed at 10:1. The HEM process was carried out by using a SPEX mixer/mill model 8000 for 5 h up to 10 h. Small amounts of as-milled reaction products were extracted at various prefixed times for further analyses.

Two kinds of powder mixtures were processed via high-energy treatment: (1) Pb–Sn elemental powders and (2) Pb–Sn elemental powders plus nano-heterogeneities (Pb–Sn powder mixture processed for 5 h by HEM). Both powder mixtures were processed under *c-P-T* vial conditions and a small amount of ethanol was used as a process controlling agent to reduce excessive cold-welding of the powders.

A third kind of sample was obtained as follows: after milling for 5 h (without and with nano-heterogeneities addition) powders were extracted; from mixtures, compacts were formed at room temperature under pressure of 82 kg/cm^2. They were in the shape of a cylinder with a diameter of 3 mm and height of 0.5 mm. Quartz ampoules containing these compacts were purged with argon and sealed under vacuum at 10^{-5} Torr. The compacts were annealed in a horizontal tube furnace (170 °C and total annealing times: 5, 10, and 20 h). After annealing, the furnace was slowly cooled down to room temperature.

12.2.2 Structural and Morphological Characterization

X-ray patterns to trace the nucleation of the $Pb_{0.26}Sn_{0.74}$ alloy were measured in Bragg-Brentano geometry with an X Pert PRO MRD Diffractometer from PANalytical. Cu-radiation was used ($K_\alpha = 1.54$ Å) at 45 kV and 40 mA for tube power. The step size was 0.03 and 300 s for time and range 20–90 for 2θ (degrees). X-Ray mirrors with a 1/32 divergence slit and a Soller slit (0.04 Rad) were used in incident optics for parallel beams. A PIXcel ultrafast X-ray detector was used for diffracted optics. The microstructure was revealed through scanning electron microscopy (SEM, JEOL JSM-7600F), and it was equipped with energy dispersive X-ray spectrometer (EDS).

12.3 Results and Discussion

Analyses of both heterogeneities and as-milled products were carried out periodically just before milling and sampling up to the point where eutectic composition was detected. The X-ray pattern of powder heterogeneities is shown in Fig. 12.1. All the diffraction sharp peaks traced were indexed correspondingly to Pb (ICSD card 04-0686) and Sn (ICSD card 04-0673) as pure phases. It is worth noting that there was no presence of eutectic phase.

The structure evolution of the Pb–Sn mixtures in several stages of the mechanical treatment (5 and 10 h) is shown in Fig. 12.2. XRD patterns of the as-prepared samples (5 and 10 h) are characterized by several distinct and sharp diffraction peaks that can all be ascribed to Pb (card no. 04-0686) and Sn (card no. 04-0673) phases, as is shown in Fig. 12.2a. No additional diffraction peaks can be observed, implying that there was no presence of eutectic phase.

It is important to note that increasing milling time (10 h) does not broaden the diffraction peaks of the phases traced. At these milling stages (5 and 10 h), the decrease in the content of the Pb-phase, as well as the increase of the Sn-phase content, was traced. Thus, XRD indices that show how chemical changes take place should be read in Fig. 12.2a.

Figure 12.2b shows the XRD patterns of the as-milled samples with the addition of nano-heterogeneities. After 10 h of mechanical treatment, some small diffraction peaks were evident and attributed to the $Pb_{0.26}Sn_{0.74}$ (card no. 98-010-5617), with

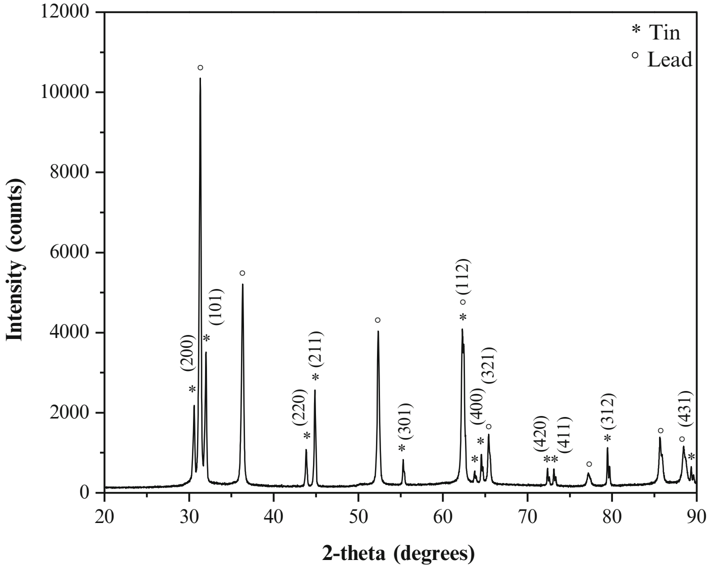

Fig. 12.1 XRD pattern of nano-heterogeneities. The Miller indices on the upper diffraction pattern correspond to the Sn-phase

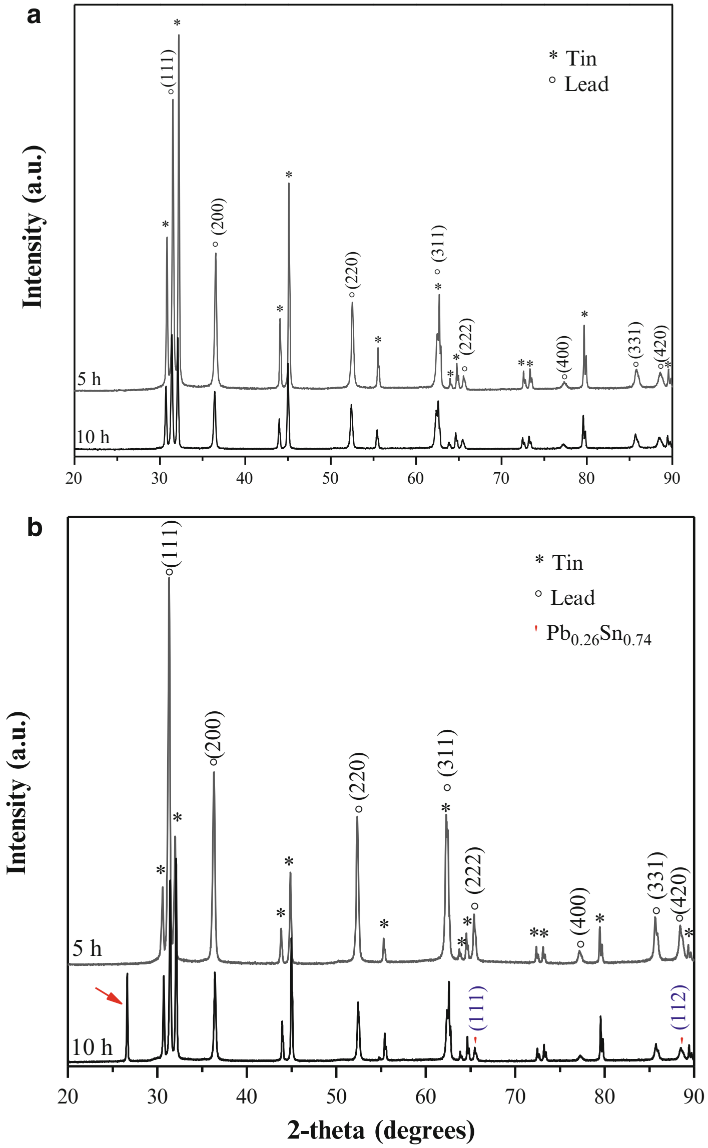

Fig. 12.2 XRD patterns of as-milled powders: (**a**) Pb–Sn mixture without nano-heterogeneities and (**b**) Pb–Sn mixture with the addition of nano-heterogeneities. The Miller indices on the upper diffraction patterns correspond to the Pb-phase

very intense diffraction peaks attributed to the powder precursors. As seen also in this figure, a well-defined diffraction peak appears at 26.63°. It is intense and sharp, as indicated by the arrow.

As shown in Fig. 12.2, at ~62.30° the Bragg reflection (311) of Pb is overlapped by the Sn diffraction peak (112). It is worth noting that the same case has already been traced in Fig. 12.1.

Structural changes of as-milled samples during thermal effect were traced using the X-ray powder diffraction technique on a series of samples annealed under argon/vacuum at different annealing times. The XRD patterns obtained are shown in Fig. 12.3.

As shown in Fig. 12.3a, the weak Bragg reflections, (010), (200), (220), and (400), of Pb imply their low quantity in the sample. At different annealing times, from 5 to 20 h, variations of diffraction intensity for Pb- and Sn-phases indicate that the Pb-phase decreases with the annealing time increasing and, simultaneously, $Pb_{0.26}Sn_{0.74}$ phase appears, which is consistent with the HEM results. The progress of the eutectic reaction will take place as a function of the input energy (mechanical or thermal).

After annealing treatment, 20 h, a thermal reaction was detected. It is confirmed by the presence of a broad diffraction peak at 26.61°, as indicated by the arrow in Fig. 12.3a. This diffraction peak is another end product of the reaction induced by the thermal energy, which is the same reaction occurring during the HEM process (10 h, Fig. 12.2b).

The peak at 26.60° is identical to those obtained in thermal annealed samples (with the addition of nano-heterogeneities) showed in Fig. 12.3b. This alternatively confirms the rapid $Pb_{0.26}Sn_{0.74}$ nucleation. Increasing the annealing time broadens the diffraction peak traced at 26.60° (Fig. 12.3b).

It is interesting to note that, in any case, the (222), (420), and (311) Bragg reflections of Pb disappeared completely after annealing decreased, as indicated by the XRD patterns shown in Fig. 12.3. The decrease of these Bragg reflections during heating is due to the reaction to nucleate $Pb_{0.26}Sn_{0.74}$ that takes place.

It is acknowledged that high-energy ball impact, during the HEM process, results in particle crystal size reduction [16]. Hence, new surface area is continuously formed during milling under ball impacts, giving rise to a very large surface area. According to thermochemical concepts, mechanical energy was gradually introduced into the powder system in such a way that this mechanical equivalent is transformed to an activation energy, which should promote a series of chemical reactions. However, in the unmodified powder mixture (without addition of nano-heterogeneities) there was no presence of the $Pb_{0.26}Sn_{0.74}$ formation (Fig. 12.2a).

Milling experiments were carried out under the same milling parameters. Additionally, to achieve the eutectic formation, a small quantity of nano-heterogeneities was added to the powder mixtures. As clearly indicated in Fig. 12.2b, after 10 h of mechanical treatment, a low quantity of $Pb_{0.26}Sn_{0.74}$ was detected in the as-milled sample.

Annealing experiments with an equivalent quantity of energy (thermal) have been carried to monitor the eutectic formation.

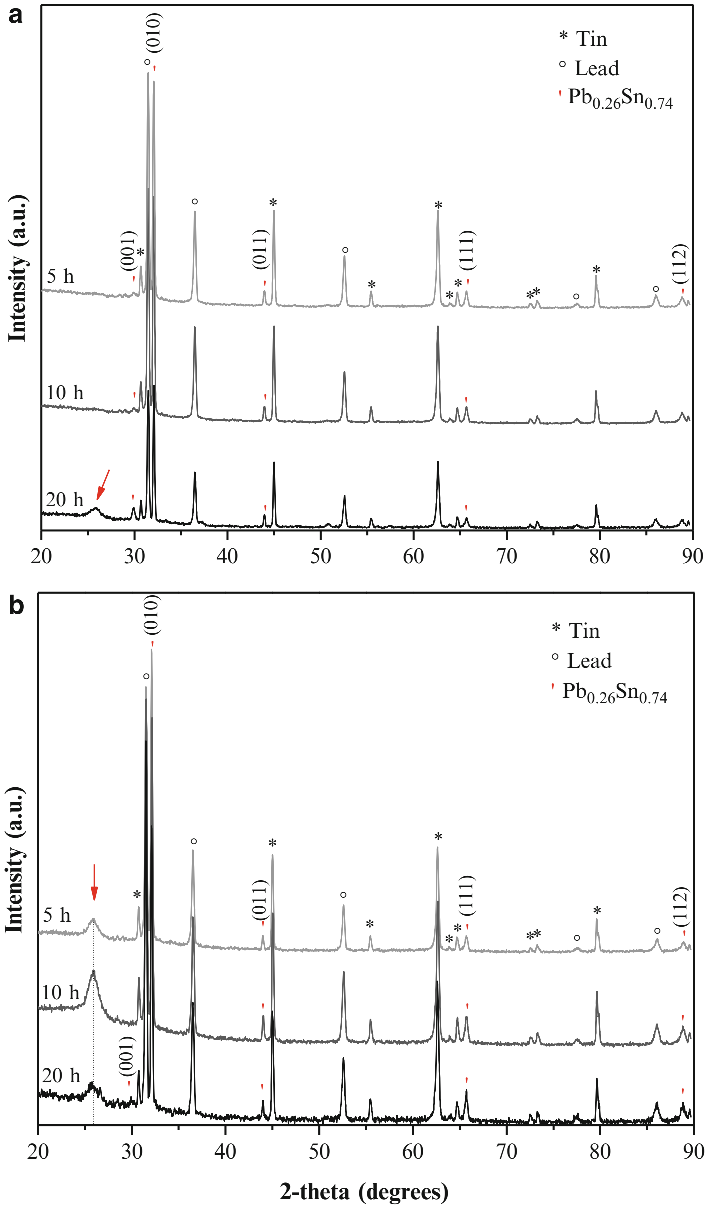

Fig. 12.3 XRD patterns of as-milled powders after annealing under argon-vacuum at different times. (**a**) Without nano-heterogeneities and (**b**) with addition of nano-heterogeneities. The Miller indices on the upper diffraction patterns correspond to $Pb_{0.26}Sn_{0.74}$ eutectic phase

Summarizing the results of annealing experiments on the samples subjected to thermal energy, it should be mentioned that the observed phenomena of eutectic formation may be interpreted as nucleation mechanisms, making their behavior similar to classical nucleation. Indeed, these results allow us to state that samples subjected to thermal energy (20 h) do not require the addition of nano-heterogeneities to achieve eutectic formation (Fig. 12.3a). The most striking difference in the annealed samples is that the nano-heterogeneities promote a significant change in the eutectic reaction; a considerably improved XRD pattern with pronounced diffraction peaks is obtained (Fig. 12.3b). It is important to note that increasing annealing time broadens the diffraction peaks of the phases traced.

In order to test structural and elemental composition of the eutectic phase, SEM/EDS analyses were carried out. SEM analysis was conducted in backscattering electron mode. With this configuration, the image shows both lead (clearer phase) and tin (darker phase). Figure 12.4 depicts the SEM micrograph of the as-milled sample (with the addition of nano-heterogeneities) at 10 h milling treatment.

Figure 12.4 shows a typical morphology of an eutectic alloy. The microstructure obtained by the high-energy milling process is more refined than that of the conventional method or even other techniques [14]. It is worth pointing out that, via EDS analysis, one can note that, compositionally, the most probable surface compositions are given in Table 12.1.

EDS analysis testifies that the average stoichiometry of darker phases is consistent with the theoretical stoichiometry of the eutectic phase.

Chemical composition of the darker phases, $\sim Pb_{0.25}Sn_{0.75}$, resembles the eutectic one, $Pb_{0.26}Sn_{0.74}$. The SEM/EDS results are in agreement with the XRD results.

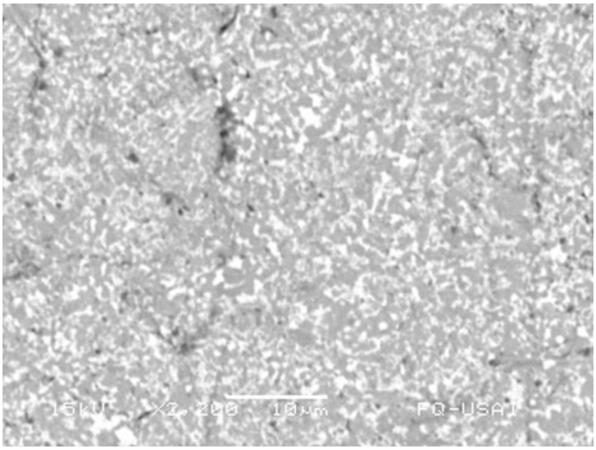

Fig. 12.4 SEM microstructure for the as-milled powders (with the addition of nano-heterogeneities) obtained at 10 h

Table 12.1 Average elemental composition of the phases traced by SEM/EDS

Phase	at.% Pb	at.% Sn	±
Dark	24.5719	75.4281	0.0060
Clear	58.4408	41.5592	0.0122
Boundary	62.0699	37.9301	0.0125

12.4 Conclusions

The chemical reactions observed during both high-energy milling and thermal annealing present significant changes. Nonetheless, these results reveal that different chemical reaction paths, HEM and thermal processes, drive the eutectic nucleation. In the former process, the eutectic nucleation will take place only if a small quantity of nano-heterogeneities is added to the powder mixture. It indicates that the addition of nano-heterogeneities is the key factor in the rapid eutectic nucleation during milling. In contrast, if an unmodified powder mixture, Pb–Sn, is used as the starting material, the $Pb_{0.26}Sn_{0.74}$ will not be detected during milling, even during a prolonged milling time (10 h).

The diffraction peak detected at ~26.61° is inconsistent with the planes attributed to the $Pb_{0.26}Sn_{0.74}$ phase (ICSD 98-010-5617). However, chemical composition, revealed by EDS analysis, demonstrated that darker phases are Sn-rich compared with the clearer, Pb-rich phases. The average stoichiometry of darker phases ($\sim Pb_{0.25}Sn_{0.75}$) is consistent with the theoretical stoichiometry of the eutectic phase, $Pb_{0.26}Sn_{0.74}$.

Powder mixtures with the addition of nano-heterogeneities processed by high-energy milling may be used to produce eutectic alloys with refined microstructure. Nano-heterogeneities contain a large number of potent supersaturated nuclei that are susceptible to achieve a rapid eutectic nucleation. This first experimental approach changes our understanding of nucleate eutectic alloys via high-energy milling.

Nonetheless statements on nucleation/growth mechanism of a eutectic mixture are valid; this work has to be considered as a preliminary study.

Acknowledgements One of the authors (H. Rojas-Chávez) gratefully thanks M.Sc. G. Gonzalez-Mancera FQ-UNAM for her technical support and Consorcio Nacional de Recursos de Informa-ciónCientífica y Tecnológica, CONRICyT, for the free access to the digital library content.

References

1. Rusell AM, Lee KL (2005) Structure-property relations in nonferrous metals. Wiley-Interscience. Wiley, New York
2. Kumar A, Pradip D, Sundarraj S, Walker MJ (2007) Remelting of solid and its effect on macrosegregation during solidification. Numer Heat Tr A 51:59–83
3. Kurz W, Fisher DJ (1992) Fundamentals of solidification. Trans Tech Publications, Brookfield
4. Sharma BL (2004) Anisotropic lamellae growth and hardness of eutectic composite alloy Pb-Sn. J Alloys Compd 385:74–85
5. Belyaev AP, Kukushkin SA, Rubets VP (2001) Crystallization of a eutectic Pb-Sn melt in the thermal field of a temperature gradient. Phys Solid State 43(4):577–580
6. Hachani N, Zaidat K, Saadi B, Wang XD, Fautrelle Y (2015) Solidification of Sn-Pb alloys: experiments on the influence of the initial concentration. Int. J. Therm. Sci. 91:34–48
7. Gomez J, Basaran C (2006) Nanoindentation of Pb/Sn solder alloys; experimental and finite element simulation results. Int J Solids Struct 43:1505–1527
8. Milea A, Gingu O, Preda S, Sima G, Nicolicescu C, Tanasescu S (2015) Thermodynamic measurements on Ag-28% Cu nanopowders processed by mechanical alloying route. J Alloys Compd 629:214–220

9. Canakci A, Varol T, Ozsahin S (2013) Analysis of the effect of a new process control agent technique on the mechanical milling process using a neural network model: measurement and modeling. Measurement 46:1818–1827
10. Zou C, Gao Y, Yang B, Zhai Q (2010) Synthesis and DSC study on Sn3.5Ag alloy nanoparticles used for lower melting temperature solder. J Mater Sci Mater Electron 21:868–874
11. Li T, Lin X, Huang W (2007) Preparation of metal alloy powder by semi-solid processing. J Mater Sci 42:2669–2674
12. Ahmed M, Fouzder T, Sharif A, Kumar Gain A, Chan YC (2010) Influence of Ag microparticle addition additions on the microstructure, hardness and tensile properties of Sn-9Zn bi-nary eutectic solder alloy. Microelectron Reliab 50:1134–1141
13. Pedersen AS, Pryds N, Linderoth S, Larsen PH, Kjøller J (2001) The determination of dynamic and equilibrium solid/liquid transformation data for Sn-Pb using DSC. J Therm Anal Calorim 64:887–894
14. Benício de Castro W, Maia ML, Kiminami CS, Bolfarini C (2001) Microstructure of undercooled Pb-Sn alloys. Mater Res 4(2):83–86
15. Khan PY, Bhattacharya V, Biswas K, Chattopadhyay K (2013) Melting and solidification behavior of Pb-Sn embedded alloy nano-particles. J Nanopart Res 15:2049
16. Rojas-Chávez H, Reyes-Carmona F, Garibay-Febles V, Jaramillo-Vigueras D (2013) Solid-solid and gas-solid interactions induced during high-energy milling to produce PbTe nanopowders. J Nanopart Res 15:1623

Part VI
Characterization of Materials for Medical Applications

This part includes two chapters related to the characterization of materials used in medical applications.

The first chapter presents a study of biosynthesis of silver nanoparticles (AgN_{ps}) using extracts of Mexican medicinal plants. Metal nanoparticles have attracted particular interest in recent years due to their unique physical and chemical properties. Silver nanoparticles have been a subject of extensive research because of their catalytic and antibacterial properties. Silver nanoparticles have several applications in food industry, in medicine, and in environment. There are different methods for the nanoparticles synthesis, being the chemical reduction the most commonly used. However, in this research work an alternative of synthesis method eco-friendly and economical called green synthesis was used. Green synthesis is based on the use of different plant extracts making a more economical process. Additionally, the antibacterial activity of silver nanoparticles synthesis was evaluated.

The second chapter presents the synthesis and thermal characterization of hydroxyapatite powders obtained by sol-gel technique. The hydroxyapatite is highly used in the development of customized cranial, maxillofacial prosthesis, dental implants, and bone substitution due to its proved biocompatibility with the human body. The synthesis of two kinds of hydroxyapatite powder samples was successfully achieved employing the sol-gel technique, for the same chemical precursors but under different mixing conditions. By means of the photoacoustic detection and infrared photothermal radiometry techniques, the thermal response of the samples was obtained. Studies of X-ray diffraction, EDS and FTIR spectrums revealed that studied samples have a stoichiometry close to the ideal for biological applications. Additionally, synthesized samples have good thermal affinity with the mandibular human bone tissue, and are suitable for biomedical applications.

The main techniques used in the characterization of these materials are:

- X-ray diffraction.
- Scanning electron microscopy (SEM).
- Energy dispersive spectroscopy (EDS).
- Ultraviolet–visible spectroscopy (UV-Vis).

- Infrared photothermal radiometry (IPTR).
- Fourier transform infrared spectroscopy (FTIR).
- Thermal conductivity.
- Photoacoustic detection.

Chapter 13
Biosynthesis of Silver Nanoparticles Using Extracts of Mexican Medicinal Plants

J.L. López, C. Baltazar, M. Torres, A. Ruíz, R. Esparza, and G. Rosas

Abstract The biosynthesis of silver nanoparticles using an aqueous extract of *Agastache mexicana* and *Tecoma stans* was carried out. The $AgNO_3$ concentration and extract concentration was varied to evaluate their influence on the nanoparticles characteristics such as size and shape. Several characterization techniques were employed. UV-Vis spectroscopy revealed the surface plasmon resonance in the range of 400–500 nm. The X-Ray diffraction results showed that the nanoparticles have a face-centered cubic structure. SEM results confirmed the formation of silver nanoparticles with spherical morphologies. Finally, the antibacterial activity of silver nanoparticles was evaluated against *Escherichia coli* bacteria.

Keywords Silver nanoparticles • Biosynthesis • *Agastache mexicana* • *Tecoma stans* • Characterization

13.1 Introduction

Metal nanoparticles have attracted particular interest in recent years due to their unique physical and chemical properties [1–4]. Among metal nanoparticles, silver has been the subject of significant and diverse research because of its catalytic and antibacterial properties [5, 6]. Silver nanoparticles (AgNps) have several applications in the food industry, in medicine, and in the environment [4]. Furthermore, there are different methods for the synthesis of nanoparticles, with chemical reduction as the most commonly used method. However, this process of synthesis involves toxic materials such as sodium borohydride and sodium citrate [7, 8]. An alternative synthesis method that is considered eco-friendly and economical is the so-called green synthesis method. Green synthesis is based on the use of

---

J.L. López (✉) • J.L. Miranda • C. Baltazar • M. Torres • G. Rosas
Instituto de Investigaciones Metalúrgicas, UMSNH, edificio U, Ciudad Universitaria, C.P. 58060
Morelia, Michoacán, Mexico
e-mail: lopezfim@gmail.com

A. Ruíz • R. Esparza
Centro de Física Aplicada y Tecnología Avanzada, Universidad Nacional Autónoma de México,
Boulevard Juriquilla 3001, Santiago de Querétaro, Querétaro, C.P. 76230. Mexico

R. Pérez Campos et al. (eds.), *Characterization of Metals and Alloys*, DOI 10.1007/978-3-319-31694-9_13

different sources such as bacteria [9], yeast [10], fungi [11], and plant extracts [12]. The use of plant extracts has more economical and technical advantages. In this process, plant extract provides the reducing agents and stabilizing agents needed to carry out the AgNps synthesis reaction. These chemical agents are organic compounds present in the plant extract. A variety of plants have been used for these purposes: *Tephrosia tinctoria* [12], *Couroupita guianensis* [13], *Nyctanthes arbortristis* [14], *Pistacia atlantica* [15], *Ziziphora tenuior* [16], *Eucalyptus oleosa* [17], *Aerva lanata* [18], *Croton sparsiflorus morong* [19], *Prosopis farcta* [20]. Other plants with medicinal properties are *Agastache mexicana* and *Tecoma stans*, which have not been explored for the AgNps synthesis. *Agastache mexicana* is used in the treatment of gastric distress like stomachache, stomach cramps, and digestion. It is also used in cardiovascular disorders, coughing, insomnia, and diabetes [21]. On the other hand, *Tecoma stans* is used to treat digestive disorders such as stomach ache, gastritis, indigestion, and liver problems [22]. Some studies of the chemical composition reveal the presence of organic compounds, suggesting potential use in the AgNps synthesis. *Agastache mexicana* leaves have a high content of phenolic and flavonoids compounds involving quercetin and hesperitin [21]. *Tecoma stans* leaves contain tecomine and tecostatine alkaloids [23, 24]. Thus, we present the experimental results of the green synthesis of AgNps using aqueous extracts of *Agastache mexicana* and *Tecoma stans*. The antibacterial activity of silver nanoparticles obtained against the bacteria *E. coli* was also evaluated.

13.2 Experimental

13.2.1 Materials

For the green synthesis of AgNps, analytical-grade $AgNO_3$ crystals were used. The precursor salt was purchased from Meyer Laboratories. $AgNO_3$ aqueous solutions at different concentrations were used (3, 5, and 7 mM). Distilled water was employed to prepare the aqueous solutions and extracts. The *Agastache mexicana* and *Tecoma stans* dry leaves that were used were collected from a local market in Morelia, México.

13.2.2 Plant Extracts Preparation

The *Agastache mexicana* and *Tecoma stans* dry leaves were milled in a ball mill SPEX 8000M for 5 min to obtain fine powders. One gram, 1.25 g, and 1.5 g plant powders were each dissolved in 50 ml of distilled water to obtain different extract concentrations. Subsequently, the mixture was heated at 70 °C for 20 min, with magnetic stirring. After that, the solutions were filtered with Whatman filter paper # 41, to separate the organic solid particles. Extracts were cooled to room temperature and stored at 5 °C for future use.

13.2.3 Synthesis of Silver Nanoparticles

The AgNps synthesis was carried out mixing 10 ml of $AgNO_3$ solution with 5 ml plant extract. The experiments were performed varying the extract concentration and also the $AgNO_3$ solution concentration. All the experiments were carried out at room temperature.

13.2.4 Characterization of Silver Nanoparticles

The synthesized silver nanoparticles were characterized by several techniques. UV-Vis spectroscopy was used to assess the formation of nanoparticles, as well as a qualitative analysis of the shape and size of the nanoparticles. The analysis was performed using a Beckman DU-20 spectrophotometer. The morphological characterization and chemical analysis of the nanoparticles were carried out using SEM (JEOL JSM 6700-F) equipment. Moreover, the nanoparticles were observed by transmission electron microscopy (TEM) to determine size, morphology, and dispersibility. This analysis was made in a Philips Tecnai F20 electron microscope operating at a voltage of 200 KeV and equipped with a field emission filament; the point resolution is 0.21 nm. The high resolution technique (HRTEM) was employed to analyze the crystallographic phases. X-ray diffraction analysis was performed on dried samples in order to confirm the AgNps formation. The experiments were conducted using a SIEMENS D5000 diffractometer with a CuKα radiation (1.5406 Å). The analysis was carried out in an angular range of 20–80° using a time step of 15 s for better collection of data during analysis.

13.2.5 Antibacterial Activity

The antibacterial activity of AgNps synthesized with both plant extracts against *E. coli* was evaluated. The disc diffusion method was used. The Mueller–Hinton Agar was employed as the medium for *E. coli* bacteria growth. Three sterile filter paper discs (5 mm diameter) were impregnated with 6 μl of AgNps synthesized with *Agastache mexicana* and *Tecoma stans*. The discs were placed in the plate containing the *E. coli*. Control disks (containing only plant extracts) were evaluated to ascertain the antibacterial activity of the plant extract. Finally, the plates were incubated at 36 °C for 24 h, then the inhibition zone was measured.

13.3 Results and Discussion

Figure 13.1 shows the UV-Vis spectra of the silver nanoparticles synthesized by the plant extracts. For the silver nanoparticles synthesized with *Agastache mexicana* extract (Fig. 13.1a), the absorbance band typical of silver nanoparticles is observed around 440 nm. As shown, the sample with 1 g extract concentration has the minimum absorbance value, indicating the lowest concentration of AgNps formed. Moreover, when the concentration of the extract is increased to 1.25 g, an increase of the absorption band was observed. In addition, a broad absorption band is observed, suggesting that the increase in the size distribution is due to the absence of stabilizing agents avoiding nanoparticles growth. Finally, for the sample with 1.5 g plant extract, the absorption intensity band was similar to those with 1 g plant extract employed. These results confirm that there are insufficient stabilizing compounds, leading to excessive growth of the particles. When *Tecoma stans* plant extract was employed (Fig. 13.1b), a different behavior in the reaction evolution was observed. For the sample with 1 g plant extract, an absorption band indicating the synthesis of nanoparticles was not observed. Moreover, when the

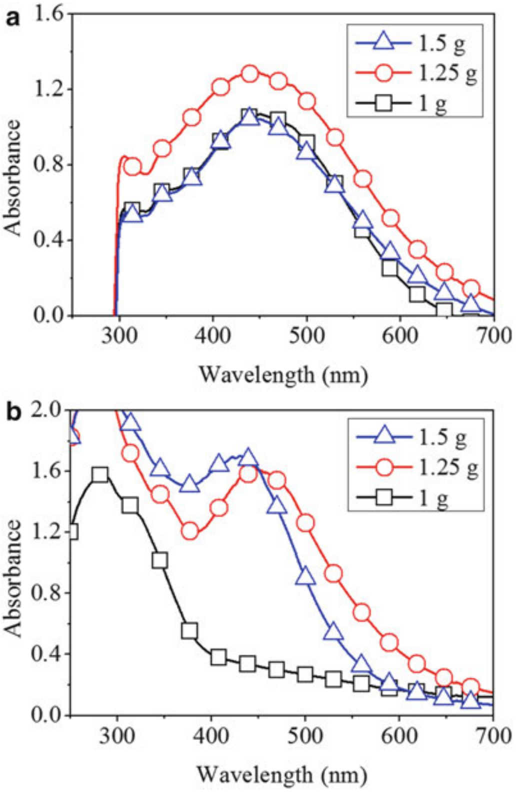

Fig. 13.1 UV-Vis spectra showing the extract concentration effect: (**a**) *Agastache mexicana* and (**b**) *Tecoma stans*

Fig. 13.2 UV-Vis spectra showing the $AgNO_3$ concentration effect: (**a**) *Agastache mexicana* and (**b**) *Tecoma stans*

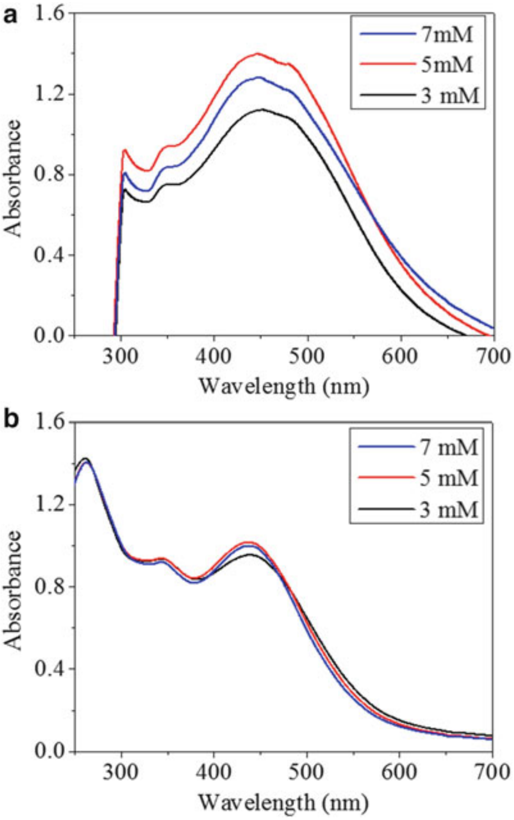

extract concentration was increased up to 1.5 g, the absorbance band is increased, indicating a high concentration of silver nanoparticles synthesized. Furthermore, the absorption band shift to the left indicates a decrease of AgNps crystallite size. Similar results have been reported by Amin et al. [25].

The effect of $AgNO_3$ concentration in the synthesis reaction of both types of plant extracts are shown in Fig. 13.2a and b, respectively. It is observed that the best results were obtained for the sample with 5 mM $AgNO_3$ concentration. The surface plasmon resonance (SPR) peak shows the best intensity and shape centered at 450 nm. For the extract of *Agastache Mexicana*, as the $AgNO_3$ concentration increases the absorption band decreases in intensity, suggesting a lower concentration of nanoparticles formed. In the case of silver nanoparticles synthesized with *Tecoma stans* extract, there is no significant effect of varying the $AgNO_3$ concentration. However, when a 5 mM concentration was used, the absorption band shows the highest intensity, suggesting a higher density of nanoparticles. These results occur because the reducing agent is not sufficient to reduce a higher concentration of ions, which occurs by increasing the concentration of $AgNO_3$. This condition leads to a smaller amount of nanoparticles synthesized, as has previously been reported [26].

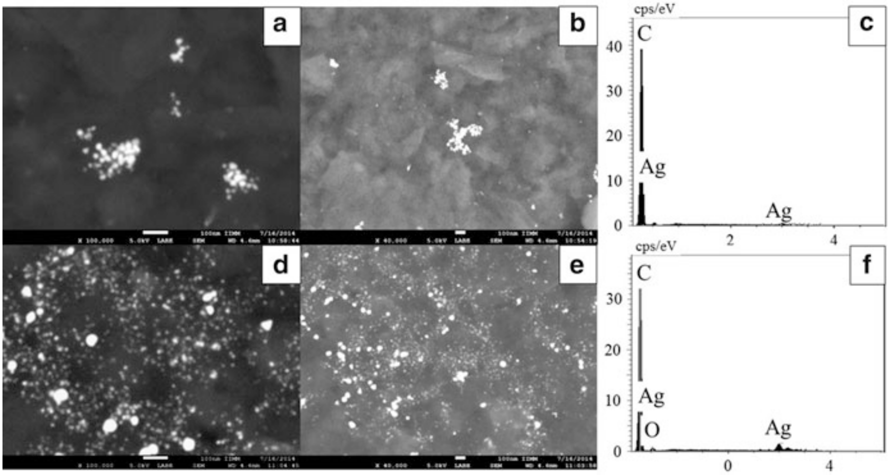

Fig. 13.3 SEM analysis of silver nanoparticles synthesized with *Agastache mexicana* (**a**)–(**c**) and *Tecoma stans* (**d**)–(**f**) aqueous extract

Figure 13.3a–c shows the SEM results of AgNps synthesized with *Agastache mexicana* extract. As can be seen, there is a low density of nanoparticles, which are in small agglomerates because organic compounds encapsulate the nanoparticles. These results are in good agreement with the UV-Vis results discussed previously. Energy Dispersive Spectrometer (EDS) chemical analysis shows only silver, a result of the bioreduction process. Moreover, carbon signal was detected from the organic compounds after the sample dried. When *Tecoma stans* extract (Fig. 13.3d–f) was used, a high concentration of silver nanoparticles was obtained, which were well dispersed. It is further noted that most of the nanoparticles have a similar size. Regarding the shape, most of the synthesized nanoparticles are spherical. EDS analysis also shows the signals of silver and carbon, due to bioreduction and organic compounds residues from the *Tecoma stans* extract, respectively.

To confirm the silver ions reduction to metallic silver, X-ray diffraction analysis was carried out. The diffractograms obtained with both plant extracts types (Fig. 13.4a and b, respectively) show five main reflections belonging to the silver face-centered cubic phase. This structure was indexed with JCPDS card No. 01-087-0720. The peaks are located at 38°, 44°, 64°, 77° and 82°. These reflections correspond to the planes (111), (200), (220), (311), and (222), respectively. Furthermore, the average crystal size was calculated using the Scherrer formula. The average width of the (111) reflection plane was used. The result showed that the crystal size was 16 and 20 nm when the extracts of *Agastache mexicana* and *Tecoma stans* were used, respectively. The findings confirm the nanocrystals formation. In the diffraction pattern of AgNps synthesized with *Tecoma stans* extract, the presence of silver chloride peaks were also observed. The latter was formed with the chlorine

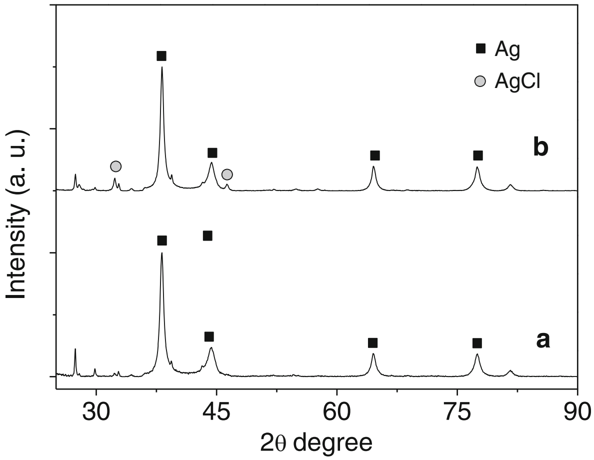

Fig. 13.4 X-Ray diffraction patterns of silver nanoparticles obtained with (**a**) *Agastache mexicana* and (**b**) *Tecoma Stans* aqueous extract

Fig. 13.5 Antibacterial activity of silver nanoparticles against *E. coli* bacteria

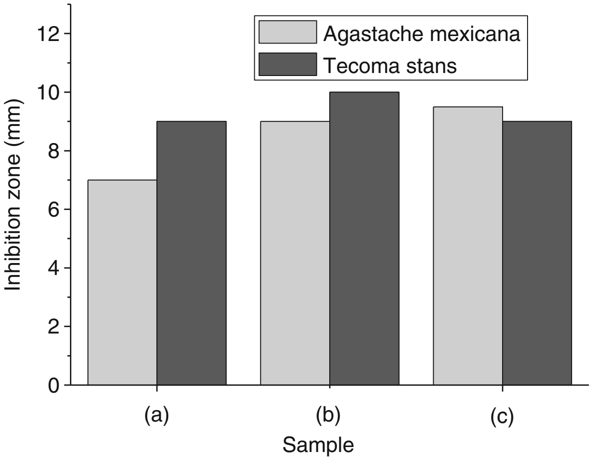

ions from organic compounds, as has been previously reported [12, 20]. Finally, in both diffractograms, the unindexed peaks from organic compounds were observed, as has been reported in other studies [27, 28].

The antibacterial activity of AgNps was analyzed against *E. coli* bacteria. To perform this analysis, the disk diffusion method was used, and the different concentrations of extract were employed (1, 1.25 and 1.5 g of the plant). The results are shown in Fig. 13.5. Both plants extracts were analyzed to determine whether they have antibacterial properties. The results showed that none of the extracts have antibacterial properties. The largest inhibition zone shown by AgNps synthesized with *Agastache mexicana* was 9.5 mm. This result was obtained when 1.5 g of leaves were used to prepare the extract. For *Tecoma stans*, the largest inhibition zone was

10 mm. The better results obtained in the *Tecoma stans* plant extract are attributed to high concentration of AgNps synthesized, as shown in the UV-Vis and SEM results. In this case, 1.25 g of leaves were used. Similar results have been reported by Miri et al. [20]. The antibacterial activity of nanoparticles depends directly on the concentration, size, and shape [29, 30]. Consequently, different behaviors in each sample were observed.

13.4 Conclusions

The synthesis of silver nanoparticles was carried out using aqueous extracts of *Agastache mexicana* and *Tecoma stans* leaves. Both plants have in their chemical composition compounds with the ability to reduce and stabilize silver nanoparticles. Concentration, size, and shape of nanoparticles depend largely on the concentration of extract used, which was demonstrated by UV-Vis. The increase in the concentration of $AgNO_3$ does not show a favorable effect on the characteristics of the synthesized, such as size, shape and size distribution of nanoparticles obtained. On the other hand, the morphology of the nanoparticles was mostly spherical with some irregular morphologies, which was shown by SEM and TEM. Finally, silver nanoparticles synthesized with *Agastache Mexicana* and *Tecoma stans* extract showed antibacterial properties against the bacteria *E. coli*.

References

1. Ajitha B, Ashok Kumar Reddy Y, Sreedhara Reddy P (2014) Biosynthesis of silver nanoparticles using Plectranthus amboinicus leaf extract and its antimicrobial activity. Spectrochim Acta A Mol Biomol Spectrosc 128:257–262
2. Guidelli EJ, Ramos AP, Zaniquelli MED, Baffa O (2011) Green synthesis of colloidal silver nanoparticles using natural rubber latex extracted from Hevea brasiliensis. Spectrochim Acta Mol Biomol Spectrosc 82:140–145
3. Song JY, Kim BS (2009) Rapid biological synthesis of silver nanoparticles using plant leaf extracts. Bioprocess Biosyst Eng 32:79–84
4. Zuas O, Hamim N, Sampora Y (2014) Bio-synthesis of silver nanoparticles using water extract of Myrmecodia pendan (Sarang Semut plant). Mater Lett 123:156–159
5. Mata R, Nakkala JR, Sadras SR (2015) Catalytic and biological activities of green silver nanoparticles synthesized from Plumeria alba (frangipani) flower extract. Mater Sci Eng C 51:216–225
6. Saxena A, Tripathi RM, Zafar F, Singh P (2012) Green synthesis of silver nanoparticles using aqueous solution of Ficus benghalensis leaf extract and characterization of their antibacterial activity. Mater Lett 67:91–94
7. Chou KS, Chang YC, Chiu LH (2012) Studies on the continuous precipitation of silver nanoparticles. Ind Eng Chem Res 51:4905–4910
8. Sileikaite A, Prosycevas I, Puiso J, Juraitis A, Guobiene A (2006) Analysis of silver nanoparticles produced by chemical reduction of silver salt solution. Mater Sci 12:287–291

9. Shivaji S, Madhu S, Singh S (2011) Extracellular synthesis of antibacterial silver nanoparticles using psychrophilic bacteria. Process Biochem 46:1800–1807
10. Yamal G, Sharmila P, Rao KS, Pardha-Saradhi P (2013) Yeast extract mannitol medium and its constituents promote synthesis of Au nanoparticles. Process Biochem 48:532–538
11. Syed A, Saraswati S, Kundu GC, Ahmad A (2013) Biological synthesis of silver nanoparticles using the fungus Humicola sp. and evaluation of their cytoxicity using normal and cancer cell lines. Spectrochim Acta Mol Biomol Spectrosc 114:144–147
12. Rajaram K, Aiswarya DC, Sureshkumar P (2015) Green synthesis of silver nanoparticle using Tephrosia tinctoria and its antidiabetic activity. Mater Lett 138:251–254
13. Vimala RTV, Sathishkumar G, Sivaramakrishnan S (2015) Optimization of reaction conditions to fabricate nano-silver using Couroupita guianensis Aubl. (leaf & fruit) and its enhanced larvicidal effect. Spectrochim Acta Mol Biomol Spectrosc 135:110–115
14. Gogoi N, Babu PJ, Mahanta C, Bora U (2015) Green synthesis and characterization of silver nanoparticles using alcoholic flower extract of Nyctanthes arbortristis and in vitro investigation of their antibacterial and cytotoxic activities. Mater Sci Eng C 46:463–469
15. Sadeghi B, Rostami A, Momeni SS (2015) Facile green synthesis of silver nanoparticles using seed aqueous extract of Pistacia atlantica and its antibacterial activity. Spectrochim Acta Mol Biomol Spectrosc 134:326–332
16. Sadeghi B, Gholamhoseinpoor F (2015) A study on the stability and green synthesis of silver nanoparticles using Ziziphora tenuior (Zt) extract at room temperature. Spectrochim Acta Mol Biomol Spectrosc 134:310–315
17. Pourmortazavi SM, Taghdiri M, Makari V, Rahimi-Nasrabadi M (2015) Procedure optimization for green synthesis of silver nanoparticles by aqueous extract of Eucalyptus oleosa. Spectrochim Acta Mol Biomol Spectrosc 136:1249–1254
18. Joseph S, Mathew B (2015) Microwave assisted facile green synthesis of silver and gold nanocatalysts using the leaf extract of Aerva lanata. Spectrochim Acta Mol Biomol Spectrosc 136:1371–1379
19. Kathiravan V, Ravi S, Ashokkumar S, Velmurugan S, Elumalai K, Khatiwada CP (2015) Green synthesis of silver nanoparticles using Croton sparsiflorus morong leaf extract and their antibacterial and antifungal activities. Spectrochim Acta Mol Biomol Spectrosc 139:200–205
20. Miri A, Sarani M, Bazaz MR, Darroudi M (2015) Plant-mediated biosynthesis of silver nanoparticles using Prosopis farcta extract and its antibacterial properties. Spectrochim Acta Mol Biomol Spectrosc 141:287–291
21. Ibarra-Alvarado C, Rojas A, Mendoza S, Bah M, Gutiérrez DM, Hernández-Sandoval L, Martínez M (2010) Vasoactive and antioxidant activities of plants used in Mexican traditional medicine for the treatment of cardiovascular diseases. Pharm Biol 48:732–739
22. Munuswamy H, Thirunavukkarasu T, Rajamani S, Elumalai EK, David E (2013) A review on antimicrobial efficacy of some traditional medicinal plants in Tamilnadu. J Acute Dis 2:99–105
23. Das V, Dash S, Sahoo DC, Mohanty A (2010) Evaluation of methanolic bark extract of Tecoma stans Linn, for wound healing in albino rats. Int J Pharm Technol 2:735–742
24. Rajamurugan R, Thirunavukkarasu C, Sakthivel V, Sivashanmugam M, Raghavan CM (2013) Phytochemical screening, antioxidant and antimicrobial activities of ethanolic extract of Tecoma stans flowers. Int J Pharma Bio Sci 4:124–130
25. Amin M, Iram F, Iqbal M, Saeed MZ, Raza M, Alam S (2013) Arabinoxylan-mediated synthesis of gold and silver nanoparticles having exceptional high stability. Carbohydr Polym 92:1896–1900
26. Peng H, Yang A, Xiong J (2013) Green, microwave-assisted synthesis of silver nanoparticles using bamboo hemicelluloses and glucose in an aqueous medium. Carbohydr Polym 91: 348–355
27. Ashokkumar S, Ravi S, Kathiravan V, Velmurugan S (2015) Synthesis of silver nanoparticles using A. indicum leaf extract and their antibacterial activity. Spectrochim Acta Mol Biomol Spectrosc 134:34–39

28. Bindhu MR, Umadevi M (2015) Antibacterial and catalytic activities of green synthesized silver nanoparticles. Spectrochim Acta Mol Biomol Spectrosc 135:373–378
29. Morones JR, Elechiguerra JL, Camacho A, Holt K, Kouri JB, Ramirez JT, Yacaman MJ (2005) The bactericidal effect of silver nanoparticles. Nanotechnology 16:2346–2353
30. Pal S, Tak YK, Song JM (2007) Does the antibacterial activity of silver nanoparticles depend on the shape of the nanoparticle? A study of the gram-negative bacterium Escherichia coli. Appl Environ Microbiol 73:1712–1720

Chapter 14
Synthesis and Thermal Characterization of Hydroxyapatite Powders Obtained by Sol-Gel Technique

Y. Jiménez-Flores, N. Camacho, J.B. Rojas-Trigos, and M. Suárez

Abstract The development of bioactive materials presents an interesting and an extremely relevant problem to solve, in the development of customized cranial and maxillofacial prosthesis, bioactive coating, and cements, for example. In such areas, one of the more employed materials is the synthetic hydroxyapatite, due to its proved biocompatibility with the human body; however, there are few studies about the thermal affinity with the biological surroundings, and most of them are centered in the thermal stability of the hydroxyapatite instead of its transient thermal response. In the present paper, the synthesis and physical–chemical characterization of hydroxyapatite samples, obtained by the sol-gel technique employing ultrasonic mixing, are reported. Employing X-ray diffraction patterns, XEDS and FTIR spectra, the crystal symmetry, chemical elements, and the present functional groups of the studied samples were determined and found to correspond to those reported in the literature, with a stoichiometry close to the ideal for biological applications. Additionally, by means of the photoacoustic detection and infrared photothermal radiometry (IPTR) techniques, the thermal response of the samples was obtained. Analyzing the photoacoustic data, the synthetized samples show photoacoustic opaqueness, responding in the thermally thick regime in the measurement range, and their thermal effusivity was also determined, having values of 1.47 folds the thermal effusivity of the mandibular human bone. Finally, from the IPTR measurements, the thermal diffusivity and thermal conductivity of the samples were also determined, having good agreement with the reported values for synthetic hydroxyapatite. The structural and thermophysical properties of the here reported samples show that the synthesized samples have good thermal affinity with the mandibular human bone tissue, and are suitable for biomedical applications.

Y. Jimenez-Flores • J.B. Rojas-Trigos (✉) • M. Suárez
Instituto Politécnico Nacional, Centro de Investigación en Ciencia Aplicada y Tecnología Avanzada, Unidad Legaria, Legaria 694, Col. Irrigación, Miguel Hidalgo, 11500 México, Distrito Federal, Mexico
e-mail: rjosebruno@yahoo.com.mx

N. Camacho
Instituto Politécnico Nacional, ESIME-SEPI, Unidad Profesional "Adolfo López Mateos", Edif. 5, 3er Piso, Col. Lindavista, Gustavo A. Madero, 07738 México, Distrito Federal, Mexico

R. Pérez Campos et al. (eds.), *Characterization of Metals and Alloys*, DOI 10.1007/978-3-319-31694-9_14

Keywords Hydroxyapatite • Infrared photothermal radiometry • Photoacoustic technique • Sol-gel technique • Thermal properties

14.1 Introduction

In recent years, the use of hydroxyapatite (HA) and hydroxyapatite nanoparticles (n-HAp) to develop composite materials for biomedical applications (which includes bone cements, dental implants and bone substitution, medical tools, and bioactive coatings, among others) has been increasing due to the great biological and structural similarities to bone tissue, which allows good compatibility with the biological systems. There are several methodologies to synthetize HA and n-HAp reported elsewhere [1–4], enabling the combination with binders, polymers, and structural proteins to increase the mechanical properties of such biocomposites without compromising their stoichiometry and biocompatibility characteristics. In this work, the sol-gel technique was chosen because of its relative simplicity and great versatility, being one of the most used methods in HA and n-HAp synthesis [5–7]. Among the structural, morphological, chemical, and biological characterizations, thermal characterization of HA and hydroxyapatite compounds can also be found. Thermal characterization of HA and hydroxyapatite compounds is essential to evaluate the thermal stability of the final synthesis product, usually determined by thermogravimetric and differential thermal analysis techniques, as a function of the synthesis parameters, for example. Specifically for bioactive coatings, cements and bone substitution applications, the determination of thermal properties is quite relevant in order to obtain materials able to emulate the heat exchange between the bone tissue and the native surroundings, being the thermal diffusivity and the thermal effusivity the main properties to keep in mind. For these purposes, the photothermal techniques have proven to be an excellent choice for the determination of the thermal properties, not only because of its great accuracy and versatility, but also because these techniques are non-invasive, non-destructive methods to study the thermal response of materials. In the present work, the synthesis of two kinds of HA samples obtained by the sol-gel method is reported based on the methodology reported by Degirmenbasi et al. [7]. One of the samples was synthesized following, as close as possible, the published methodology while for the other one, the mixture stage was improved by increasing the drip rate at which the precursor solutions were added, and substituting the stirring process by ultrasonic agitation during the mixture stage. The structural and chemical characterization of both samples was performed. Furthermore, the thermal effusivity was determined by means of the frequency-resolved photoacoustic technique (PA-*f*) and the thermal diffusivity and thermal conductivity were determined by the infrared photothermal radiometry (IPTR) technique. Finally, the difference between the data obtained from both samples was discussed.

14.2 Experimental

The studied samples were obtained by the sol-gel technique employing, as precursors, aqueous solutions of calcium nitrate tetrahydrated ($Ca(NO_3)_2{\cdot}4H_2O$); sodium phosphate (Na_3PO_4); and sodium hydroxide (NaOH), purchased in Sigma-Aldrich to ensure an appropriate purity in the chemical precursors. One of the samples was obtained following, as possible, the methodology reported by Degirmenbasi et al. [7]; meanwhile, the other one was obtained modifying the mixing stage in the Degirmenbasi methodology. In both cases, the NaOH solution was employed not only to maintain the pH at 10, but also to balance the chemical reaction.

14.2.1 Materials

As was mentioned before, the synthesis procedure was based on the methodology reported by Degirmenbasi et al. [7], starting with aqueous solutions of $Ca(NO_3)_2{\cdot}4H_2O$, Na_3PO_4, and NaOH in deionized (DI) water, as precursors. The reaction equation considered is expressed in Eq. (14.1):

$$10Ca(NO_3)_2{\cdot}4H_2O+6Na_3PO_4+2NaOH \rightarrow Ca_{10}(PO_4)_6(OH)_2+20NaNO_3+40H_2O. \tag{14.1}$$

In Table 14.1, the volumes and molarities of the precursor solutions are shown. Here, two different ways to perform the chemical reaction are described:

- Method A. The $Ca(NO_3)_2{\cdot}4H_2O$ solution was added drop-by-drop (at a rate of six drops per minute) to the mixture of Na_3PO_4 and NaOH solutions under continuous stirring at room temperature, following the methodology reported by Degirmenbasi et al. [7].
- Method B. The $Ca(NO_3)_2{\cdot}4H_2O$ solution was added drop-by-drop (at a rate of 12 drops per minute) to the mixture of Na_3PO_4 and NaOH solutions under ultrasonic agitation, at room temperature.

For both methods, the resultant suspension was then filtered on a Büchner and washed with DI water until a white moist gel was obtained (xerogel). Subsequently, the obtained gel was pre-heated by a linear ramp (1.33 °C/min) until a temperature of 80 °C was reached, and dried at such temperature for 24 h, the final product being a brittle white ceramic (dry gel). In Fig. 14.1, the appearance of the synthesized samples is shown.

Table 14.1 Volumes and molarities of the precursor solutions used during the synthesis

Solution	Volume (mL)	Molarity (M)
$Ca(NO_3)_2{\cdot}4H_2O$	80	0.1
Na_3PO_4	48	0.1
NaOH	16	0.1

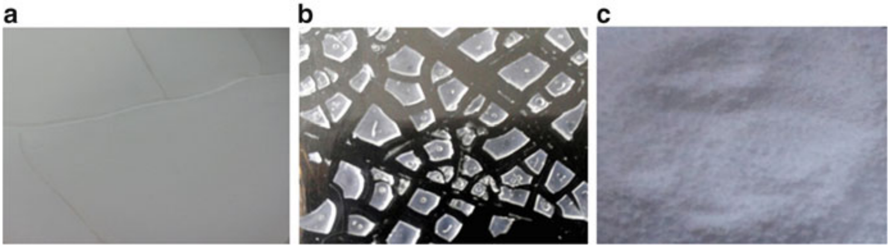

Fig. 14.1 Typical appearance of the: (**a**) The xerogel, (**b**) The dry gel (ceramic), and (**c**) pulverized sample

14.2.2 Structural Characterization

For the structural characterization, sections of the obtained samples were taken and pulverized to obtain fine, compact powder and X-ray diffraction patterns were obtained using an X-ray diffractometer (Bruker, D-8 Advance) employing the Cu-K line ($\lambda = 1.5418\,\text{Å}$). The samples were scanned in the Bragg angle, 2Θ, ranging from 19° to 90°.

14.2.3 Surface Morphology

Surface micrographs of samples were taken employing a scanning electron microscope (JEOL, JSM-6390LV), with analytical capabilities, using an accelerating voltage of 15 kV.

14.2.4 Chemical Characterization

The spectral transmittance of powdered samples was obtained using a Fourier transform infrared (FTIR) spectrophotometer (Shimadzu, IRAffinity-1S), ranging from 4000 to 750 cm^{-1}.

Complementary to the FTIR spectra analysis, the elemental chemical composition of the condensed samples was obtained using an energy dispersive X-ray spectroscopy (XEDS) system, integrated into SEM microscope (JEOL, JSM-6390LV), which employs an Si-Li detector (Oxford Pentafet, mod. 7582). The XEDS spectra were obtained for acceleration voltages ranging from 0.2 to 15 kV.

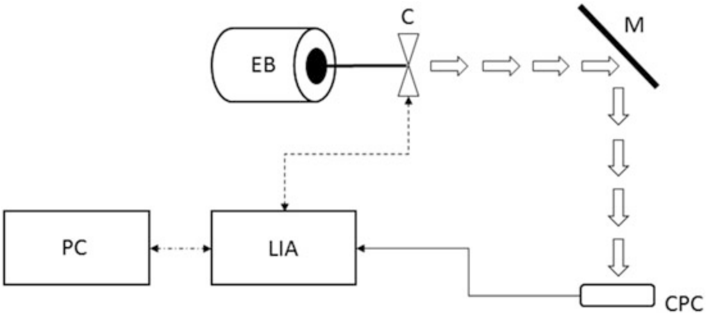

Fig. 14.2 Components of the PA measurement system: *EB* excitation beam, *C*, mechanical modulator, *M* mirror, *LIA* lock-in amplifier, *CPC* closed photoacoustic cell

14.2.5 Thermal Characterization

For the thermal characterization of the synthetized samples, the frequency-resolved photoacoustic detection (PA-*f*) and IPTR techniques were employed [8–12], to determine the thermal effusivity and the transient thermal response of the samples of interest at room temperature $T_{\text{room}} = 25\,^{\circ}\text{C}$. For analysis purposes, a reference sample was also analyzed to obtain relative thermal effusivity values. In this work, a sample of mandibular human bone was used as the reference.

14.2.5.1 Photoacoustic Detection

The PA-*f* signals were obtained by means of a typical photoacoustic measurement system (Fig. 14.2) which includes a PA measurement cell (MTEC, mod. 300), a 400 mW Ar^{+} laser (Omnichrome, 543-200 MA) as excitation beam source, and a mechanical chopper (Stanford Research Systems, SR-540). The signals for the modulation frequency ranged from 50 to 400 Hz and were amplified and filtered by a lock-in amplifier (Stanford Research Systems, SR-850). The measurement system is controlled by a standard PC.

The excitation beam from the source EB is modulated by the chopper C, and the pulse train is re-directed by the mirror M to the PA measurement cell CPC. The output from the CPC is amplified by the lock-in LIA, and sent to the PC for storage and further analysis.

14.2.5.2 Infrared Photothermal Radiometry

As it was mentioned before, the transient thermal response was sensed by an IPTR measurement system, described schematically in Fig. 14.3.

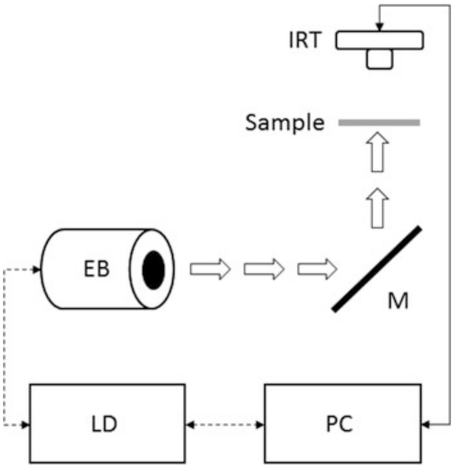

Fig. 14.3 Components of the IPTR measurement system: *EB* excitation beam source, *LD* laser driver, *M* mirror, *IRT* infrared sensor

The excitation beam from the source EB is modulated electronically by a TTL signal generated by the PC, interfaced with the laser driver (LD). The pulse train is re-directed by the mirror M to the sample, and the temperature in the opposite surface of the sample is sensed by the infrared sensor (IRT). The signal from the IRT is sent to the PC for storage and further analysis.

The IPTR measurement system includes a 100 mW diode laser (Lasever Inc 12030701, $\lambda = 405\,\text{nm}$) as excitation beam source controlled by a microcontroller (TTL ATmega 8535) as driver, and an IR sensor (PSC-SSS IR Sensor). The measurement system is controlled by a standard PC.

14.3 Results and Discussion

As it was mentioned in Sect. 14.2, two methods in the mixing stage were employed (methods A and B). Henceforth, the condensed samples (white ceramics) processed by methods A and B will be called CS-A and CS-B samples, respectively; whereas the powders obtained by mechanical pulverization, as PS-A and PS-B samples, correspondingly.

14.3.1 Structural Characterization

The X-ray diffractograms of PS-A and PS-B samples are displayed in Fig. 14.4, showing the peaks corresponding to (0 0 2), (3 1 0), (2 2 2), and (0 0 4) diffraction planes.

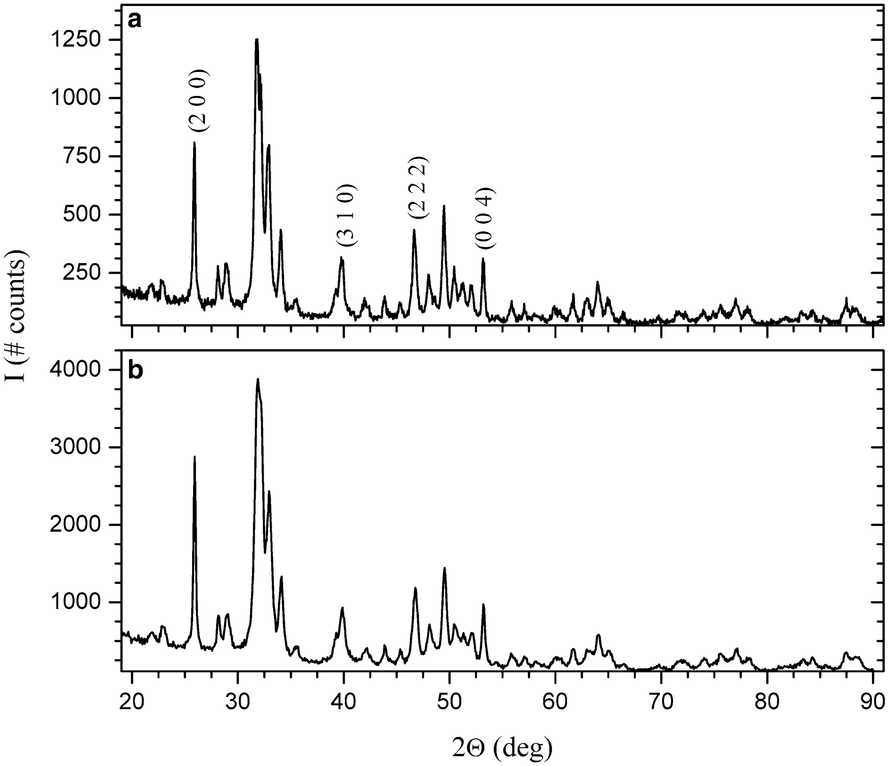

Fig. 14.4 Diffractograms of the studied samples: (**a**) PS-A and (**b**) PS-B

The average values of crystallite size, D, and the fraction crystallinity, X_c, of the samples were determined using the diffraction peaks corresponding to (0 0 2), (3 1 0), (2 2 2), and (0 0 4) planes (equally weighed) and the Scherrer equation [13].

$$D = \frac{K\lambda}{\beta \cos \Theta} \tag{14.2}$$

$$X_c = \left(\frac{0.24}{\beta}\right)^3 \tag{14.3}$$

Where K is an instrumental factor close to the unity, and β is the full width at half maximum. The data was compared with the crystallographic charts published in the database of the International Centre for Diffraction Data (ICDD, entry no. 00-009-0432), having good agreement along the peaks in range. Tables 14.2 and 14.3 summarize the results.

Making a comparison between the determined average values for the crystallite size and fraction crystallinity, with average values for D (27.6 nm) and X_c (0.35) reported by Degirmenbasi et al. [7], the here presented values were found to be lower

Table 14.2 Matching results from the analysis of the X-ray diffractogram samples

Sample	Chemical formula	Crystal system	No. of peaks matched
PS-A	$Ca_5(PO_4)_3(OH)$	Hexagonal	52
PS-B	$Ca_5(PO_4)_3(OH)$	Hexagonal	38

Table 14.3 Average values of β, D, and X_c of the PS-A and PS-B samples

Sample	$\langle\beta\rangle$	$\langle D\rangle$	$\langle X_c\rangle$
PS-A	0.392	25.739	0.23
PS-B	0.478	22.799	0.13

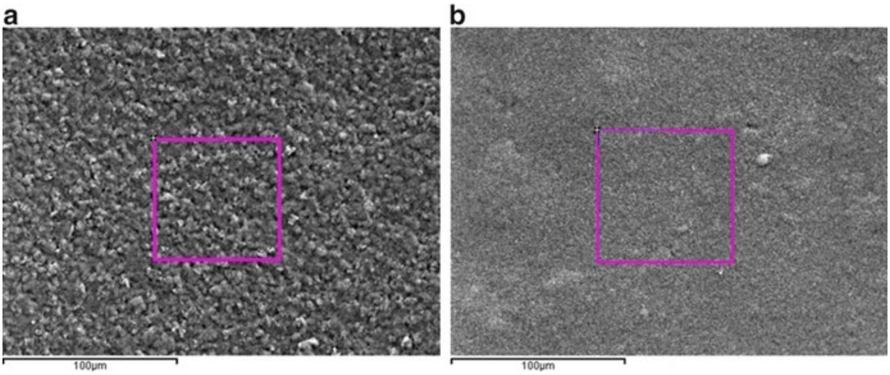

Fig. 14.5 SEM surface micrographs of the studied samples: (**a**) CS-A and (**b**) CS-B. The *rectangles* mark the XEDS scanning area

than the expected. The higher differences were observed in sample PS-B, where higher dripping rates along ultrasonic agitation were used during the corresponding synthesis procedure. A possible explanation, since the pH values are fixed at 10, is that the higher dripping rate and ultrasonic agitation prevent the increase of crystallite size, by adding energy to the system during the chemical reaction, which makes the chemical reaction faster.

14.3.2 Surface Morphology

The surface morphology of CS-A and CS-B samples can be observed in Fig. 14.5.

The micrographs show that the sample CS-A has a homogeneous granular surface morphology (which increases the superficial area), while sample CS-B exhibits a much more compact surface. This is consistent with the results obtained by XRD. This difference in the surface morphology, as will be discussed later, has a great relevance in the ability of such surfaces to exchange heat with their surroundings.

14.3.3 Chemical Characterization

The spectral transmittance of PS-A and PS-B, obtained by FTIR, is displayed in Fig. 14.6, and the presence of the functional groups OH^-, $PO_4{}^{-3}$, and $CO_3{}^{-2}$ was detected and identified in both samples, as Table 14.4 specifies it.

As can be seen from Fig. 14.6 and Table 14.4, the signals associated with hydroxyapatite are all present [6, 14–16]. Also, there is a well-defined signal associated with the presence of the HPO_4 ion, which is related to a calcium deficiency, and therefore the molar ratio $nR = n_{Ca}/n_P$ lies between 1.5 and 1.67 [15, 16] (n_{Ca} and n_P being the number of moles of Ca and PO_4, respectively). Appropriate molar ratio values are extremely important to evaluate if the compound

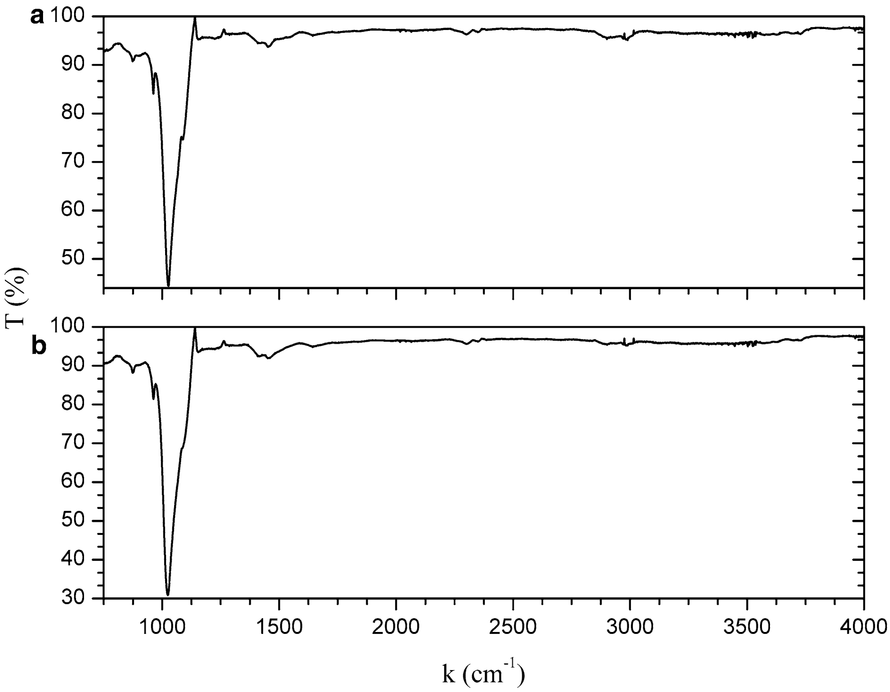

Fig. 14.6 Transmittance spectra of the studied samples: (**a**) PS-A and (**b**) PS-B by FTIR

Table 14.4 Functional groups present in samples

Signal band position (cm^{-1})	Associated functional group	Sample	
		PS-A	PS-B
2983, 2900, 1644	OH^-	Present	Present
1028	PO_4^{-3}	Present, strong	Present, strong
1450	CO_3^{-2}	Present	Present
873	HPO_4^{-2}	Present	Present

Table 14.5 Elemental chemical composition of samples CS-A and CS-B by XEDS

	% Weight		% Atomic	
Element	CS-A	CS-B	CS-A	CS-B
Ca	32.98	35.30	17.64	20.16
P	17.15	18.35	11.86	13.56
O	41.54	46.34	55.64	66.29
C	8.33	0	14.86	0

is suitable for biomedical applications. Some authors mention that compounds with nR values less than 1 are not suitable for biological applications [7, 15], $nR = 1.67$ being the optimal value for these.

On the other hand, the elemental chemical composition of CS-A and CS-B samples was obtained from the XEDS spectra, and the results are summarized in Table 14.5.

The XEDS results reveal the presence of calcium, phosphorus, and oxygen in a proportion consistent to the desired stoichiometry, corroborating the results obtained by FTIR. Also there is no detectable presence of sodium in any of the samples and, therefore, the washing procedure was shown to be effective for removing sodium byproducts. However, sample CS-A also shows the presence of carbon (not detectable in sample CS-B) even when, during the synthesis process, the exposition to the atmosphere was carefully limited in all cases. It is possible that the presence of carbon in the sample CS-A is due to atmospheric carbon absorption after the synthesis was finished, which would be also consistent with the observed surface morphology.

14.3.4 Thermal Characterization

From the non-stationary thermal response of PS-A and PS-B samples, the thermal diffusivity and the thermal conductivity were determined, as well as the relative thermal effusivity (at room temperature). Those thermophysical parameters are fundamental to analyze the thermal affinity to the human bone, and therefore, provides an insight to the possible thermal affinity with the biological surroundings.

14.3.4.1 Photoacoustic Detection

As it can be seen from the PA signals for PS-A and PS-B samples (Fig. 14.7), the amplitude $|S|$ of the photoacoustic signal shows a dependence on the modulation frequency as f^{-1}, whereas the photothermal phase shift shows no dependence on the modulation frequency (not shown here).

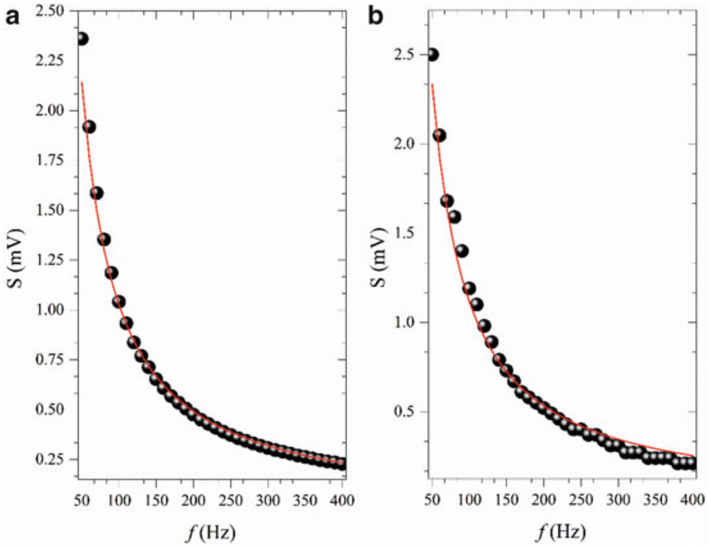

Fig. 14.7 PA amplitude of: (**a**) PS-A and (**b**) PS-B. The continuous line represents the best fit

The PA signals show that the samples exhibit photoacoustic opaqueness, behaving as thermally thick samples, and therefore, the PA signal has a modulation frequency dependence expressed by Eq. (14.4) as follows:

$$S = K_{\text{cell}} \cdot \frac{(1 - \mathrm{R})}{\varepsilon \cdot f}. \tag{14.4}$$

Here, R and ε are the reflectivity and the thermal effusivity of the sample, respectively; and K_{cell} is an instrumental factor. The reflectivity of the samples was determined by spectral reflectance measurements on a UV-Vis spectrophotometer (E-Chrome Tech, CT-5). A reflectivity value of 0.87 was found for samples PS-A and PS-B, and 0.75 for the reference sample, at 457 nm (corresponding to the excitation beam wavelength).

Normalizing the PA signals from PS-A and PS-B samples by the reference PA signal, the relative thermal effusivity ε_r was determined for the studied samples, having corresponding values of 1.56 and 1.47, respectively. These results are consistent with the morphology shown in Sect. 14.3.2, because a more compact structure implies higher thermal diffusivity, and consequently, a lower thermal effusivity.

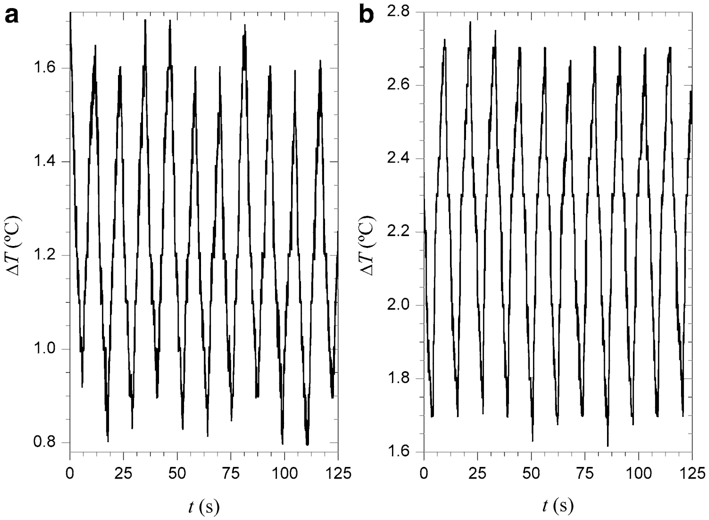

Fig. 14.8 Temperature oscillations measured by the IPTR system of PS-A (**a**) and PS-B (**b**) samples at 100 mHz

14.3.4.2 Infrared Photothermal Radiometry

In Fig. 14.8, the temperature variations ΔT from room temperature, measured at the modulation frequency $f = 100\,\text{mHz}$, are presented.

The observed variations in the amplitude of the temperature oscillations in Fig. 14.8 are due to the self-mixing effect, occurred by the overexcitement of the laser source (induced by partial reflections from the incidence surface impinging into the laser objective). To estimate the thermal diffusivity α and the thermal conductivity κ of the samples from the IPTR measurements, a theoretical model was employed to perform a parametric fitting considering an overall heat exchange coefficient $h \approx 1.75\times 10^{-3}\,\text{W}\,(\text{cm}^2\,\text{K})^{-1}$. A more extensive discussion about the general model (developed by solving the one-dimension parabolic heat diffusion equation under homogenous Robin boundary conditions) can be consulted elsewhere [11, 12].

$$\Delta\text{T}(t,l)\text{=A}\sum_m \frac{C_m}{\sigma_m}\left[\frac{\exp\left(i\omega_m t\right)}{\left[\left(1+r_m^2\right)\sinh\sigma_m l + 2r_m\cosh\sigma_m l\right]}\right] \tag{14.5}$$

Here, l is the sample thickness (0.2 cm), $\omega_m = 2\pi m f$, m is an integer, C_m are the Fourier coefficients spanning the modulated heat source, A is a proportionality constant, $\sigma_m = (i\omega_m/\alpha)$ is the square of the so-called complex diffusion coefficient, and $r_m = h(\kappa\sigma_m)^{-1}$. The results of the parametric fitting are summarized in Table 14.6.

Table 14.6 Thermal properties determined by IPTR

Sample	$\alpha(\mathrm{cm^2\,s^{-1}})$	$\kappa(\mathrm{W\,(cm\,K)^{-1}})$	ε^{a} $(\mathrm{W\ s^{1/2}\,(cm^2\,K)^{-1}})$
PS-A	2.92×10^{-3}	5.1×10^{-3}	0.094
PS-B	3.41×10^{-3}	5.2×10^{-3}	0.089

[a] Calculated by $\varepsilon = \kappa\alpha^{-1/2}$

From the thermal effusivity calculated from the estimations of α and κ, obtained from the parametric fitting of the IPTR measurements, and the relative thermal effusivity ε_r, obtained from PA-*f*, the thermal effusivity of mandibular human bone was estimated to be $0.06\,\mathrm{W\,s^{1/2}\,(cm^2\,K)^{-1}}$ (consistent to reported values for thermal effusivity of human bone tissue [17]). The values of the thermal properties are in good agreement to the reported values for HAp [18, 19] in the literature. The remark here is that the more compact sample (PS-B) exhibits a higher thermal diffusivity value than the less compact sample, but with similar value for the thermal conductivity. Therefore, considering that the PS-B sample has the smaller thermal effusivity, and the smaller superficial area (which signify a lower total heat loss), there will be more thermal affinity with the human bone tissue.

14.4 Conclusions

The synthesis of two kinds of hydroxyapatite powder samples was successfully achieved employing the sol-gel technique, for the same chemical precursors but under different mixing conditions, at room temperature. The X-ray diffraction patterns, the FTIR and XEDS spectra confirm that the structure and chemical composition of the samples corresponds to hydroxyapatite in the hexagonal phase, with a stoichiometry close to the ideal for biomedical applications but exhibiting a calcium deficiency; however, the sample synthesized under ultrasonic mixing at higher dripping rate reveals a more compact surface morphology and no tendency to absorb atmospheric carbon, contrary to the sample synthetized following closely the reported mixing process. From the photoacoustic and IPTR data, the principal thermal properties were determined, and although the thermal properties values for both samples have good agreement to the reported values for hydroxyapatite, the sample synthesized under ultrasonic mixing at higher dripping rate presents a higher thermal diffusivity value, and a thermal effusivity value closer to the typical value of the thermal effusivity of mandibular human bone. Hence, the samples of HAp synthesized at higher dripping rate under ultrasonic agitation have a closer thermal affinity with the mandibular human bone, keeping an appropriate stoichiometry for biomedical applications, such as bioactive coatings or bone cements, for example.

Acknowledgements This work has been supported partially by CONACYT and COFAA-IPN (through the BEIFI Program), Mexico. Authors also thank to Kelly J. Martínez-González for helping with measurements.

References

1. Riman RE, Suchanek WL, Byrappa K, Chen C-W, Shuk P, Oakes CS (2002), Solution synthesis of hydroxyapatite designer particulates. Solid State Ion 151:393–402
2. Pataquiva-Mateus AY, Ferraz MP, Monteiro FJ (2013), Nanoparticles of hydroxyapatite: preparation, characterization and cellular approach – an overview. Revista Mutis 3(2):43–57
3. Banerjee A, Bandyopadhyay A, Bose S (2007), Hydroxyapatite nanopowders: synthesis, densification and cell–materials interaction. Mater Sci Eng C 27:729–735
4. Nasser Mostafa Y (2005), Characterization, thermal stability and sintering of hydroxyapatite powders prepared by different routes. Mater Chem Phys 94:333–341
5. Ferraz MP, Monteiro FJ, Manuel CM (2004), Hydroxyapatite nanoparticles: a review of preparation methodologies. J Appl Biomater Biomech 2:74–80
6. Taheriana MH, Tamizifara M, Fathib MH, Maleki Ghalehc H (2012), Modified sol-gel method for synthesis of hydroxyapatite-bioglass nanocomposite. In: Proceedings of the 4th international conference on nanostructures (ICNS4), Institute for Nanoscience & Nanotechnology (INST), Sharif University of Technology, Tehran, Iran
7. Degirmenbasi N, Kalyon DM, Birinci E (2006), Biocomposites of nanohydroxyapatite with collagen and poly(vinyl alcohol). Colloids Surf B 48:42–49
8. Rosencwaig A, Gersho A (1976), Theory of the photoacoustic effect with solids. J Appl Phys 47(1):64–69
9. M. Heya et al (2003), Real-time monitoring of the surface modification of root dentin using photoacoustic spectroscopy and photothermal radiometry. In: Rechmann P, Fried D, Hennig T (eds) Lasers in dentistry IX. Proceedings of SPIE, Vol. 4950. The International Society for Optical Engineering
10. Bento AC (1995), Thermal wave non-destructive thickness measurements of hydroxyapatite coatings applied to prosthetic hip stems. J Mater Sci Mater Med 6:335–339
11. Rojas-Trigos JB, Bermejo-Arenas JA, Marín E (2012), On heat transfer through a solid slab heated uniformly and periodically: determination of thermal properties. Eur J Phys 33:135–148
12. Rojas-Trigos JB, Calderón A (2012), Heat diffusion in a homogenous slab with an arbitrary periodical heat source: the case of heat source with square wave modulation function. Lat Am J Phys Educ 6(1):59–66
13. Rusu VM, Ng C-H, Wilke M, Tiersch B, Fratzl P, Peter MG (2005), Size-controlled hydroxyapatite nanoparticles as self-organized organic–inorganic composite materials. Biomaterials 26:5414–5426
14. Miller A, Wilkins CH (1952), Infrared spectra and characteristic frequencies of inorganic ions. Anal Chem 24(8):1253–1294
15. Berzina-Cimdina L, Borodajenko N (2012), Research of calcium phosphates using Fourier transform infrared spectroscopy. In: Theophile T (ed) Infrared spectroscopy - materials science, engineering and technology. InTech, Croatia (European Union)
16. Agrawal K, Singh G, Puri D, Prakash S (2011), Synthesis and characterization of hydroxyapatite powder by sol-gel method for biomedical application. J Miner Mater Charact Eng 10(8):727–734
17. Stanczyk M, Telega JJ (2002), Modelling of heat transfer in biomechanics – a review Part II. Orthopaedics. Acta Bioeng Biomech 4(2):3–33
18. Coelho TM, Nogueira ES, Weinand WR, Lima WM, Steimacher A, Medina AN, Baesso ML, Bento AC (2007), Thermal properties of natural nanostructured hydroxyapatite extracted from fish bone waste. J Appl Phys 101:084701–1
19. Calderón A, Peña Rodríguez G, Muñoz Hernández RA, Díaz Góngora JAI, Mejía Barradas CM (2004), Thermal diffusivity in bone and hydroxyapatite. In: Medical physics: eighth mexican symposium on medical physics, vol. 724, No. 1, AIP Publishing, Melville, NY

Part VII

Characterization of Materials for Industrial Applications

This part includes three chapters related to the characterization of materials of industrial applications.

The first chapter is about synthesis and characterization of Pt-TiO_2 and Au-TiO_2 synthetized by a microwave-assisted sol-gel method and characterized by means of X-ray diffraction techniques (XRD) and ultraviolet–visible spectroscopy (UV-Vis). Titanium dioxide (TiO_2) has been widely used and investigated due to the stability of its chemical structure, biocompatibility, and its physic, optic, and electric properties. Its photocatalytic properties have been utilized in many environmental applications to remove pollutants in water and air.

The second chapter includes a study of a detector based on a boron doped hydrogenated amorphous silicon film (a-Si:B:H), employed as a thermosensor layer in bolometer arrays. The sensitive layer was deposited on the micromachined silicon wafer by plasma enhanced chemical vapor deposition technique. Thermal detector has played an important role in the exploration and exploitation of infrared radiation. These detectors have been developed for infrared (IR) spectroscopy, medical examinations, security systems, scientific applications, and for many consumer products.

The third chapter studies the influence of drilling parameters by electrical discharge machining (EDM) on the high strength low alloy (HSLA) steel microstructure. Pieces made of HSLA steels are difficult to machine by conventional cutting methods. In order to overcome this limitation, it is proposed to use electric discharge machining (EDM) on HSLA steels. This research work is focused on studying the effect of parameters on the microstructures due to thermal effects that are present during removal of material, in order to achieve a better understanding of the parametric selection during machining of high technology components.

The main techniques used in the characterization of these materials are:

- X-ray diffraction (XRD).
- Raman spectroscopy.
- Ultraviolet–visible spectroscopy (UV-Vis).
- Radio frequency (RF).
- Energy-dispersive X-ray spectroscopy (EDS).
- Scanning electron microscopy (SEM).
- Optical microscopy.

Chapter 15
Microwave Assisted Sol-Gel Synthesis and Characterization of M–TiO_2 (M=Pt, Au) Photocatalysts

R. Hernández, S.M. Durón-Torres, K. Esquivel, and C. Guzmán

Abstract Pt–TiO_2 and Au–TiO_2 photocatalysts have been synthetized by a microwave assisted sol-gel method and characterized by means of X-ray diffraction (XRD) techniques and UV-Vis diffuse reflectance spectroscopy. Particle sizes have been determined by means of Scherrer equation. Depending on the weight percentage of dopant, some changes in the band gap energy can be observed. X-ray diffractions patterns were recorded to study the formation of TiO_2 crystalline species. The diffraction peaks detected after the calcination process indicate the presence of the crystalline anatase phase and no presence of rutile phase was observed. For the Pt–TiO_2 sample, the peaks detected in 2θ (39.4°, 45.9°, and 67°) indicate the presence of particles of metallic platinum. For the Au–TiO_2 sample, the peaks detected in 2θ (38°, 44.2°, 64.4°, and 77.2°) indicate the presence of particles of metallic gold. The Pt-loaded samples have a crystal size slightly smaller than the Au-loaded samples, from 3.09 to 4.74 nm. UV-Vis DSR technique was used to study the influence of metal load and type. The band gap decreases according to the metal load; it shows that at higher metal load (5 %) the band gap changes from 3.2 eV (pure TiO_2) to 2.98 eV and 3.04 eV for the samples loaded with gold and platinum, respectively. For the Pt–TiO_2 sample, the band gap varies from 3.04 eV (5 wt.%) to 3.2 eV (0.1 wt.%), the same behavior is found on the Au-loaded samples, with a band gap energy variation from 2.98 eV (5 wt.%) to 3.21 eV (0.01 wt.%).

Keywords Titanium dioxide • Photocatalysis • Pt-TiO_2 • Au-TiO_2 • X-ray diffraction

---

R. Hernández • S.M. Durón-Torres • C. Guzmán (✉)
UACQ—UAZ, CU Siglo XXI Edificio 6, Km 6 Carr. Zac – Gdl, La Escondida Zacatecas, Zac C.P. 96160, Mexico
e-mail: rafita_bot@hotmail.com; cgm1909@hotmail.com; cguzman@uaq.mx

K. Esquivel
Facultad de Ingeniería, Universidad Autónoma de Querétaro, Cerro de las Campanas, C.P. 76000 Santiago de Querétaro, Queretaro, Mexico

R. Pérez Campos et al. (eds.), *Characterization of Metals and Alloys*, DOI 10.1007/978-3-319-31694-9_15

15.1 Introduction

Titanium dioxide (TiO_2) has been widely used and investigated due to the stability of its chemical structure, biocompatibility, and its physical, optic, and electric properties. Its photocatalytic properties have been utilized in many environmental applications to remove pollutants in water and air. The main feature of the photocatalytic process is that it breaks the complex organic molecules into simple molecules such as carbon dioxide and water; this process has been used for a variety of applications such as decomposition of organic pollutants [1].

TiO_2 exists as three different polymorphs: anatase, rutile, and brookite. The most stable form of TiO_2 is rutile. Anatase form has a crystalline structure corresponding to a tetragonal system and is used mostly in photocatalytic applications due to its photocatalytic activity under UV radiation. Rutile form of TiO_2 has a tetragonal structure and brookite an orthorhombic structure [2].

Typically, titanium dioxide is an n-type semiconductor. The energy gap is 3.2 eV for anatase, 3.0 eV for rutile, and 3.2 eV for brookite. Generally, anatase form of TiO_2 is desired owing to its higher photo activity, high superficial area, and low toxicity. Due to its high photoinduced reduction, anatase form is a better photocatalytic material for degradation of organic pollutants in both water and air [3].

The application of TiO_2 is limited due to its low photoactivity under visible light. Therefore, attempts to extend its photoactivity to the visible region have been made by substitution of Ti^{4+} on the crystalline structure for metallic ions such as Fe, Ni, Co, Ag, Au, Pt, etc. [4–8].

Sol-gel synthesis technique has been widely used for catalysts development, such as TiO_2 nanopowders. In comparison to traditional techniques, it offers many advantages. For instance, in supported metals catalysis, the active metal and support can be prepared in a single step. This allows an economy in the catalyst preparation [9].

In the present paper, we report the synthesis and characterization of Pt–TiO_2 and Au–TiO_2 catalyst prepared by the microwave assisted sol-gel technique.

15.2 Experimental

The synthesis of the TiO_2 catalyst was carried out by dissolving the titanium precursor (titanium isopropoxide) in an organic solvent (isopropanol, 99.9 %), and the titanium solution was magnetically stirred for 20 min under nitrogen atmosphere. The hydrolysis process was then performed by adding water into the precursor/solvent solution and was magnetically stirred for 1 h in a dark box. For the Pt-modified TiO_2 samples, the platinum precursor was $H_2Pt(NO_2)_2SO_4$, and for the Au-modified TiO_2 samples, the precursor was $NaAuCl_4\cdot 2H_2O$. These precursors were added by dissolving them into the water used for the hydrolysis process in different weight percentage (0.01, 0.05, 0.1, 0.5, 1, and 5 wt.%). The obtained sol was transferred into Teflon vessels and placed on a microwave reaction system. The heating procedures were carried for 30 min at 220 °C. The obtained product was filtered and dried at room temperature for 12 h. A calcination process was carried out at 450 °C for 3 h to promote the anatase form of TiO_2.

15.2.1 Photocatalyst Characterization

Elemental analysis was performed by Energy Dispersive X-ray Spectroscopy (EDS) (EDS Oxford Inca X-Sight coupled to an MT 1000, Hitachi). Particle size was determined using Scherrer equation [10]. Band gap energy (Ebg) values were determined from diffuse reflectance measurements (Cary 5000 UV-Vis-NIR Varian spectrophotometer) by applying Kubelka–Munk [11] function and Tauc's graphics.

15.3 Results and Discussion

15.3.1 X-ray Diffraction

X-ray diffractions (XRDs) patterns were recorded to study the formation of TiO_2 crystalline species. The diffraction peaks detected after the calcination process indicate the presence of the crystalline anatase phase and no presence of rutile phase was observed. For the Pt–TiO_2 samples (Fig. 15.1a), the peaks detected in 2θ (39.4°, 45.9°, and 67°) indicate the presence of particles of metallic platinum. For the Au–TiO_2 samples (Fig. 15.1b), the peaks detected in 2θ (38°, 44.2°, 64.4°, and 77.2°) indicate the presence of particles of metallic gold. As can be seen from the XRD patterns crystallinity of the photocatalyst decreased on platinum and gold doping.

The crystallite sizes were calculated by the Scherrer equation and are compiled in Table 15.1. The Au-loaded samples have a crystallite size between 4.74 nm for 5 wt.% of gold and 3.17 nm for 0.05 wt.% of gold. The Pt-loaded samples have sizes between 3.17 and 10.7 nm for 5 and 0.1 wt.% of platinum, respectively.

15.3.2 Raman Spectroscopy

Another technique widely used to characterize various polymorphs of TiO_2 is Raman spectroscopy. Some advantages of using this technique are the sample preparation and the simplicity with which each spectrum is collected [12].

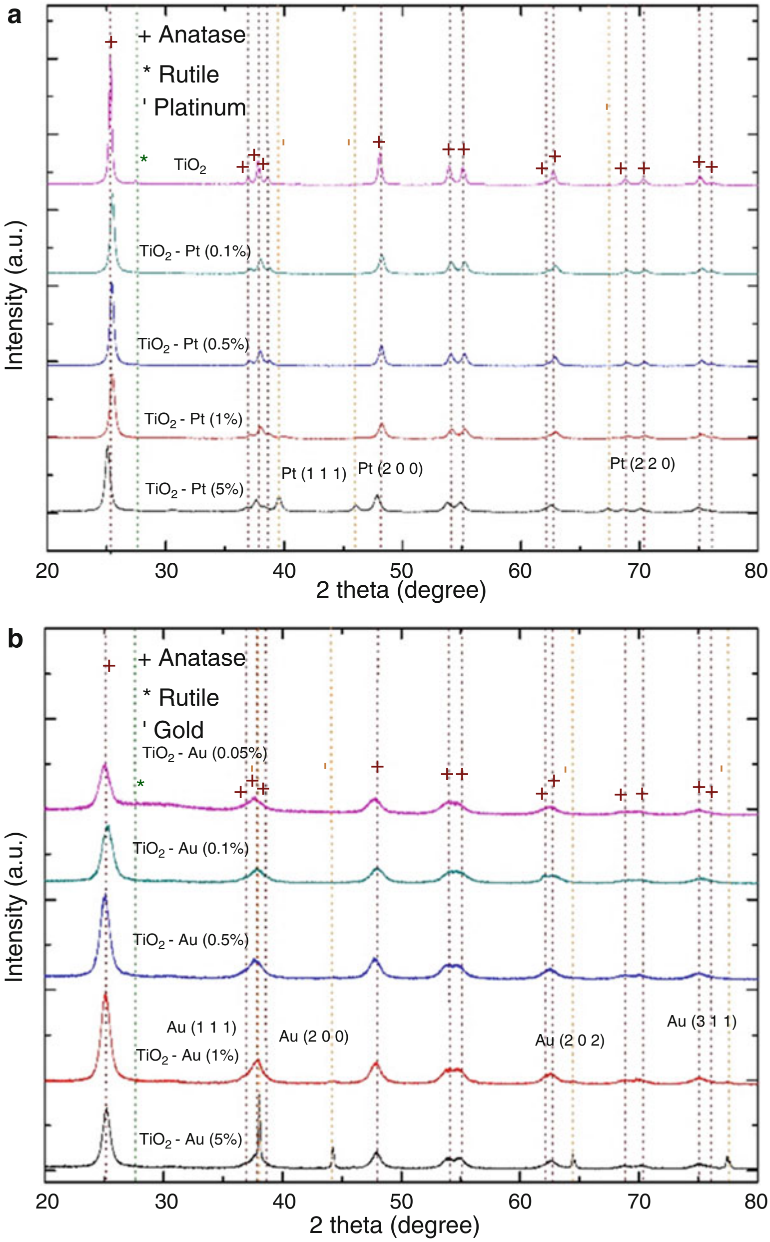

Fig. 15.1 XRD diffraction patterns of synthetized TiO_2, (**a**) Pt-TiO_2 and (**b**) Au-TiO_2

Table 15.1 Crystallite sizes

Photocatalyst	Crystallite sizes (nm)	Crystallite sizes (nm)	Photocatalyst
TiO_2–Au (5 %)	4.74	3.71	TiO_2–Pt (5 %)
TiO_2–Au (1 %)	4.10	11.2	TiO_2–Pt (1 %)
TiO_2–Au (0.5 %)	3.97	10.8	TiO_2–Pt (0.5 %)
TiO_2–Au (0.1 %)	3.59	10.7	TiO_2–Pt (0.1 %)
TiO_2–Au (0.05 %)	3.17	–	–

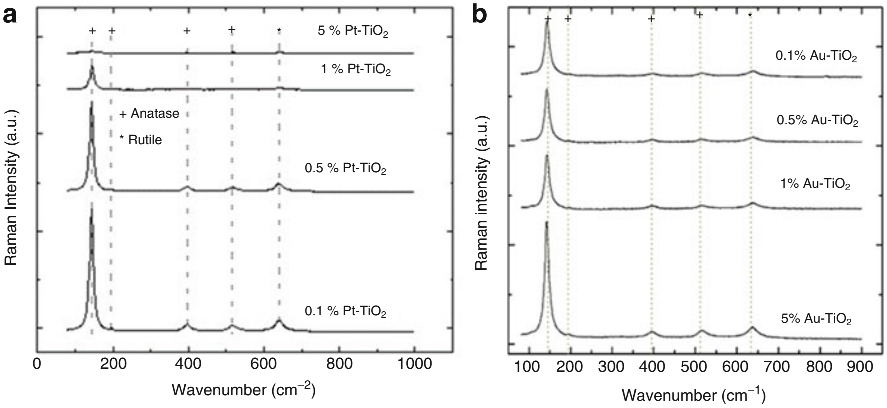

Fig. 15.2 Raman spectroscopy patterns of synthetized TiO_2, (**a**) Pt-TiO_2 and (**b**) Au-TiO_2

For anatase, characteristic vibration modes are located at 144, 197, 399, 515, and 639 cm^{-1}. For rutile, there are four modes at 143, 235, 447, and 612 and a broadband at 826 cm^{-1}. Brookite has 36 vibration modes, some of them located at 132, 138, 152, 197, 212, 245, 278, 325, 370, 406, 457, 500, 550, 587, and 630 cm^{-1}. The most intense vibration mode for anatase is at 144 cm^{-1}, and the weakest for rutile is at 143 cm^{-1} [13].

Figure 15.2 shows the Raman spectra for samples synthetized at different dopant loads. In order to make identification of the vibration modes easer, the spectra were arbitrarily displaced on the vertical axis. Pt-loaded samples show a spectrum with well-defined vibration modes assigned to anatase (144, 197, 399, and 515 cm^{-1}) and rutile (612 cm^{-1}). Au-loaded samples show a spectrum with well-defined vibration modes assigned to anatase (144, 197, 399, 515, and 639 cm^{-1}) and no characteristic vibration modes of rutile or brookite were observed.

15.3.3 Band Gap Measurements

UV-Vis DSR technique was used to study the influence of metal load and type. The Tauc's graphics showed in Fig. 15.3a, b for Pt–TiO_2 and Au–TiO_2, respectively, are utilized to estimate the band gap energies by means of Kubelka–Munk method.

The band gap energies estimated are listed in Table 15.2. The band gap decreases according to the metal load; it shows that at higher metal load (5 %) the band gap changes from 3.2 eV (pure TiO_2) to 2.98 eV and 3.04 eV for the samples loaded with gold and platinum, respectively.

For the Pt–TiO_2 sample, the band gap varies from 3.04 eV (5 wt.%) to 3.2 eV (0.1 wt.%), the same behavior is found on the Au-loaded samples, with a band gap energy variation from 2.98 eV (5 wt.%) to 3.21 eV (0.01 wt.%). It is interesting to note that the band gap energies increase on metal doping for both platinum and gold.

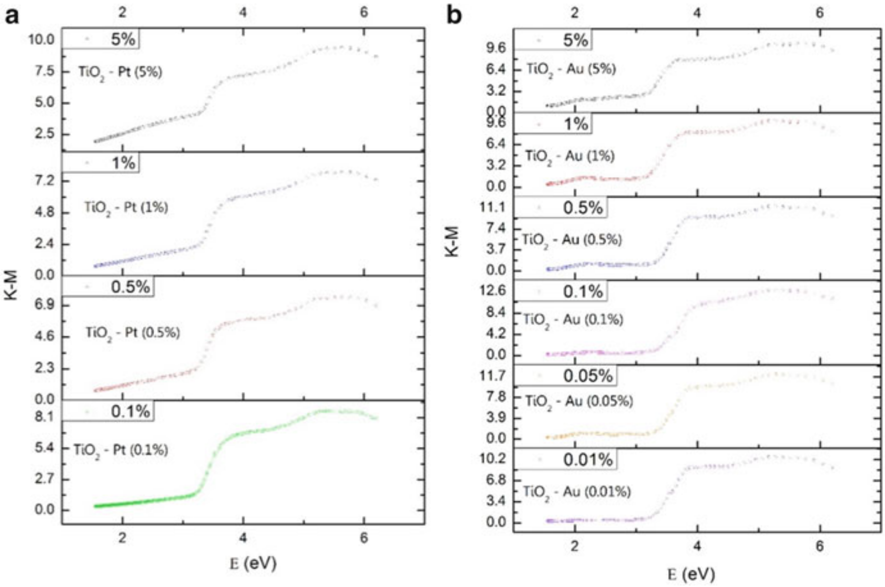

Fig. 15.3 Raman spectroscopy patterns of synthetized TiO_2, (**a**) Pt-TiO_2 and (**b**) Au-TiO_2

Table 15.2 Band gap energies

Photocatalyst	Band gap (eV)	Band gap (eV)	Photocatalyst
TiO_2–Au (5 %)	2.98	2.87	TiO_2–Pt (5 %)
TiO_2–Au (1 %)	3.05	3.09	TiO_2–Pt (1 %)
TiO_2–Au (0.5 %)	3.23	3.05	TiO_2–Pt (0.5 %)
TiO_2–Au (0.1 %)	3.24	3.15	TiO_2–Pt (0.1 %)
TiO_2–Au (0.05 %)	3.19	–	–

15.4 Conclusions

Microwave assisted synthesis methodology can be applied for the preparation of TiO_2-based photocatalysts and modify its properties using a dopant metal such as Au and Pt. With these metals it is possible to observe a change in the band gap energy, which can be related to the metal load in the photocatalyst.

References

1. Macwan DP, Dave PN, Chaturvedi S (2011) A review on nano-TiO2 sol–gel type syntheses and its applications. J Mater Sci 11:3669–3686
2. Pelaez M, Nolan NT, Pillai SC, Seery MK, Falaras P, Kontos AG, Dunlop PSM, Hamilton JWJ, Byrne JA, O'Shea K, Entezari MH, Dionysiou DD (2012) A review on the visible light active titanium dioxide photocatalysts for environmental applications. Appl Catal B Environ 125:331–349
3. Esquivel K, Nava R, Zamudio-Méndez A, González MV, Jaime-Acuña OE, Escobar-Alarcón L, Peralta-Hernández JM, Pawelec B, Fierro JLG (2013) Microwave-assisted synthesis of (S)Fe/TiO2 systems: effects of synthesis conditions and dopant concentration on photoactivity. Appl Catal B Environ 140:213–224
4. Khan AW, Ahmad S, Mehedi Hassan M, Naqvi AH (2014) Structural phase analysis, band gap tuning and fluorescence properties of Co doped TiO2 nanoparticles. Opt Mater 38:278–285
5. Kobayashi Y, Ishii Y, Yamane H, Watanabe K, Koda H, Kunigami H, Kunigami H (2014) Fabrication of TiO2/Pt core–shell particles by electroless metal plating. Colloids Surf Physicochem Eng Asp 448:88–92
6. Lei XF, Xue XX, Yang H (2014) Preparation and characterization of Ag-doped TiO2 nanomaterials and their photocatalytic reduction of Cr(VI) under visible light. Appl Surf Sci 321:396–403
7. Liu Q, Ding D, Ning C, Wang X (2015) Black Ni-doped TiO2 photoanodes for high-efficiency photoelectrochemical water-splitting. Int J Hydrog Energy 40:2107–2114
8. Park H, Park Y, Kim W, Choi W (2013) Surface modification of TiO2 photocatalyst for environmental applications. J Photochem Photobiol Photochem Rev 15:1–20
9. Sánchez E, López T, Gómez R, Bokhimi, Morales A, Novaro O (1996) Synthesis and characterization of sol–gel Pt/TiO2, catalyst. J Solid State Chem 122:309–314
10. Patterson AL (1939) The Scherrer formula for X-ray particle size determination. Phys Rev 56:978–982
11. Escobedo Morales A, Sánchez Mora E, Pal U (2007) Use of diffuse reflectance spectroscopy for optical characterization of un-supported nanostructures. Rev Mex Fis Suppl 53:18–22
12. Leyva-Porras C, Toxqui-Teran A, Vega-Becerra O, Miki-Yoshida M, Rojas-Villalobos M, García-Guadarrama M, Aguilar-Martinez JA (2015) Low-temperature synthesis and characterization of anatase TiO2 nanoparticles by an acid assisted sol–gel method. J Alloys Compd 647:627–636
13. Zhang J, Li M, Feng Z, Chen J, Li C (2006) UV raman spectroscopic study on TiO2. Phase transformation at the surface and in the bulk. J Phys Chem B 110:927–935

Chapter 16
Micromachined and Characterization of Cooled a-Si:B:H Microbolometer Array in the Terahertz Region

A. Orduña, C.G. Treviño, A. Torres, R. Delgado, and M.A. Dominguez

Abstract This work presents the fabrication and characterization of microbolometer array operating in the Terahertz region. The detector is based on a boron-doped hydrogenated amorphous silicon film (a-Si:B:H) employed as a thermosensor layer in bolometers arrays. The sensitive layer was deposited on the micromachined silicon wafer by the plasma-enhanced chemical vapor deposition technique. The array was fabricated using conventional lithography. The 5×5 microbolometer array was characterized at a base temperature of $-196\,^{\circ}\mathrm{C}$, using liquid nitrogen, under black body radiation from 0.1 to 10 THz frequency range. The responsivity value of 0.187 A/W is obtained at 3 V.

Keywords Bolometer • Micromachined • Radiation • Terahertz frequency • Responsivity

16.1 Introduction

For many years, thermal detectors have played an important role in the exploration and exploitation of infrared radiation, operated at room temperature and with cooled thermal detectors. Infrared radiations are the electromagnetic waves in the wavelength, from 0.75 to 1000 μm or 1.65 eV–1.24 meV. A wide variety of applications are used, and new applications are constantly being developed. The advances in

---

A. Orduña (✉) • R. Delgado
Centro de Investigación en Biotecnología Aplicada (CIBA), del Instituto Politécnico Nacional, IPN, Tlaxcala, Tlax. 72197, Mexico
e-mail: abdueve@hotmail.com

C.G. Treviño • A. Torres
Instituto Nacional de Astrofísica, Óptica y Electrónica Apdo Postal 51 y 216, Puebla Pue 72000, Mexico

M.A. Domínguez
Centro de Investigaciones en dispositivos Semiconductores, Instituto de Ciencias, BUAP, Puebla 72570, Mexico

R. Pérez Campos et al. (eds.), *Characterization of Metals and Alloys*, DOI 10.1007/978-3-319-31694-9_16

detector fabrication technology and microelectronics process technology have led to the development of a large format array of IR detectors [1]. These detectors have been developed for infrared (IR) spectroscopy, medical examinations [2, 3], security systems [4], scientific applications, using nanostructural materials [5], and many consumer products. Detection mechanisms of infrared may be classified into two groups: thermal detection and photon detection. Thermal detectors convert radiated power into a more readily measured parameter; three types exist: thermopile detectors [6], pyroelectric detectors [7], and resistive bolometers [8, 9]. All thermal detectors convert incident radiation into heat, thereby raising the temperature of the detector element. This change in temperature leads to a change in the measurable property of the material, such as the electrical resistance (bolometers) or spontaneous polarization (pyroelectric detectors).

Bolometers employ an electrical resistance thermometer to measure the temperature of the radiation absorber, heated by incoming radiation usually in the infrared and microwave regions of the electromagnetic spectrum and cooled by thermal conduction through its electrical lead wires. Bolometers are discrete semiconductor or superconductor elements used to measure temperature; their performance is characterized by the temperature coefficient of resistance (TCR), typically IR absorbing areas are formed by a micromachined membrane suspended usually by two or more arms in the same plane over etched pits on the substrate. An efficient good thermal insulation is usually obtained by micromachined, depositing a film resistor onto a thermally and electrically insulated membrane, obtaining an increment in the detectivity of detector. Typical membrane materials are silicon nitride or silicon oxide. In this paper, we describe the design, micromachined, and characterization of 5×5 cooled microbolometer array, based on hydrogenated amorphous silicon thermo sensing layer boron doped to reduce the high resistance, obtaining the result of principal figures of merit from 0.1 to 10 THz frequency range.

16.1.1 Terahertz Applications

Terahertz range is broadly applied to submillimeter-wave energy that fills the wavelength range between the radiofrequency (RF) and infrared (IR) bands, a largely unexploited region of the electromagnetic spectrum. THz rays are non-ionizing and present an alternative in comparison to X-rays for imaging through paper, cloths, and many plastic materials. In particular, THz imaging holds large potential in the field of nondestructive testing, different types of detectors for the THz-IR radiation have been researched and are already used in industrial applications for THz systems [10] and microbolomter [11]. For many years, thermal detectors have played an important role in the exploration and exploitation of infrared radiation, operated at room temperature and cooled thermal detectors. Infrared radiation are the electromagnetic waves in the wavelength, from 0.75 to 1000 μm or 1.65 eV–1.24 meV. They are used in a wide variety of applications, and new applications are constantly being developed. The advances in detector fabrication technology and microelectronics process technology have led to the development of the large format array of IR detectors [1]. These detectors have been developed for infrared (IR) spectroscopy, medical examinations [2, 3], security systems [4], scientific applications, using nanostructural materials [5], and many consumer products. Detection mechanism of infrared may be classified into two groups: thermal detection and photon detection. Thermal detector converts radiated power into a more readily measured parameter; it has three types: thermopile detectors [6], pyroelectric detectors [7], and resistive bolometers [8, 9]. All thermal detectors convert incident radiation into heat, thereby raising the temperature of the detector element. This change in temperature leads to a change in the measurable property of the material, such as the electrical resistance (bolometers) or spontaneous polarization (pyroelectric detectors).

Bolometer employs an electrical resistance thermometer to measure the temperature of the radiation absorber, heated by incoming radiation usually in the infrared and microwave regions of the electromagnetic spectrum and cooled by thermal conduction through its electrical lead wires. Bolometers are discrete semiconductor or superconductor elements used to measure temperature; their performance is characterized by the temperature coefficient of resistance (TCR), typically IR absorbing areas are formed by a micromachined membrane suspended usually by two or more arms in the same plane over etched pits on the substrate. An efficient good thermal insulation is usually obtained by micromachined, depositing a film resistor onto a thermally and electrically insulated membrane, obtaining an increment in the detectivity of detector. Typical membrane materials are silicon nitride or silicon oxide.

16.1.2 Principles of Bolometer Operation

Bolometers are usually used for astrophysical applications at millimeter wavelengths and infrared imaging systems. The original bolometer was developed by Lanley in 1878. Thermosensor layer is formed by a micromachined membrane, usually suspended by arms in the same plane over etched pits on the substrate. The incident power induces an increase of the temperature of a sensitive layer absorber that is connected to the thermal bath through supports having a thermal conductance (GTh), as is shown in Fig. 16.1. The resistor should have a large temperature coefficient of resistance, defined as TCR, a small temperature increase gives rise to a significant change in the bolometer resistance. CMOS terahertz [12] and development are motivated by biology [13], astronomy [14], telecommunications [15, 16], and other disciplines. For infrared or Terahertz range, bolometers are among the most sensitive detectors available.

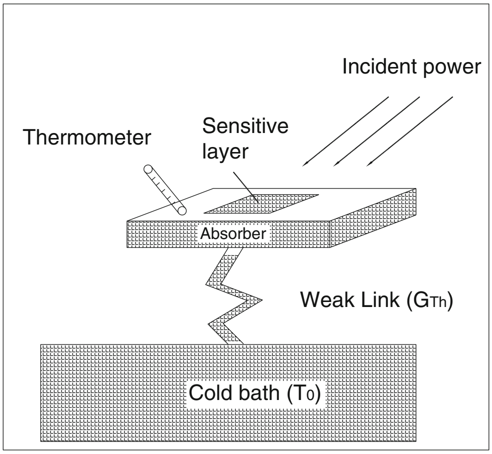

Fig. 16.1 Simplified bolometer layout

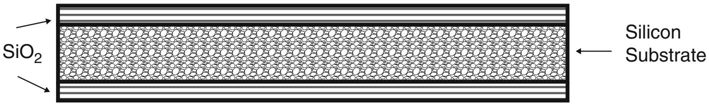

Fig. 16.2 SiO_2 thermally grown by CVD on the c-Si wafer

16.2 Experimental

The array was fabricated of 5 × 5 bolometers. The fabrication process is summarized as follow: The wafers used were cleaned in trichloroethylene, followed with acetone in an ultrasonic bath, both for 10 min of process time. Later, the samples were cleaned with the RCA1 and RCA2 solutions. The microbolometer array was fabricated on p-type crystalline silicon wafer (c-Si) in which 1 μm thick SiO_2 layer on both faces was thermally grown, as is shown in Fig. 16.2. Figure 16.3 shows a 0.4 μ-thick silicon nitride (Si_3N_4) deposited on silicon oxide layer using the low pressure chemical vapor deposition technique (LPCVD). The Si_3N_4 also works as IR absorbing material, mechanical support, and protective layer. A mask is used to define the diaphragm by removing the c-Si by wet chemical etching in a bulk micromachining process. We used the Hydrogenated amorphous silicon (a-Si:H) as a thermo-sensing film, showed high activation energy (Ea) and consequently a high value of thermal coefficient of resistance (TCR), necessary for the performance of the microbolometer, the material was deposited using plasma enhanced chemical vapor deposition technique (PECVD) at low frequency. The parameters for the a-Si:H deposition was described in previous work [17]. Finally, the electrodes were deposited by electron beam evaporation and patterning was performed by photolithography obtaining the microbolometer structure, as is shown in Fig. 16.4.

Figure 16.5 shows the packaged 5 × 5 array of bolometers, for measurements in a liquid nitrogen cryostat.

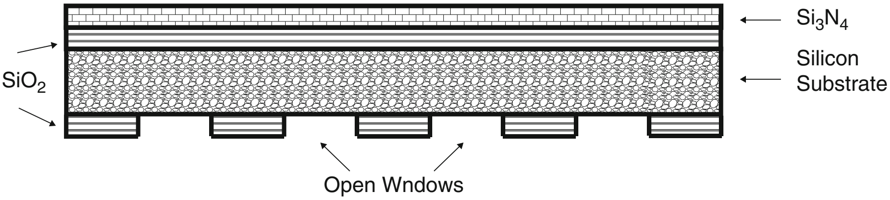

Fig. 16.3 Deposited Si_3N_4 layer and opening the window of SiO_2 by micromachined

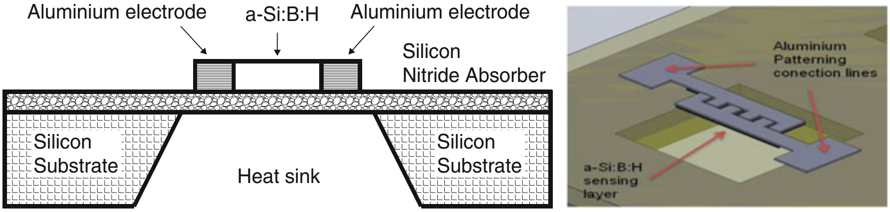

Fig. 16.4 Microbolometer structure, obtaining the deposition of a-Si:B:H sensitive layer and aluminum electrodes

Fig. 16.5 Package of microbolometers array

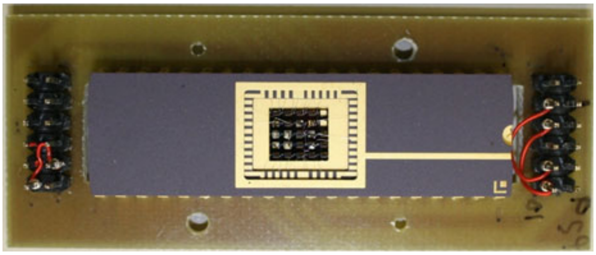

16.3 Results and Discussion

The bolometer array was set in a vacuum cryostat operating at liquid nitrogen temperature of 77 K. Normalizing the signal with respect to the detector area and illumination source bandwidth, we obtain the detectivity, which gives us information about the performance of the bolometer. The characterization of the bolometers array was performed using a commercially available black body (Mikron M300), operating at 573, 973, 1173, and 1373 K from 0.1 to 10 THz frequency range.

The response of black Polyethylene (R_{BPoly}) and Gore-Tex (R_{GTex}) were incorporated and set in front of the detector as band pass filters [18, 19] to determine the power falling in the microbolometer array, we must consider a geometrical correction defined by the detector solid angle (Ω_{det}) viewed from the black body and the black body area (A_{BB}). Therefore, the net power arriving to the microbolometer array (P_{abs}) is determined from the black body radiation ($B_{(\nu,T)}$), filters response, and geometrical correction are shown in Table 16.1.

Table 16.1 Black body emissivity and integrated power arriving to the bolometer considering geometrical correction and filter transmission

	Black body temperature (K)			
	573	973	1173	1373
Black body radiance (nW/m^2Sr)	42.29	82.43	102.71	124.07
Power incident on the bolometer (nW)	0.933	1.793	2.227	2.683

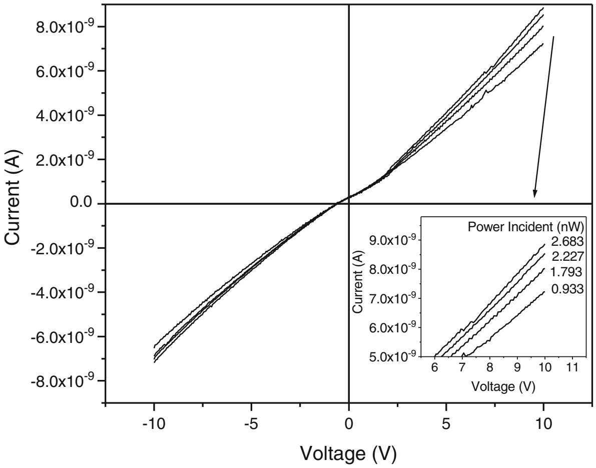

Fig. 16.6 Measurements of microbolometer current-voltage characteristics at 77 K and exposed to 0.933, 1.793, 2.227, and 2.683 nW filtered black body radiation power

$$P_{\text{abs}} = B_{(\nu,t)}\Omega_{\text{det}}A_{\text{BB}}R_{\text{BPoly}}R_{\text{GTex}} \tag{16.1}$$

The I–V characteristic curves were measured for different elements in the −10 to 10 V range and shown in Fig. 16.6. We tested microbolometers to account for edge, corner, and center response and obtained uniform response among the different elements. The I–V slope characteristics show a current increase with respect to radiation power incident as a function of bias voltage. It is important to note that the measurement was performed at 77 K. At this temperature, the DC current conductivity is generally expressed as:

$$\sigma = \sigma_0\left[-\left(\frac{\Delta}{kT}\right)^{\beta}\right] \tag{16.2}$$

where σ_0 is a characteristic value and β depends on the material and temperature range. For a-Si:B:H, β has values ranging from 0.5 at room temperature and a substantial drop down to 0.25 at low temperatures. The result is a very high

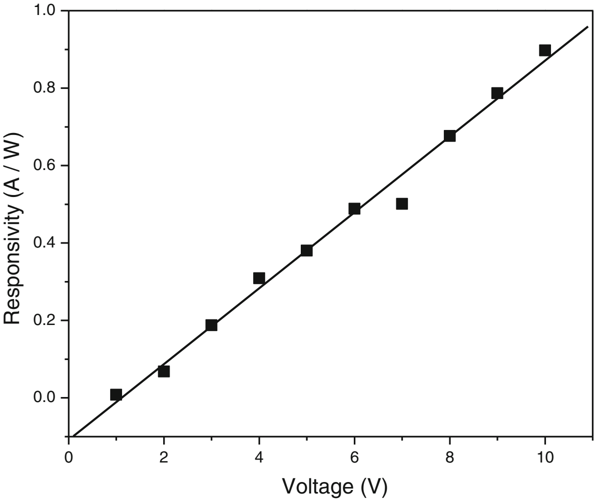

Fig. 16.7 Responsivity ($\mathfrak{R}$) of microbolometers as a function of the voltage

resistivity material in which it is difficult to obtain an Ohmic contact. The annealed aluminum metal electrodes induce crystallization in such a way that the barriers become near ohmic. The result is an Al-a-Si:B:H near Ohmic contact, which does not go through zero, but keeps the linear I–V response to be considered as a resistor.

The Responsivity ($\mathfrak{R}$) was determined by considering the ratio between generated current as a function of the incident power at a given bias voltage. The results are shown in Fig. 16.7.

From these measurements, we were able to determine a responsivity in the hundredths of milliampere per Watt range at liquid nitrogen temperature. In particular, a responsivity of 0.187 A/W is observed at 3 V. These values are large enough that the boron-doped amorphous silicon bolometer is a feasible candidate for Terahertz detection systems comparable [19, 20] with similar devices.

16.4 Conclusions

We presented the construction and characterization of a microbolometer array compatible with CMOS technology that can be used as focal plane detector in the THz region of the EM spectrum. The a-Si:B:H sensor film was prepared by PECVD, in order to obtain thermal isolation, the microbolometer was fabricated on a thick silicon nitride membrane, which was made on a p-type crystalline silicon wafer by micromachining techniques. The final array has 550 μm × 260 μm dimensions, and responsivity (from 100 GHz to 10 THz range) in the 10-1 A/W range at $-196\,^{\circ}$C was obtained. These values are large enough that the boron-doped amorphous silicon bolometer is a feasible candidate for Terahertz detection systems comparable with similar devices.

Acknowledgements The authors would like to thank Dr. David Hughes and Dr. Edgar Castillo for their technical support in the astrophysics laboratory, as well as Mr. Mauro Landa, Manuel Escobar, Adrian Itzmoyotl, and Ignacio Juarez for their assistance in the microelectronics laboratory.

References

1. Srivastav V, Sharma RK, Bhan RK, Dhar V, Venkataraman V (2013) Exploring novel methods to achieve sensitivity limits for high operating temperature infrared detectors. Infrared Phys Technol 61:290–298
2. Matsui T, Hagisawa K, Ishizuka T, Bonpei T, Ishihara M, Kikuchi M (2004) A novel method to prevent secondary exposure of medical and rescue personnel to toxic materials under biochemical hazard conditions using microwave radar and infrared thermography. IEEE Trans Biomed Eng 51:2184–2188
3. Caplan JD, Waxman S, Nesto RW, Muller JE (2006) Near-infrared spectroscopy for the detection of vulnerable coronary artery plaques. J Am Coll Cardiol 47(8) Suppl C:92–95
4. Kastek M, Madura H, Morawski M, Piatkowski T, Powiada E, Polakowski H (2007) Test bed for measurement of angular parameters of passive infrared sensors. Infrared Phys Technol 49:198–201
5. Fung CK, Xi N, Shanker B, Lai KW (2009) Nanoresonant signal boosters for carbon nanotube based infrared detectors. Nanotechnol 20:85–201
6. Wu H, Grabarnik S, Emadi A, de Graaf G, Wolffenbuttel RF (2008) A thermopile detector array with scaled TE elements for use in an integrated IR microspectrometer. J Micromech Microeng 18:064017
7. Sun XY, Luo WB, Meng J, Qing X, Fu WY, Shuai Y, Wu CG (2015) Monolithic pyroelectric infrared detectors using SiO_2 aerogel thin films. Sens Actuators A Phys 228:69–74
8. Tenconi M, for the LUMINEU collaboration (2015) LUMINEU: a pilot scintillating bolometer experiment for neutrinoless double beta decay search. Phys Proc 61:782–786
9. Richards PL (1994) Bolometers for infrared and millimeter waves. J Appl Phys 76:1–24
10. Jansen C, Wietzke S, Peters O, Scheller M, Vieweg N, Salhi M, Krumbholz N, Jördens C, Hochrein T, Koch M (2010) Terahertz imaging: applications and perspectives. Appl Opt 49:E48–E57
11. Kosarev A, Rumyantsev S, Moreno M, Torres A, Boubanga S, Knap W (2010) SixGey:H-based micro-bolometers studied in the terahertz frequency range. Solid State Electron 54:417–419
12. Seok E, Shim D, Mao C, Han R, Sankaran S, Cao C, Kenneth KO (2010) Progress and challenges towards terahertz CMOS integrated circuits. IEEE J Solid State Circ 45(8):1554–1564
13. Nagel M, Först M, Kurtz H (2006) Terahertz biosensing devices: fundamentals and technology. J Phys Condens Matter 18:601–618
14. Nakagawa T, Murakami H (2007) Mid- and far-infrared astronomy mission SPICA. Adv Space Res 40:679–683
15. Piesiewicz R, Koch JM, Schoebel J, Kürner T (2008) Performance analysis of future multi-gigabit wireless communication systems at THz frequencies with highly directive antennas in realistic indoor environments. IEEE J Sel Top Quantum Electron 14:421–430
16. Orduña-Diaz A, Treviño-Palacios CG, Rojas-Lopez M, Delgado-Macuil R, Gayou VL, Torres-Jacome A (2010) FTIR and electrical characterization of a-Si:H layers deposited by PECVD at different boron ratios. Mater Sci Eng B 174:93–96

17. Koller D, Ediss GA, Mihaly L, Carr GL (2006) Infrared measurements of possible IR filter materials. Int J Infrared Millimeter Waves 27:835–846
18. Afsar MN, Chi H, Tkachov II (1995) Millimeter-and submillimeter-wave transmission and dielectric properties of radome materials. In: SPIE's international symposium on optical science, engineering, and instrumentation. International Society of Optics and Photonics, Bellingham, pp 73–85
19. Moreno M, Kosarev A, Torres A, Ambrosio R (2007) Fabrication and performance comparison of planar and sandwich structures of microbolometers with Ge thermo-sensing layer. Thin Solid Films 515:7607–7610
20. Moreno M, Kosarev A, Torres A, Juarez I (2008) Arrays of un-cooled microbolometers based on amorphous silicon–germanium thin films deposited by plasma. J Non-Cryst Solids 354:2552–2555

Chapter 17
Influence of Drilling Parameters by EDM on the HSLA Steel Microstructure

L.M. Zúñiga, H.M. Hernández, E.E. Granda, W.N.P. Hung, and R. Muñoz

Abstract Samples of SAE 945X steel were drilled by Electrical Discharge Machining (EDM). Statistical techniques were implemented to study the process parameters on surface quality and the material removal rate, but mainly how the material microstructure is affected. Scanning electron microscopy and energy dispersive X-ray spectroscopy show a Cu-rich recast layer formed at high discharge energy. The formation of the recast layer results in shrinkage stresses due to the difference of the thermal expansion coefficient between copper and steel. This phenomenon produces micro cracks in the recast layer and the propagation of them to the base metal. Likewise, the heat affected zone has a transformation of martensitic between 14 and 35 μm in depth at low current level and at high current levels, respectively. By contrast, low energy levels show a thickening of cementite and ferrite recrystallization. In this context, this research is aimed at studying the effect of parameters by electrical discharge machining process on the microstructures due to thermal effects and copper diffusivity that are present during removal of material by the electrical discharge machining process at different energy discharge levels, with the purpose of evaluating the feasibility of this process for the machining of high-strength materials. In addition, it is postulated that at high conditions of machining, copper can be diffusive inside lattice of martensite and induce plastic strains greater than the yield stress of the steel, generating microcracks in areas with high cooling rates on the walls of the perforations.

Keywords EDM • HSLA Steel • Micro cracking • Diffusivity • Recast layer

---

L.M. Zúñiga (✉) • H.M. Hernández • R. Muñoz
COMIMSA-Saltillo Ciencia y Tecnología No. 790, Col. Saltillo 400,
25290 Saltillo, Coah., Mexico
e-mail: lmariozo55@gmail.com; luismzo02@hotmail.com

E.E. Granda
Universidad Autónoma del Estado de México, Toluca, Estado de México, Mexico

W.N.P. Hung
Texas A&M University, College Station, TX, USA

R. Pérez Campos et al. (eds.), *Characterization of Metals and Alloys*, DOI 10.1007/978-3-319-31694-9_17

17.1 Introduction

High Strength Low Alloy (HSLA) are widely used steels in the automotive industry and structural components, where weight-saving is desirable, mainly due to its high strength-to-weight ratio [1, 2]. These steels are characterized by their specific mechanical properties such as weldability, corrosion, and abrasion resistance [3, 4]. Pieces made of HSLA steels become difficult to machine by conventional cutting methods to get the final shape. When conventional methods are used, the operation cost related to wear on tools increases. In order to overcome this limitation, it is proposed to use electric discharge machining (EDM) on HSLA steels [5].

The EDM process has the advantage that, regardless of workpiece hardness, it usually minimizes distortions and vibration problems during the machining. EDM is a thermal process for machining of conductive materials [6]; therefore, it is reported [7, 8] that the machined surface is modified due to the high temperature that produces microstructural and micro hardness changes, element distribution modification, heat affected zone (HAZ), as well as thermal and tensile residual stresses. All of these effects are not desirable on automotive HSLA steel components.

It is important to mention that EDM is based on spark discharges, because each of these discharges generates a plasma channel with high temperature (above of 8000 K) and high energy density capable of melting and vaporizing the workpiece material, but also from the tool electrode [9], in which some of electrode material surface is eroded and deposited onto the workpiece surface [7] producing surface modification. Moreover, the decomposition of dielectric is another way that the workpiece surface becomes contaminated with elements such as C, O, and H [10].

The amount of material removed by a sequence of discharges between the workpiece and electrode generates a re-solidified material layer (known as recast or white layer) on the machined surface. In the literature [11], it is reported that the recast layer has complex chemical products that increase surface hardness due to the gradient transfer of elements from the electrode and the pyrolytic carbon from the dielectric [12]. The increase in hardness promotes a decrease in the ductility of the surfaces and micro cracks appears in the subsurface region. In addition, EDM discharge energy has a direct relationship between surface finish and mechanical properties on the machined surface [13].

In this context, this research aims to study the effect of parameters on the microstructures due to thermal effects that are present during the removal of material, by the EDM process, in order to achieve a better understanding of the parametric selection during machining of high-technology components.

17.2 Experimental

An experimental design 2^K was designed and conducted in random order. The factors of the experiment were selected, including discharge current intensity, duty cycle, and auxiliary capacitance. The different experimental conditions as well as their initial levels are shown in Table 17.1, resulting in sixteen runs (with a replica). The aim of this experimental set is to obtain information about the perforations integrity, measuring the material removal rate (MRR), and the ratio between exit diameter and entrance diameter, as a measure of machining precision. The "MINITAB" statistical software was utilized to design and analyze experimental data.

The parameters are chosen based on reports in literature [14, 15], and they were the independent controllable EDM parameters. As it is reported, current has a great influence on the MRR because current increases the discharge energy; the duty cycle is the percentage fraction between the pulse on-time and signal period, which also can influence the discharge energy. Moreover, the capacitance is used to stabilize the shape of pulse during the process.

Different machining tests were performed on the SODICK K1C EDM drilling system. SAE945X HSLA steel plates were used for drilling, while a brass electrode tube was chosen with a circular cross section of 0.800 mm diameter and "VITOL" as dielectric medium. The pulse frequency was fixed at 25 kHz; the gap voltage was fixed to 22 V. The resulting specimens were characterized by Philips scanning electron microscope (SEM). The base metal was also characterized by optical microscopy. After the experiment, the workpiece was examined with optical microscope OLYMPUS STM6.

Prior to drilling, two plates of steel were cut at dimensions of 47 × 24 mm. Both plates were prepared with a grinded cross section face, in order to put them face to face and ensure full contact, the two pieces were held together in a bench vice. Drills were done just in the joint between the plates, and every hole was separated by 2 mm from the next (see Fig. 17.1).

The machining time was measured by two observers using stopwatches, one observer starts to take time when the electrode begins sparking at the top of workpiece and stops when the electrode is visible out of the workpiece; the second observer starts to take time when the voltmeter shows an increase in applied voltage and stops when the voltmeter shows significant decrease in variation. The average of both sampled times was taken as the real machining time. To estimate the MRR, the entrance and exit diameters of the hole were measured, while the volume was calculated using the truncated cone formula; then it was divided by machining time, which provides the removal of material as a function of time.

Table 17.1 Experimental conditions (factors) and their levels for the initial set of experiments

Factors	Level (high and low)
Peak current (A)	35 (+) and 13 (−)
Duty cycle (%)	70 (+) and 50 (−)
Capacitance (μF)	0.22 (+) and 0.02(−)

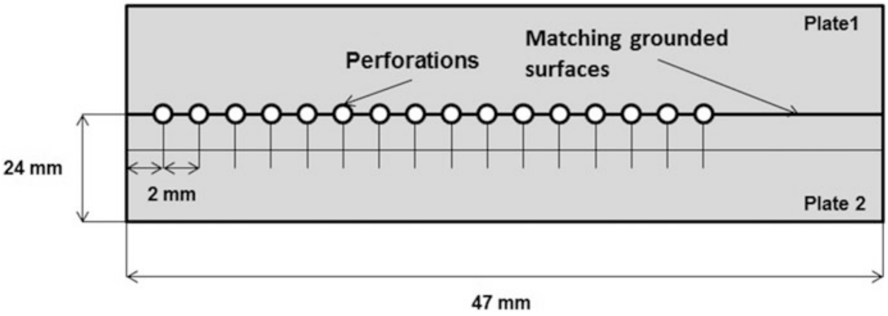

Fig. 17.1 Schematic diagram of EDM setup

Table 17.2 Chemical composition of SAE 945X HSLA by OES (wt%)

Fe	C	S	Mn	P	Si	Cr	Ni	Mo	Cu	V	Nb	Ti	W
Balance	0.19	0.003	0.8	0.014	0.11	0.01	<0.04	0.01	0.026	<0.004	<0.004	0.005	<0.002

These plates were subsequently separated and then evaluated by microscope technique, after metallographic preparation using a standard polish technique. An ultrasonic cleaner "Kendal HB-S-49DHT" in each step was used. Nital 2 % was used for chemical etching to reveal the ferrite boundary.

17.3 Results and Discussion

17.3.1 Characterization of Material and Influence of Parameter on Perforation Integrity

A specimen of HSLA steel, in as-received condition, was analyzed by optical emission spectroscopy (OES) to determine chemical compositions (see Table 17.2), and the microstructure of HSLA steel was evaluated by optical microscopy (Fig. 17.2). Phase distributions of pearlite, martensite, and ferrite embedded in a banded microstructure [16] are exhibited in Fig. 17.2 due to the direction of the rolling process. This initial microstructural condition is crucial to analyze the effects of parameters on the drilling of steel because of the characteristics in chemical composition and hardness of the phases.

Likewise, Table 17.3 shows the results of the experiments after drilling the HSLA steel. The first output parameter is machining time, then with the time machining the MRR was calculated. The value of the ratio between the exit diameter and the entrance diameter ($\phi_{\text{ext}}/\phi_{\text{ent}}$) means that as the value approaches one, the perforation has a cylindrical shape.

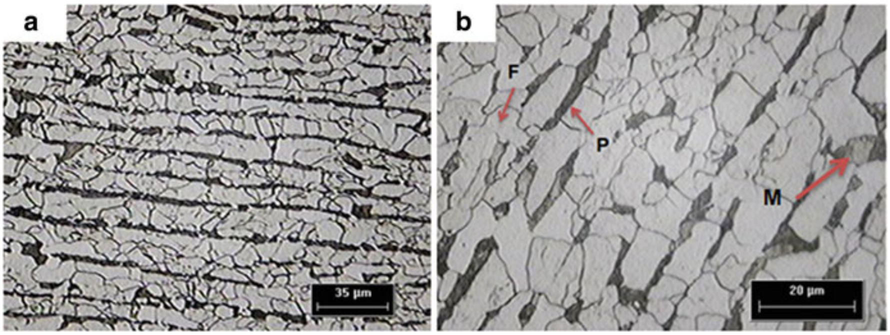

Fig. 17.2 Micrograph of SAE 945X SHLA steel as-received, (**a**) Microstructural banding and (**b**) Closed up image showing ferrite (F), pearlite (P), and martensite (M)

The regression coefficients in coded form are given in Table 17.4, which indicates the individual and interaction effects of discharge current, duty cycle, and capacitance. The predictors with significant contributions in mathematical models are identified with their P values less than 0.05.

Figure 17.3 shows the main effects and interaction effect for MRR. As can be seen in Fig. 17.3a, the discharge current has a steeper slope, which indicates a factor that has a greater impact on the output measure in Fig. 17.3b. Discharge current (I), capacitance (C), and the interaction of current-duty cycle (I-DC), current-capacitance (I-C) are the significant parameters that promote material removal. The higher the level of current and capacitance, the more material is removed (Fig. 17.3). This behavior is achieved because MRR is proportional to the amount of energy supplied during each pulse [10]. The latter agrees with literature [17], where the discharge energy (W_e in Joules) is influenced by the current intensity (I_e in Amperes), discharge voltage (U_e in volts), and time machining (t in seconds);

$$W_e = \int_0^{t_{\mathrm{on}}} U_e(t)\, I_e(t)\, dt \tag{17.1}$$

Equation (17.1) shows the discharge energy as a function of time; this behavior explains the increasing of MRR when the current and duty cycle are increased. In literature [14], it is reported that the increasing of energy discharge causes the plasma channel to expand, resulting in more material being melted. Thus, more material is removed taking less time to drill.

The relationship $\phi_{\mathrm{ext}}/\phi_{\mathrm{ent}}$ is only influenced by the interaction of duty cycle and capacitance. Figure 17.4 shows a steeper slope in duty cycle and capacitance. It appears that when the lower level for duty cycle approaches one, the perforation becomes more of a perfect cylinder. In the case of capacitance, it is the opposite result that holds true; the higher value of capacitance results closer to one. This phenomenon can be attributed to the stability of plasma arc formed in each spark; when short pulse off-time is not possible, remove the melted material, causing

Table 17.3 Experimental design and replica results

Number experiment	Current (A)	Duty cycle (%)	Capacitance (µF)	On time (µs)	Off time (µs)	Machining time (s)	MRR (mm^3/s)	Ratio (ϕ_{ext}/ϕ_{ent})
1	13	50	0.02	20	20	43	0.485	0.954
2	35	50	0.02	20	20	24	0.969	0.858
3	13	70	0.02	28	12	46	0.486	0.916
4	35	70	0.02	28	12	30	0.919	1.009
5	13	50	0.22	20	20	42	0.453	1.008
6	35	50	0.22	20	20	17	1.272	1.043
7	13	70	0.22	28	12	35	0.589	0.936
8	35	70	0.22	28	12	18	1.342	0.941
9	13	50	0.02	20	20	44	0.419	0.959
10	35	50	0.02	20	20	20	1.113	1.024
11	13	70	0.02	28	12	33	0.609	0.972
12	35	70	0.02	28	12	31	0.627	0.961
13	13	50	0.22	20	20	40	0.457	1.036
14	35	50	0.22	20	20	15	1.399	1.048
15	13	70	0.22	28	12	31	0.632	0.940
16	35	70	0.22	28	12	25	0.977	0.959

Table 17.4 Regression coefficients of experimental design

	Estimated regression coefficients for MRR		Estimated regression coefficients for ϕ_{ext}/ϕ_{ent}	
	Coefficient	*P* value	Coefficient	*P* value
Constant	0.79682	0.000[a]	0.97276	0.000[a]
Discharge current	0.2805	0.000[a]	0.0076	0.527
Duty cycle	−0.0241	0.484	−0.0185	0.146
Capacitance	0.09328	0.022[a]	0.01613	0.198
Current - Duty cycle	−0.08682	0.030[a]	0.00564	0.637
Current - Capacitance	0.07688	0.047[a]	0.00121	0.919
Duty cycle - Capacitance	0.01912	0.576	−0.02632	0.051[a]
Current - Duty cycle - Capacitance	0.00394	0.908	−0.00844	0.484

[a] Indicates the significant term

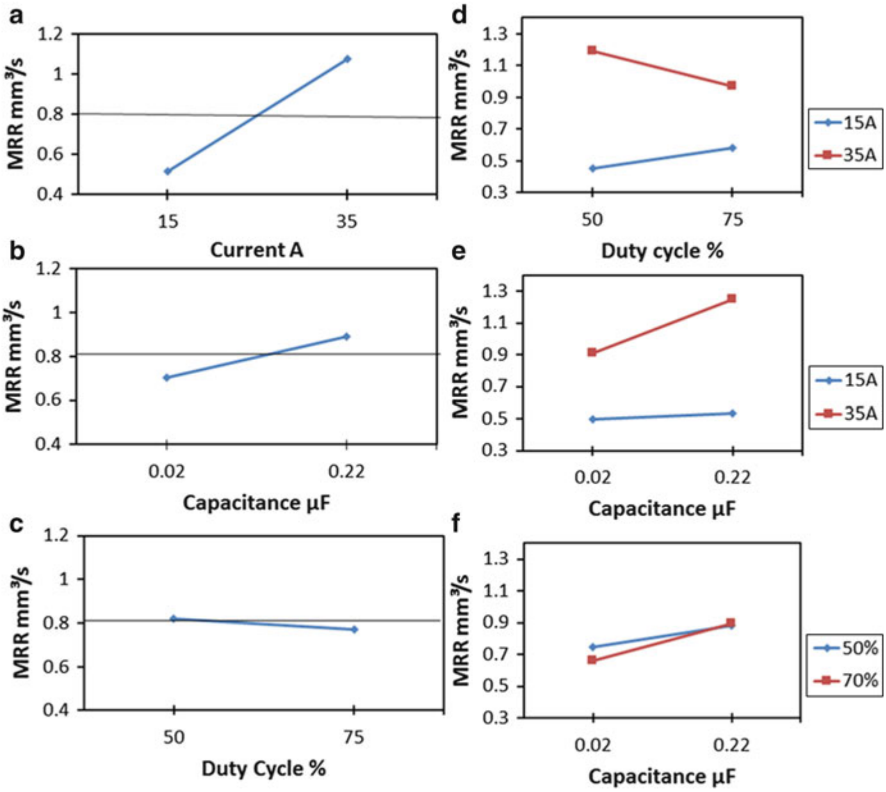

Fig. 17.3 Main effects plot for MRR (*left*) and, interaction effects plot for MRR (*right*)

subsequent sparks to be unsteady, which increases the possibility the next discharge occurs in the same place, promoting the erosion in only one place. The more duty cycle increases, the more energy discharges, which produces more electrode erosion, so that the electrode loses its original dimensions [14].

17.3.2 Characterization of Holes Drilled by EDM

In order to investigate the role that the parameters of EDM process play on the microstructure, selected samples with and without burr were inspected. Figure 17.5 shows holes made in the HSLA steel by EDM process under the parameters that are shown in the Table 17.1. As it can be seen, Fig. 17.5b shows melted material on the top. By contrast, Fig. 17.5a shows a hole without melted material. In addition, the melted material showed segregation at the top and edge, which is demonstrated and explained in detail in the following paragraph.

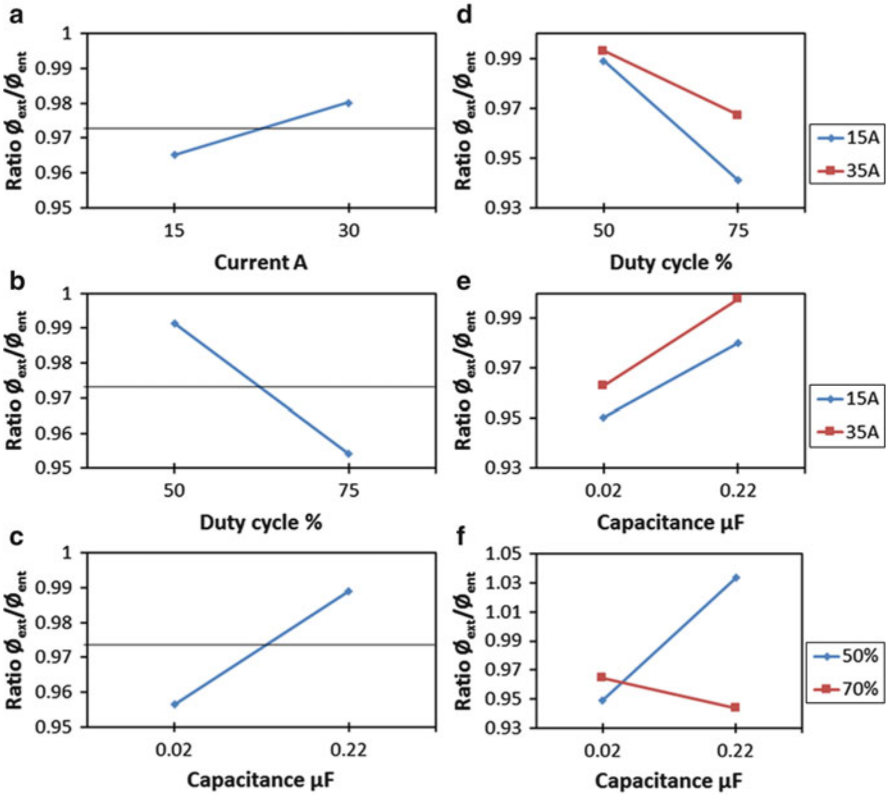

Fig. 17.4 Main effects plot for ϕ_{ext}/ϕ_{ent} (*left*) and interaction effects plot for ϕ_{ext}/ϕ_{ent} (*right*)

In order to study the thermal effect using the parameters of the experimental design, these specimens were observed by SEM. Figure 17.6a–e shows the burr on the hole of the specimen as well as chemical composition by EDX. Unsurprisingly, the high current parameter value used in the experimental design can increase the temperature that melts the copper electrode in a large quantity and deposits onto the workpiece. This result is consistent with the Cu-rich zones detected in the EDX spectrum (Fig. 17.6b). Others elements such as Mn and Si from the steel workpiece were detected at the top and edges of the hole (Fig. 17.6c, d). The content of oxygen is associated to the oxidation of iron (Fig. 17.6e). These findings indicate that at high temperature, segregation in the base metal may occur at rapid rate due to high pressurized dielectric flow, therefore, changing the mechanical behavior in these zones and leading to phase transformations.

The ε-Cu precipitates can destroy the austenite interphase boundary by the martensitic transformation during quench as well as influence on the kinetics of pro-eutectoid cementite precipitation [18]. Likewise, segregation of Cu can increase the susceptibility to hydrogen cracking, which is particularly related to the steel

Fig. 17.5 SEM image of perforations made by EDM process; (**a**) 15 A, 50 % duty cycle,0.02 μF capacitance; (**b**) 35 A, 50 % duty cycle, 0.02 μF capacitance

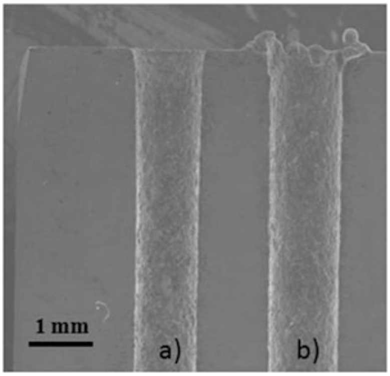

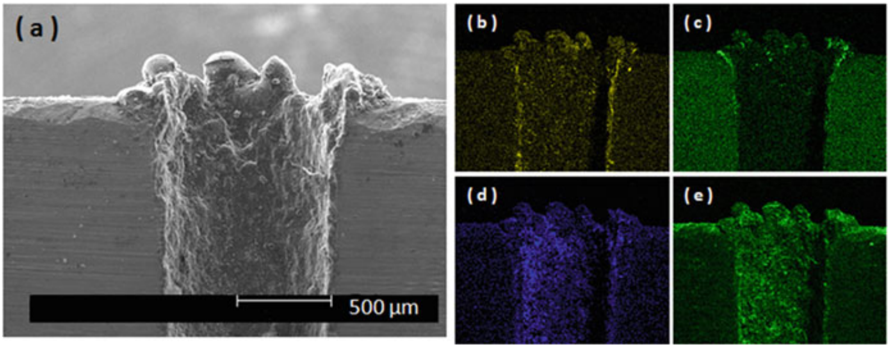

Fig. 17.6 SEM image and EDX of the hole using 35 amperes, 50 % duty cycle, 0.02 μF capacitance. (**a**) Burr formation; (**b**) Cu; (**c**) Mn, (**d**) Si, and (**e**) O

composition and kind of nonmetallic inclusions (type, size, and morphology) and the material ability to accommodate hydrogen. Reports in the literature [19] suggest that copper affects hydrogen uptake; above 0.2 %, Cu susceptibility is reduced. Moreover, it reduces the concentration of hydrogen at the surface but does not alter the threshold of hydrogen concentration for cracking. Over 1 % Mn increases the susceptibility of cracking, but the cooling rate can remove the detrimental Mn effect [20, 21].

Inspections near to the martensitic transformation zones show, in detail, the presence of microcracks as well as pro-eutectoid cementite precipitates in the boundary with a small content of copper analyzed by EDX (Fig. 17.7a, b). It is postulated that copper as a substitutional atom inside the lattice of martensite can lead a plastic strain so that it exceeds the yield stress of steel and begins microcrack growth.

Hashimoto and Kunieda [22] reported that a surface temperature can reach up to 5000 K during the EDM process. The combination of high temperature, which vaporize and/or melt material of both electrode and workpiece, and the rate of cooling (due to high pressurized dielectric fluid) contributes in a wide heat affected

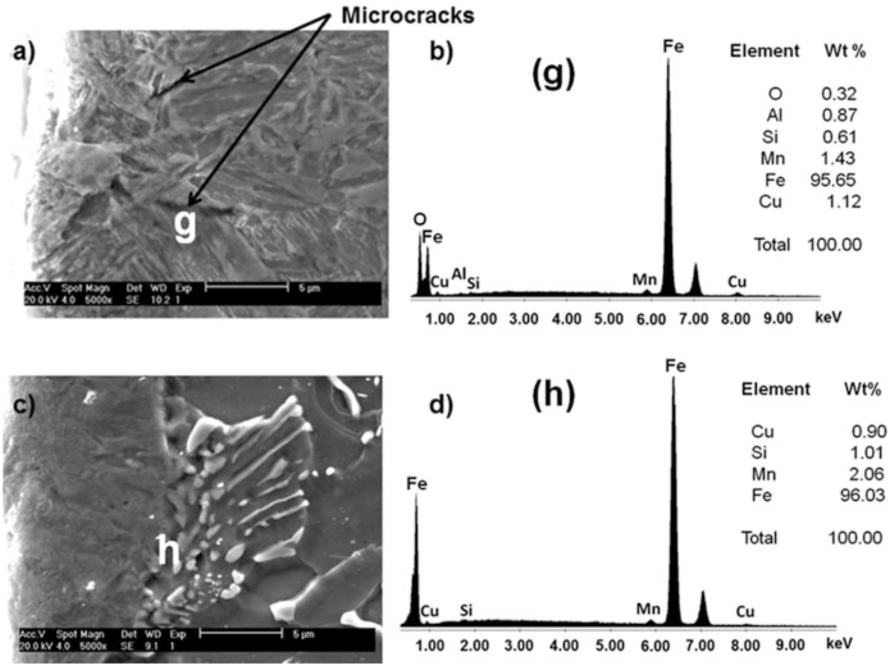

Element	Wt %
O	0.32
Al	0.87
Si	0.61
Mn	1.43
Fe	95.65
Cu	1.12
Total	100.00

Element	Wt%
Cu	0.90
Si	1.01
Mn	2.06
Fe	96.03
Total	100.00

Fig. 17.7 SEM images of samples with 35 amperes, 70 % Duty cycle, 0.02 µF Capacitance. (**a**) Microcracks inside martensite and EDX and (**b**) Pro-eutectoid cementite precipitates and EDX on the boundary

zone (HAZ) that is associated with the transformations from austenite to martensite as well as the deposition of molten copper from the electrode onto the base metal, when the following parameters are used 35 A, 50 % duty cycle, 0.02 µF. This finding agrees with other reports in the literature [23–25] that suggest the deposited copper is caused by trapping of the molten electrode in the recast layer on the workpiece surface.

On the contrary, the foremost difference between the low current value and the high current value conditions is that segregation clusters of Cu, Mn, and Si do not present at the top and edge of the specimen without melted material (Fig. 17.8a–e). This condition shows a better homogenous chemical composition than at high conditions of machining.

Figure 17.9 shows a deeper HAZ with approximately 35 µm, and it exhibits phase transformation to martensite at the edge of perforation. This occurs when 35 A are used (50 % duty cycle, 0.02 µF capacitance. Under a minor current level (15 A, 50 % duty cycle, 0.02 µF), HAZ is about 14 µm.

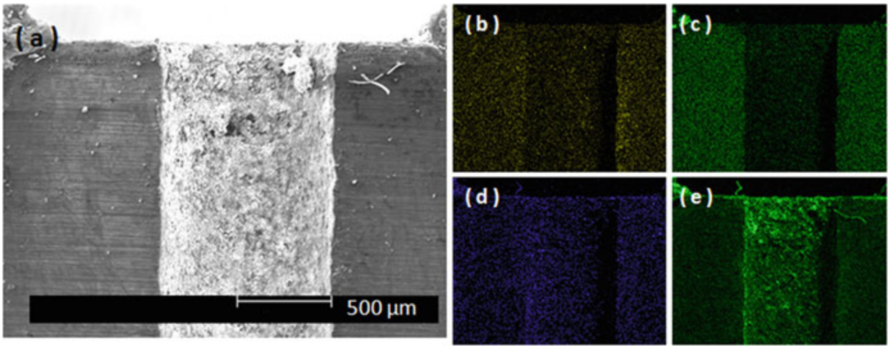

Fig. 17.8 SEM image and EDX of the hole using 15 amperes, 50 % duty cycle, 0.02 µF capacitance according to experimental design. (**a**) Melted material at the top; (**b**) Cu; (**c**) Mn; (**d**) Si; and (**e**) O

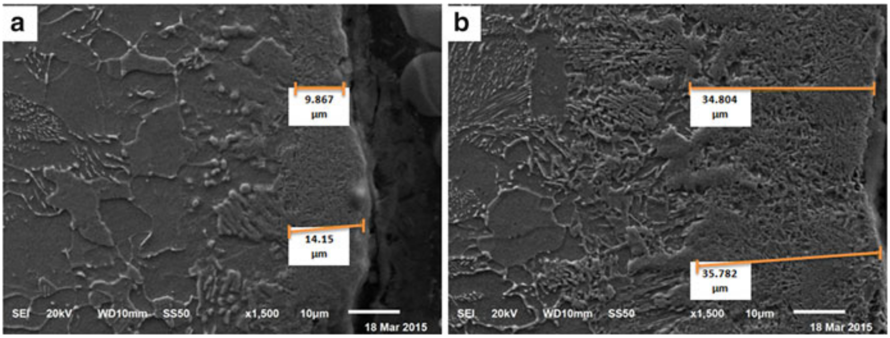

Fig. 17.9 SEM image of the edge of perforation at (**a**) 15 A, 50 % duty cycle, 0.02 µF capacitance (**b**) 35 A, 50 % duty cycle, 0.02 µF capacitance

17.4 Conclusions

From the statistical analysis, it can be inferred that the discharge current intensity has a greater influence on the MRR, while capacitance has a reduced influence on the increase of MRR. Regarding the integrity of the perforations, the most influential parameters are the capacitance and duty cycle; to produce holes without taper, both low duty cycle and high capacitance are required.

With high current levels, trapping of copper particles in the recast layer of the perforations are found, producing changes in material properties. In addition, the change of ferrite-pearlite phases to martensite is promoted.

The transformation to martensite phase in the presence of segregated copper causes the formation of microcracks, which could reduce the corrosion, mechanical resistance, and fatigue resistance of the EDM'ed surface. On the other hand, it is postulated that copper as substitutional atom inside lattice of martensite can lead a plastic strain and increase the feasibility of microcracks and the same fragile nature of martensite.

Different levels of discharge energy produce a HAZ near the subsurface region, which has some variation in thickness along the EDM'ed surface. The discharged energy increases the plasma temperature, which affects a deeper zone. The HAZ is about 15 μm at 15 A discharging current, but it is more than double to 36 μm at 35 A. Also, in this strip, martensite phase and thickening of cementite plates precipitation are formed.

After completion of statistical analysis, this work suggests that EDM is a good choice for machining high-strength steels at high MRR, when the machining parameters are carefully combined. However, some secondary effects must be taken into account, namely: surface finish and geometric precision.

If reliability of the EDM's surface is a concern, then a subsequent process could be required in order to remove damaged zones. Since the holes are small, internal honing is not suitable, but electrochemical polishing should be considered as a good alternative to improve the surface finish quality.

Acknowledgements This research project is supported by SENER-CONACYT project number 174568. The kind support from METALSA Mexico is greatly appreciated.

References

1. Oberg E (2008) In: McCauley CJ (ed) Machinery's handbook, 28th edn. Industrial Press, New York, pp 420–421
2. Ageen G, Akstens W (2005) In: ASM International Handbook Committee (ed) ASM handbook: properties and selection: irons, steels and high performance alloys. vol 1, 10th edn. ASM International, Eds., ASM International, pp 262–264, 589–591
3. Smallman RE, Ngan AHW (2007) Physical metallurgy and advanced materials. Elsevier, New York, pp 450–451
4. Illescas S, Fernández J, Guilemany JM (2009) Study of the mechanical proprieties of low carbon content HSLA steels. Metall Mag 45:424–431
5. Sharma N, Rajesh K, Rahuldev G (2013) Multi quality characteristics of WEDM process parameters with RSM. Proc Eng 64:710–719
6. Sommer C, Sommer S (2005) Complete EDM handbook. Advance Publications, New York, pp 19–26
7. Perverj J, Muhammad W, San Y, Rahman M (2009) A comparative experimental investigations of deep-hole micro-EDM drilling capability for cemented carbides (WC-Co) against austenitic stainless steel (SUS 304). Proc Eng 60:1145–1160
8. Klink A, Guo YB, Klocke F (2011) Surface integrity evolution of powder metallurgical tool steel by main cut and finishing trim cuts in wire-EDM. Proc Eng 62:178–183
9. Suleiman A, Ahsan AK, Konneh M (2009) Reducing electrode wear ratio using cryogenic cooling during electrical discharge machining. Int J Adv Manuf Technol **45**, 1146–1151
10. Zhang Y (2014) Investigation on the influence of the dielectrics on the material removal characteristics of EDM. J Mater Proc Technol 214:1052–1061
11. Kumar S, Batra U (2012) Surface modification of die steel materials by EDM method using tungsten powder-mixed dielectric. J Manuf Proc 14:35–40

12. Kumar S (2009) Surface modification by electrical discharge machining: a review. J Mater Proc Technol 209:3675–3687
13. Jahan MP, Rahman M, Wong YS (2011) A review on the conventional and micro-electro discharge machining of tungsten carbide. Int J Mach Tools Manuf 51:837–858
14. Sohani MS, Gaitonde VN, Siddeswarappa B (2009) Investigation into the effect of tool shapes with size factor consideration in sink electrical discharge machining (EDM) process. Int J Adv Manuf Technol **45**, 1131–1145
15. Simao J (2002) Workpiece surface modification using electrical discharge machining. Int J Adv Manuf Technol **43**, 121–128
16. Caballero FG (2006) Evolution of microstructural banding during the manufacturing process of dual phase steels. Mater Trans 47:2269–2276
17. Lauwers B, Liu K, Reynaerts D (2010) Process capabilities of Micro-EDM and its applications. Int J Adv Manuf Technol 47:11–19
18. Wasynczuk JA, Fisher RM, Thomas G (1986) Effects of copper on proeutectoide cementite precipitation. Metal Trans 17A:2163–2173
19. Beidokhti B, Dolati A, Koukabi AH (2009) Effects of alloying elements and microstructure on the susceptibility of the welded HSLA steel to hydrogen-induced cracking and sulfate stress cracking. Mater Sci Eng A 507:167–173
20. Watkins M, Ayer RS (1995) Corrosion, Paper No. 50, NACE Int
21. Charles J (1990) Corrosion, Paper No. 90, 207
22. Hashimoto H, Kunieda M (1997) Spectroscopic analysis of temperature variation of EDM arc plasma. J JSEME 31:32–40
23. Khan A (2007) Electrode wear and material removal rate during EDM of aluminum and mild steel using copper and brass electrodes. Springer, Berlin, pp 482–487
24. Kumara S (2008) Surface modification by electrical discharge machining: a review. J Mater Proc Technol **209**, 3675–3687
25. Zhang Y (2011) Study of the recast layer of a surface machined by sinking electrical discharge machining using water-in-oil emulsion as dielectric. Appl Surface Sci 257:5989–5997

Part VIII
Characterization of Welding and Joining of Materials

This part includes two chapters related to the characterization of welded materials.

The first chapter presents a study about evaluation of distortion in welding joints of 304 stainless steel by effect of the welding temperature and the microstructural changes. Microstructural evaluation was performed on transversal sections of the welding bead. Distortion evaluation demonstrates the variation of the final piece. This method can be described as effective as long as the steps of the process are developed with quality and precision, the relation of the temperature with the base metal with distortion can be evaluated with an exhaustive microstructural study.

The second chapter presents a study of the weld bead geometry of Ni-based alloy deposited by plasma transferred arc (PTA) process for pipe conduction of shale gas. The transportation of shale gas has the problem that the piping used for the extraction does not resist the erosion generated by the amount of solids and it is necessary to extend the life of the pipelines. In addition, the mechanisms of corrosion by hydrogen embrittlement. In order to minimize these problems nickel based materials and stainless steels are commonly used, however its cost is very high. This paper studied the use of Ni-based filler metal as weld bead deposits on A36 steel substrates by PTA, in order to determine the suitable conditions to ensure coating quality on the substrate a design of experiments (DOE) was determined.

The main techniques used in the characterization of these materials are:

- Optical microscopy (OM).
- Scanning electron microscopy (SEM).
- Energy dispersive spectroscopy (EDS).
- Mechanical tests.

Chapter 18
Evaluation of Distortion in Welding Unions of 304 Stainless Steel with Elliptic Trajectory Using a Welding Robot

L.A. Carrasco-González, E. Hurtado-Delgado, and F.A. Reyes-Valdés

Abstract The aim of this investigation is to evaluate the distortions generated in welding unions of stainless steel 304 by effect of the welding temperature and the microestructural changes. The joint design is a 100 × 100 mm steel plate of 3 mm thickness. The plate was joined to a tube of 50 mm diameter and 2 mm thickness, which has a defined angular cut; therefore, the trajectory followed by the seam has an elliptic form. Temperature data acquisition was developed by type K thermocouples, placed in pairs at 0°, 90°, 180° and 270° along the welding trajectory and connected to a data acquisition device yo obtain the measures to generate time-temperature plots. The welding process was executed by a KUKA® KR16 welding robot with an integrated GMAW (Gas metal arc welding) process where the input parameters of voltage, wire feed and travel speed are set to constant. The distortion of the work piece was measured using a laser scanning technique that generates a point cloud with the VXelements TM software for comparison between the pre and post-weld condition. Microstructural evaluation was performed on transversal sections of the seam, at the mentioned angles for correlation.

Keywords Distortion • Elliptic trajectories • Arc welding • Stainless • Thermocouple

18.1 Introduction

The linear and circular welding trajectory are the most common type of investigation, this is associated with the most popular industries for which welding is employed, namely automotive, aerospace, and construction [1]. Elliptical sections are present like a new type of development in the structural tube industry with a need for further investigation to be sure about its efficiency [2]. In the development

---

L.A. Carrasco-González (✉) • E. Hurtado-Delgado • F.A. Reyes-Valdés
Corporación Mexicana de Investigación en Materiales, Ciencia y Tecnología 790,
Saltillo, Coahuila, Mexico
e-mail: leo.carrasco@comimsa.com

R. Pérez Campos et al. (eds.), *Characterization of Metals and Alloys*, DOI 10.1007/978-3-319-31694-9_18

of welding, the quick thermal affection can generate some distortions throughout the piece, affecting the integrity of the joint, for the common joint design, the type of distortion can be classified as [3]:

- Transverse shrinkage
- Angular change
- Rotational distortion
- Longitudinal shrinkage
- Longitudinal bending distortion
- Buckling distortion

Nevertheless, the elliptical joint design is a complex form, and for that the common distortion classifications cannot describe completely all the distortion types in the resulting piece. A complete work regarding all the phenomena that has mechanical influence over the piece must be carried out with the final objective of avoiding repair work or scrap generation in a continuous production process [1–4]. During welding, the thermal changes are very quick; the best way of monitoring that phenomenon is by the use of thermocouples [5], where the distribution of the thermocouples depends of the geometry of the piece. It is important to select multiple points with some relation between them, as this is vital information for the analysis of the data acquisition and further correlations. The GMAW process is one of the most common in welding for the automotive industry. In it, the main purpose of using a robotic welding is to reduce the variability of the parameters in the welding process, which represents an advantage in the study since the human factor variation will not influence the final development. A significant research work is available in the literature, describing an investigation focusing on longitudinal welding or circumferential welding, the second as a complex case [6], where the distortion results were used to verify the efficiency of the simulation process. These studies take as their main point of reference double ellipsoids of Goldak [7] in which two sections of heat distribution, front and rear, are contemplated, where the thermal effect of the heat source occurs before and after passing through a point of the material section for the temperature from the front and back of the double ellipsoid model.

18.2 Experimental

18.2.1 Materials

The selected material for the present study is an austenitic stainless steel in two shapes, a steel plate of 3 mm thickness for the base of the union design and a tube of 50 mm diameter and 2 mm thickness (Fig. 18.1). A 3D schematic design is shown in Fig. 18.2. The chemical composition, mechanical and thermal properties are shown in Tables 18.1 and 18.2.

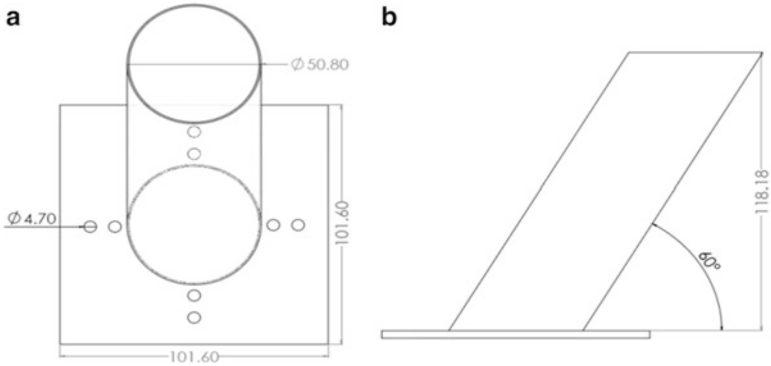

Fig. 18.1 Schematic illustration of the joint design. (**a**) Front view. (**b**) Side view

Fig. 18.2 3D illustration of the plate-tube joint design

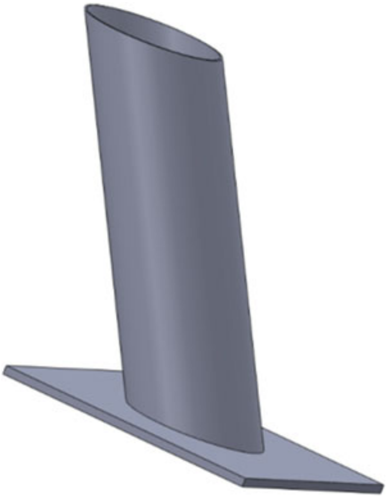

Table 18.1 Chemical composition wt. % of 304 austenitic stainless steel

C	Mn	Si	P	S	Mo	Nb	Cu	Cr	Ni	V	Ti
0.04	1.40	0.42	0.024	0.02	0.11	0.05	0.10	18.3	8.75	0.09	0.04

Table 18.2 Mechanical and thermal properties of 304 austenitic stainless steel

Yield strength (MPa)	Elongation 2” (mm)	Hardness (Hv)	Heat capacity (J/g °C)	Thermal conductivity W/m-K (500 °C)
205	40	192	0.5	21.4

The welding conditions of the robotic GMAW short circuiting process used for the development of the joint are show in Table 18.3. The welding process was developed with a KR16 KUKA robot welding in the manufacturing cell at COMIMSA.

Table 18.3 GMAW parameters

Electrode	ER-308 L (AWS)
Voltage	22 V
Gas (Ar)	100 %
Weld speed range	0.6 m/min
Feed rate	17.78 m/min

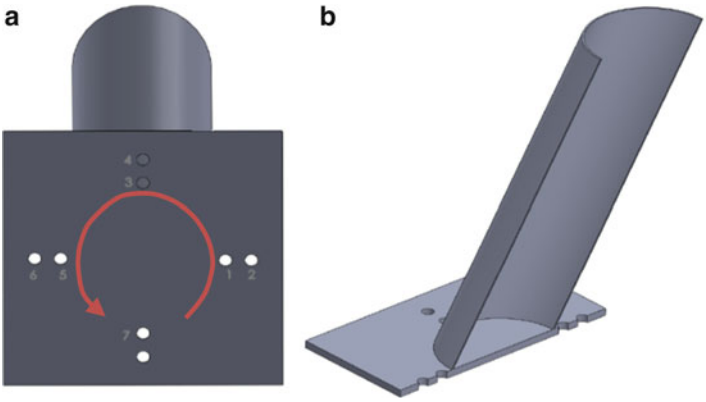

Fig. 18.3 Illustration of joint design. (**a**) Bottom view of the joint, with thermocouples distribution and identification in the welding trajectory. (**b**) Half section view

Temperature measurements were performed at four points of the joint design, every point having two K type thermocouples with 0.47 cm of diameter and the same value of separation between two thermocouples (Fig. 18.3). The thermocouple was connected to a PICO USB TC-08 data acquisition card with eight channels and the ability to collect two sample measurements per second. The schematic distribution of the thermocouples and the welding trajectory are presented in Fig. 18.3a.

Creaform Scanner EXA scan was employed for the post welding cloud points generation of the welding piece. With the VXelements TM software, all data was collected from the real piece to an electronic data file, then with GeoMagic®, Design^{TM} X converts the cloud points file into a mesh file and a CAD model. After that, the mesh file and the original model of the design are compared with the software GOM Inspect V8 to measure the distortion in the tube and plate for the welding process.

In the metallographic preparation of the samples, the standard techniques for mounting and polishing were used. Chemical etching was performed with "regia" water (15 ml of HCl and 5 ml of HNO_3), which has an effective life time of around 10 min before it is ineffective. Weld and base metals were performed by the same SEM operated at 10 kV.

18.3 Results and Discussion

18.3.1 *Materials*

The material (304 SS type) was the same used in the base and tube, which is an austenitic stainless steel. Figure 18.4 shows the optical micrograph of the base material where an austenitic matrix is observed; the grain type is characteristic of this material [8].

18.3.2 *Elliptical Joint*

The main interest of the investigation is to evaluate the distortion generated for a complex welding trajectory. In order to achieve an elliptical trajectory, a 60° cut is performed in both sides of the tube, the side in contact with the plate makes the elliptical form. The rear face (where the thermocouples 7 and 8 are positioned) is a very difficult access area for the welding robot, which is why the full trajectory is not possible (this applies for 50 mm or less in tube diameter). Stereoscope micrographs were taken in seven points along the weld bead, three of them in the same line of the thermocouples (thermocouples 1–6) and the rest at 45° between the positions of the thermocouples. All the weld areas are measured in root, toe, face, leg, and throat (Fig. 18.5). The sections (a) and (e) are the only approved sections, because in the other five sections the weld bead has fusion with the entire base material [9]. The dimensional values of the welds are concentrated in the Table 18.4.

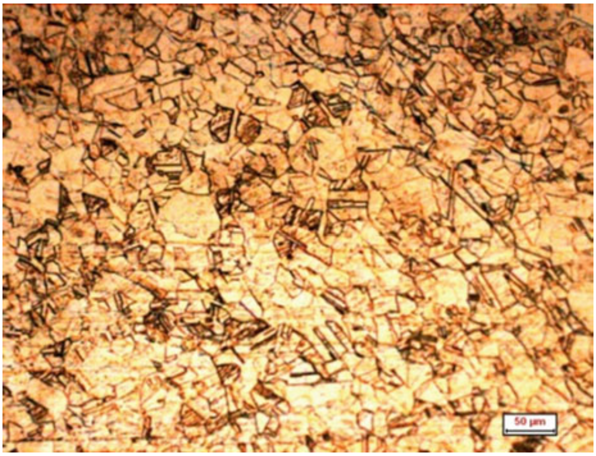

Fig. 18.4 Optical micrograph of base metal

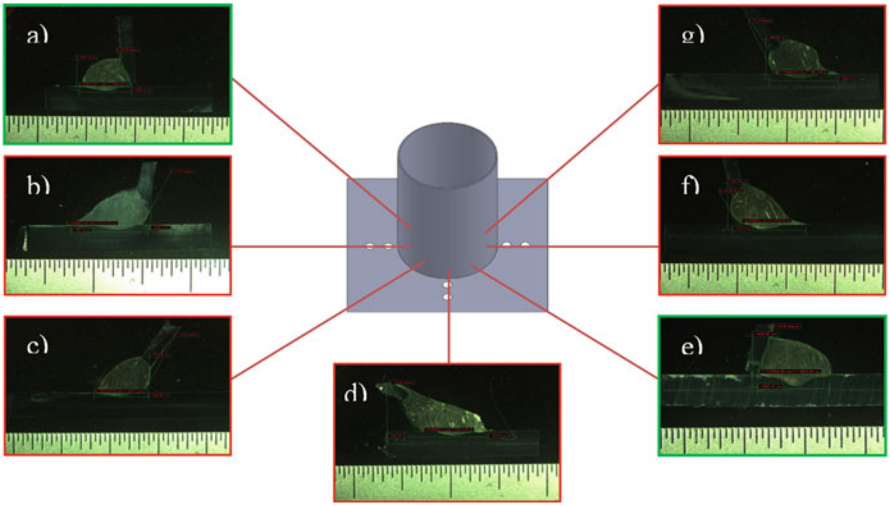

Fig. 18.5 Stereoscope micrograph distribution

Table 18.4 Measured values of the weld bead cut sections

Section	Leg (vertical mm)	Leg (horizontal mm)	Weld area (mm^2)	Weld perimeter (mm)
a	3.81	5.30	13.92	15.96
b	5.26	7.96	24.59	23.177
c	4.77	5.30	16.52	16.347
d	6.39	7.91	23.78	26.47
e	4.84	5.60	17.57	16.62
f	5.86	7.70	23.10	22.07
g	4.66	6.60	17.20	18.41

18.3.3 Microstructural Characterization

Figure 18.6 shows the resulted microstructure of the fusion zone (FZ) and heat affected zone (HAZ) of the section (a) where in the fusion zone the dendritic formation (Fig. 18.6b) is present, in the affected zone the grain morphology changes compared with the base metal (Fig. 18.4), with a coarse austenitic grains.

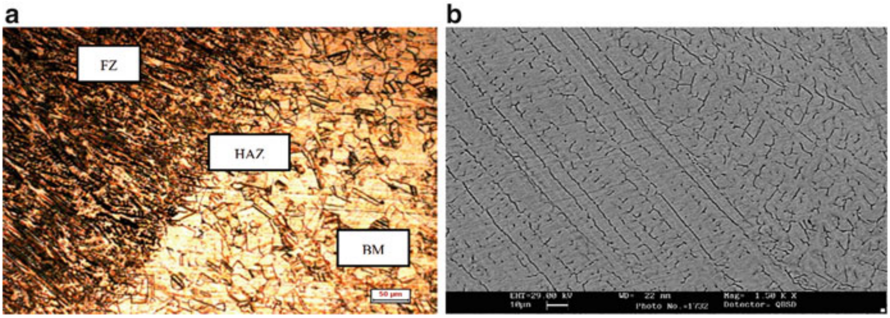

Fig. 18.6 (**a**) Optical microscope image of the fusion zone. (**b**) SEM micrograph of the dendritic formation in the fusion zone

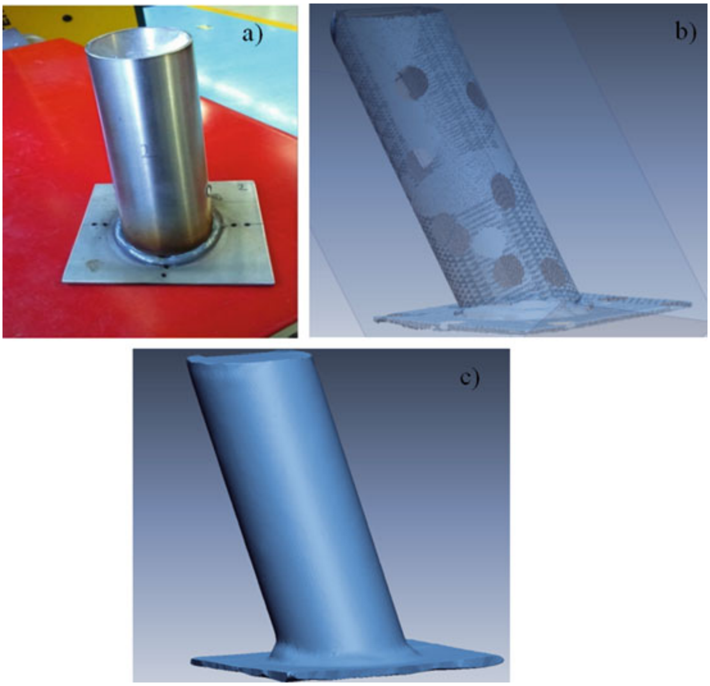

Fig. 18.7 Scan process. (**a**) Scanning resulting piece. (**b**) Point cloud generation of the welded piece (**c**) Mesh generation of the welded piece

18.3.4 Distortion Analysis

The distortion analysis was performed in three steps [10]:

1. Scan the welded piece with Exascan to obtain a cloud point data (Fig. 18.7a).
2. Clean the cloud point data (Fig. 18.7b) and generate a mesh of the piece with Geomagic software (Fig. 18.7c).

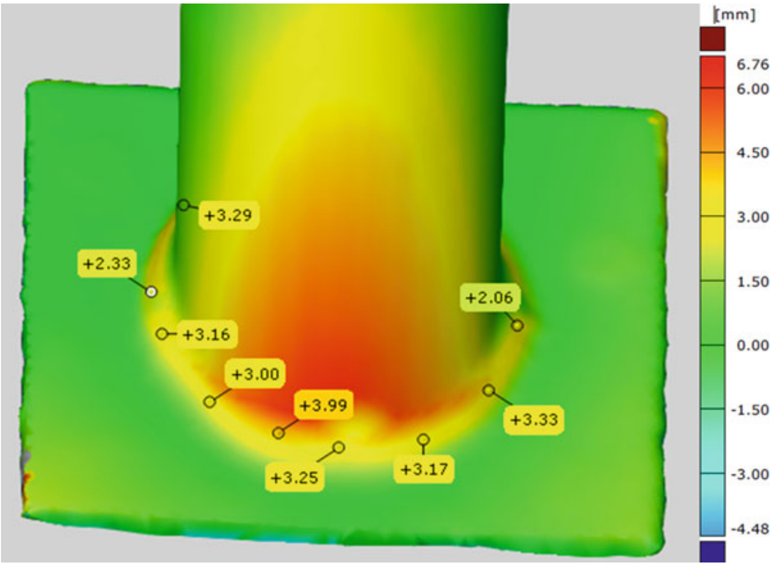

Fig. 18.8 Distortion analysis in the weld bead

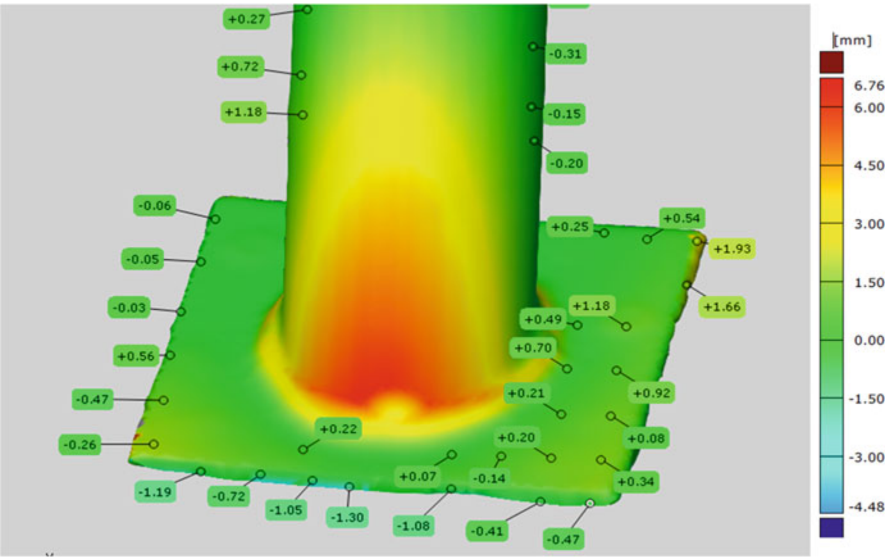

Fig. 18.9 Distortion analysis in the plate and tube

3. Compare the mesh and the perfect solid design and take values of distortion (Figs. 18.8 and 18.9).

The distortion analysis in Fig. 18.8 shows that the values measured belong to the weld bead, the maximum value is +3.99 mm, and the positive sign describes an increment in the geometry after the welding process. In addition, the frontal section of the tube has an important red zone that represents a distortion in the tube associated with the contraction of the welding. Considering that the rear part of the piece does not have a welding bead, it can be said that the tube shifted its position to the frontal side.

The distortion in the Fig. 18.9 describes a frontal and left contraction of the geometry, disassociated with the negative sign, and the right side of the piece has a general increment in the resultant geometry. Also, the distortion in the tube is more evident with a progressive increment in the left side of the tube. In general terms, the resultant contraction of the elliptical welding process distorts the plate, increasing the material in the contact face with the tube, and the tube has shifted to the left and front sides.

18.3.5 Thermal Analysis

The K-type thermocouples used in the data acquisition of the temperature during development of the welding are represented in Fig. 18.10. The total time of welding was 16 s, with the red line marking the end of the welding process. Data acquisition was performed for 15 min (maximum data acquisition record time) with 77 °C of temperature as the maximum record in the thermocouples in the plate. Figure 18.10 represents the first 5 min of record, where the maximum value was registered in the channel 3 with 1261 °C, the principal reason of this measure is evidenced in Fig. 18.11, where the weld bead covers the thermocouple completely. Channel 7 got out of the hole after the welding process stopped due to the deformation of the plate and a bad attaching method [11, 12].

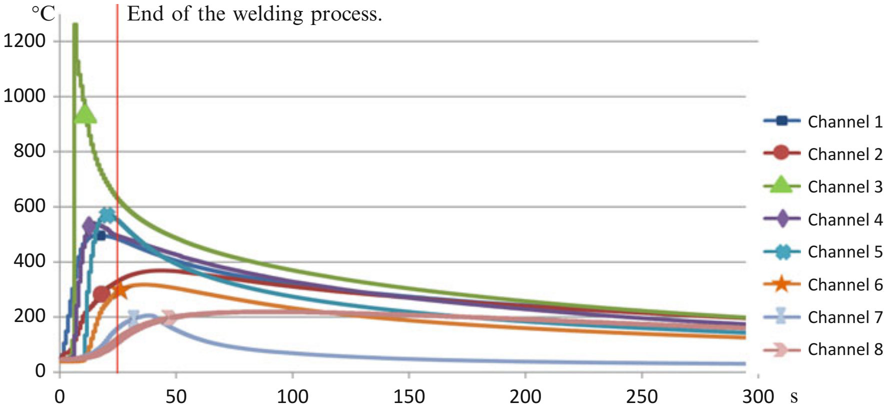

Fig. 18.10 Thermocouples measurements of the eight channels

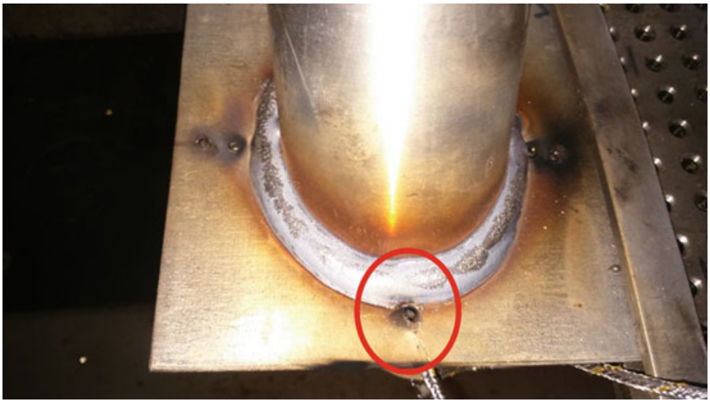

Fig. 18.11 Frontal view of the real weld bead

18.4 Conclusions

The elliptical stainless steel tube and plate using GTAW robotic process was carried out. The complete process analysis concludes as follows:

- The development of elliptical welding trajectories is possible with the KUKA KR16 for a tube bigger than 50.8 mm, using one single pass. The end result indicated no porosities or visual defects evident in the weld bead.
- In comparison with the reference investigation, in the thermal measure, we can obtain high measures of temperature with drill holes through the plate, with the thermocouples positions at the same level of the plate top.
- We can measure temperatures around 1250 °C if we positioned the thermocouples below the weld bead, although the thermocouple preparation will probably fail.
- The resulting weld bead measures in the sections show that just two sections (a and e) are acceptable, the other zones presented an excessive penetration in the vertical leg (tube). This can be solved with better parameter optimization and a correction of the attack angle.
- Distortion evaluation demonstrates the variation of the final piece; this method can be describe as effective as long as the steps of the process are develop with quality and precision and the relation of the temperature with the base metal with distortion can be evaluated with an exhaustive microestructural study.
- Additional experiments are recommended with thermal data acquisition in both pieces (tube and plate) to further understand the complete thermal effect in the joint design. A data acquisition card with more speed would be advantageous.

References

1. Miranda AF, Pérez GY, Hurtado E, Reyes FA (2015) Distortion evaluation in dissimilar stainless steels joints welded by GMAW process. In: Materials characterization. Springer, New York, pp 15–23
2. Haque T, Packer JA (2012) Elliptical hollow section T and X connections. Can J Civil Eng 39(8):925–993
3. Micheleris P, DeBiccari A (1997) Prediction of welding distortion. Weld J 76(4):172–180
4. Muhammad A, Jawad Q (2009) 3D thermal finite element analysis of single pass girth welded low carbon steel pipe-flange joints. Turk J Eng Environ Sci 33(4):281–294
5. Nakhodchi S, Shokuhfar A, Iraj SA, Thomas BG (2015) Evolution of temperature distribution and microstructure in multipass welded AISI 321 stainless steel plates with different thicknesses. J Press Vessel Technol Trans ASME 137:061405–1
6. Velaga SK, Rajput G, Murugan S, Ravisankar A, Venugopal S (2015) Comparison of weld characteristics between longitudinal seam and circumferential butt weld joints of cylindrical components. J Manufact Proc 18:1–11
7. Goldak J, Chakravarti A, Bibby M (1984) A new finite element model for welding heat sources. Metall Trans B 15B:299–305
8. Kou S (2003) Welding metallurgy. Wiley, Hoboken, NJ
9. Kotecki DJ, Lippold JC (2005) Welding metallurgy and weldability of stainless steels. Wiley, Hoboken, NJ
10. Barbero B, Ureta E (2011) Comparative study of different digitization techniques and their accuracy. Comput Aided Des 43:188–206
11. Ueda Y, Murakawa H, Ma N (2012) Welding deformation and residual stress prevention. Butterworth-Heinemann Elsevier, Boston, MA
12. Kim D (2003) Welding simulation of ship structures using coupled shell and solid volume finite elements. Thesis, Lehigh University, Bethlehem, PA

Chapter 19
Weld Bead Geometry of Ni-Based Alloy Deposited by PTA Process for Pipe Conduction of Shale Gas

C. Echavarria-Figueroa, F. García-Vázquez, J. Ruiz-Mondragón, H.M. Hernández-García, D. González-González, and A. Vargas

Abstract The transportation of shale gas has the problem that the piping used for the extraction does not resist the erosion generated by the amount of solids causing cracks over the surface and it is necessary to extend the life of the pipelines. Plasma transferred arc (PTA) welded coatings are used to improve the surface properties of mechanical parts. Therefore, in this paper is studied the use of Ni-based filler metal as weld bead deposits on A36 steel substrates by PTA. In order to determine the suitable conditions to ensure coating quality on the substrate a design of experiments (DOE) was determined. Welding current, feed rate, and travel speed were used as input parameters and the dilution percentage as the response variable. The composition and properties of hardfacing or overlay deposited are strongly influenced by the dilution obtained. Control of dilution is important, where typically low dilution is desirable. When the dilution is low, the final deposit composition will be closer to that of the filler metal, and the wear and corrosion resistance of the hardfacing will also be maintained. To evaluate the features on the weld beads/substrate interface a microstructural characterization was performed by using scanning electron microscopy and to evaluate the mechanical properties was carried out hardness test.

Keywords Plasma transferred arc (PTA) • Weld bead geometry • Ni-based alloy • A36 steel • Dilution

---

C. Echavarria-Figueroa (✉) • F. García-Vázquez • J. Ruiz-Mondragón • H.M. Hernández-García • D. González-González
Corporación Mexicana de Investigación en Materiales (COMIMSA), Calle ciencia y tecnología No. 790, Col. Saltillo 400, C.P. 25290 Saltillo, Coahuila, Mexico
e-mail: cechavarria@comimsa.com

A. Vargas
Innovación Tecnológica en Soldadura y Superficies S.A. de C.V., Zacatecas No. 573, Col. República Oriente, C.P. 25280 Saltillo, Coahuila, Mexico

R. Pérez Campos et al. (eds.), *Characterization of Metals and Alloys*, DOI 10.1007/978-3-319-31694-9_19

19.1 Introduction

The decrease of non-renewable resources has brought the need to explore other unconventional energy sources as the shale gas. This activity has promoted an important development in technology acquisition, recovery, and transportation of this resource. The transportation is the most critical aspect, because the amount of solids generates erosion, in addition, the mechanisms of corrosion by hydrogen embrittlement causing cracks on the pipes. In order to minimize these problems nickel-based materials and stainless steels are commonly used; however, its cost is very high. Alternatively it proposed a coating over the cracks to extend the lifetime of the pipelines. Previously, conventional welding processes were used with the purpose of making coatings on mechanical components to increase the properties and extend the life of the material.

In recent years, overlays deposited by PTA or hardfacing have an extensive use in applications such as valve industries, hydraulic machineries, mining industries, and coatings [1]. PTA process employs the plasma principle hence it may be considered an evolution of GTAW process, where the high-energy concentration is due to the use of a constrictor nose, which restrains the column diameter of an electric arc established between a tungsten electrode and the workpiece in an inert gas atmosphere, usually argon. Feeding material is carried to the plasma jet by a gas stream, which might be inert, active, or a mixture of active and inert gases. A third gas flow is employed to protect the metal pool from atmospheric contamination. Even though there is the possibility of using mixtures of active and inert gases, argon is typically employed for all three-gas systems [2, 3].

This process stands out for its high quality, metallurgically bonded with substrate and low diluted overlays. These overlays also exhibit high homogeneity, low oxide content, and low concentrations of other unwanted inclusions [4]. The composition and properties of hardfacing or overlay deposited are strongly influenced by the dilution obtained. Control of dilution is important, where typically low dilution is desirable. When the dilution is low, the final deposit composition will be closer to that of the filler metal, and the wear and corrosion resistance of the hardfacing will also be maintained [5].

To provide a coating with higher wear resistance is chosen N-625 filler metal based on its properties (hardness, wear, and corrosion resistance). Through a design of experiments (DOE) they are looking to get proper values to make coatings of N-625 filler metal with low dilution rate values sought to be less than 5 % in order to increase the mechanical properties on A36 base metal.

19.2 Experimental Procedure

In this work, automatic PTA hardfacing was carried out for depositing Ni-based filler metal alloy over A36 steel plates approximately of size 15 × 8 × 1.5 cm. Chemical composition (wt.%) of the N-635 filler metal is shown in Table 19.1. Microstructural characterization of the overlays was performed by using a JEOL scanning electron microscope equipped with EDS semiquantitative analysis using an accelerating voltage of 25 kV, spot size of 4.7, and a working distance of 6.5 mm. The controllable process parameters identified based on their significant effect on weld bead geometry were welding current, feed rate, and welding speed with values showed in Table 19.2 and constant parameters in Table 19.3. On the other hand, dilution was evaluated as the area ratio between the substrate melted area and total melted area as indicated in Fig. 19.1.

Table 19.1 Chemical composition (wt.%) of the N-625 filler metal

Cr	C	Mo	Nb	Fe	Ni
21	0.05	9.2	3.5	3	Balance

Table 19.2 Processing PTA parameters

	Factor levels		
Variable parameters	−1	0	1
Feed rate (gr/min)	20	26	32
Welding speed (cm/min)	15	17	19
Welding current (A)	140	160	180

Table 19.3 Processing PTA constant parameters

Constant parameters	
Plasma gas (l/min)	5
Shield gas (l/min)	12
Powder gas (l/min)	5

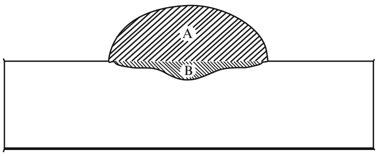

$$\delta = \frac{\text{Substrate melted area}}{\text{Total melted area}} \times 100 = \frac{\mathrm{B}}{\mathrm{A+B}}$$

Fig. 19.1 Procedure used to evaluate dilution levels

Table 19.4 Parameters used in the design of matrix of experiments

Piece	Feed rate (gr/min)	Welding speed (cm/min)	Welding current (A)	Dilution (%)
1	1	1	1	4.67
2	1	1	−1	0.27
3	1	−1	−1	3.19
4	1	1	1	12.17
5	−1	−1	1	25.84
6	−1	−1	−1	1.24
7	−1	1	−1	1.79
8	−1	1	1	17.35
9	0	0	0	5.38
10	0	0	0	6.22
11	0	0	0	5.74
12	0	0	0	5.12

The chosen matrix design (Table 19.4) to conduct the experiment was a 2^3 design with central points. It consists of 12 steps of coded conditions and comprising a half replication of $2^3 = 8$ factorial design with four central points [6]. In the matrix DOE welding parameters at the middle level (0) constitute center points whereas the combination of each welding parameter at its lower value (−1) or higher value (1). Thus these 12 experimental runs allow observe the effect of welding parameters over the percentage of dilution.

19.3 Results and Discussion

Dilution is a determining factor whenever one wants to assess coating properties. Compared to other welding processes PTA requires less quantity of material to be deposited with improved metallurgical properties and allows precise metering of metallic powder feedstocks [7, 8]. The shape of the weld bead geometry is affected by the values of PTA process parameters kept during deposition [9, 10]. Dilution results measured by stereoscopy for the different processing conditions are shown in Fig. 19.2.

Based on the best dilution level the sample 6 (Fig. 19.2c) was selected because it presented suitable weld bead geometry; although there are samples with a smaller dilution, but these do not have the appropriate geometry and properties for an expected overlay. The microstructure of sample 6 shown in Fig. 19.3a shows the interface zone without chemical attack, Fig. 19.3b is the zone between interface-HAZ-base metal and Fig. 19.3c shows the microstructure of interface zone with chemical attack using optical microscopy.

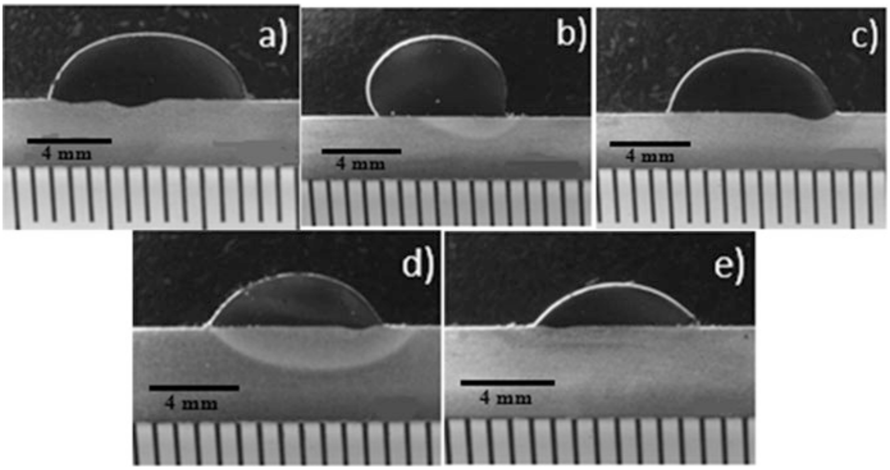

Fig. 19.2 Evaluation of dilution by stereoscopy (**a**) P1, (**b**), P2, (**c**) P3, (**d**) P6, (**e**) P7

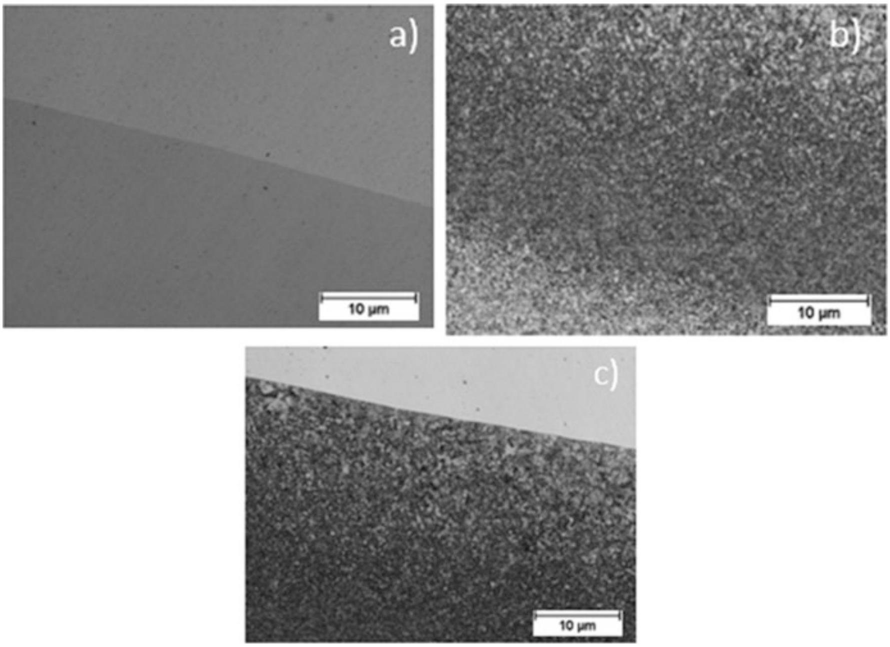

Fig. 19.3 Microstructure of piece 6 using optical microscopy, (**a**) interface zone without attack, (**b**) zone between interface-HAZ-base metal, and (**c**) interface zone

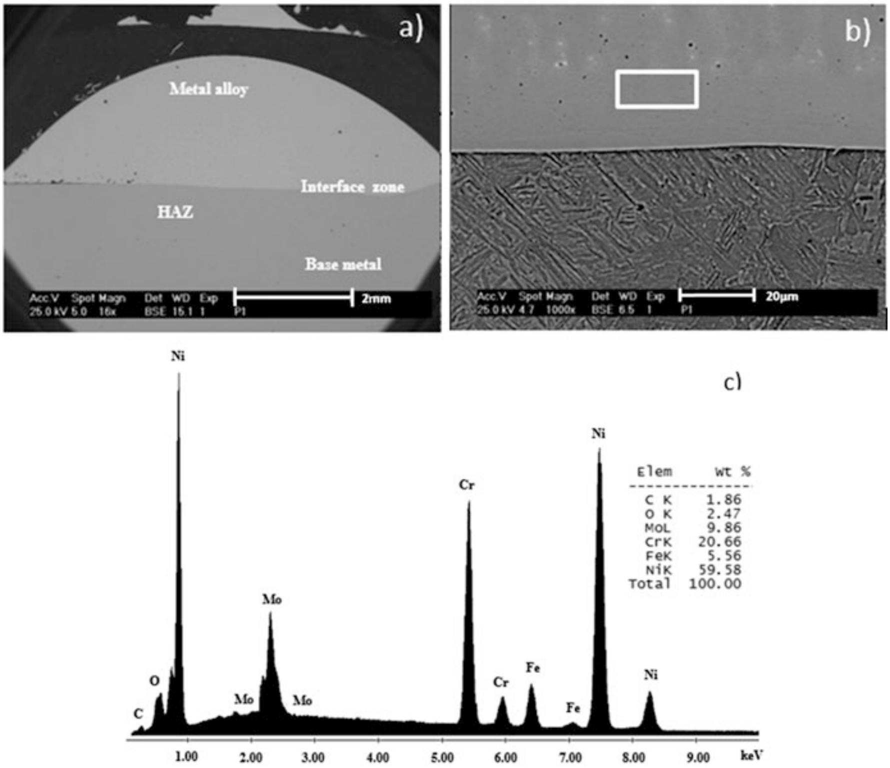

Fig. 19.4 (**a**) Back scattered electron image of the cross section of the weld bead, (**b**) microstructure of the weld bead and zone for EDS spectrum analysis, and (**c**) EDS spectrum of the overlay (metal alloy)

Figure 19.4a shows a back scattered electron image of the cross section microstructure of the weld bead or overlay deposited by PTA process. As it can be observed the microstructure consists of the weld bead (nickel base alloy), interface zone, the heat affected zone (HAZ), and a base metal [11]. Figure 19.4b shows a microstructure of base metal and the rectangle specifies an amplified zone for a sample of base metal selected to examine by EDS. The EDS spectrum corresponding to base metal presents high content of Ni and Cr, Fig. 19.4c. The deposits obtained using a low feed rate, welding current, and speed parameters of plasma transferred arc process exhibit a low percentage of dilution and good geometry on the weld bead.

The results of the hardness test of the samples with Ni base filler metal are shown in Fig. 19.5a, the microstructure in Fig. 19.5b illustrates the zones where hardness was measured. The hardness traverse of sample 6 presents a homogeneous progress, thus again it is checked that the sample 6 shows the best combination of parameters, specifically the parameters with low values. The sample 6 does not

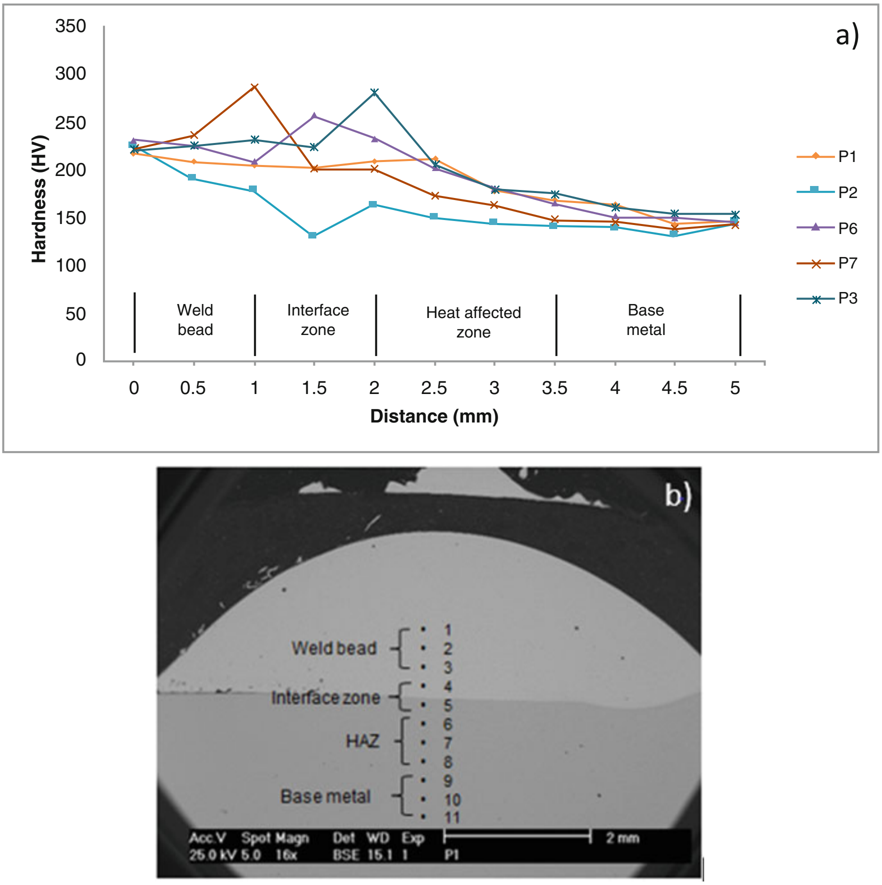

Fig. 19.5 (**a**) Hardness profiles for coatings using Ni base filler metal on A36 steel and (**b**) microstructure illustrating the indentation zones performed in the sample

present significant changes in hardness profile obtained but hardness of base metal increases by coating performed and provides longer life to the material.

In comparison with results obtained by Siva et al. [12], the plots of main effects for dilution showed in Fig. 19.6a obtained by DOE, showed a similar behavior in relation at welding current range. When the current welding are low, there is a decrease of the percentage of dilution, as is shown in Fig. 19.6b. This is attributed to the fact that the heat input to the base metal increases when this parameter is increased. Dilution percentage decreases steadily with increase in welding speed (S). This is attributed to the reduced heat input per unit length of weld bead when S is increased (Fig. 19.6c) [13, 14].

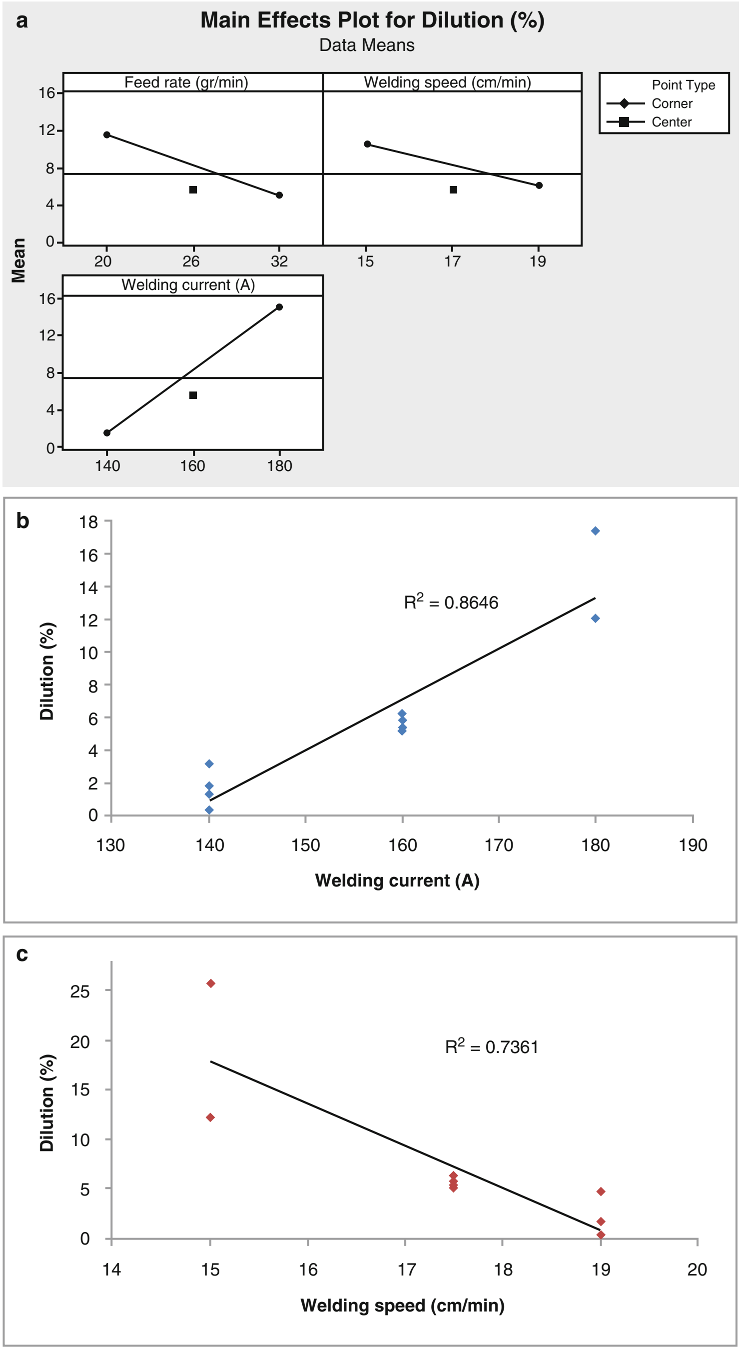

Fig. 19.6 (**a**) Main effects plot for dilution (**b**) Welding current effect over dilution (**c**) Welding speed effect over dilution

19.4 Conclusions

Dilution percent increases with an increase in welding current as a result of the heat input.

Dilution percent decreases with an increase in welding speed.

According to results obtained from design of experiments (DOE) it is suggested that feed rate has not relationship with the parameters of welding speed and welding current but it's necessary the control of this parameter.

The N-625 filler metal can be used like a coating over the pipes to bring more lifetime, such a result can be measured by the profile hardness.

The optimal conditions to obtain a good coating in order of low dilution percent are: welding speed (19 cm/min), welding current (140 A), and feed rate (20 gr/min).

The combination of parameters with lower values enables a dilution less than 5 %.

References

1. Balamurugan S, Murugan N (2013) Simulation of plasma transferred arc (PTA) hardfaced on structural steel with titanium carbide. J Eng Comput Appl Sci 2:10–14
2. Davis JR (1993) Hardfacing, weld cladding and dissimilar metal joining. In: ASM handbook-welding, brazing and soldering, 10th edn. ASM, Metals Park
3. Lucas W (1990) TIG and PLASMA welding, Abington Publishing, Cambridge
4. Gruzdys E, Meskinis S (2011) Influence of plasma transferred arc process parameters on structure and mechanical properties of wear resistive NiCrBSi-WC/Co coatings. Mater Sci 17:140–144
5. Kumar S, Mondal DP, Khaira HK (1999) Improvement in high stress abrasive wear property of steel by hardfacing. J Mater Eng Perform 8:711–715
6. Silva Prasad K, Srinivasa Ch, Nageswara D (2011) Prediction of weld bead geometry in plasma arc welding using factorial design approach. J Miner Mater Charact Eng 10:875–886
7. Eschnauer H (1980) Hard material powders and hard alloy powders for plasma surface coating. Thin Solid Films 73:1–17
8. Das CR, Albert SK, Bhaduri AK, Kempulraj G (2003) A novel procedure for fabrication of wear-resistant bushes for high-temperature application. J Mater Process Technol 141:60–66
9. Gunaraj V, Murugan N (1999) Prediction and comparison of the area of the heat-affected zone for the bead-on-plate and bead-on-joint in submerged arc welding of pipes. J Mater Process Technol 95:246–261
10. Kou S (2002) Welding metallurgy, 2nd edn. Wiley, Hoboken
11. Vergara V, Dutra J, Climaco S (2011) Hardfacing by plasma transferred arc process. InTech, Croatia
12. Siva K, Murugan N, Raghupathy VP (2009) Modeling, analysis and optimization of weld bead parameters of nickel based overlay deposited by plasma transferred arc surfacing. Int Sci J 1:174–182
13. Balasubramian V, Babu S, Lakashminarayanan AK (2008) Understanding the parameters controlling plasma transferred arc hardfacing using response surface methodology. Mater Manuf Process 23:674–682 (Taylor and Francis group)
14. Wilden J, Bergmann JP, Frank H (2006) Plasma transferred arc welding modeling and experimental optimization. J Therm Spray Technol 15(4):779–784 (ASM International)

Part IX
Characterization of Intermetallic Materials

This part includes a chapter related to the characterization of FeAl intermetallic obtained by chemical reduction method. Iron aluminides offer relatively low material cost, conservation of strategic elements, and a lower density than stainless steels. The results represent a simpler route via chemical synthesis to obtain Fe-Al based intermetallic nanoparticles for potential biomedical applications. This research is focused on the size and shape synthesis of iron–aluminum with a simple, reproducible, and low-cost wet chemical process. The obtained nano-dimensional powders were characterized by X-Ray diffraction and scanning electron microscopy to study the influence and the morphological control and reaction mechanism in the shape and size of the particles.

The results suggest that chemical synthesis method to obtain Fe-Al based intermetallic nanoparticles is a feasible process with low energy supply. Nanoscale sizes of intermetallic particles have higher potential in nanostructured biomaterials for biomedical applications.

The main techniques used in the characterization of these materials are:

- Differential scanning calorimetry (DSC).
- Thermogravimetric analysis (TGA).
- X-ray diffraction (XRD).
- Scanning electron microscopy (SEM).
- Optical microscopy.
- Energy-dispersive X-ray spectroscopy (EDS).

Chapter 20
Chemical Reduction Synthesis of Iron Aluminum Powders

N.N. Zurita-Méndez, G. Carbajal-De la Torre, L. Ballesteros-Almanza, M. Villagómez-Galindo, A. Sánchez-Castillo, and M.A. Espinosa-Medina

Abstract In this study, a chemical reduction synthesis method of iron aluminum (FeAl) nano-dimensional intermetallic powders is described. The process has two stages: a salt reduction and solvent evaporation by a heat treatment at 1100°C. The precursors of the synthesis are ferric chloride, aluminum foil chips, a mix of Toluene/THF in a 75/25 volume relationship, and concentrated hydrochloric acid as initiator of the reaction. The reaction time was 20 days, the product obtained was dried at 60 °C for 2 h and calcined at 400, 800, and 1100 °C for 4 h each. To characterize and confirm the obtained synthesis products, X-Ray Diffraction (XRD), and Scanning Electron Microscopy (SEM) techniques were used. The results of morphology and chemical characterization of nano-dimensional powders obtained showed a formation of agglomerated particles of a size range of approximately 150 nm to 1.0 µm. Composition of powders was identified as corundum (Al_2O_3), iron aluminide ($FeAl_3$), and iron-aluminum oxides $(Fe_{0.53}Al_{0.47})_2O_3$ phases. The oxide phases formation were associated with the reaction of atmospheric concentration-free oxygen during synthesis and sintering steps, reducing the concentration of the iron aluminum phase.

Keywords Iron-aluminum • Chemical reduction synthesis • Nano-dimensional powders

20.1 Introduction

Determination of regularities that allow one to obtain nanocompositions with the specified properties by methods of chemical dispersion is very important, first of all, for the possibility of affecting the dimensional characteristics of the final

---

N.N. Zurita-Méndez • G. Carbajal-De la Torre • M. Villagómez-Galindo • A. Sánchez-Castillo • M.A. Espinosa-Medina (✉)
Facultad de Ingeniería Mecánica, UMSNH, C.P. 58000, Morelia, Michoacán, Mexico
e-mail: marespmed@gmail.com

L. Ballesteros-Almanza
Facultad de Biología, UMSNH, C.P. 58000, Morelia, Michoacán, Mexico

R. Pérez Campos et al. (eds.), *Characterization of Metals and Alloys*, DOI 10.1007/978-3-319-31694-9_20

product [1]. The improved understanding of the factors that control microstructure and properties of Al-based intermetallics entails the development of methods to improve its mechanical properties by microstructural control. Refinement of grain sizes to nanometer dimensions is predicted to enhance the ductility, fracture toughness, and strength of intermetallics. Iron aluminides offer relatively low material cost, conservation of strategic elements, and a lower density than stainless steels. Electrical resistivity of iron aluminides increases with the increase of aluminum content, and the electrical resistivity of FeAl-based alloys are 50–100 % higher than those of commercially available heating-element materials. Alternatively, the excellent corrosion and oxidation resistance of iron aluminides suggests their possible usefulness as a coating against corrosion, wear, and thermal adjustment [2–5]. The processing and application of iron aluminides intermetallics are very difficult because of the difference between iron and aluminum melting points, which demands an optimized processing technique, and embrittlement at ambient temperature [6]. Nano-dimensional materials are of special interest for a number of important technological applications [7].

Concerning FeAl-based intermetallics, an increase in the mechanical properties at room temperature has been observed with decreasing particle size [8]. In this sense, it is expected that the reduction in size to nanoscale substantially increases the strength of the material [9]. Thus, in order to obtain nanometric-sized FeAl particles, the laser vaporization method [10] has be used, resulting in particles with magnetic properties, but condensation controlled by laser vaporization [11] and spray pyrolysis [12] are common methods to produce small size particles. In the chemical reduction method, the use of a precursor to promote the nanoparticle (as FeAl) formation should be included, reacting in solid state by heat treatment application. In this route, the energy needed to obtain the solid-state reaction decreases due to precursor homogeneous mixture [13].

In the chemical reduction method, borohydrides such as $NaBH_4$ and $LiBH_4$, the super-hydrides $NaBEt_3H$ and $LiBEt_3H$, alkaline or $[K^+(15C5)2e^-]$ dissolved electrolytes (where C5 is a ringed ether), the $M(MgCl)_m$ Grignard reagents (where M = metal vapor and Mg) are used as reducers of metallic salts to obtain the nanometric size particles [14, 15]. Then, with the use of this method, Haber et al. [16, 17] synthesized nickel and titanium aluminides satisfactorily. But, Pithawalla and Deevi [18] had obtained iron aluminide (FeAl) and iron aluminum carbide ($Fe_3AlC_{0.5}$) nanopowders by reduction of iron chloride ($FeCl_3$) with lithium aluminum hydride ($LiAlH_4$) chemical synthesis followed by heat treatment at 550 °C; both FeAl and $Fe_3AlC_{0.5}$ nanoparticles formed were embedded within aluminum oxide matrices. In this paper, we will focus on the size and shape synthesis of iron–aluminum with a simple, reproducible, and low-cost wet chemical process. The obtained nanodimensional powders were characterized by XRD and SEM to study the influence and the morphological control and reaction mechanism in the shape and size of the particles.

20.2 Experimental

The synthesis of iron–aluminum nano-dimensional powders was prepared by mixing under continuous stirring ferric chloride in a solution of toluene/THF with a 75/25 volume relationship and heating at 70 °C for 1 h. Then aluminum foil chips and HCl were added to the $FeCl_3$ solution. As the reduction reaction was developed at an environmental atmosphere, the oxygen present in the air reacted with the aluminum forming alumina, and an iron–aluminum oxide, so the general reaction is:

$$\begin{aligned}2.84FeCl_3 + 6Al_0 + 8HCl + 3O_2 \rightarrow FeAl + Fe_{1.84}Al_{0.16}O_3 + Al_2O_3 + 2.84AlCl_3 \\ + 2HCl + 2H_2\uparrow + 3Cl_2\uparrow\end{aligned}$$

The reaction persisted for 20 days with permanent stirring and was then dried for 2 h in an oven at 60 °C. Then a thermal treatment at 400, 800, and 1100 °C was performed on the powder for 4 h each. The gray-colored powders were then crushed and taken for thermal gravimetric analysis (TGA) and the differential scanning calorimetry (DSC/TGA) in nitrogen gas flow, XRD analysis and characterized by SEM.

The morphology and size of nanopowders were observed using SEM (JSM-6400), operated at an accelerating voltage of 15 kV. The powders were mounted in a sample holder using double-sided conductive carbon tape and then were coated with copper by sputtering. XRD (D8 Advance BRUKER) analysis was performed for all powders using Cu K_α radiation, $\lambda = 1.54$ Å, angle 2θ from 20° to 90° with an increment of 0.04 and a passing time of 0.3 s.

20.3 Results and Discussion

According to the proposed reaction, it can be inferred that the aluminum chloride salt formed and the hydrochloric acid excess were decomposed upon completion of the thermal treatment at 800 and 1100 °C, which is why those species do not appear in the XRD analysis. However, for quantitative analysis by Energy Dispersive X-ray Spectroscopy (EDS), traces of chlorine were detected. Figure 20.1 shows the TGA/DSC results of the powder as was obtained by chemical reduction synthesis. Around 200 °C, lost mass was associated with evaporation of hydrochloric acid, endothermal peak in the DSC (at 158 °C) is observed, which was associated to the energy observed in order to break chemical bonds of amorphous solid particles of acidic compounds. Around 460 °C, maximus DSC exothermal peak was associated with the recrystallization step of amorphous phases to crystalline ones. It requires some time for microstructure transition associated with the heating temperature, when approximately 800 °C temperature is reached, the expected crystalline transition is completed, after which the temperature sample lost minimus mass. These results were the basis to explore heat treatments at 400, 800, and 1100 °C.

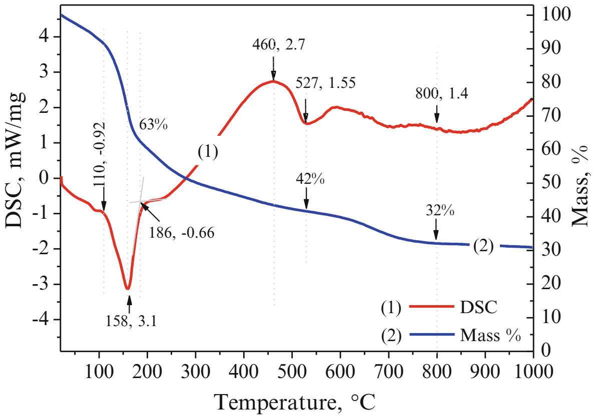

Fig. 20.1 DSC and TGA results of powder obtained by chemical reduction synthesis

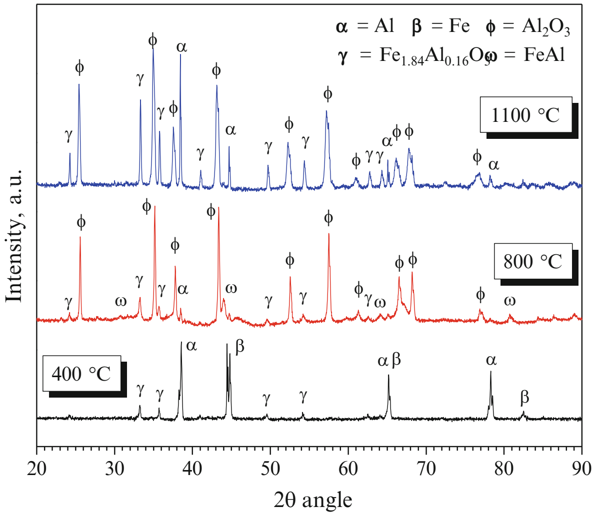

Fig. 20.2 XRD patterns of the prepared powder sample

XRD patterns of the samples obtained after different thermal treatment are shown in Fig. 20.2. The XRD analysis confirms the presence of the principal precursors (Fe and Al) and the incipient formation of an iron–aluminum oxide $Fe_{1.84}Al_{0.16}O_3$ phase when the thermal treatment was at 400 °C. The diffraction pattern when the calcination process was at 800 °C shows the alumina (α-Al_2O_3) phase, the iron–aluminum oxide $Fe_{1.84}Al_{0.16}O_3$, and the iron–aluminum FeAl. The Powder Diffraction File (PDF) 00-045-0983 corresponds to the cubic structure of $Fe_{0.5}Al_{0.5}$. The thermal treatment at 1100 °C just steps up the iron–aluminum oxide phase.

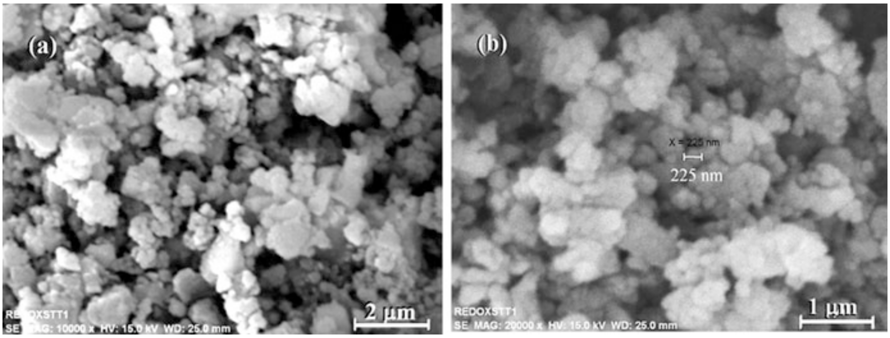

Fig. 20.3 SEM micrographs of the synthesized particles treated at 400 °C. (**a**) Agglomerates of particles. (**b**) Arbitrary measure of a particle

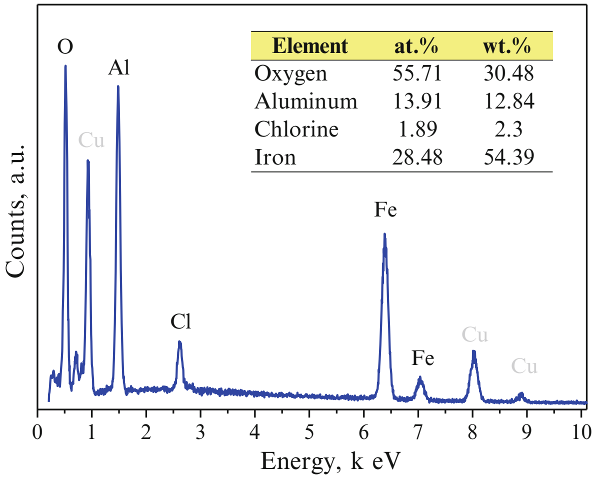

Element	at.%	wt.%
Oxygen	55.71	30.48
Aluminum	13.91	12.84
Chlorine	1.89	2.3
Iron	28.48	54.39

Fig. 20.4 Quantitative EDS analysis of agglomerates of nano-dimensional powders showed in Fig. 20.3

The distribution and morphology of the synthesized particles heat treated at 400 °C visualized by SEM show that, in all cases, the prepared particles are nano-sized, nearly spherical in shape, and tend to agglomerate, and they can be observed in Fig. 20.3. These microphotographs show agglomerates of nano-dimensional powders and the EDS (Fig. 20.4) exhibit traces of chlorine.

Figure 20.5 shows the morphology and distribution of the synthesized nano-dimensional powders at 800 °C of thermal treatment; in this sample, we can find three different shapes: (a) spheres, (b) nano rods and (c) nanoparticles agglomerates.

From the morphologies observed in Fig. 20.5, the quantitative EDS analysis of the representative areas was made. Table 20.1 showed the semi-quantitative atomic proportion of comparative chemical elements: iron, aluminum, and oxygen. Figure 20.6 shows spectrograms of EDS of three particles or zones. EDS quantifications

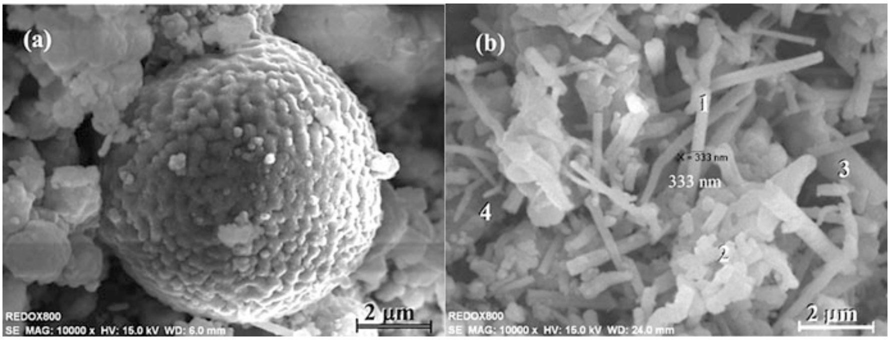

Fig. 20.5 SEM microphotographs of the synthesized particles treated at 800 °C. (**a**) Micrometric sphere (7.3 µm approx.). (**b**) Nano-rods of 333 nm diameter

Table 20.1 Quantitative analysis EDS of representative zones of microphotographs in Fig. 20.5

Element	Zone 1 at. %	Zone 2 at. %	Zone 3 at. %	Zone 4 at. %	Sphere at. %
Oxygen	79.88	78.49	49.11	63.54	63.39
Aluminum	18.46	19.06	31.46	31.88	28.30
Iron	1.66	2.44	19.44	4.58	8.31

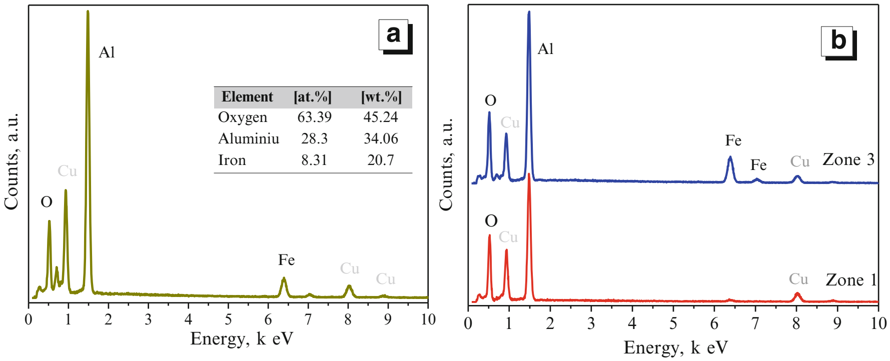

Element	[at.%]	[wt.%]
Oxygen	63.39	45.24
Aluminiu	28.3	34.06
Iron	8.31	20.7

Fig. 20.6 Quantitative EDS analysis of (**a**) Spherical particle in Fig. 20.5a. (**b**) Zone 1 and zone 3 of Fig. 20.5b

shows that the atomic percentage of nano-rods indicated with the number 1 and the particle agglomeration indicated by number 2 correspond to the crystal phase α-Al_2O_3 alumina. Number 3 represents a 1:1 stoichiometry of elements Fe and Al belonging to the crystalline phase FeAl; while number 4 describes the iron–aluminum oxide $Fe_{1.84}Al_{0.16}O_3$. The sphere corresponds to an iron–aluminum oxide, but with a $FeAl_{3.4}0_{7.6}$ stoichiometry. It should be emphasized that particles formed by iron from solution on an aluminum are always spherical.

Continuing with the heat treatment and increasing the temperature to 1100 °C, the Fe-Al phase becomes oxidized, turning into iron–aluminum oxide and changing its morphology, which is observable in the SEM micrographs shown in Fig. 20.7.

In those images, the agglomeration of nanoparticles iron–aluminum oxides can be observed. The chemical synthesis of the nano-dimensional FeAl intermetallic powders was worked at atmospheric conditions, which is why the surrounding oxygen caused the oxidation of metals, especially aluminum forming the α-Al_2O_3 phase whose morphology as nano-rods are of great interest in applications such as temperature insulators for metals and polymers [19]. A disadvantage of these particles is the crystallization of the α-Al_2O_3 at high temperature (1100 °C), which increased grain growth by approximately the diameter of the particles as is shown in Fig. 20.8, which in turn drastically reduced its mechanical properties [20].

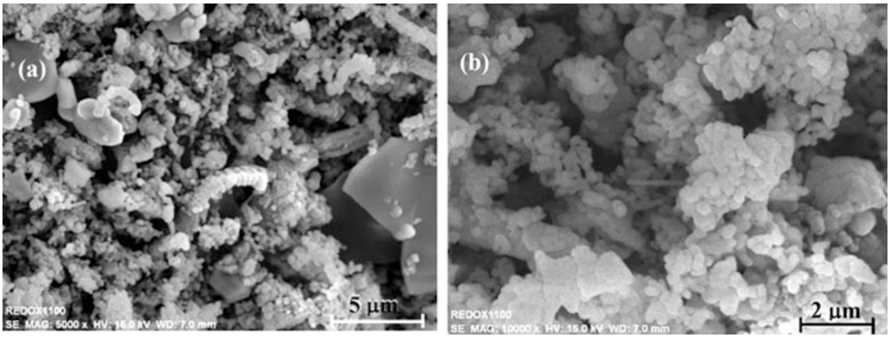

Fig. 20.7 SEM microphotographs of the reduction synthesis treated at 1100 °C

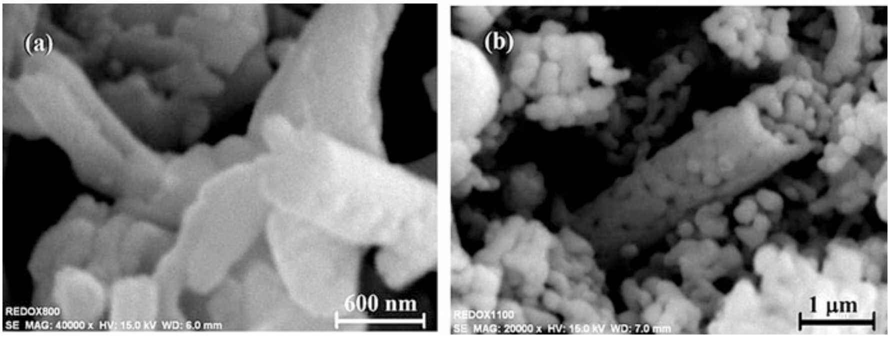

Fig. 20.8 (**a**) Alumina nano-rods. (**b**) Alumina crystal growth at 1100 °C

20.4 Conclusions

Nano-dimensional intermetallic FeAl powders by a chemical reduction synthesis in atmospheric conditions followed with an 800 °C heat-treatment application were obtained. The time of reaction was 20 days.

Composition of powders was identified as corundum: Al_2O_3, iron aluminide: $FeAl_3$, and iron–aluminum oxides: $(Fe_{0.53}Al_{0.47})_2O_3$ phases. The formation of oxides phases were associated with the reaction of oxygen from atmosphere during synthesis and sintering steps, reducing the formation of iron–aluminum phases.

The results of morphology and chemical characterization of nano-dimensional powders obtained showed a formation of agglomerated particles of a size range around 150 nm–1.0 μm. The SEM characterization showed the obtained alumina particles morphology from heat treatment at 800 °C was nano-rod of approximately a 333 nm diameter. The iron–aluminum oxide spheres showed an approximate 7.3 μm diameter size.

Acknowledgements The present research was supported by CONACYT for the project financing Number: 243236 of CB-2014-02, I0017 Fund.

References

1. Ryzhonkov DI, Levina VV, Dzidziguri EL, Khrustov EN (2008) Controlling the properties of nanodimensional metal oxide powders via introduction of dispersing additions. Russ J Non Ferr Met 49:308–313
2. Marulanda-Arevalo JL, Castañeda-Quintana S, Remolina-Millan A (2013) Coating deposited by CVD-FBR for protection at high temperature. Dyna 80:181–191
3. McKamey CG, DeVan JH, Tortorelli PF, Sikka VK (1991) A review of recent developments in Fe3Al-based alloys. J Mater Res 6:1779–1805
4. Stoloff NS, Liu CT, Deevi SC (2000) Emerging applications of intermetallics. Intermetallics 8:1313–1320
5. Deevi SC, Sikka VK (1996) Nickel and iron aluminides: an overview on properties, processing and applications. Intermetallics 4:357–376
6. Banovic SW, DuPont JN, Tortorelli PF, Marder AR (1999) The role of aluminum on the welding and sulfidation behavior of iron-aluminum cladding. Weld J 78:23s–30s
7. Khachatryan A, Sarkissyan R, Hassratyan L, Khachatryan V (2004) Influence of ultrasound on nanostructural iron formed by electrochemical reduction. Ultrason Sonochem 11:405–408
8. Amils X, Nogués J, Suriñach S, Baro MD, Muñoz-Morris MA, Morris DG (2000) Hardening and softening of FeAl during milling and annealing. Intermetallics 8:805–813
9. Provenzano V, Valiev R, Rickerby DG, Valdre G (1999) Mechanical properties of nanostructured chromium. Nanostruct Mater 12:1103–1108
10. Reddy V, Khanna SN, Deevi (2001) SC electronic structure and magnetism in $(FeAl)n(n \leqslant 6)$ clusters. Chem Phys Lett 333:465–470
11. Pithawalla YB, El-Shall MS, Deevi S (2003) Laser based synthesis of intermetallic Cu–Zn nanoparticles and filaments. Scr Mater 48:671–676
12. Eroglu S, Zhang SC, Messing GL (1996) Synthesis of nanocrystalline Ni–Fe alloy powders by spray pyrolysis. J Mater Res 11:2131–2134

13. Gonsalves KE, Rangarajan SP, Wang J (2000) In: Nalwa HA (ed) Handbook of nanostructured materials and nanotechnology: synthesis and processing, vol 1. Academic, San Diego
14. Lu Q, Hu J, Tang K, Qian Y, Zhou G, Liu X (1999) Benzene-thermal co-reduction reaction for nanocrystalline intermetallics Fe3Si and Ni3Al. Solid State Ion 124:317–321
15. Sohn HY, Paldey S (1998) Synthesis of ultrafine particles of intermetallic compounds by the vapor-phase magnesium reduction of chloride mixtures: part II. Nickel Aluminides Metall Mater Trans B 29:465–469
16. Haber JA, Gunda NV, Balbach JJ, Conradi MS, Buhro WE (2000) Chemical syntheses of nanocrystalline nickel aluminides. Chem Mater 12:973–982
17. Haber JA, Gunda NV, Buhro WE (1998) Nanostructure by design: solution-phase-processing routes to nanocrystalline metals, ceramics, intermetallic, and composites. J Aerosol Sci 29:637–645
18. Pithawalla YB, Deevi S (2004) Chemical synthesis of iron aluminide [FeAl] and iron aluminum carbide [Fe3AlC0.5] nanopowders. Mater Res Bull 39:2303–2316
19. Lucuta PG, Halliday JD, Christian B (1992) Phase evolution in Al2O3 fibre prepared from an oxychloride precursor. J Mater Sci 27:6053–6061
20. Haberkorn N, Zolotucho HA, González-Oliver CJR (2000) Precursores de fibras de alúmina pura y alúmina dopada y la transformación δ-Al_2O_3 a α-Al_2O_3, mediante análisis diferencial térmico. In: Jornadas SAM 2000 - IV Coloquio Latinoamericano de Fractura y Fatiga, Agosto de 2000, pp 917-923

Author Index

R. Pérez Campos et al. (eds.), *Characterization of Metals and Alloys*, DOI 10.1007/978-3-319-31694-9

Subject Index

R. Pérez Campos et al. (eds.), *Characterization of Metals and Alloys*, DOI 10.1007/978-3-319-31694-9